The Superconductor-Insulator Transition in the $LaAlO_3$-$SrTiO_3$ Electron System

Tunneling and Field Effect Investigations

MAX-PLANCK-GESELLSCHAFT

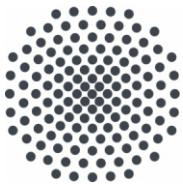

Universität Stuttgart

Lukas Kürten

Max-Planck-Institut für Festkörperforschung
Universität Stuttgart

MAX-PLANCK-GESELLSCHAFT

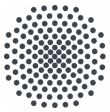

Universität Stuttgart

The Superconductor-Insulator Transition in the $LaAlO_3$ – $SrTiO_3$ Electron System

Tunneling and Field Effect Investigations

Von der Fakultät Mathematik und Physik der Universität Stuttgart
zur Erlangung der Würde eines Doktors der Naturwissenschaften (Dr. rer. nat.)
genehmigte Abhandlung

vorgelegt von

Lukas Kürten

aus Lindlar

Hauptberichter: Prof. Dr. Jochen Mannhart
Mitberichter: Prof. Dr. Martin Dressel

Tag der mündlichen Prüfung: 14.11.2017

Max-Planck-Institut für Festkörperforschung
Universität Stuttgart
2017

CONTENTS

LIST OF FIGURES

GLOSSARY

2DES two-dimensional electron system

ABS Andreev bound states

AFM atomic force microscopy

BCS Bardeen-Cooper-Schrieffer

BKT Berezinski-Kosterlitz-Thouless

FET field-effect transistor

JJA Josephson junction array

MBE molecular beam epitaxy

MBS Majorana bound states

PCC piston cylinder cell

PLD pulsed laser deposition

PPMS physical property measurement system

RHEED reflectivity high energy electron diffraction

SC superconductor

SIS superconductor-insulator-superconductor

SIT superconductor-insulator transition

SMU source measure unit

u.c. unit cell

VI virtual instrument

YSR Yu-Shiba-Rusinov

ZUSAMMENFASSUNG

Supraleitung in korrelierten Elektronensystemen in Übergangsmetall-Oxiden ist ein faszinierendes und komplexes Phänomen, welches in den vergangenen drei Jahrzenten intensiv erforscht wurde [1–3]. Der Mechanismus der Supraleitung in diesen Systemen ist jedoch noch immer nicht vollständig verstanden und bleibt weiterhin eine der wichtigen offenen Fragen der Festkörperphysik. Die vorliegende Arbeit soll zum Verständnis der Supraleitung in Übergangsmetall-Oxiden beitragen, insbesondere im Elektronensystem der $LaAlO_3$–$SrTiO_3$-Grenzfläche.

Elektronen in dotierten Halbleitern und in Metallen bilden ein Fermi-Gas mit geringer Dichte und können in einem auf die Molekularfeldnäherung gestützten Bändermodell beschrieben werden. Im Gegensatz dazu sind in isolierenden Materialien die Elektronen fest an ihre Orbitale gebunden. In Übergangsmetall-Oxiden jedoch befinden sich die Elektronen in Übergangszuständen zwischen Energiebändern und Orbitalen. Diese Zustände können delokalisiert sein, d.h. Ladungstransport ist möglich, aber die Elektronen zeigen weiterhin charakteristische Eigenschaften ihres Orbitals. In dieser komplexen Situation, in der das Verhalten der Elektronen weder im Bänder- noch im Orbital-Modell beschrieben werden kann, bringen elektronische Korrelationen, sich gegenseitig bedingende Ordnungen von Spin, Ladung und Orbitalen und emergente Phänomene neue und faszinierende Eigenschaften hervor, zum Beispiel den kolossalen Magnetowiderstand [4, 5], Ferroelektrizität [6] oder spintronische Effekte [7, 8]. Eines der faszinierendsten Phänomene, die in korrelierten Elektronensystemen in Oxiden beobachtet werden, ist die Hochtemperatur-Supraleitung in Kupferoxid-Materialien [2, 3].

Die große Vielseitigkeit der Übergangsmetall-Oxide, zum Beispiel ihre Fähigkeit verschiedene Valenzzustände anzunehmen, impliziert, dass es entscheidend ist die Materialeigenschaften präzise kontrollieren zu können. Zu diesem Zweck spielen mittels Aufdampftechniken gewachsene Dünnschicht-Filme und Heterostrukturen komplexer Materialien eine besonders wichtige Rolle [9]. Aufdampfmethoden wie Molekularstrahl-Epitaxie (engl. molecular beam epitaxy, MBE) und gepulste Laser-Deposition (engl. pulsed laser deposition, PLD) ermöglichen das Wachstum dünner Materialschichten mit wohldefinierter Struktur und Stöchiometrie. Zwei der wichtigsten Beispiele sind die zweidimensionalen Elektronengase mit hoher Ladungsträgermobilität in mittels MBE gewachsenen Heterostrukturen von Halbleitern [10] und Hochtemperatur-Supraleitung in Dünnschichtfilmen von Oxiden, z.B. mittels PLD gewachsenes $YBa_2Cu_30_{7-\delta}$ [3].

Im Fall dieser beiden Beispiele (wie auch in vielen anderen) liegen die beweglichen Elektronen in zweidimensionalen Ebenen vor. Solche zweidimensionalen Elektronensysteme (engl. two-dimensional electron system, 2DES) unterscheiden sich in vielerlei Hinsicht von dreidimensionalen Elektronensytemen. Für den Fall, dass das 2DES einen supraleitenden Grundzustand aufweist, kann beispielsweise ein Quantenphasenübergang zwischen supraleitendem und isolierendem Zustand beobachtet werden [11–13]. Im Gegensatz zu herkömmlichen *thermodynamischen*

Phasenübergängen findet dieser *Quanten*phasenübergang bei der Temperatur des absoluten Nullpunkts statt. Da in allen Hochtemperatur-Kupferoxid-Supraleitern die Supraleitung in den Kupfer-Sauerstoff-Ebenen stattfindet und diese Supraleiter in Abhängigkeit von der Dotierung einen solchen Supraleiter-Isolator-Übergang (engl. superconductor-insulator transition, SIT) durchlaufen, können Untersuchungen des SIT neue Erkenntnisse über diese Systeme liefern. Der SIT ist aufgrund der drastischen Veränderung des Widerstands von einem perfekt verlustfreien Leiter zu einem Isolator auch für praktische Anwendungen relevant. In der Tat gibt es Voraussagen, dass einer der Endpunkte des SIT ein *superisolierender* Zustand mit außergewöhnlich hohem Widerstand sein könnte [14–16].

Ein weiterer besonderer Phasenübergang, der in zweidimensionalen Supraleitern beobachtet werden kann, ist der topologische Berezinksi-Kosterlitz-Thouless (BKT)-Phasenübergang, welcher bei endlicher Temperatur auftritt, aber topologische Eigenschaften besitzt. Da in der Theorie des BKT-Phasenübergangs zum ersten Mal das Konzept der Topologie in der Physik verwendet wurde, welches nun in der Festkörperphysik zu einem wichtigen Feld geworden ist, wurden Kosterlitz und Thouless dafür im Jahr 2016 mit dem Nobelpreis geehrt. Der BKT-Phasenübergang ist jedoch schwer zu beobachten, da er nur in einem sehr kleinen Temperaturbereich auftritt und die Auswirkungen von Temperaturschwankungen leicht mit den Merkmalen des Phasenübergangs verwechselt werden können [17].

Die vorliegende Arbeit beschreibt Untersuchungen der Supraleiter-Isolator- und BKT-Phasenübergänge in einem zweidimensionalen Supraleiter aus Übergangsmetall-Oxiden: dem Elektronensystem an der $LaAlO_3$–$SrTiO_3$-Grenzfläche. Dünne Schichten des Isolators $LaAlO_3$, welche epitaktisch auf Substrate aus dem Isolator $SrTiO_3$ gewachsen werden, erzeugen ein 2DES an der Grenzfläche der beiden Materialien. Der Grundzustand kann mittels einer Gate-Spannung von Supraleiter zu Isolator umgeschaltet werden. Daher ist das Grenzflächen-2DES ein nützliches Instrument zur Untersuchung dieser Phasenübergänge. Zudem zeigt $LaAlO_3$–$SrTiO_3$ eine Phase, welche der Pseudogap-Phase in den Kupferoxid-Supraleitern ähnlich ist: In dieser Phase wird ein endlicher Widerstand für den Transport von Elektronen gemessen, aber Tunnel-Experimente zeigen eine Lücke in der Zustandsdichte der Elektronen [18]. Diese Beobachtungen sind in der gewöhnlichen Bardeen-Cooper-Schrieffer (BCS) - Theorie der Supraleitung nicht zu erklären.

Die Phasenübergänge wurden mittels zweier komplementärer Methoden untersucht: Einerseits durch Tunnel-Experimente an Proben mit Gate-Elektroden an der Rückseite und andererseits durch die Konstruktion supraleitender Transistoren, in denen das Elektronensystem durch eine Gate-Spannung an der Oberfläche kontrolliert wird. Tunnelspektroskopie ist ein wertvolles Instrument um Supraleiter zu untersuchen, da es eine direkte Messung der elektronischen Zustandsdichte möglich macht und somit die supraleitenden Bandlücke Δ und andere Eigenschaften des supraleitenden Kondensats bestimmt werden können [19]. Das 2DES an der $LaAlO_3$–$SrTiO_3$-Grenzfläche ist für Tunnelexperimente besonders geeignet, denn die $LaAlO_3$-Schicht an der Oberfläche dient intrinsisch als die für Tunnelexperimente benötigte isolierende Barriere. Werden Tunnelexperimente gemeinsam mit Messungen des Ladungstransport ausgeführt, kann bestimmt werden ob der Übergang von Supraleiter zu Isolator durch das Aufbrechen von Cooper-Paaren (d.h. $\Delta \to 0$) oder durch den Verlust der Kohärenz zwischen den Paaren (d.h. $\xi \to 0, \Delta > 0$) geschieht.

Ein Transistor ist für die Untersuchung des SIT nützlich, denn das Anlegen einer Gate-Spannung kann die Leitfähigkeit des darunter liegenden Kanals um mehrere Größenordnungen ändern. Das $LaAlO_3$–$SrTiO_3$-Elektronensystem ist der einzige bekannte Supraleiter der auf kurzen Zeitskalen durch Anlegen einer Gate-Spannung ein- und ausgeschaltet werden kann. Da ein supraleitender Transistor Strom mit Ladungsträgern in der Form von Cooper-Paaren und

nicht von einzelnen Elektronen transportier, kann erwartet werden, dass sich seine Eigenschaften von denen eines normalen Transistors erheblich unterscheiden.

Die vorliegende Arbeit beinhaltet einige neue Einblicke in die Natur des vielseitigen 2DES an der $LaAlO_3$–$SrTiO_3$-Grenzfläche, die zum besseren Verständnis dieses zweidimensionalen Elektronensystems und seines supraleitenden Grundzustands beitragen. Der Schwerpunkt der Arbeit liegt auf der Untersuchung der nur in zweidimensionalen Supraleitern beobachtbaren Phasenübergänge, der SIT und dem BKT-Phasenübergang. Die Beobachtung von Zuständen innerhalb der supraleitenden Bandlücke mittels Tunnelspektroskopie deutet darauf hin, dass noch viel über das 2DES an der $LaAlO_3$–$SrTiO_3$-Grenzfläche zu lernen ist.

Ein wichtiges Anwendungsgebiet zweidimensionaler Elektronensysteme sind Feldeffekt-Transistoren (FETs). In Kapitel 4 wird ein neuer Entwurf von FETs präsentiert. Diese Transistoren vereinen die vorherigen Arbeiten zu $LaAlO_3$–$SrTiO_3$-Transistoren [20–22] mit den Untersuchungen an $LaAlO_3$–$SrTiO_3$ unter hydrostatischem Druck [23, 24]. Dies ist die erste Untersuchung von oxidischen Transistoren unter Druck und eröffnet damit eine neue Achse des Phasendiagramms von $LaAlO_3$–$SrTiO_3$-Transistoren. Diese Messungen sind nicht nur eine Bestätigung der früheren Ergebnisse aus Referenz [23], sondern zeigen auch, dass kleinste $LaAlO_3$–$SrTiO_3$-Bauelemente auch unter extremen physikalischen Bedingungen wie einem Druck von 1.8 GPa funktionstüchtig bleiben.

Im zweiten Teil von Kapitel 4 werden die an kombinierten Transistor-Hall-Steg-Bauelementen gewonnenen Ergebnisse vorgestellt, welche neue Erkenntnisse über die Multiband-Eigenschaften des $LaAlO_3$–$SrTiO_3$-2DES ergeben. Insbesondere ermöglicht die Analyse der Transistor-Charakteristika die Existenz eines Bandes von positiven Ladungsträgern auszuschließen, welches oft bei der Analyse der Hall-Daten auftaucht. Zudem wird die Eignung von Transistoren einerseits und Hall-Stegen andererseits zur Bestimmung der Ladungsträgerdichten und Mobilitäten diskutiert, ein Ergebnis welches für alle leitfähigen Materialien relevant ist.

In Kapitel 5 wird die Änderung des senkrechten kritischen Magnetfelds H_{c2} des supraleitenden 2DES mit der Temperatur untersucht. Im Gegensatz zu der für einen herkömmlichen BCS-Supraleiter zu erwartenden parabolischen Kurve ist die Temperaturabhängigkeit von H_{c2} linear bis zur niedrigsten gemessenen Temperatur von 50 mK. Verschiedene Mechanismen können das lineare Verhalten von $H_{c2}(T)$ erklären, unter anderem Multiband-Supraleitung. Die Zweidimensionalität des supraleitenden Elektronensystems kann jedoch an sich schon eine lineare $H_{c2}(T)$-Kurve verursachen. Da in $LaAlO_3$–$SrTiO_3$, wie in allen zweidimensionalen Supraleitern, der Phasenübergang zur Supraleitung nicht scharf ist, sind die Fehlergrenzen für $H_{c2}(T)$ groß und verhindern eine klare Unterscheidung der theoretischen Modelle.

Der zu Beginn von Kapitel 6 vorgestellte ausführliche Prozess der Wachstumsoptimierung verdeutlicht die große Herausforderung bei der Untersuchung des $LaAlO_3$–$SrTiO_3$-Systems: Wegen einer großen Anzahl nicht kontrollierbarer (und manchmal unbekannter) äußerer Einflüsse können sich die Eigenschaften von nominell unter gleichen Bedingungen gewachsenen Proben signifikant unterscheiden. Offensichtlich sind weitere Fortschritte bezüglich des Wachstumsprozesses wünschenswert, insbesondere um den Einfluss des Substrats zu minimieren.

Die in Kapitel 6 vorgestellte kombinierte Analyse von Messungen in hohen magnetischen Feldern und tunnelspektroskopischen Daten legt einen Zusammenhang zwischen der Besetzung eines zusätzlichen Bandes und dem Rückgang der Supraleitung im überdotierten Bereich des $LaAlO_3$–$SrTiO_3$-Phasendiagramms nahe. Hier wurden zum ersten Mal Tunnel- und Hall - Ergebnisse der selben Probe kombiniert. Obwohl der genaue Mechanismus noch nicht klar ist, durch den die Ladungsträger des zweiten Bandes die Supraleitung der überdotierten Phase

zerstören, liefert dies eine mögliche Erklärung für das von der BCS-Theorie abweichende Verhalten des Elektronensystems in diesem Bereich des Phasendiagramms.

Die in Kapitel 6 beschriebenen Versuche, den BKT-Phasenübergang im gesamten Bereich des $LaAlO_3$–$SrTiO_3$-Phasendiagramms von Supraleiter bis Isolator zu messen waren aufgrund einer Vielzahl von Schwierigkeiten nicht erfolgreich. Das wichtigste und fundamentalste dieser Probleme ist mit Sicherheit der Wärmeeintrag in das Elektronensystem. Es sticht in Systemen wie dem $LaAlO_3$–$SrTiO_3$-Elektronensystem, welche bei Millikelvin-Temperaturen untersucht werden, besonders hervor, denn bei diesen Temperaturen ist das Elektronensystem nur schwach an die Phononen des Gitters gekoppelt, was eine effektive Kühlung erschwert. Daher werden Messungen des BKT-Übergangs in zweidimensionalen Supraleitern mit Sprungtemperaturen im Bereich des flüssigen Heliums oder darüber verlässlichere Ergebnisse liefern. Die entscheidende Frage ist, ob ein supraleitendes System existiert, in dem Supraleitung so stark ist, dass sie bei genügend hohen Temperaturen existiert und dennoch schwach genug ist, um mittels einer Gate-Spannung schaltbar zu sein.

Am Ende von Kapitel 6 wird die Gestaltung eines supraleitenden Transistors vorgestellt, in dem das Grenzflächen-Elektronensystem als supraleitender Kanal fungiert. Die Leistung dieses Transistors ist durch Einschränkungen bei der Herstellung begrenzt, aber das Schalten des Kanals mittels einer Top-Gate Spannung wurde demonstriert und das unterschiedliche Verhalten des Transistors im normal- und supraleitenden Zustand wurde gezeigt. Des Weiteren wurde deutlich, dass der Kanal beim Schalten vom supraleitenden zum isolierenden Zustand eine dazwischen liegende metallische Phase durchläuft.

Die in Kapitel 7 vorgestellten Zustände innerhalb der supraleitenden Bandlücke des $LaAlO_3$–$SrTiO_3$-2DES sind beispielhaft für die vielen faszinierenden, jedoch bisher unerklärten Phänomene die an der $LaAlO_3$–$SrTiO_3$-Grenzfläche auftreten. Obwohl eine endgültige Bestimmung der Herkunft dieser Zustände wegen ihres nicht-deterministischen Vorkommens noch aussteht, ist es durch eingehende Analyse der Daten möglich, einige der vorgeschlagenen Mechanismen mit großer Sicherheit auszuschließen. Viele der verbleibenden Hypothesen sagen die Existenz von Zuständen mit außergewöhnlichen Eigenschaften voraus, zum Beispiel gebundene Majorana-Zustände.

Ein wiederkehrendes Thema dieser Arbeit ist es, den Beitrag verschiedener Bänder zur Leitfähigkeit und Supraleitung an der $LaAlO_3$–$SrTiO_3$-Grenzfläche herauszustellen. Das sich abzeichnende Modell ist konsistent mit dem in Referenz [25] vorgestellten: Schon bei niedriger Ladungsträgerdichte sind zwei Unterbänder besetzt, und zwar das energetisch am tiefsten liegende d_{xy}-Unterband und eines der durch Rashba-Spin-Orbit-Kopplung aufgespaltenen $d_{xz/yz}$-Unterbänder. Diese Besetzung mehrerer Bänder auch bei niedriger Ladungsträgerdichte kann mit dem folgenden Argument begründet werden: Tunnelströme senkrecht zur Oberfläche können wegen der Impulserhaltung nur von den energetisch höher liegenden $d_{xz/yz}$-Unterbändern aufgenommen werden, aber ein Tunnelstrom ist für alle Gate-Spannungen, bei denen das Elektronensystem leitfähig ist, zu beobachten. Dies impliziert, dass das energetisch niedriger liegende d_{xy}-Unterband auch besetzt sein muss. Die Beobachtung mehrerer Frequenzen in den in Abschnitt 6.1.2 beschriebenen Shubnikov-de Haas-Oszillationen ist ein weiterer Hinweis für Transport in mehreren Bändern auch bei niedriger Ladungsträgerdichte.

Für höhere Ladungsträgerdichten wird ein weiteres Band besetzt, wie die Hall-Messungen in Abschnitt 6.1.1 zeigen. Die Ladungsträger in diesem zusätzlichen Band, das energetisch höher liegende der Rashba-gespaltenen $d_{xz/yz}$-Unterbänder, tragen nicht zur Supraleitung bei, sondern verringern T_c, möglicherweise durch verstärkte Elektron-Elektron-Streuung. Daher zeigen die Tunneldaten, dass das niedriger liegende der $d_{xz/yz}$-Unterbänder supraleitend ist, die

Hall-Messungen jedoch lassen vermuten, dass dies für den energetisch höher liegenden Partner nicht zutrifft. Die Frage, ob das d_{xy}-Unterband ebenfalls supraleitend ist, konnte durch die Messungen in Kapitel 5 nicht abschließend geklärt werden und bleibt weiterhin offen. Wenn es jedoch supraleitend wäre, könnte seine Wechselwirkung mit dem anderen supraleitenden Band ein möglicher Ursprung der in Kapitel 7 beschrieben Zustände in der supraleitenden Bandlücke sein.

In einem anderen Szenario ist es aber auch möglich, dass das d_{xy}-Unterband überhaupt nicht leitfähig ist: Die Ladungsträger sind zwar vorhanden, aber weil die Elektronen sich so nahe an der Grenzfläche und der damit verbundenen hohen Dichte von Defekten befinden, sind sie so gut wie lokalisiert [26]. Diese Hypothese könnte erklären, warum die in dieser Arbeit vorgestellten Hall-Messungen Einzelband-Verhalten bei negativen Back-Gate-Spannungen zeigen, warum die gemessene Ladungsträgerdichte an der Grenzfläche immer kleiner ist als im Modell der polaren Katastrophe vorhergesagt und warum Photoemissions-Messungen eine höhere Ladungsträgerdichte zeigen als Transportmessungen [27].

Die Ergebnisse der vorliegenden Arbeit zeigen, dass das 2DES an der $LaAlO_3$–$SrTiO_3$-Grenzfläche sowohl im Hinblick auf Anwendungen interessant ist, da widerstandsfähige und sogar supraleitende Transistoren daraus hergestellt werden können, als auch im Hinblick auf die Grundlagenforschung, da dort viele neue und ungewöhnliche Phänomene beobachtet werden. Die Schwierigkeiten des präzisen und sauberen Probenwachstums sowie der Messungen bei Millikelvin-Temperaturen stellen jedoch weiterhin eine Herausforderung für den Experimentator dar.

Equipped with his five senses,
man explores the universe around him
and calls the adventure Science.
Edwin Hubble

1 INTRODUCTION

1.1 Motivation

Superconductivity in correlated electron systems in transition-metal oxides is a fascinating and complex phenomenon and has been the subject of intense research for the last three decades [1–3, 28]. However, the nature of the superconducting state in these systems is still not entirely understood and remains an open question in solid state physics. This thesis aims to contribute to the understanding of superconductivity in transition metal oxides, in particular in the $LaAlO_3$–$SrTiO_3$ interface electron system.

Electrons in doped semiconductors and metals form a dilute Fermi gas and can be described in a mean-field based energy band picture, whereas in insulating materials, electrons are rigidly bound to their orbitals. In transition metal oxides, however, electronic states exist in an intermediate regime between energy bands and orbitals. These states can be delocalized, *i.e.*, conductivity is possible, but the electrons retain a part of their orbital character. In this complex situation, in which it is not possible to describe the electronic behavior in the simple forms of either a band or orbital model, phenomena such as electronic correlations, inter-dependent ordering of spin, charge and orbitals and emergent phenomena lead to new and intriguing properties such as colossal magnetoresistance [4, 5], ferroelectricity [6] or spintronic effects [7, 8]. One of the most fascinating phenomena observed in correlated electron systems in oxides is the high-temperature superconductivity found in copper oxide materials [2, 3].

The great variability of transition metal oxides, *e.g.*, their possible multivalency, implies that it is crucial to control the material properties precisely. For this purpose, thin films and heterostructures of complex materials grown by vapor deposition techniques play a particularly important role [9]. Deposition methods such as molecular beam epitaxy (MBE) and pulsed laser deposition (PLD) allow the creation of thin films of materials with well-defined structure and stoichiometry. Two of the most prominent examples are the high-mobility two-dimensional electron gases at MBE-grown semiconductor-heterointerfaces [10] or high-temperature superconductivity in oxide thin films, *e.g.*, $YBa_2Cu_3O_{7-\delta}$ grown by PLD [3]. In the case of these examples (and many others), the mobile electrons are confined to two-dimensional planes. Such two-dimensional electron systems (2DESs) differ in many aspects from bulk electron systems.

For example, if the 2DES has a superconducting ground state, a quantum phase transition between superconducting and insulating state may be observed [11–13]. Unlike conventional *thermodynamic* phase transitions, it is a *quantum* phenomenon occurring at zero temperature. Since in all high-temperature cuprate superconductors, the conductivity is due to 2DESs in the copper-oxygen planes and these superconductors undergo such a superconductor-insulator transition (SIT) as a function of doping, investigations of the SIT in general can reveal more

about the nature of these systems. The SIT is also relevant from a practical perspective, because of the drastic change in resistance from a perfect lossless conductor to an insulator. In fact, it has been speculated that a SIT may terminate in a *superinsulating* state with extraordinarily high resistance [14–16].

Another special phase transition of 2D superconductors is the topological Berezinski-Kosterlitz-Thouless (BKT) transition, which occurs at finite temperature but has a special topological character. Since the theory of the BKT transition was the first to employ the concept of topology, now an important field in physics, its discovery was recently honored with the Nobel prize. However, the BKT transition is difficult to observe, because it occurs only in a very narrow temperature range and temperature effects can easily be mistaken for BKT signatures [17].

The work described in this thesis investigated the superconductor-insulator- and BKT-transitions in a two-dimensional superconductor based on transition-metal oxides: the electron system at the $LaAlO_3$–$SrTiO_3$ interface. Thin films of insulating $LaAlO_3$ grown onto insulating $SrTiO_3$ substrates exhibit a 2DES with a superconducting ground state at the interface of the two materials. The ground state can be switched from superconducting to insulating behavior by application of a gate voltage. Therefore it is a useful tool for the investigation of these phase transitions. Additionally, $LaAlO_3$–$SrTiO_3$ exhibits a phase similar to the cuprate pseudogap phase in which electron transport is resistive, but a gap can be observed in the density of states in tunneling experiments [18] which is not explicable by the standard Bardeen-Cooper-Schrieffer (BCS) theory of superconductivity.

The phase transitions were investigated by two complimentary pathways: by tunneling experiments on backgated samples and through the construction of superconducting transistors in which the electron system is influenced by the application of topgate voltages. In the investigation of superconductors, tunneling spectroscopy is a valuable tool because it allows direct imaging of the electronic density of states and thereby it is possible to determine the pairing strength Δ [19] and other properties of the superconducting condensate. The $LaAlO_3$–$SrTiO_3$-interface 2DES lends itself to tunneling experiments, because the $LaAlO_3$ top layer intrinsically serves as the insulating barrier required for tunneling experiments. When performing tunneling measurements in parallel with measurements of the in-plane electron transport, it is possible to determine whether the transition from superconductor to insulator is due to the breaking of pairs (*i.e.*, $\Delta \to 0$) or due to the loss of coherence between the pairs, indicated by a vanishing coherence length ξ (*i.e.*, $\xi \to 0, \Delta > 0$).

A transistor is a useful device for the investigation of the SIT, because the application of a topgate voltage can change the conductivity in the underlying channel by several orders of magnitude. The $LaAlO_3$–$SrTiO_3$ electron system is the only superconductor which can be switched on and off by the application of a gate voltage on short timescales. Since a superconducting transistor transports current as Cooper pairs and not as electrons, its characteristics have to be expected to be fundamentally different from that of a normal transistor.

1.2 Overview of this thesis

This thesis aims at answering a number of open questions concerning the $LaAlO_3$–$SrTiO_3$ interface and the SIT of its electron system, for example: How does the BKT transition in the $LaAlO_3$–$SrTiO_3$ 2DES evolve as the electron system is tuned from superconducting to insulating? Is it possible to construct a superconducting transistor using the $LaAlO_3$–

$SrTiO_3$ 2DES as channel and in which way are the switching characteristics of this transistor different from a similar transistor in the normal state? What can we yet learn fom tunneling spectroscopy at the interface? How can the contribution of the different bands to conductivity be disentangled?

In the following section, the $LaAlO_3$–$SrTiO_3$-interface electron system will be introduced, which is the subject of the investigations presented in this thesis. This also includes a brief description of its constituent materials $LaAlO_3$ and $SrTiO_3$.

Chapter 2 gives an overview over the theoretical background required: the theory of superconducting quasiparticle tunneling, fundamentals of the BKT transition and the characteristics of field-effect transistors (FETs).

Chapter 3 describes the experimental methods which were employed: the preparation of substrates, sample growth using pulsed laser deposition and photolithographic patterning of the electrodes and the electron system. Additionally, an overview of the sample designs and low temperature measurement methods is given.

In Chapter 4, $LaAlO_3$–$SrTiO_3$ transistors are described which were subjected to hydrostatic pressure. The analysis of transistor characteristics at different temperatures and pressures confirmed previous results on the response of the $LaAlO_3$–$SrTiO_3$ 2DES to pressure obtained in Hall-bar structures [23]. In a further experiment, combined transistor-Hall-bar samples were measured under pressure, revealing subtle differences between Hall-bar and transistor results and also giving indications of a multiband character of the 2DES at the interface.

Chapter 5 describes measurements of the critical magnetic field H_{c2} of the $LaAlO_3$–$SrTiO_3$ superconductor as a function of temperature. The measurements showed that the $H_{c2}(T)$-curve follows a linear trend down to far lower temperatures than expected for a standard BCS-superconductor. Non-standard behavior of $H_{c2}(T)$ can be due to the two-dimensionality of the system, but can also indicate multiband superconductivity or an anisotropy of the Fermi surface. Because of the large error margin of the data, definite conclusions are challenging.

Chapter 6 describes several aspects of the SIT in $LaAlO_3$–$SrTiO_3$ which were investigated in this thesis. First, it was necessary to optimize the PLD growth conditions for $LaAlO_3$–$SrTiO_3$-samples to obtain electron systems which were both superconducting and could be turned insulating with a back-gate voltage. Then, investigations of the BKT transition are described, which were obscured by intrinsic heating in the electron system. Also, an increase of resistivity directly before the onset of the superconducting transition is described, which was observed in the $R(H)$ and $R(T)$ curves of several $LaAlO_3$–$SrTiO_3$-samples. Such an increase in resistance can be caused by the presence of incoherent preformed pairs in the electron system, a hypothesis which is corroborated by measurements of the superconducting parameters Δ and Γ in the corresponding region of the phase diagram. At the end of Chapter 6, a superconducting transistor with the $LaAlO_3$–$SrTiO_3$ 2DES as channel is discussed. In a transistor geometry, the SIT can be controlled by applying a voltage to the topgate. It is shown that the switching speed of the transistor is not improved by superconductivity because of an intermediate metallic state between the insulating and the superconducting region. However, the conductivity of the transistor in the ON state is improved in the superconducting region.

Chapter 7 describes tunneling measurements of in-gap features observed in superconducting tunneling spectra of $LaAlO_3$–$SrTiO_3$ samples and describes a number of physical phenomena which can be the origin of such states. While the data allowed the exclusion of some of these phenomena, it was not possible to determine the origin of the in-gap features with certainty.

In Chapter 8, the results of this thesis are summarized and an outlook is given on further questions to be answered.

The appendices at the end of this thesis were written to educate the writer rather than the reader, who found that *"The best way to understand a topic is to write a book about it."* (Barry McCoy). They are not necessary for the understanding of the thesis, but may be found useful for detailed reference on their respective topics.

1.3 The $LaAlO_3$-$SrTiO_3$ interface

The 2DES at the interface of the two insulators $LaAlO_3$ and $SrTiO_3$ is a case in point for the fascinating versatility that electronic correlations lend to transition metal oxides. The present thesis describes several aspects of the superconductor-insulator transition in this peculiar electron system. This section gives a brief overview over the $LaAlO_3$–$SrTiO_3$ system. More in-depth information concerning the $LaAlO_3$-$SrTiO_3$ interface 2DES and its history can be found in several review articles [28–30]. In order to better understand the properties of the interface, the constituent materials will be introduced first.

1.3.1 $SrTiO_3$

Strontium titanate ($SrTiO_3$) is a transparent, colorless compound with high refractive index. Its appearance in nature is very rare, but it can be readily synthesized. $SrTiO_3$ single crystals are grown using the defect-prone Verneuil method, which limits the purity and quality of the available $SrTiO_3$ samples. At room temperature, $SrTiO_3$ is of the standard perovskite ABO_3 structure with lattice parameter 3.905 Å and a cubic unit cell. At 105 K, $SrTiO_3$ undergoes a transition to a tetragonal low-temperature phase due to a rotation of the oxygen octahedra. $SrTiO_3$ has a very high dielectric constant, which varies from 300 at room temperature up to 25 000 at low temperatures [31–33] due to an incipient ferroelectric transition [34]. There are several ways to turn ordinarily quantum paraelectric $SrTiO_3$ ferroelectric, *e.g.*, by the application of epitaxial strain [35].

$SrTiO_3$ is insulating with an indirect bandgap of 3.2 eV, but it becomes semiconducting when doped by Nb^{5+} substitution for Ti^{4+}, La^{3+} substitution for Sr^{2+} or O^{2-} vacancies. Thus, when working with $SrTiO_3$, it is essential to avoid reducing conditions in order to prohibit the creation of oxygen vacancies, which would result in undesired conductivity.

The conduction electrons of doped $SrTiO_3$ reside in the Ti-3d-orbitals. The degeneracy of these orbitals is lifted by the crystal field splitting, *i.e.*, the electrons in the Ti orbitals have different energies depending on their positions relative to the electrons of the surrounding oxygen octahedron. The $d_{3z^2-r^2}$ and $d_{x^2-y^2}$ states have higher energy and are collectively referred to as e_g orbitals. The d_{xy}, d_{xz}, d_{yz} orbitals have lower energy and are collectively referred to as t_{2g} orbitals. The degeneracy of the t_{2g} orbitals is lifted by spin-orbit coupling ($\Delta_{SO} = 18\,\mathrm{meV}$) and a second crystal field splitting due to the tetragonal transition ($\Delta_t = 1.54\,\mathrm{meV}$) [36, 37]. The band structure of $SrTiO_3$ has been calculated [38, 39]. The calculated band energies differ, however, from the spectroscopic measurements cited above. Nonetheless it is clear that the minimum of the conduction band is at the Γ point, *i.e.*, in the center of the Brillouin zone and that it consists of the 3d-t_{2g} band which is split up into three subbands with different effective masses. These subbands are empty for stoichiometric $SrTiO_3$ and become subsequently populated with electrons as the doping level is increased, which can be observed, *e.g.*, by the appearance of additional frequencies in Shubnikov-de Haas oscillations once multiple bands are occupied [40].

$SrTiO_3$ becomes superconducting when doped with Nb, La or O vacancies with transition temperatures usually below 0.4 K, even though a transition temperature of 1.2 K has been reported [41]. It was the first superconducting semiconductor to be discovered [1] and is noted for its unusually low charge carrier concentration between $1 \times 10^{18}\,\mathrm{cm}^{-3}$ and $1 \times 10^{21}\,\mathrm{cm}^{-3}$. Measurements of superconducting tunneling spectra [42] and quantum oscillations [40] indicate multiband superconductivity at high doping levels, whereas recent spectroscopic measurements contradict this hypothesis [43]. The region of superconductivity in the T_c vs n phase diagram has a dome shape, similar to that of the high-T_c cuprate superconductors. It is an interesting question why T_c decreases above a certain doping level, since in standard BCS theory, T_c should monotonously increase with the density of states at the Fermi level. Likely explanations are the decrease of the electron-phonon coupling constant V due to plasmon shielding above a doping level of $n \approx 1 \times 10^{20}\,\mathrm{cm}^{-3}$ [39, 44] and the occupation of an additional, non-superconducting band [40].

1.3.2 $LaAlO_3$

$LaAlO_3$ is also a perovskite, but in contrast to $SrTiO_3$ it is rhombohedral with a lattice parameter of 3.790 Å at room temperature. Its high dielectric constant of 24 [45] (which is reduced in thin films [46]) and large bandgap of 5.6 eV [47] make it attractive as a gate dielectric. Furthermore, the possibility to grow clean $LaAlO_3$ single crystals using the Czochralsky method makes it a valuable substrate material for cases where the rhombohedral crystal twinning is unproblematic.

1.3.3 $LaAlO_3$-$SrTiO_3$

In 2004, Akira Ohtomo and Harold Hwang discovered that a conducting 2DES is generated when $LaAlO_3$ is grown epitaxially onto $SrTiO_3$ [48]. Since doped $SrTiO_3$ is a well-known semiconductor, a seemingly likely explanation for the conductivity at the interface would be doping induced by the $LaAlO_3$ growth, specifically La substitution or O vacancy creation. However, the $LaAlO_3$–$SrTiO_3$ interface is only conductive if $LaAlO_3$ is grown onto $SrTiO_3$ terminated by a TiO_2-layer, and only if the thickness of the $LaAlO_3$ top layer exceeds 3 unit cells [49]. These are just two examples of observations which are not explicable with a simple doping scenario.

In the original publication (Ref. [48]), a scenario of polar catastrophe was put forward to explain the appearance of conductivity: The $LaAlO_3$ films were grown on $SrTiO_3$ substrates cut perpendicular to the (001) crystallographic direction. In this direction, $SrTiO_3$ is composed of electrically neutral layers of TiO_2 and SrO, whereas $LaAlO_3$ is composed of electrically charged layers of LaO^+ and AlO_2^-. The polar discontinuity at the interface leads to a potential buildup with each $LaAlO_3$ unit cell. At 4 unit cells of $LaAlO_3$, the potential buildup exceeds the band-gap of $SrTiO_3$ and in the naive case, half an elementary charge per unit cell is transferred to the interface via an electronic reconstruction, compensating the polar discontinuity. The observation of conductivity, *e.g.*, in $LaAlO_3$–$SrTiO_3$ interfaces in the non-polar (110) crystal direction and the fact that the observed charge density is much less than the predicted $0.5e$ per unit cell indicate that this picture is probably too simplistic and other mechanisms may play a role. It is beyond the scope of this introduction to discuss all the numerous different scenarios which have been theoretically proposed for the origin of the 2DES and the experimental evidence for and against them. However, it should be emphasized that it has been conclusively shown

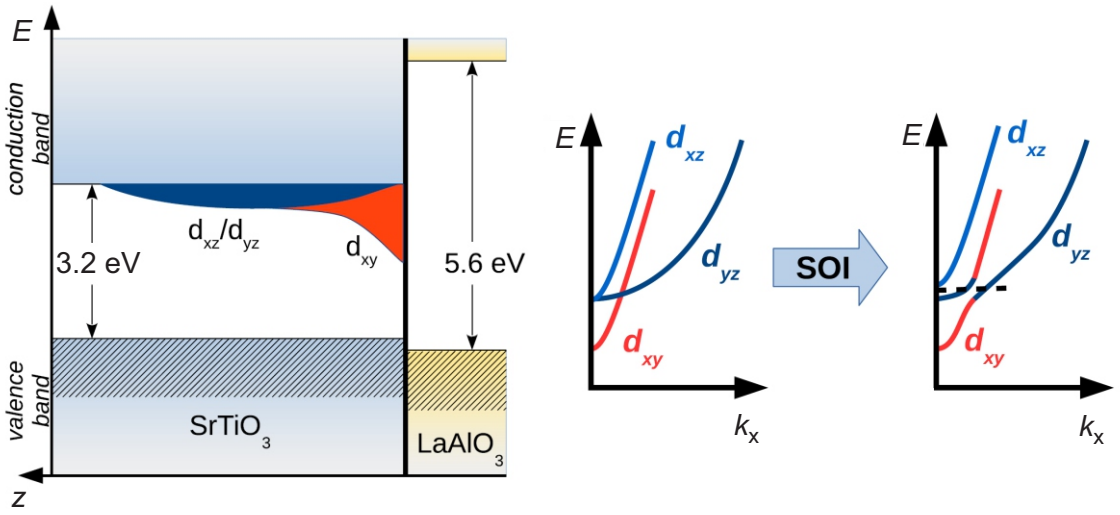

(a) (b) (c)

Figure 1.1: Band structure of the 2DES at the $LaAlO_3$–$SrTiO_3$ interface. The conduction electrons are located in the Ti 3d orbitals on the $SrTiO_3$ side of the interface, which form the bands relevant for conduction. Because mirror symmetry is broken at the interface, the t_{2g}-d_{xy} sub-band is shifted with respect to the d_{xz} and d_{yz} subbands. An additional shift is caused by Rashba spin-orbit interaction, which also causes anti-crossing of the bands, so that the initially degenerate d_{xz} and d_{yz} sub-bands are spin-split into a new pair of bands. (a) Distribution of the electronic bands in real space, where z denotes the distance from the interface. Band structure in momentum space, without (b) and with (c) spin-orbit interaction (SOI). Reproduced from Ref. [29].

that conductivity at the interface is not a simple oxygen vacancy effect and that the electronic structure is distinctly different from a thin layer of doped $SrTiO_3$ [50].

The conduction electrons of the $LaAlO_3$–$SrTiO_3$ interface reside in the conduction band created by the Ti 3d orbitals of the $SrTiO_3$ side. Since electrons in these orbitals are correlated, the electron system at the interface is referred to as a 2-dimensional electron *liquid* (2DEL) [50] rather than as an electron gas as found in conventional semiconductor heterostructures. The band structure of $LaAlO_3$–$SrTiO_3$ is different from that of doped $SrTiO_3$: At the interface, for example, the mirror symmetry along the z-axis is broken. Most notably, the t_{2g}-d_{xy}-subband is shifted down by 250 meV [23, 27, 51]. In addition, all bands are spin-split due to Rashba spin-orbit coupling [52–54]. This an causes anti-crossing of the bands, so that the initially degenerate d_{xz} and d_{yz} sub-bands are spin-split into a new pair of bands. The distribution of the bands relevant for conduction is shown in Fig. 1.1.

The most interesting aspect of the $LaAlO_3$–$SrTiO_3$ interface for this thesis is that it exhibits a superconducting ground state below a transition temperature of approximately 300 mK [55] and that the interface can be switched from superconducting to insulating across a quantum phase transition controlled by the application of a gate voltage [56]. The region of superconductivity in the T_c vs n diagram is dome-shaped as in doped $SrTiO_3$ and in the cuprates. Tunneling spectroscopy reveals that the superconducting gap can be observed in a part of the underdoped region where transport is resistive, a phenomenon similar but not necessarily related to the pseudogap in the cuprates [57]. It was shown that superconducting

phase coherence persists in those regions of the phase diagram where superconductivity is no longer measured in transport [58] and that in fact the width of the superconducting gap increases in this region, which can be attributed to an increased electron-phonon coupling strength [25]. Another peculiar feature of superconductivity at the $LaAlO_3$–$SrTiO_3$ interface is that it has been reported to coexist with magnetic ordering [26, 59, 60]. The transition temperature of superconductivity in $LaAlO_3$–$SrTiO_3$ is very close to that in doped $SrTiO_3$. However, measurements such as the angular dependence of the critical magnetic field have clearly established that the superconducting region is two-dimensional, *i.e.*, its thickness ($\approx$ 10 nm at optimum doping) is smaller than the superconducting coherence length ($\approx$ 40 nm at optimum doping).

Another question which is still under debate is whether the $LaAlO_3$–$SrTiO_3$ interface 2DES is also a multiband superconductor. Latest studies have revealed the hierarchy of the Ti-3d subbands near the Fermi energy of the system [61, 62]. The bulk crystal field-split lower t_{2g} orbitals are now entirely non-degenerate, owing to the presence of $LaAlO_3$ layers close to the interface that distort the Ti-octahedra-induced field [61, 63, 64]. It has been argued [65] that there exists a critical density that marks the onset of population of different subbands close to the Fermi energy and is characteristic of the $LaAlO_3$–$SrTiO_3$ system. This very point in carrier density marks a Lifshitz transition which implies that transport switches from single to multi-carrier type [66]. However, Fourier analysis of the Shubnikov-de Haas oscillations on bulk $SrTiO_3$ [44] indicates that across the entire superconducting phase diagram multiple bands are occupied. This result is corroborated by the analysis shown in the present thesis (see section 6.1.2). Tunneling studies show only a single superconducting gap [25, 57, 58]. Yet, tunneling spectroscopy in planar $LaAlO_3$–$SrTiO_3$ and Au tunnel-junctions is orbitally selective since only contributions from the $d_{xz/yz}$ orbitals are measured. The observation of the superconducting gap therefore verifies that one of these sub-bands is superconducting; it is yet unclear whether the d_{xy} sub-band also is.

Mathematics is the gate and key to the sciences.
ROGER BACON

2 THEORY

This chapter comprises three sections describing the theoretical fundamentals of different aspects of the physics described in this thesis. Section 2.1 describes the fundamentals of tunneling spectroscopy in superconductors. Section 2.2 introduces the topological BKT-transition in two-dimensional superconductors. Finally, section 2.3 describes the theoretical framework for field-effect transistors and their realization using $LaAlO_3$–$SrTiO_3$ interfaces.

2.1 Superconducting tunneling spectroscopy

Spectroscopy using tunneling of electrons across an insulating barrier, either from a normal metal into a superconductor or from one superconductor to another, has become an invaluable tool for the investigation of superconductors because it allows direct measuring of the density of states of the superconductor. The field of tunneling spectroscopy was pioneered by Giaever [19]. This chapter is based on the introductions to tunneling in [67, 68]. A brief introduction to the BCS theory of superconductivity and the concept of quasiparticles can be found in Appendix A, where it is shown that the density of states N_S at $T = 0$ of a superconductor as a function of the energy $E_\mathbf{k}$ close to the Fermi edge for a wavevector $\mathbf{k}$ is given by:

$$N_S(E_\mathbf{k}) = \frac{dn}{dE_\mathbf{k}} = \frac{dn}{d\xi_\mathbf{k}}\frac{d\xi_\mathbf{k}}{dE_\mathbf{k}} = N(0) \cdot \begin{cases} \frac{E_\mathbf{k}}{\sqrt{E_\mathbf{k}^2 - \Delta^2}} & (E_\mathbf{k} > \Delta) \\ 0 & (E_\mathbf{k} < \Delta) \end{cases}, \tag{2.1}$$

where $\xi_\mathbf{k}$ is the quasiparticle energy and Δ the superconducting energy gap.

In order to describe tunneling from one electron system to another, the difference in chemical potential μ between the two systems has to be considered. For an electronic excitation, the energy including the chemical potential will be $E_{e\mathbf{k}} = (E_\mathbf{k} + \mu)$, and for a hole $E_{h\mathbf{k}} = (E_\mathbf{k} - \mu)$. When transferring an electron elastically from system 1 to system 2 with a potential difference V_{12}, the energy of the hole created in system 1 must be equal to the energy of the electron arriving in system 2 and therefore:

$$E_{\mathbf{k}1} + E_{\mathbf{k}'2} = \mu_1 - \mu_2 = eV_{12}. \tag{2.2}$$

Tunneling is described by a Hamiltonian of the form

$$H_T = \sum_{\sigma\mathbf{kq}} T_\mathbf{kq} c^\dagger_{\mathbf{k}\sigma} c_{\mathbf{q}\sigma} + cc. \tag{2.3}$$

This term transfers an electron from one metal where its momentum is $\mathbf{q}$ to another metal where its momentum is $\mathbf{k}$, and the complex conjugate part describes the opposite process.

The index σ indicates the summation over the spin states. The phenomenological tunneling matrix element $T_{\mathbf{kq}}$ depends on the nature of the barrier. Describing this process using the quasiparticle formalism introduced in Appendix A, the single electron operators are written as

$$c^{\dagger}_{\mathbf{k}\uparrow} = u_{\mathbf{k}}\gamma^{\dagger}_{\mathbf{k}0} + v_{\mathbf{k}}\gamma_{\mathbf{k}1}. \tag{2.4}$$

Therefore, the superconducting occupation probabilites $u_{\mathbf{k}}$ and $v_{\mathbf{k}}$ appear indirectly in the tunneling Hamiltonian. One could therefore conclude that the tunneling current would depend on the structure of the superconducting ground state. However, this is not the case: because the energies of the quasiparticle excitations are symmetric around the Fermi energy (see Fig. A.1 (b)) and $|u(-\xi)| = |v(\xi)|$, the contributions of opposite energy from the Fermi surface add up and the structure of the ground state is not relevant for tunneling. Thus only the excited states have to be considered.

Because the coherence factors vanish from the tunneling Hamiltonian, it is possible in many cases to treat tunneling between superconductors in an independent-particle approximation called the *semiconductor model* by treating the electrons individually and neglecting the superconducting correlations. Only the modified density of states (Eq. 2.1) is taken into account. This model is very useful in many respects, but should be treated with care. For example, it can not explain the Josephson current at zero bias arising from pair tunneling in a superconductor-insulator-superconductor (SIS)-junction. In the semiconductor model, the tunneling current $I_{1\to2}$ from metal 1 to metal 2 can be expressed as an integral in energy over the available states:

$$I_{1\to2} = \int_{-\infty}^{\infty} |T|^2 N_1(E) f(E) N_2(E+eV)[1-f(E+eV)]dE, \tag{2.5}$$

with T the tunneling matrix element (assumed constant in the present approximation), N_i the respective density of states in the two metals, V the voltage bias applied across the junction and f the Fermi distribution which describes which states are occupied and thus if electrons are available for tunneling and holes available on the other side to accommodate them. The current from metal 2 to metal 1 can be described equivalently. Summing these two contributions gives the total tunneling current I:

$$I = |T|^2 \int_{-\infty}^{\infty} N_1(E) N_2(E+eV)[f(E)-f(E+eV)]dE. \tag{2.6}$$

In the simple case that both 1 and 2 are normal metals, their density of states can be approximated to be constant in the vicinity of the Fermi surface $N_i(E) \approx N_i(0)$. Then the current becomes a linear function of the voltage with normal-normal-conductance G_{NN}:

$$I_{NN} = |T|^2 N_1(0) N_2(0) \int_{-\infty}^{\infty} [f(E)-f(E+eV)]\, dE = |T|^2 N_1(0) N_2(0) eV = G_{NN} V. \tag{2.7}$$

In the more interesting case that 2 is a superconductor, the current is calculated by:

$$I_{NS} = |T|^2 N_1(0) \int_{-\infty}^{\infty} N_2(E)\, [f(E)-f(E+eV)]\, dE. \tag{2.8}$$

Expressing $N_1(0)$ in terms of G_{NN}, which can be measured more easily, and calculating the conductance dI/dV:

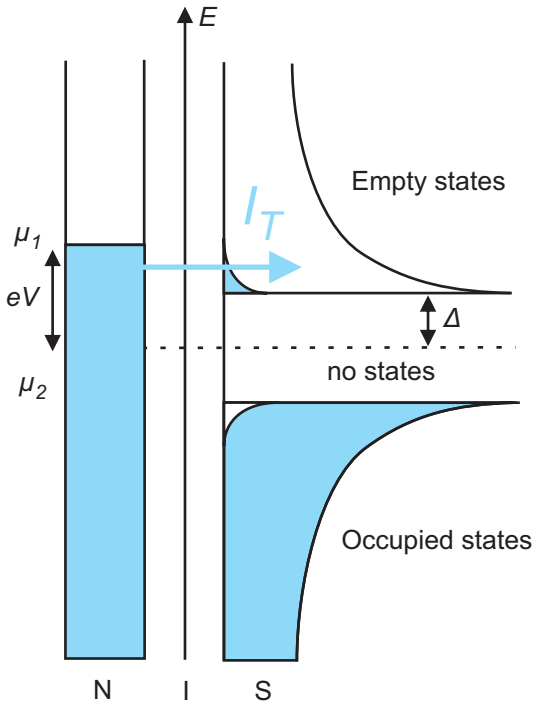

Figure 2.1: Sketch illustrating tunneling from a normal metal (N) across an insulating barrier (I) into a superconductor (S) at finite temperature in the semiconductor model. The density of states for the normal metal is assumed to be constant in energy, whereas the density of states of the superconductor is given by Eq. 2.1. The applied voltage shifts the chemical potentials μ_1 and μ_2 out of their equilibrium positions. At $T = 0$, no current can flow from the normal metal into the forbidden states of the superconducting gap, therefore the tunneling current is suppressed for $|eV| < \Delta$. Once the Fermi edge of the normal metal exceeds the superconducting gap, a tunneling current I_T can flow. At finite temperature, excited states above the gap are populated in the superconductor as illustrated here, and consequently empty states exist below the gap, allowing a small tunneling current already for $|eV| < \Delta$.

$$\left.\frac{dI}{dV}\right|_{NS} = G_{NN} \int_{-\infty}^{\infty} \frac{N_2(E)}{N_2(0)} \cdot \frac{-\partial f(E+eV)}{\partial(eV)} dE. \tag{2.9}$$

Since the Fermi function at low temperature can be well approximated by a step function, its derivative is approximately a delta function and therefore the equation simplifies to:

$$\left.\frac{dI}{dV}\right|_{NS} = G_{NS} = G_{NN} \frac{N_2(e|V|)}{N_2(0)}. \tag{2.10}$$

Clearly, the tunneling conductivity allows a direct measurement of the superconducting density of states. The tunneling process from a normal conductor across an insulating barrier into a superconductor is illustrated in Fig. 2.1.

2.2 The Berezinski-Kosterlitz-Thouless transition

2.2.1 Introduction to BKT

The BKT transition represents a special class of phase transitions, which occur only in two-dimensional systems and have no associated order parameter and break no symmetry. For this class of transitions, perturbative approaches are impossible because there is no (locally) continuous transformation from the unperturbed state to the perturbed state because they are topologically different. The following introduction is coarsely based on references [69] and [70], which, in turn, closely correspond to the publications by Kosterlitz and Thouless [71, 72], who, in turn, refer back to the publication by Berezinski [73].

A good model system to explain the concept of a BKT transition is the 2D-XY model. It consists of a 2D lattice with a two-component variable on each site. This could be, for example, a complex scalar $\exp(i\phi)$, *e.g.*, for the modeling of the phase of a Josephson junction array (JJA). However, to make the following arguments more intuitive, it will be assumed that each model object is a 2D vector (or spin) in the plane. If all spins have the same magnitude and there is only interaction between nearest neighbors with an exchange energy J, the Hamiltonian for a 2D-XY system of spins $\mathbf{S_i}$ depends only on the angle θ of the spins. The two-component system is then completely described by a single variable:

$$H = -J \sum_{<ij>} \mathbf{S}_i \cdot \mathbf{S}_j = -J \sum_{<ij>} \cos\left(\theta_i - \theta_j\right), \tag{2.11}$$

where $< ij >$ denotes summation over nearest neighbors and θ_i and θ_j are the angles of the spins at sites i and j, respectively.

In order for H to be definite, the phase θ must observe the condition

$$\oint \nabla\theta \cdot d\mathbf{l} = \oint d\theta = 2\pi n, \tag{2.12}$$

i.e., going around a closed loop, the same phase up to multiples of 2π must be obtained. It is not possible to calculate this system with a perturbative approach because there is no continuous transformation from a field with *topological charge* n to a field with different charge n'. There will be in every case a discontinuous jump of n, for example when going from $n = 0$ (Fig. 2.2(a)) to a vortex with $n' = 1$ (Figs. 2.2(b), 2.2(c)). Therefore, these states are called *topological states*.

Assuming that the direction of the spins varies only slowly and smoothly, the cosine in the Hamiltonian can be approximated by:

$$\cos\left(\theta_i - \theta_j\right) = 1 + \left(\theta_i - \theta_j\right)^2. \tag{2.13}$$

This allows a separation of the Hamiltonian into two parts, a ground state energy E_0 representing the state in which all spins are aligned and a perturbation representing a small deflection of the spins from the aligned position. Assuming that the lattice spacing is much smaller than the other length scales in the system,it is possible to change the difference in angles to a derivative and the sum into an integral. Finally:

$$H = E_0 - \frac{J}{2} \int d^2x |\nabla\theta(x)|^2. \tag{2.14}$$

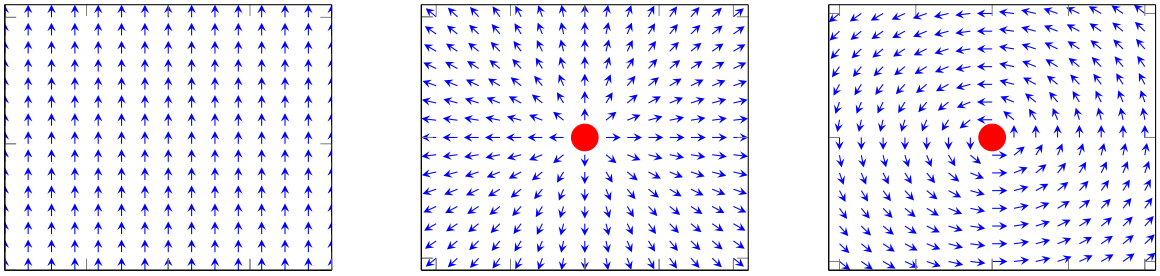

(a) (b) (c)

Figure 2.2: Illustration of the concept of the topological charge or winding number n. (a) Spins with $\theta(\mathbf{r}) = 0$, $n = 0$. (b) A vortex of spins with $\theta(\mathbf{r}) = \arctan(y/x)$, $n = 1$. (c) Gradient of (b), showing that a circular path around the center will amount to a change of 2π.

The ground state energy E_0 is not relevant for the following calculations and will be neglected.

A vortex with $n = 1$ can be parametrized by:

$$\theta\left(\mathbf{r}\right) = \arctan\left(\frac{x}{y}\right) \tag{2.15}$$

$$\nabla\theta = \frac{1}{|\mathbf{r}|^2}\left(-y, x\right). \tag{2.16}$$

as shown in Fig. 2.2(b). In general, equation 2.12 can be satisfied for arbitrary n by a field with the gradient:

$$\nabla\theta = \frac{n}{r}\hat{\mathbf{e}}_r \times \hat{\mathbf{e}}_z, \tag{2.17}$$

where $\hat{\mathbf{e}}_r$ and $\hat{\mathbf{e}}_z$ are the unit vectors in radial and z-direction, respectively. The integer n is usually referred to as the *winding number* of the vortex.

As can be seen from Fig. 2.2(b), the approximation of small angles is not valid in the core of the vortex, therefore a core area of radius a will be excluded from the integration of the Hamiltonian and a core energy E_{core} will be substituted. Integration of Eq. 2.17 gives:

$$H(n) = E_{core}(n) + \frac{J}{2}\int d^2x|\nabla\theta(x)|^2 = E_{core}(n) + J\pi n^2\int_a^L dr\frac{1}{r} = E_{core}(n) + \pi J n^2 \ln\frac{L}{a}, \tag{2.18}$$

where L is the size of the system. For sufficiently large L, $E_{core}(n)$ can be neglected. Clearly, for the macroscopic limit $L \to \infty$, the energy of a single vortex diverges. However, there are $(L/a)^2$ possible ways to position a vortex of size a^2 on a plane of size L^2, therefore the entropy of a vortex is

$$S = 2k_B \ln\left(\frac{L}{a}\right), \tag{2.19}$$

where k_B is the Boltzmann constant. Using $\langle H\rangle = U$, the free energy is

$$F = U - TS = \left(\pi J n^2 - 2k_B T\right) \ln\left(\frac{L}{a}\right). \tag{2.20}$$

Above a critical temperature,

$$T_{\mathrm{BKT}} = \frac{\pi J n^2}{2k_B}, \tag{2.21}$$

the free energy turns negative because of the entropy term, and vortices can be created.

The energy for creating vortices can be considerably reduced when they appear in pairs of opposite direction and equal magnitude (in the BKT theory, the magnitude of a vortex is the topological charge). Like a dipole of electrical charge, the pairing leads to a much faster decay of the field perturbation with distance as compared to a single charge. As can be seen from Fig. 2.3, the gradient created by the vortex pair is negligibly small at length scales larger than the vortex separation R. Therefore, instead of using L as the upper limit of integration in Eq. 2.18, the integration can be cut off at R:

$$E = const \cdot \ln(R/a). \tag{2.22}$$

This dependence of $E(R)$ implies an attractive force between the vortices and anti-vortices. Therefore, the energy of a pair of vortices of equal magnitude and opposite direction does not diverge with system size L, but scales with the vortex separation R. This energy is finite, and pairs of vortices may exist at any temperature. Hence the critical temperature defined by Eq. 2.21 is the temperature above which single vortices may exist, but vortices in pairs can be present below this temperature. There is still a minimum in the free energy since single vortices have a higher entropy than pairs (each single vortex may independently occupy random sites). Thus T_{BKT} defined in Eq. 2.21 can be considered the critical temperature of a vortex binding-unbinding transition.

If paired vortices are present, they modify the interaction between single vortices, similar to dipoles modifying the interaction between electrical charges. Therefore, the number of vortex pairs determines the dielectric constant of the material for vortices. The change in interaction with number of vortex pairs is described by renormalization group theory (see Appendx B).

The existence of a phase transition in 2D systems is unexpected because the Mermin-Wagner theorem states that there can be no long-range order in two dimensions [74]. The reason why the phase transition exists rests with the precise meaning of the words *long-range* and *order*.

Usually, ordered and disordered states are distinguished by the decay of the correlation function with distance:

$$\langle e^{i\theta(\mathbf{r})} e^{i\theta(0)} \rangle \propto \begin{cases} const & \text{ordered} \\ e^{-r} & \text{disordered} \end{cases}. \tag{2.23}$$

However, the 2D-XY model is in an intermediate regime where the correlations do not decay exponentially, but only with a power law:

$$\langle e^{i\theta(\mathbf{r})} e^{i\theta(0)} \rangle \propto \left(\frac{a}{r}\right)^{\eta(T)}, \tag{2.24}$$

so that if the system is sufficiently small with respect to the superconducting coherence length ξ, the correlation function may be nonvanishing throughout the entire system.

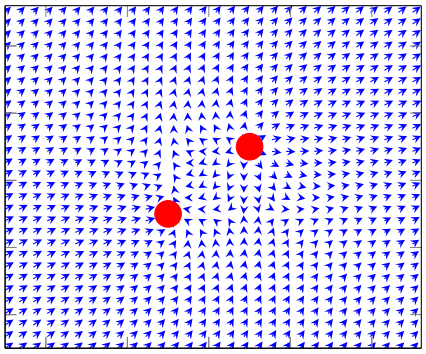

Figure 2.3: Plot of the parameter $\theta(\mathbf{r})$ for a pair of two vortices of opposite charge. The perturbation of the field decays rapidly with distance from the vortex cores.

Additionally, the phase below the BKT transition temperature is not ordered in the sense that it has an order parameter which appears at the transition temperature and is zero above, and there is no symmetry breaking associated with the transition. It thus circumvents the Mermin-Wagner theorem.

2.2.2 The BKT transition in Josephson junction arrays

Having introduced the BKT transition in the rather abstract 2D-XY-model, it will now be illustrated in a superconducting model system. Arrays of two-dimensional Josephson junctions are a prime example for the application of the BKT theory. They are frequently used to describe the transition from superconductor to insulator in two dimensions. Homogeneously disordered thin films, such as the $LaAlO_3$–$SrTiO_3$ interface, can be considered the continuous analogue to the discrete Josephson arrays [75]. Following Ref. [67], for simplicity a square lattice of Josephson junctions without external magnetic field will be considered and screening effects will be neglected. A schematic diagram of such an array is shown in Fig. 2.4. The squares represent superconducting islands and the crossed lines are the Josephson junctions between them. The energy for a single Josephson junction can be calculated by assuming that is adiabatically changed from its ground state $\phi_0 = 0$ to a given state ϕ during the time t:

$$E_J = \int_0^t I_S V dt = \frac{\Phi_0}{2\pi} \int_0^t I_S \frac{d\phi}{dt} dt = \frac{\Phi_0}{2\pi} \int_0^\phi I_C \sin\phi d\phi = \frac{\Phi_0 I_C}{2\pi} (1 - \cos\phi) , \tag{2.25}$$

where the Josephson equations have been used and $\Phi_0 = h/(2e)$ is the quantum of magnetic flux. The energy of the entire array is given by the sum of the Josephson energies across the junctions i with phase differences ϕ_i:

$$E = \sum_i \frac{\Phi_0 I_C}{2\pi} (1 - \cos\phi_i) = E_J \sum_i (1 - \cos\phi_i) , \tag{2.26}$$

which has the same form as Eq. 2.11. The trivial ground state of the system is $\phi_i = 0 \, \forall i$. As an elementary excitation, consider a magnetic vortex of flux $n \cdot \Phi_0$ penetrating the array, assuming that the vortex is centered in the highlighted square (or "plaquette") in Fig 2.4. The phase difference going once around a plaquette depends on the magnetic flux penetrating it:

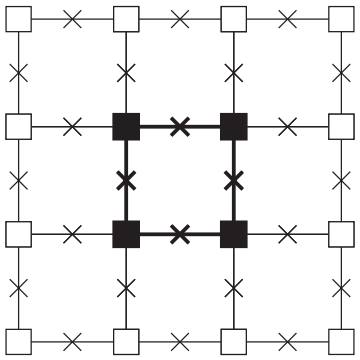

Figure 2.4: Schematic drawing of a Josephson junction array. Squares represent superconducting islands, crossed lines are Josephson junctions. A single plaquette is highlighted.

$$\sum_{plaquette} \phi_i = 2\pi \frac{\Phi}{\Phi_0} = 2\pi \left(f - n\right), \tag{2.27}$$

where f is the frustration index, *i.e.*, the remainder of the division Φ/Φ_0 and n is the integer quotient, corresponding to the topological charge n from section 2.2.1. Furthermore, when summing this equation around a contour of multiple plaquettes, the internal phase contributions cancel because they enter twice with opposite signs and only the phase along the outer contour remains, depending on the flux in all enclosed cells:

$$\sum_{contour} \phi_i = 2\pi \sum_{cells} \left(f_i - n_i\right). \tag{2.28}$$

It is clear that any contour enclosing the vortex will have $\sum \phi_i = 2n\pi$. Considering an approximately circular contour of radius r around the vortex center, the phases of the single junctions ϕ_i in the contour will decrease approximately as $\phi_i \approx 2n\pi a/2\pi r$ with increasing r, which is the same form as Eq. 2.17. Integrating in the same way as in Eq. 2.18, again a logarithmic divergence of energy on system size L is obtained:

$$E = n^2 \pi E_J \ln \frac{L}{a}. \tag{2.29}$$

If the array contains a pair of vortices with opposite magnitude, any contour enclosing both vortices will have a net phase difference of 0. Consequently, the integration can be cut off at the separation distance R of the vortices and the energy for vortex pairs becomes:

$$E_{12} = 2n^2 \pi E_j \ln \frac{R}{a}. \tag{2.30}$$

Analogous to Eq. 2.20 the free energy of the system can be calculated and the temperature of the vortex binding-unbinding transition estimated:

$$T_{BKT} \approx \frac{\pi E_J}{k_B}. \tag{2.31}$$

The key experimental signal of a BKT transition can be observed in the $I-V$ characteristics of a 2D superconducting film: Above T_{BKT}, there are free single vortices experiencing a Lorentz

force and correspondingly generating a linear resistance $V \propto I$. Below T_{BKT}, there are only vortex pairs, experiencing no net Lorentz force. Single vortices are generated when the current dissociates pairs through the Lorentz force. The number of single vortices generated by the current just below T_{BKT} is proportional to I^2. Therefore, below T_{BKT} the voltage depends on the current as $V \propto I^3$.

In the dirty limit, it is possible to find an expression relating the BKT transition temperature T_{BKT} to the mean-field superconducting critical temperature T_{c}. Close to the critical temperature this can be approximated by

$$\frac{T_{BKT}}{T_c} = \left[1 + 0.173\frac{R}{R_c}\right]^{-1}, \tag{2.32}$$

where $R_c = \hbar/e^2$ is the quantum of resistance and R is the resistance of the film in the normal state [75]. As can be seen from the equation, T_{BKT} will only be appreciably different from T_{c} for films with a sufficiently high resistance.

2.2.3 Charge-vortex duality

The JJA model is peculiar because not only vortices can undergo a BKT transition, but also the charges on the islands. [76, 77]. In two dimensions, the Coulomb energy E between two charges q separated by a distance R is given by

$$E = 2q^2 \ln\frac{R}{a} \tag{2.33}$$

where a is the closest possible distance between the two charges. Therefore not only vortex-antivortex pairs, but also charge dipoles can undergo a BKT transition in JJAs. The ratio of Josephson energy E_J and charging energy $E_C = e^2/2C$ determines which of the two dominates the dynamics of the system [78]. This duality has led to the prediction of a *superinsulating* state with extraordinarily high resistance as endpoint of the Coulomb BKT transition [15, 79, 80].

2.3 Transistor fundamentals

A transistor (a portemanteau of "transfer" and "resistor") is a solid-state device which is used to switch currents or voltages. Historically, the first operational devices were bipolar transistors based on p-n-p or n-p-n semiconductor junctions [81]. Modern digital electronics, however, is almost exclusively based on field-effect transistors (FETs). Since this is also the type of the $LaAlO_3$–$SrTiO_3$ transistors developed in the present work, the working principle of FETs and the basic equations will be introduced below.

For the sake of simplicity, the FET equations will be explained with the example of a standard semiconductor FET, following the introduction given in Ref. [82]. Fig. 2.5 shows a schematic drawing of an n-channel FET with the important components, voltages and currents identified. The conducting channel of the transistor is formed by the inversion region (blue) at the contact between the p-type semiconducting substrate and the gate insulator. The transistor switches between conducting and insulating states by the application of a gate voltage: either the inversion layer is built-into the transistor and can be depleted by applying a negative voltage V_{G} to the gate (normally-on), or the inversion layer is not present in the equilibrium state and

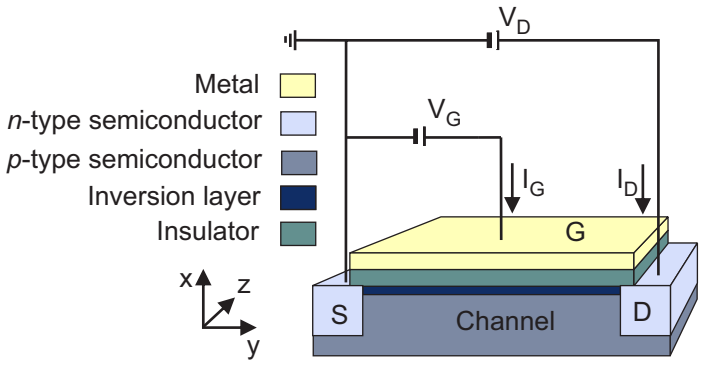

Figure 2.5: Schematic drawing of a n-channel FET illustrating the important components, voltages and currents.

can be generated by a positive voltage V_G at the gate (normally-off). The gate voltage at which the channel switches between the conducting and the insulating state is referred to as threshold voltage V_T.

In order to pass a current through the channel, a voltage V_D is applied between source and drain, with the convention that the source is considered to be on ground and a positive bias is applied to the drain for n-channel devices as illustrated here. In the "on"-state of the transistor, *i.e.*, $V_\mathrm{G} > V_\mathrm{T}$, for $V_\mathrm{D} > 0$, a potential drop in the y-direction along the channel is added to the drop in the x-direction from gate to channel. From source to channel, electrons traverse a n-p junction in forward bias, but from channel to drain, they traverse a p-n junction in reverse bias. For small V_D, the current I_D in the channel increases linearly with the applied voltage. However, if V_D reaches a critical value $V_{D,sat}$, at the drain the depletion region of the p-n junction supersedes the inversion layer. For voltages higher than $V_{D,sat}$, further increases in V_D will not increase I_D, but only extend the depletion layer from the drain further towards the source. This is called the *saturation region* of the transistor. Since the gate voltage determines the channel potential, $V_{D,sat}$ is a function of V_G:

$$V_{D,sat} = \frac{V_\mathrm{G} - V_\mathrm{T}}{M}, \tag{2.34}$$

where M is a constant close to unity.

The dependence of the drain current I_D on the gate and drain voltages V_G and V_D is illustrated in Fig. 2.6. The drain current in the two regions is given by:

$$I_D = \begin{cases} \frac{Z}{L}\mu C_{ox}\left(V_G - V_T - \frac{V_D}{2}\right)\cdot V_D & ; V_D < V_{D,sat}, V_D << (V_G - V_T) \\ \\ \frac{Z}{2ML}\mu C_{ox}\left(V_G - V_T\right)^2 & ; V_D > V_{D,sat}) \end{cases}, \tag{2.35}$$

where Z and L are the width and length of the channel, respectively. μ is the mobility of the charge carriers and C_{ox} the capacitance of the oxide layer.

In the sub-threshold region, where $V_G < V_T$, there is no capacitive carrier accumulation and only thermally excited carriers contribute to conduction. These carriers have to overcome the potential barrier $e \cdot (V_G - V_T)$ and hence their density and the corresponding drain current is given by:

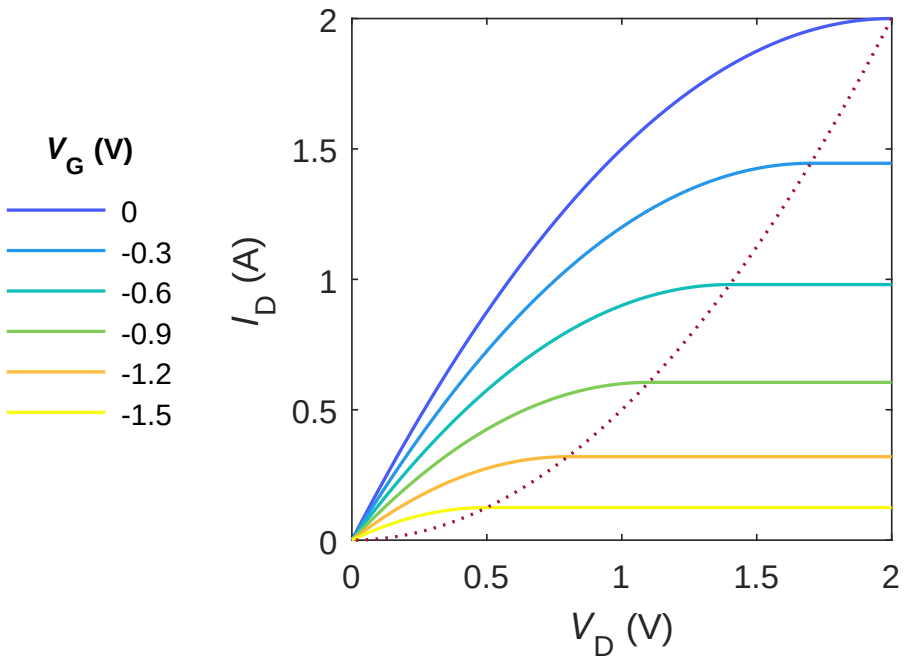

Figure 2.6: Simulated ideal dependence of the drain current I_D on the gate and drain voltages V_G and V_D for a FET. The dotted red curve indicates the onset of current saturation.

$$I_D \propto \exp\left[e\frac{V_G - V_T}{k_B T}\right]. \tag{2.36}$$

The inverse of the logarithmic slope of this equation defines the sub-threshold swing S_{s-th}, which measures the increase in conductivity per applied gate voltage:

$$S_{s-th} = \left[\frac{\partial \log(I_D)}{\partial V_G}\right]^{-1} = \ln(10)\frac{k_B T}{e}, \tag{2.37}$$

where the last equality holds for an ideal transistor. It corresponds to a tenfold current increase for every change of the gate voltage of 60 mV at room temperature.

The charge $Q_n(y)$ of the inversion layer at position y along the channel is given by

$$|Q_n(y)| = C_{ox}\left(V_G - V_T - M\Delta\Psi_i(y)\right), \tag{2.38}$$

where $\Delta\Psi_i(y)$ is the variation of the potential along the channel direction, which can be neglected for small V_D. Therefore, the intrinsic charge carrier density of the channel without external voltages can be calculated from

$$n_{sheet} = -\frac{V_T C_{ox}}{e}, \tag{2.39}$$

where e is the elementary charge.

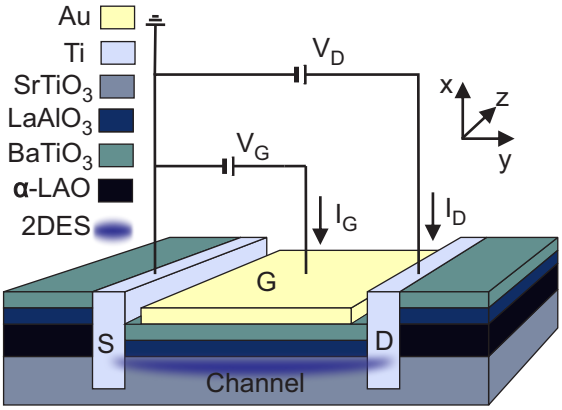

Figure 2.7: Cross-sectional sketch of an $LaAlO_3$–$SrTiO_3$ transistor illustrating the important components, voltages and currents. The principle of operation is explained in the text.

2.3.1 $LaAlO_3$-$SrTiO_3$ transistors

A basic sketch of an $LaAlO_3$–$SrTiO_3$ transistor is shown in Fig. 2.7. $LaAlO_3$–$SrTiO_3$ transistors with an $LaAlO_3$ layer thicker than the critical thickness of three unit cells are normally-on n-channel FETs in which the conducting channel is provided by the oxide 2DES. The $LaAlO_3$ layer serves both as the generator of the 2DES and as insulating gate electrode. It is supplemented by a layer of $BaTiO_3$ to ensure low gate leakage even at high gate voltages. Electrons flow through the 2DES from source to drain. In standard semiconductor transistors, the conduction electrons can be treated in a single-particle mean-field approach. However, in $LaAlO_3$–$SrTiO_3$ transistors the correlations of the electrons play a crucial role and the underlying band structure has to be considered. This provides opportunities, but also challenges.

Grau, teurer Freund, ist alle Theorie.
Johann Wolfgang von Goethe

3 METHODS

This chapter comprises three sections: The first describes the individual steps of sample growth from a bare substrate to a complete sample, the second describes the different sample designs used during the work presented in this thesis. The third describes the methods and setups used for electrical measurements of the samples.

3.1 Sample preparation

The fabrication of a $LaAlO_3$–$SrTiO_3$ sample is a process with numerous steps. This process usually takes several days to complete. It can be divided into three main steps (see Fig. 3.1): First, the substrate has to be cleaned, etched and annealed to obtain a well-defined TiO_2 single termination of the surface. Then, the desired heterostructure is grown by PLD. Finally, electrical contacts are defined on the sample by photolithography.

The sample designs employed for $LaAlO_3$–$SrTiO_3$ samples fall into two categories: For some samples, the conducting interface electron system is patterned into defined channels. For the others, the electron system is left unpatterned and only the electrodes are defined. For samples with patterned electron system, additional processing steps have to be performed on the terminated substrate, which will be described at the end of this section. All processing steps are summarized in a concise list given in section 3.1.6.

3.1.1 Substrate preparation

$LaAlO_3$ can be grown epitaxially on $SrTiO_3$ (001) substrates both with TiO_2 and SrO termination. However, only interfaces grown on TiO_2-terminated $SrTiO_3$ are conductive. Therefore, control of the substrate surface termination is essential. A method to remove SrO layers from the $SrTiO_3$ surface using hydrofluoric (HF) acid etching is well established [83] and was

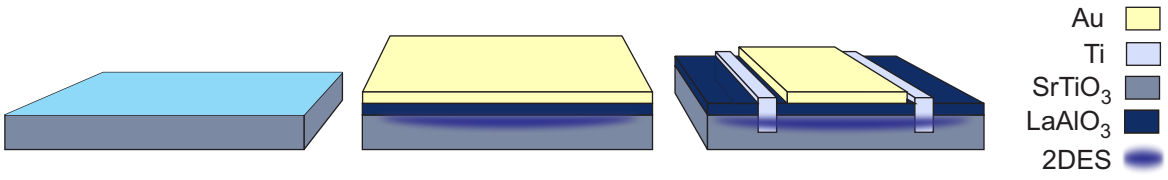

Figure 3.1: The three main steps in the fabrication of $LaAlO_3$–$SrTiO_3$ samples with unpatterned electron systems. From left to right: $SrTiO_3$ substrate with TiO_2 termination; $LaAlO_3$–$SrTiO_3$ interface with gold top layer; complete sample with electrodes.

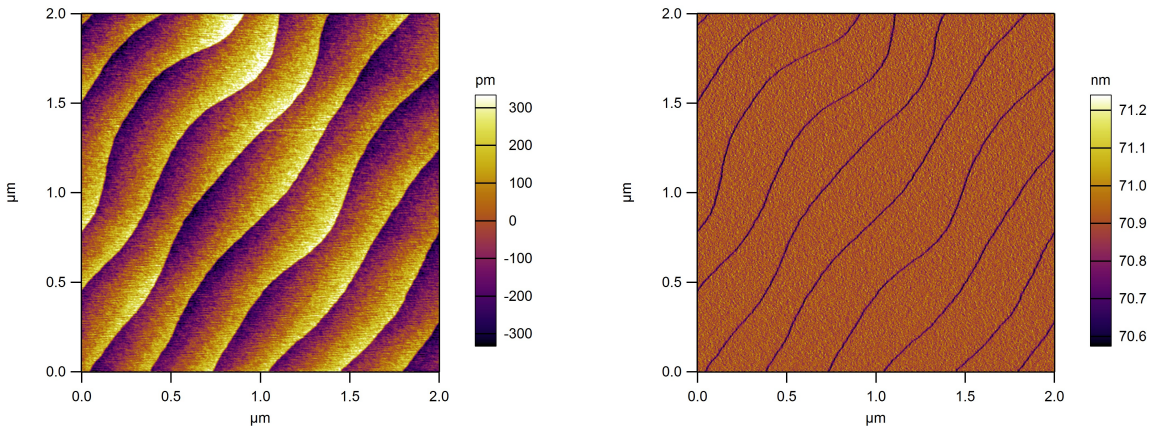

Figure 3.2: AFM images of a prepared $SrTiO_3$ substrate. (a) Height Signal (b) Amplitude Signal

improved shortly after its publication by an additional step in which the SrO is hydroxylated in water prior to etching [84]. The preparation of substrates used in this thesis closely follows the process outlined in the latter publication. Since HF is not only caustic but also highly toxic, safety measures are necessary during the etching.

For the growth of $LaAlO_3$–$SrTiO_3$ interfaces, one-side polished 5 mm × 5 mm × 1 mm $SrTiO_3$ substrates were purchased from CrysTec, Germany and Shinkosha, Japan. The substrates were prepared for deposition using the following procedure:

- Gentle polishing on lens paper wetted with isopropanol.
- Successive ultrasonic cleaning in acetone (10 min), isopropanol (10 min) and ultrapure water (30 min). Ultrasonic cleaning in water hydroxylizes the SrO on the surface.
- Blow-drying with nitrogen (optional).
- Etching in buffered 87.5 % NH_4F- 12.5% HF solution for 30 s in a sonicator to remove SrO layers from the surface.
- Sonication in ultrapure water for 30 s and successive rinsing in two water beakers to remove remaining HF.
- Sonication in ispropanol for 10 s.
- Annealing in a tube furnace with a dwell time of 2 h at 1000 °C in oxygen atmosphere.

All substrates were screened by atomic force microscopy (AFM) after the termination process. Only substrates with a smooth terrace structure without particles were used for sample growth. A typical image of a terminated substrate is shown in Fig. 3.2.

3.1.2 Pulsed laser deposition

All $LaAlO_3$–$SrTiO_3$ heterostructures discussed in this thesis were grown by PLD. PLD is a vapor deposition method specifically suited for the growth of materials with high melting points and of compounds [85–87]. Thin film growth using PLD has several advantages:

- PLD can operate at relatively high pressures (up to 0.1 mbar), which is useful, *e.g.*, when depositing materials that are quickly reduced and require a sufficient oxygen background pressure to avoid the formation of oxygen vacancies.
- The ability to tune both the ablation laser energy and the background gas pressure also allows control of the kinetic energy of the species arriving at the substrate surface. The energy of the species depends on the type of ablation laser, the ablation laser settings and the gas pressure in the chamber, but is usually between the energy ranges found in MBE (≈ 0.1 eV) and sputtering (a few 10 eV) [87].
- The laser quasi-instantaneously ablates a section of the target surface, therefore all constituents of a compound are ejected simultaneously, regardless of their vapor pressures. This allows the stoichiometric growth of films of complex materials.
- The growth of oxides with PLD is relatively fast compared to MBE, thus reducing the high-temperature exposure of the sample and thereby limiting interdiffusion.
- The pulsed deposition causes a high nucleation density on the substrate and consequently a flat film surface.

An overview of a PLD system is given in Fig. 3.3: in an ultrahigh-vacuum chamber pulses of a high-energy laser beam are focused at a target of the desired material. The laser pulse ablates the impact area of the target in approximately 1 ns, creating a plume of plasma. The plasma is slowed by a background gas in the chamber (for oxide growth, oxygen is usually used) before it is deposited on the substrate surface. The surface is heated to ensure good surface diffusion of the arriving species, which is necessary for layer-by-layer growth and correct film stoichiometry and phase formation at the surface.

3.1.3 RHEED

During deposition, the growth process is monitored *in situ* by reflectivity high energy electron diffraction (RHEED) in order to achieve control of the film thickness with single unit cell precision. This diffraction method is surface-sensitive: electrons with a kinetic energy of 30 kV hit the surface at glancing angles, thus penetrating only into the first few atomic layers of the substrate surface. The diffracted electrons are detected by a fluorescent screen. The exact interpretation of RHEED images is complicated, but it is usually possible to observe the growth of unit cells by oscillations in the diffraction intensity: a complete substrate layer gives maximal intensity. When new material appears on the surface during growth, the intensity starts to decrease until about one half of the initial surface is covered. From there, the intensity increases again, until the new material has completed a full unit layer and the RHEED intensity recovers (ideally) its original value. However, this simplistic view is not entirely correct. A complete oscillation of the RHEED intensity always corresponds to a thickness variation of an entire unit cell, except for the first few layers where surface reconstructions and changes of the electron

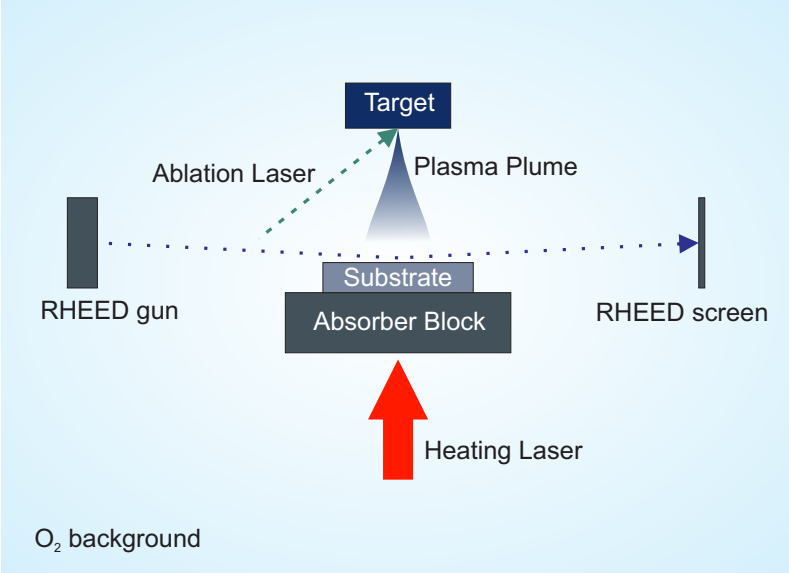

Figure 3.3: Schematic of a Pulsed Laser Deposition system. Explanations of the individual components are given in the text.

potential in the sample can induce a phase shift. However, interpreting the phase of the RHEED pattern is less straightforward: depending on the initial incident angle of the beam, a maximum in intensity does not necessarily correspond to a complete unit cell [88]. However, RHEED oscillations can always only give an upper limit on the growth rate, since they are insensitive to step-flow growth, where new material is deposited laterally at the step edges, thus not changing the surface roughness. In order to keep the RHEED signal reproducible between different depositions, the incident angle of the electron beam is always adjusted to the same inclination for each deposition. An initial RHEED pattern and typical oscillations monitoring the growth of $LaAlO_3$ on $SrTiO_3$ are shown in Fig. 3.4.

3.1.4 Sample growth procedure

The growth parameters for the $LaAlO_3$–$SrTiO_3$ interfaces described here were varied extensively between different samples to achieve the desired 2DES properties. Therefore, the following account describes only the general procedure for sample growth. The parameters for each sample are listed in table 6.1.

A semiconductor laser (Amtron, Germany) is used to heat the sample to the desired deposition temperature. Because the $SrTiO_3$ substrate is transparent for the infrared radiation with wavelength 974 nm emitted by the semiconductor laser, it is glued to a $1\,\text{cm} \times 1\,\text{cm} \times 2\,\text{mm}$ block of Haynes alloy with silver glue. Precise dosage of the silver glue is important, because the entire backside of the substrate must be covered for homogeneous thermal contact, but as little silver glue as possible should reach the substrate sides to minimize the risk of contaminating the surface. Therefore, a pipette is used to transfer 2.5 µL of silver glue liquid onto the Haynes block, onto which the substrate is placed. Then, the glue is baked for 30 min at 80 °C to evaporate the solvents and harden the glue.

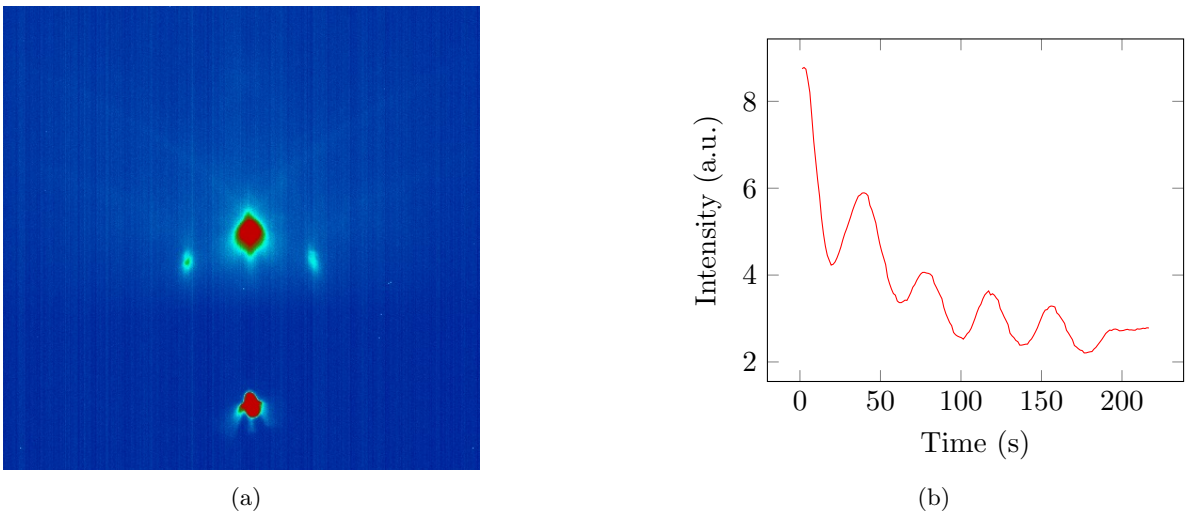

(a) (b)

Figure 3.4: (a) RHEED diffraction pattern of a $SrTiO_3$ substrate surface at 400 °C and 2×10^{-4} mbar O_2. (b) RHEED signal of growth of 5 u.c. of $LaAlO_3$ on a $SrTiO_3$ substrate at 800 °C and 8×10^{-5} mbar O_2.

All targets are polished before each deposition to ensure reproducible growth conditions. If the target has been ablated for too long, its stoichiometry and surface morphology may have changed. Therefore, the topmost layers of the target are polished away to remove the ablated regions and restore the bulk stoichiometry.

The sample on the Haynes block and the polished targets are loaded into the PLD chamber and the oxygen pressure is adjusted to the desired value. The background pressure in the chamber needs to be high enough to slow the plasma particles, otherwise re-sputtering from the substrate may be caused by particles of high energy. However, background pressures that are too high may slow the growth or lead to undesired oxidation (if oxygen is used). An optimization of oxygen pressure for the desired sample properties was performed (see Chapter 6).

Before heating the sample, preablation of the target(s) is performed. Preablation ensures that the ablation is brought to a steady state for the deposition and possible contaminations are removed from the target surface. For preablation, the shutter is closed between target and substrate and the ablation laser is scanned over the ablation area such that every part of the area is ablated 12 times. The shutter remains open for the remainder of the growth process to prevent contamination from the shutter to the substrate.

After preablation, the sample is heated to the deposition temperature with a ramp of 30 °C min^{-1}. During the heating process the RHEED beam is adjusted onto the sample and the sample is rotated to the correct angle and height to produce the desired diffraction pattern. The temperature of the substrate during deposition must be high enough to allow for a high surface mobility of deposited material to ensure epitaxial growth. On the other hand, the substrate temperature must be low enough to avoid decomposition, *e.g.*, formation of oxygen vacancies or interdiffusion between different sample layers. All samples discussed in the present work were grown either at 800 °C or 750 °C. When the sample has reached the desired growth temperature, deposition from the $LaAlO_3$ target is started, while monitoring the oscillations of the RHEED signal. For tunneling samples, a $LaAlO_3$ layer of 4 u.c. is deposited, which is thick

enough to generate a conducting 2DES, but still thin enough to allow for sizable tunneling currents. For transistors, a layer of 6 u.c. of $LaAlO_3$ is deposited and an additional layer of 10-20 u.c. of $BaTiO_3$ is deposited on top of the $LaAlO_3$ as supplemental gate dielectric.

After the deposition, the sample is annealed under high oxygen pressure to remove potential oxygen vacancies. The sample is first annealed at 600 °C for 1 h and then at 400 °C for 1 h. The oxygen pressure for both annealing steps is 400 mbar.

After the sample has cooled to room temperature, a gold top electrode is deposited *in situ* with PLD to prevent an exposure of the surface to air. In order to ablate the strongly reflective gold, a high laser fluence of $3\,J\,cm^{-2}$ and a special striped mask is used. In order to avoid re-sputtering of the sample surface by high-energy gold particles, the chamber contains a high background pressure of 0.1 mbar of Argon during the gold deposition. The use of an inert process gas is necessary since under the extreme physical conditions in the plasma, compounds such as Au_2O_3 can form from the normally non-reactive gold which significantly decrease the conductivity of the electrode.

3.1.5 Patterning of electrodes and electron system

The gold surface is patterned into electrodes using photolithography and etching with KI + I_2 solution. Contacts to the two-dimensional electron system are defined by photolithography, etched by argon-ion milling and subsequently filled *in situ* with titanium and gold using electron beam evaporation. In this process, metal is also deposited on the sides of the sample. Therefore, the edges of the sample are cut with a wiresaw before liftoff of the photoresist to prevent leakage currents from the backside of the sample to the 2DES.

The sample designs employed for the $LaAlO_3$–$SrTiO_3$ samples of this thesis fall into two categories: for some samples, the conducting interface electron system is patterned into defined channels. For the others, the electron system is left complete and only the electrodes are defined. For samples with patterned electron system, additional processing steps have to be performed on the terminated substrate:

Because a critical $LaAlO_3$ thickness is necessary for conductivity at the $LaAlO_3$–$SrTiO_3$ interface and the 2DES exists only at epitaxial interfaces, a straightforward pathway is available to create patterned electron systems at the interface [20, 21, 89]. In the first step, a single unit cell of crystalline $LaAlO_3$ is grown on a TiO_2-terminated $SrTiO_3$ substrate. This $LaAlO_3$ layer is below the threshold for conductivity but protects the delicate $SrTiO_3$ substrate surface. Then, the conductive regions are defined on the sample by optical lithography. Because photoresist is not stable at the high temperatures required for epitaxial growth, a hardmask of amorphous $LaAlO_3$ is grown on the photolithographically defined regions using PLD at room temperature. Lifting off the photoresist under the amorphous $LaAlO_3$ reveals the crystalline surface in the desired regions. Finally, the remaining epitaxial $LaAlO_3$ layers are grown in the patterned regions by the process described in the previous section. The first step of depositing a single epitaxial $LaAlO_3$ layer was found to have only minor influence on the 2DES quality. Therefore, it is skipped in some of the samples and photolithographic patterning is performed directly on the $SrTiO_3$ substrate.

A series of samples with patterned electron system showed no superconductivity in the patterned channel. It appears that the patterning process affects the interface so strongly that it prohibits the formation of a superconducting condensate. A number of different cleaning steps (*e.g.*, oxygen plasma cleaning, high-temperature annealing) were introduced after the liftoff of the hardmask and before the deposition of the final crystalline layer. Furthermore,

growth was performed both with and without inital $LaAlO_3$ layers on the substrate before patterning. However, none of these measures were successful in restoring superconductivity to the normal levels expected for $LaAlO_3$–$SrTiO_3$ (see chapter 6).

3.1.6 Sample growth overview

The following list gives an overview over the processing steps described in this section. Steps 2 a)-d) are only necessary for samples with patterned electron system. The most important items of the list are illustrated in Fig. 3.5, which shows the fabrication of a transistor sample.

1. Substrate cleaning, etching and annealing.
2. 2DES patterning
   a) PLD of 1 u.c. of $LaAlO_3$ to protect the sensitive $SrTiO_3$ substrate surface (optional).
   b) Definition of conducting channels using photolithography.
   c) PLD of 40 nm of amorphous $LaAlO_3$ as high-temperature hardmask for the conducting channels.
   d) Liftoff of photoresist and amorphous $LaAlO_3$ from the conductive channels defined by photolithography: in the channels, the crystalline surface is preserved, whereas the surroundings are covered by amorphous $LaAlO_3$, which is not conducting.
3. PLD of crystalline $LaAlO_3$ to generate the conducting interface. Total $LaAlO_3$ thickness was typically 4 u.c. for tunnel junctions and 6 u.c. for transistors.
4. PLD of 10 u.c. of $BaTiO_3$ gate dielectric (transistors only).
5. Annealing at 600 °C for 1 h and then at 400 °C for 1 h at 400 mbar oxygen atmosphere.
6. PLD of 40 nm of gold top electrode.
7. Definition of gold top electrode using photolithography.
8. Etching of top electrode using I_2-KI-solution.
9. Definition of contacts to the 2DES using photolithography.
10. Etching of holes for contacts to the 2DES using argon-ion milling.
11. Deposition of 30 nm of titanium and 10 nm of gold into etch holes to create contacts to the 2DES.
12. Cutting off sample edges to prevent shorts to backgate.
13. Liftoff of photoresist by soaking in acetone for at least 2 h and sonicating twice for 10 s in successive beakers.

A detailed description of the sample growth process can be found in Ref. [46].

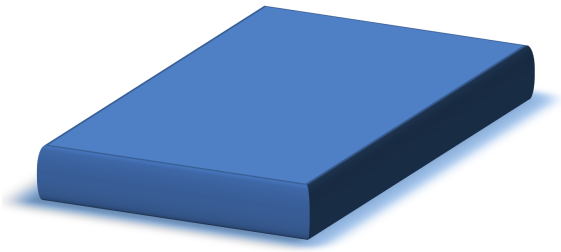

(a) Step 1: prepared $SrTiO_3$ substrate

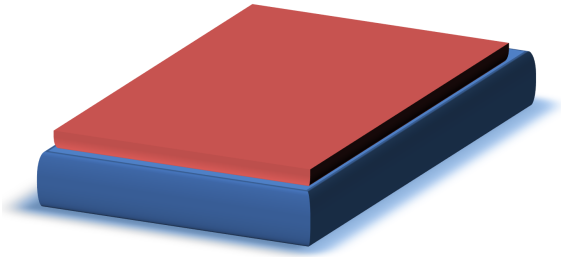

(b) Step 2 a): 1 u.c. of $LaAlO_3$

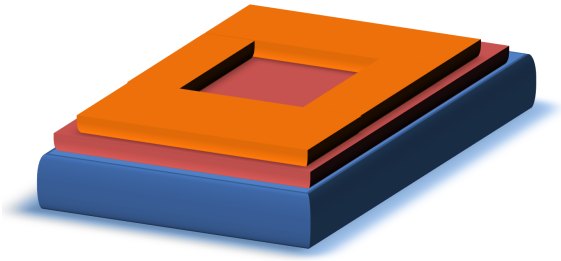

(c) Step 2 c): amorphous $LaAlO_3$ hardmask after liftoff

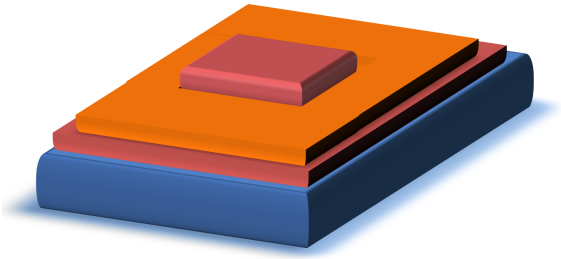

(d) Step 3: crystalline $LaAlO_3$ conductive channel

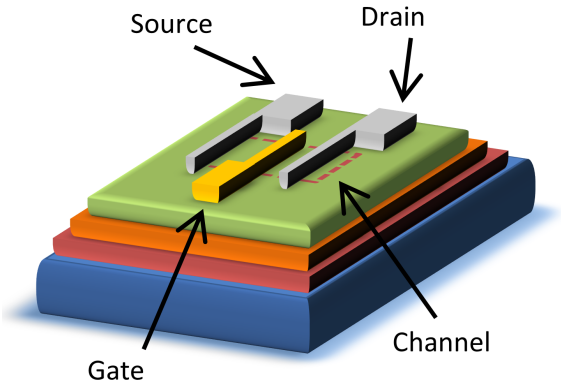

(e) Step 10: Electrodes for gate, source and drain

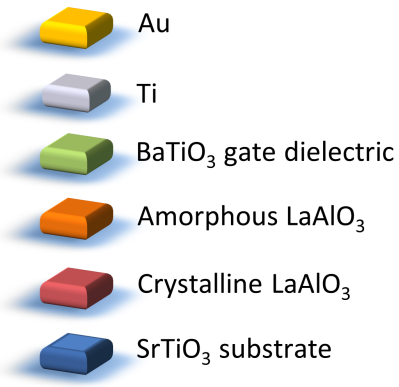

(f) Legend

Figure 3.5: Schematic of different steps in the growth of $LaAlO_3$–$SrTiO_3$ transistors. Detailed explanations of the steps are given in Sec. 3.1.6.

3.2 Device designs

This section gives an overview over the different sample designs used for the measurement of $LaAlO_3$–$SrTiO_3$ samples. Each sample was designed for a specific purpose. For the circular junction, superconducting transistor and van der Pauw sample designs, the conducting channel was not patterned, and only electrodes were defined by photolithography. For the pressurized transistors and pressurized junctions, the conducting channel was patterned by photolithography using the intermediate step of an amorphous $LaAlO_3$ hardmask. It was found that this patterning process is detrimental to the quality of the interface, in particular electron mobilities were lower than in unpatterned samples and superconductivity was absent in the patterned electron system.

First, the three device designs with unpatterned electron system will be described:

3.2.1 Circular junctions

This sample design, shown in Fig. 3.6, was created to allow both tunneling and four-wire sheet resistance measurements. The four devices on each sample are defined by an outer titanium ring which is grounded during measurements and acts as shielding. At the center of the outer titanium ring is a smaller titanium ring acting as the current source. Both the inner and outer ring are supplemented by separated voltage probes for four-wire measurements. The space between the two rings is covered with a gold top electrode for tunneling measurements. The advantage of this sample design is that it provides a well-defined sample geometry for both four-wire and tunneling measurements without need to pattern the electron system. After several experiments with samples in the circular junction geometry, two major drawbacks of this sample design became clear: It is not possible to measure the Hall-voltage in this configuration, therefore carrier density and mobility of the samples remain unknown. In addition, a current flowing from the inner ring electrode of the sample through the 2DES to the outer ring electrode yields a decreasing current density from the inside to the outside. This non-uniform current density leads to increased heating in the inner part of the sample which may obscure intrinsic effects; in particular it makes it impossible to reliably measure the BKT transition.

3.2.2 Van der Pauw-geometry

In order to overcome the drawbacks of the circular junction geometry, a new sample design was needed which allowed both in-plane four-wire and tunneling measurements. Attempts to produce superconductivity in the patterned electron system had met with no success, therefore the active electron system of the sample had to be kept pristine. All these requirements are met by this sample geometry: Eight titanium electrodes are positioned at the corners and at the center of the edges of a $5\,\mathrm{mm} \times 5\,\mathrm{mm}$ $LaAlO_3$–$SrTiO_3$ sample, and the remaining $LaAlO_3$–$SrTiO_3$ is covered with a gold tunnel electrode (inset in Fig. 3.7). Several of these samples were grown without shorts between the gold electrode and the 2DES, even though the thickness of the insulating layer of 4 u.c. of $LaAlO_3$ is just 2 nm whereas the total electrode surface is $25\,\mathrm{mm}^2$. The large tunnel electrode size allows for a comparably large tunnel current even at low voltages, resulting in very high-resolution tunnel spectra of the two-dimensional superconducting condensate (Fig. 3.7). The drawback of the high tunnel conductivity is that when depleting the electron system, the sheet resistance easily becomes comparable to the

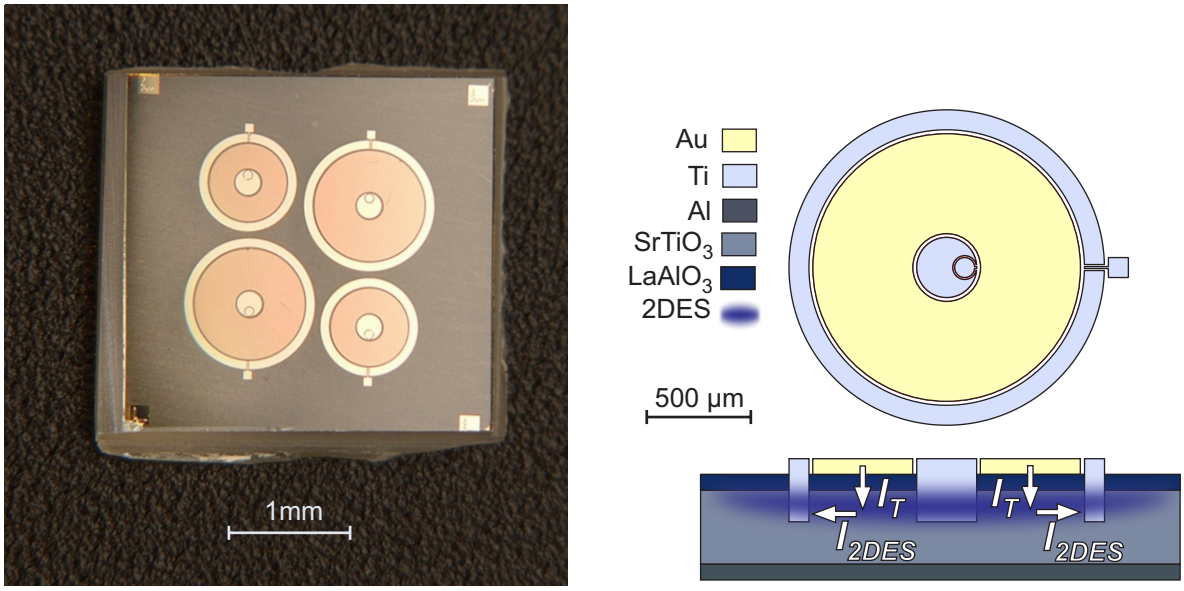

(a) (b)

Figure 3.6: Microscope image and schematic cross section of a circular tunnel junction sample. (a) Sample overview micrograph. (b) Schematic drawing of a single device as top view and cross-sectional cut.

tunnel resistance and tunneling measurements are no longer possible. For this reason, Fig. 3.7 does not show tunneling curves for backgate voltages below $-100\,\mathrm{V}$.

3.2.3 Superconducting transistor

In order to measure transistor characteristics in the superconducting state of the $LaAlO_3$–$SrTiO_3$ 2DES, it was necessary to create samples in transistor geometry without patterning of the electron system. In this sample design (Fig. 3.8), gate, source and drain electrodes are deposited over the whole width of the sample, with additional voltage probes defined close to the source and drain electrodes and the gate. The electron system is not patterned photolithographically, instead the sample is only cut into two parts in the middle. This way, a transistor geometry which also allows Hall measurements is realized without the need to pattern the electron system. The main drawbacks of this sample design are that because of the large size of the devices inhomogeneities of the 2DES may play an important role, and the saw-cut edges can be susceptible to leakage from the top electrode.

For the following device designs, the interface 2DES was patterned:

3.2.4 Patterned tunnel junctions

These samples with 16 devices on each chip, shown in Fig. 3.9 (a), were designed with two purposes in mind: First, to have a tunneling sample with the possibility to perform Hall measurements in the channel and second to provide tunnel junctions small enough to be loaded into a piston cylinder cell for high-pressure experiments. However, because of the deterioration of

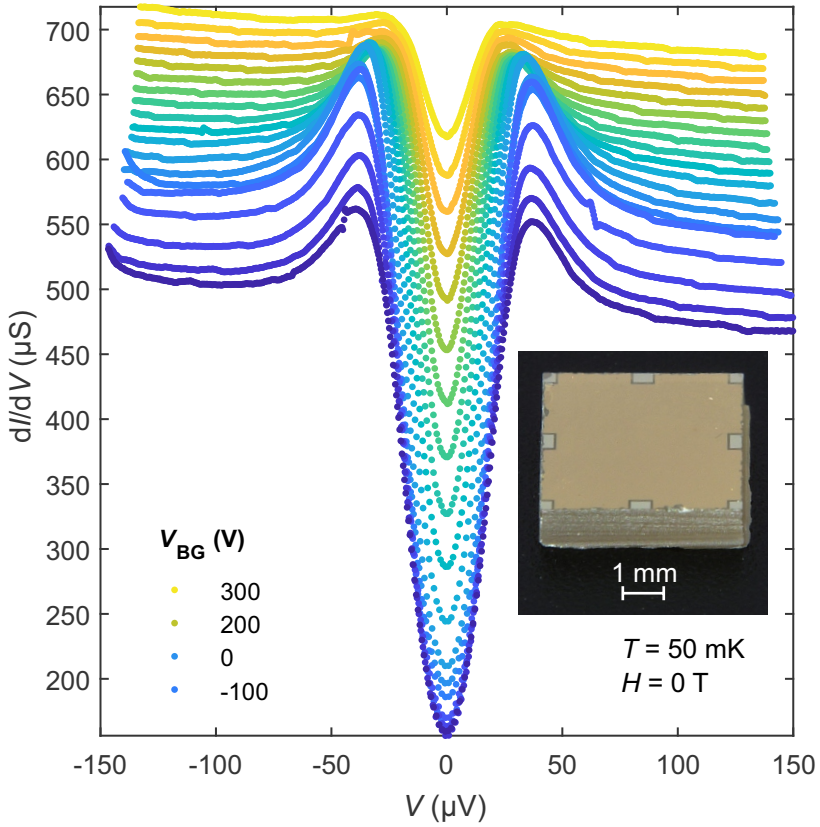

Figure 3.7: Sample in van der Pauw geometry with gold tunneling electrode. The main graph shows high-resolution tunneling spectra of the superconducting gap at different backgate voltages. The curves are shifted by 10 µS each for visibility. The inset shows an optical micrograph of a sample. The electrode edges are slightly frayed from cutting the sides of the sample, one of the cut edges can be clearly seen at the front.

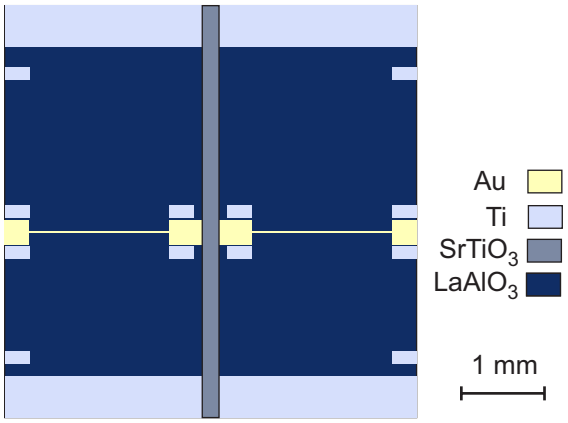

Figure 3.8: Schematic of a superconducting transistor design which avoids the need to pattern the electron system. The vertical separation line is cut with a wiresaw.

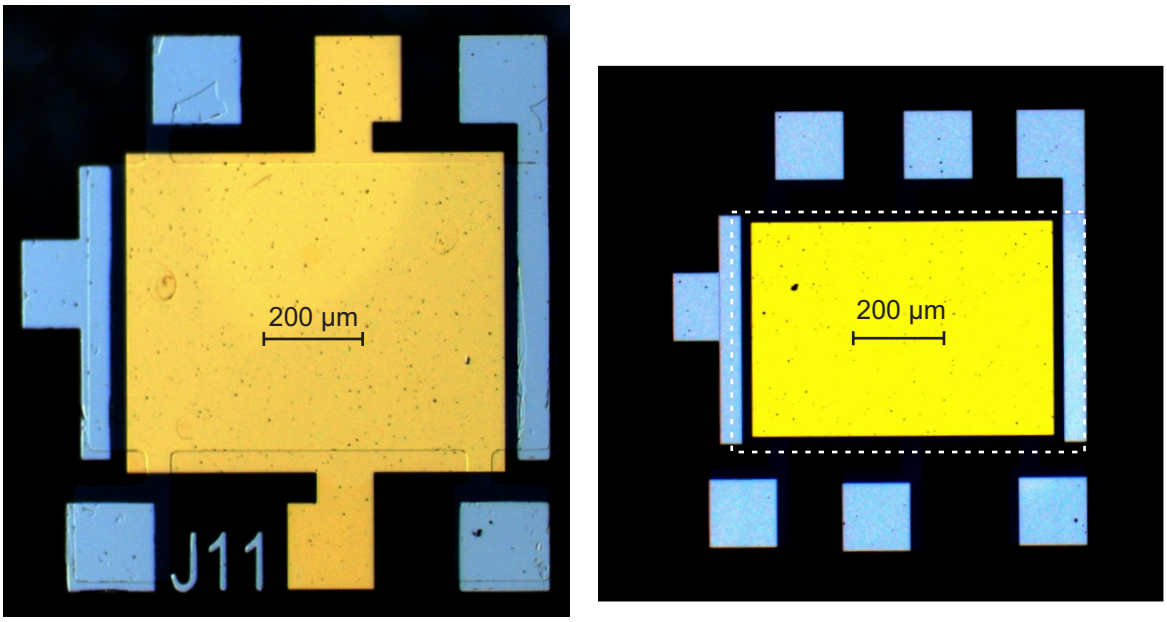

(a) (b)

Figure 3.9: Microscope images of a tunnel junction devices with patterned electron system. (a) Sample with gold electrode covering the edge of the 2DES. The step in height from the hardmask of amorphous $LaAlO_3$ to the conducting channel can be clearly seen under the metal electrodes. One 5 mm × 5 mm chip contains 16 such devices. (b) Sample in which the gold electrode is confined to the 2DES region only. The dashed box indicates the conductive region. The black dots visible on the gold and titanium surfaces are residuals from wiresaw cutting of the sample edges.

superconductivity in the patterned electron system, combined Hall and tunneling investigations of superconductivity were not possible in these samples. In addition the leakage from the topgate to the electron system was unusually high in all samples of this type. This is most likely due to imperfections in the tunnel barrier at the edge of the conducting channel. Therefore, a second design for a patterned junction was developed, in which the gold top electrode is confined to the conducting channel (Fig. 3.9 (b)). With this design, the problem of high gate leakage was overcome, but since no superconductivity could be observed in any patterned samples, tunneling experiments in this sample design were not successful either.

3.2.5 Transistors

$LaAlO_3$–$SrTiO_3$-transistor samples were grown to investigate their behavior under hydrostatic pressure. The basic fabrication process with gold top electrodes and titanium contacts to the interface is identical to the process used for tunnel junctions. In contrast to tunnel junctions, in transistor samples the area of the gold top electrode is kept as small as possible in order to minimize leakage currents and obtain a short conductive channel. In addition, for transistor samples an additional layer of 10 or 20 unit cells (u.c.s) of $BaTiO_3$ is deposited on top of the $LaAlO_3$ layer to supplement the insulating layer. These transistor samples (Fig. 3.10) contain 16 transistor devices on each chip, which are cut apart to obtain individual samples small enough to fit into the piston cylinder cell (PCC) for hydrostatic pressure experiments. Each small

(a) (b)

Figure 3.10: Microscope images of a transistor sample with patterned electron system. (a) Sample overview. (b) Magnification of one conducting channel with two FETs defined by electrodes. The cross-section of these samples is identical to the one shown in Fig. 2.7.

sample consists of a conducting channel with two sets of electrodes, one with channel length 40 µm and one with channel length 30 µm, both with gate length of 20 µm. The transistors were measured on the uncut substrate and again after the cutting procedure to ensure that no damage occurred during the process.

3.2.6 Transistor-Hall bars

Building on the experience collected with the standard transistor layout, these samples were designed to allow for both transistor and Hall-bar measurements in the same device by elongating the conducting channel and adding additional voltage probe contacts. This allows the determination of charge carrier density and mobility of the electron system in two independent ways from Hall measurements and from transistor characteristics. However, the long channel is detrimental to the ON/OFF ratio of the transistor. A micrograph of this sample design is shown in Fig. 3.12 (a).

3.3 Measurement of the phonon peaks in inelastic tunneling

For all samples on which tunneling measurements were possible, tunneling spectra at energies up to 150 mV were recorded to resolve the peaks due to phonon-assisted inelastic tunneling. The energies at which these peaks occur can be identified as the energies of longitudinal optical (LO) phonons in the $SrTiO_3$ substrate, as shown in Fig. 3.11. The very good agreement between the tunneling curves from ten different samples with different device designs and growth parameters indicates reproducible and reliable sample growth, independent from the individual device designs.

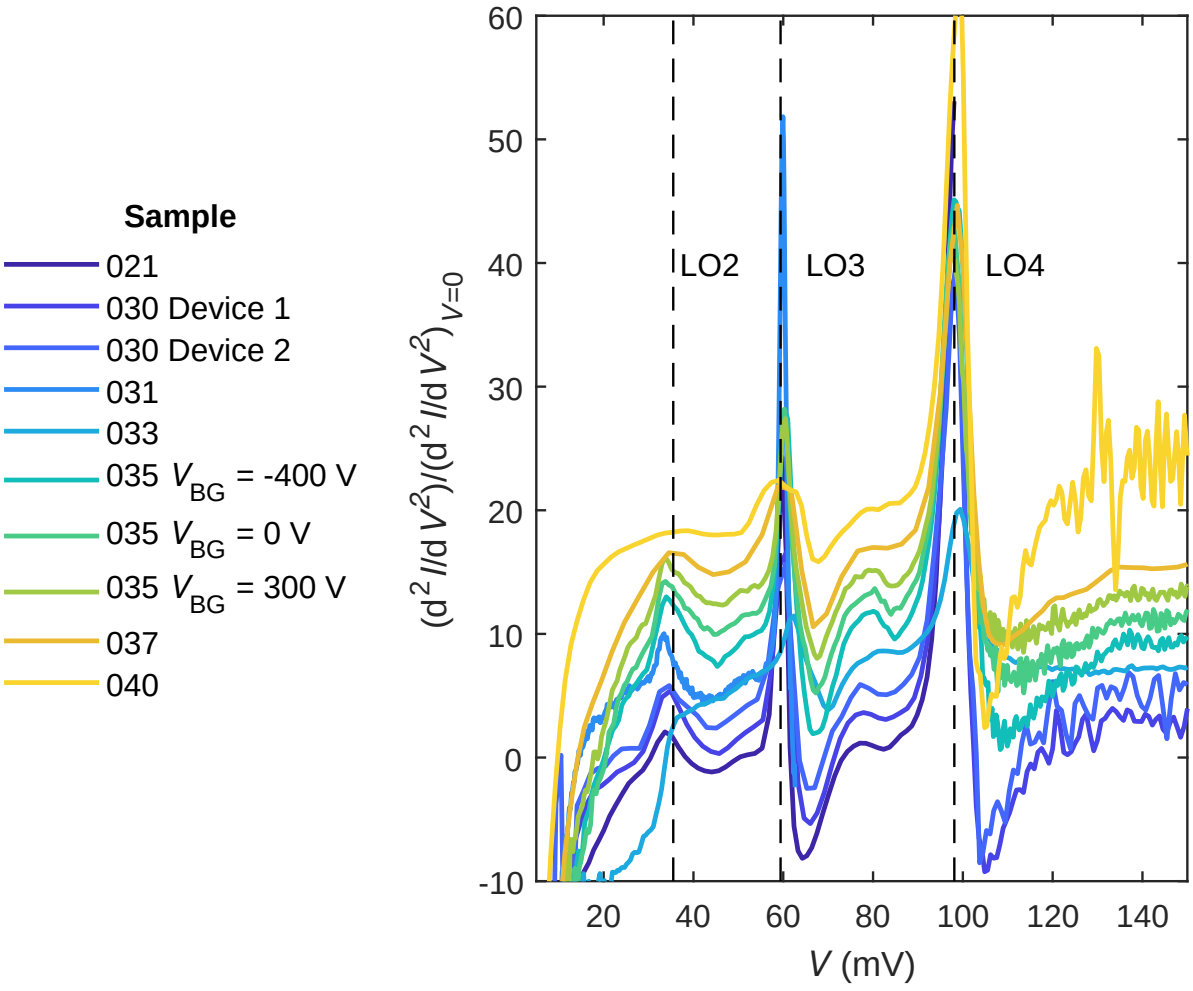

Figure 3.11: Second derivative of the tunneling current $\mathrm{d}^2I/\mathrm{d}V^2$ of eight different devices at different gate voltages measured at 50 mK exhibiting peaks due to inelastic phonon-assisted tunneling. The curves are normalized with respect to $\mathrm{d}I/\mathrm{d}V_{V=0}$ and shifted for visibility by 2 each. The energies of the corresponding longitudinal optical phonons in $SrTiO_3$ are shown for comparison. Here, as in all other tunneling graphs, positive bias corresponds to electrons tunneling from the interface 2DES into the top electrode.

3.4 Measurements

3.4.1 Low-temperature measurements

For measurements at low temperatures, three different setups were available, each with different advantages and disadvantages.

One of the measurement stations was a self-built probestick which could be lowered into a suitable helium dewar. This setup was equipped with a selection of source measure units (SMUs) and lock-in amplifiers. It was suitable for quick test measurements of the low-temperature characteristics of samples, but the temperature range was limited from room temperature to 4.2 K and it was not possible to apply a magnetic field.

Another setup was a physical property measurement system (PPMS) by LOT-Quantum Design. This setup allows measurements in the temperature range 2 K to 400 K and magnetic fields of ±10 T. It features a built-in AC measurement system, but it is also possible to connect external measurement devices such as DC SMUs for transistor measurements. The sample bay of the PPMS is large enough to hold a PCC for hydrostatic pressure experiments.

Finally, a dilution refrigerator (Oxford Cryogenics) was available for the measurement of superconductivity in $LaAlO_3$–$SrTiO_3$ at millikelvin temperatures. The working principle of a dilution refrigerator is discussed in Appendix C. The temperature directly at the sample was measured using a ruthenium oxide sensor, which showed that the sample was usually significantly warmer than the mixing chamber. The base temperature of the mixing chamber was 16 mK, corresponding to a sample temperature of approximately 50 mK. The magnet of the superconductor was able to supply magnetic fields up to ±12 T. All DC electrical measurements in the dilution refrigerator were performed using a Keithley6430 sourcemeter with preamplifier as a current source and a Keithley2001 multimeter or Keithley2182 nanovolt meter as a voltage meter. Sweeps were controlled by a custom made LabView virtual instrument (VI). AC electrical measurements in the dilution refrigerator were performed with Stanford Research SR830 lock-in amplifiers with preamplifiers, using low frequencies, usually 8.333 Hz.

3.4.2 High-pressure experiments

When subjecting a crystalline material to pressure, its crystal structure deforms to accommodate the resulting strain. The most straightforward of these deformations is a reduction of the lattice constants and consequently the unit cell volume. However, more complex deformation mechanisms such as distortions and changes of the crystal structure are possible as one moves on the pressure axis of the phase diagram. In this thesis, the effect of hydrostatic pressure on $LaAlO_3$–$SrTiO_3$ transistors is presented.

Experiments on samples under hydrostatic pressure were performed using a commercially available PCC purchased from Almax easyLab. Daphne oil was used as pressure medium and a manganin coil as pressure gauge. The PCC electrical leads were contacted to an adapter connecting to the measurement channels of the PPMS, allowing measurements at low temperature and in magnetic fields.

The as-grown sample chips were cut and thinned by the in-house crystal preparation group to produce small samples with individual devices, which were then mounted on the feedthrough for electrical contacts and inserted into the PCC (Fig. 3.12). This task was performed by Jone Zabaleta and Sarah Parks. More details on the preparation of $LaAlO_3$–$SrTiO_3$ samples for measurements in pressure cells can be found in Refs. [23, 90].

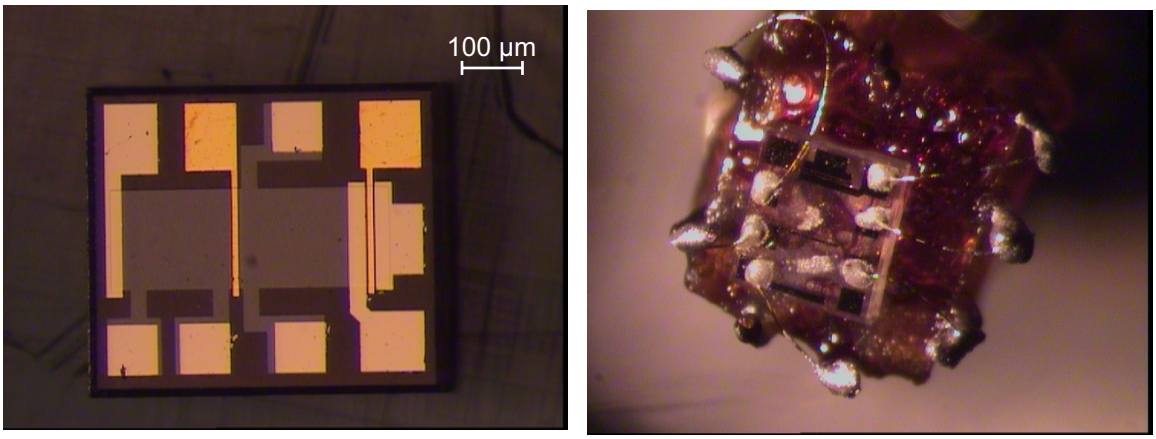

(a) (b)

Figure 3.12: Transistor 3 of sample P-LUK053 in preparation for mounting in the pressure cell. (a) Cut and free-standing (b) Mounted on feedthrough, wires attached and secured for insertion in pressure cell.

To achieve great things, two things are needed;
a plan, and not quite enough time.
Leonard Bernstein

$LaAlO_3$ – $SrTiO_3$ TRANSISTORS UNDER HYDROSTATIC PRESSURE 4

This chapter describes measurements under hydrostatic pressure of FETs in which the $LaAlO_3$–$SrTiO_3$ 2DES constitutes the conducting channel. The carrier density and by consequence also the conductivity of the $LaAlO_3$–$SrTiO_3$ interface can be tuned by the application of a gate voltage. This allows for the construction of $LaAlO_3$–$SrTiO_3$ FETs in which the current between source and drain contact is modulated by the gate voltage applied to a conducting channel. FETs made from $LaAlO_3$–$SrTiO_3$ have been demonstrated previously [20]. It was shown that these transistors can be monolithically integrated to form complete circuits [21] and recently $LaAlO_3$–$SrTiO_3$-transistors in very small dimensions have been fabricated [89].

The investigation of transistors under high-pressure conditions was motivated by earlier experiments measuring the electrical transport properties of the $LaAlO_3$–$SrTiO_3$ interface under pressure using Hall-bar structures [23, 90, 91]. The goal of the present measurements was to elucidate how the transistor characteristics would change along the pressure axis of the phase diagram. Transistor measurements under hydrostatic pressure have been performed previously, *e.g.*, on semiconductor quantum wells and on organic transistors [92–94], but the present work is the first demonstration of oxide transistors subjected to hydrostatic pressure. Pressurizing transistors is more challenging than pressurizing Hall-bars, because any short through the thin insulating gate barrier can destroy the transistor. It is therefore a demonstration of the stability of the $LaAlO_3$–$SrTiO_3$ system that entire devices with insulating layers of few nanometers can be subjected to high pressures without breakthrough or leakage.

As is discussed in section 2.3, it is possible to extract the values of the sheet carrier density and the mobility from transistor characteristics. Measurements of these characteristics were performed on samples of the standard transistor design presented in section 3.2.5 using the measurement methods described in section 3.4.2. The evolution of these parameters was found to reproduce that of the previous Hall-bar investigations.

In a second set of experiments, samples were grown in a combined transistor-Hall-bar geometry as described in section 3.2.6 and shown in Fig. 4.4. These samples allowed *in situ* comparison of transistor and Hall-bar results and revealed subtle differences between results of the two methods. Both methods can be used to determine carrier densities and mobilities, however both have their particular shortcomings. When determining the carrier density from a transistor transfer curve, the capacitance between gate and channel has to be known precisely, which does not only depend on the material properties and thickness of the insulator, but may also be dependent on the voltage applied. On the other hand, determining the carrier density from Hall measurements can be complicated by the anomalous Hall effect in ferromagnetic materials or it can require sophisticated data fitting if multiple bands contribute

to conductivity. From an experimental point of view, it is usually easier to add a gate to a device than to structure a Hall-bar, and transistor measurements are performed more easily than Hall measurements because they do not require magnetic fields. Therefore, transistor measurements constitute the easier approach to the measurement of carrier densities, whereas Hall measurements give more precise results, if the data analysis is performed correctly.

4.1 Standard transistors

Fig. 4.1 shows transfer curves from the standard transistor sample 029 (described in section 3.2.5) under different pressures for two different temperatures. The $LaAlO_3$ layer of this sample was grown at an oxygen pressure of 8×10^{-4} mbar with a laser fluence of $1.2\,\mathrm{J\,cm^{-2}}$ at a temperature of 800 °C. The $LaAlO_3$ layer had a thickness of 5 u.c. and the $BaTiO_3$ gate dielectric a thickness of 10 u.c. With a sub-threshold-swing of $80\,\mathrm{mV\,dec^{-1}}$ and ON/OFF-ratio $> 10^5$, the transistor is functional already at room temperature (Fig. 4.1 (a)). The ON-state sheet resistance of 70 kΩ, however, is high compared to semiconductor devices. Cooling the electron system increases the conductivity of the $LaAlO_3$–$SrTiO_3$ interface, hence at 2 K the ON/OFF-ratio increases to $> 10^6$ and the sub-threshold-swing drops to $30\,\mathrm{mV\,dec^{-1}}$ (Fig. 4.1 (b)). At this temperature, the sheet resistance in the ON-state is reduced to 1 kΩ. These transistor characteristics are representative also for the other standard transistor samples which were measured.

A first aspect of the evolution of the 2DES with pressure can be seen in these curves: at both temperatures, increasing pressure causes a shift to more negative threshold voltages, indicating an increase in sheet carrier density.

For all temperatures and pressures, the sheet resistance of the channel was calculated from the ON-state resistance ($V_\mathrm{G} = 0\,\mathrm{V}$). In addition, charge carrier density and mobility were extracted from the transfer curves at $V_\mathrm{D} = 0.05\,\mathrm{V}$ in the saturation region. According to textbook semiconductor knowledge (e.g. [82],) the dependence of the drain current I_D on the gate voltage V_G in the saturation region of the transistor is given by:

$$I_\mathrm{D} = A\mu C_\mathrm{ox} \left(V_\mathrm{G} - V_\mathrm{T}\right)^2 . \tag{4.1}$$

Where A is a constant depending on the transistor geometry, μ is the mobility of charge carriers, C_ox the capacitance of the oxide gate stack and V_T the threshold voltage (cf. Eq. 2.35). Thus, plotting $\sqrt{I}$ as a function of V_G, the threshold voltage is extracted as the x-intercept of a linear fit line. The sheet carrier density as a function of threshold voltage is then given according to Eq. 2.39. For this purpose the capacitance C_ox of the oxide layer is calculated. Because the dielectric constant of $BaTiO_3$ is significantly higher than that of $LaAlO_3$, only the capacitance of the $LaAlO_3$ layer has to be taken into account. The dielectric constant for thin films of $LaAlO_3$ with thickness 6 u.c. was determined to be $\epsilon = 7$, a significantly different value from the bulk dielectric constant of 24 [46]. Assuming a perfect thickness d of 6 u.c. (*i.e.*, 3 nm) for the $LaAlO_3$ layer, the capacitance per unit area is calculated as:

$$C_\mathrm{ox} = \frac{\epsilon\epsilon_0}{d} = 0.045\,\mathrm{F\,m^{-2}} \tag{4.2}$$

However, this value is subject to a number of uncertainties: Since the 2DES is located inside the $SrTiO_3$ and not precisely at the interface, the value of d may be larger than the nominal $LaAlO_3$ thickness. Furthermore, the dielectric constant of $SrTiO_3$ changes with temperature

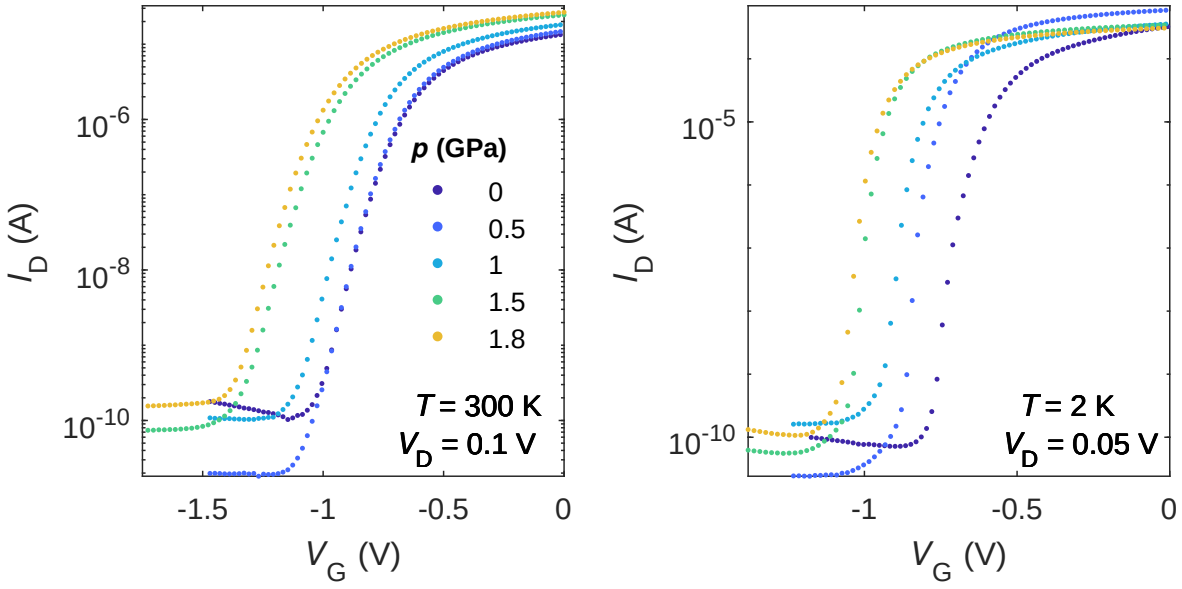

Figure 4.1: Transfer characteristics of sample 029 at different temperatures and pressures. (a) Transfer characteristics at 300 K. (b) Transfer characteristics at 2 K are significantly improved with respect to room temperature. At both temperatures, increasing pressure causes a shift to more negative threshold voltages, indicating an increase in sheet carrier density.

and under applied pressure, so that the extension of the 2DES in the $SrTiO_3$ and consequently d changes. Most importantly, in previous measurements of $LaAlO_3$–$SrTiO_3$ samples in parallel plate geometry it was found that the value of ϵ depends on the applied back- and topgate voltages [46]. An additional uncertainty is introduced when the drain voltage is comparable to the gate voltage. In this case the term $\Delta\Psi_i(y)$ in equation 2.38 is no longer negligible, so that equation 2.39 no longer holds. On the other hand, the drain voltage should be large in order to to ensure that the transistor is in the saturation region, making the choice of a suitable drain voltage for the carrier density determination important.

From the threshold voltage, the carrier density was calculated according to Eq 2.39. Results are shown in Fig. 4.2. Good agreement was found with previous measurements on simple Hall-bar structures [23]: The threshold voltage becomes more negative, *i.e.*, the carrier density increases (Eq. 2.39) with pressure for all temperatures (Fig. 4.2 (a) and (b)). This is attributed to a lattice rearrangement of the $LaAlO_3$ layer and a subsequent change of the polarization at the interface. At low temperatures, the mobility decreases with pressure, because the dielectric constant of $SrTiO_3$ is reduced with increasing pressure, and consequently screening of defects is reduced. On the other hand, the suppression of lattice vibrations with pressure and the corresponding reduction of electron-phonon scattering causes an increase of mobility with pressure at room temperature (Fig. 4.2 (c)). For the sheet resistance, the large change in mobility is more significant than the smaller change in carrier density, hence sheet resistance decreases with pressure at low temperature and increases with pressure at high temperature (Fig. 4.2 (d)).

The data presented so far were obtained during the pressurization of the sample. Upon depressurization, the threshold voltage did not decrease immediately, but exhibited the hysteresis-

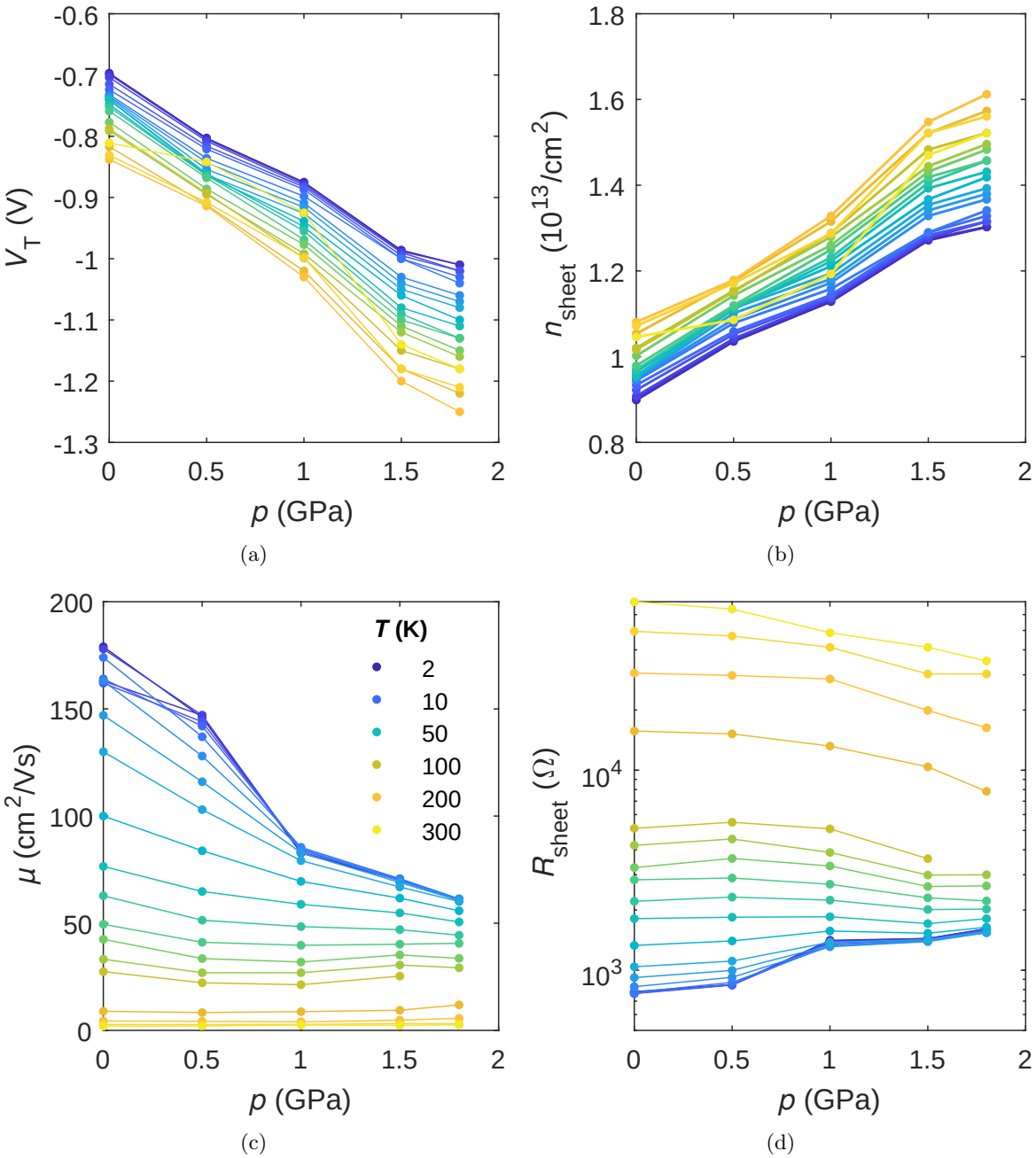

Figure 4.2: Summary of the measurement results on sample 029 as function of hydrostatic pressure for different temperatures extracted from transfer curves at $V_D = 0.05\,V$. (a) Threshold voltage. (b) Charge carrier density. (c) Charge carrier mobility. (d) ON-state sheet resistance ($V_G = 0\,V$). Results are consistent with Fig. 3 of Ref. [23] and Fig. 6 of the supplementary of Ref. [23].

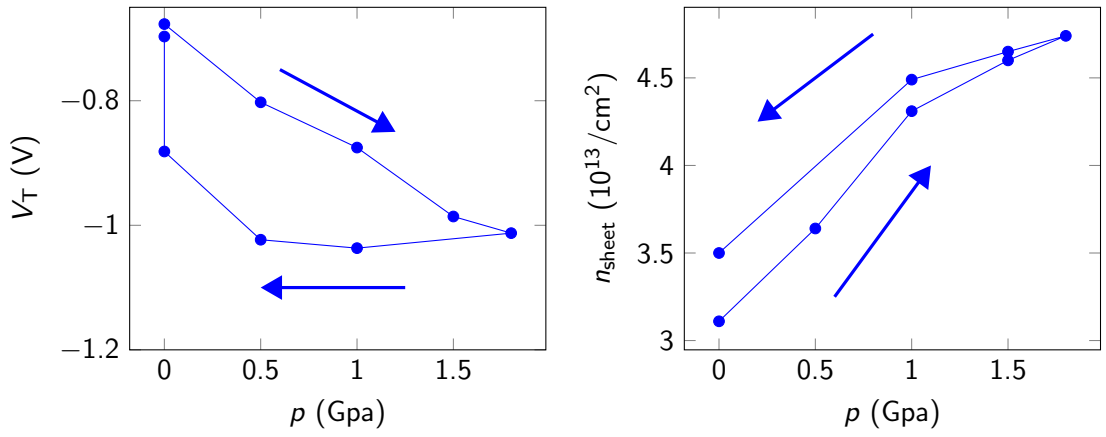

(a) (b)

Figure 4.3: Hysteretic behavior of threshold voltage and sheet carrier density at T=2 K with pressure. (a) Evolution of threshold voltage of sample 029 during pressurization and depressurization. More negative threshold voltages correspond to higher carrier densities. (b) Evolution of carrier density as extracted from Hall measurements of sample 053 during pressurization and depressurization. The hysteretic behavior is less pronounced in the Hall data, likely indicating a contribution of the ferroelectric $BaTiO_3$ gate dielectric to the hysteretic behavior.

like behavior shown in Fig. 4.3 (a). Only after waiting for 192 h at 0 GPa was the original threshold voltage recovered. The Hall measurements on sample 053 shown in Fig. 4.3 (b) reproduce this trend, albeit in a weaker form. The fact that the hysteretic behavior is less pronounced in the Hall data possibly indicates a contribution of the ferroelectric $BaTiO_3$ gate dielectric to the hysteretic behavior. The hydrostatic pressure applied to the $BaTiO_3$ reduces the size of the unit cell, which can be accommodated by a reduction of the tetragonality. Since the ferroelectric polarization is reduced with the tetragonality, the capacitance of the oxide layer and hence the threshold voltage is expected to be affected. In the previous measurements of Hall-bars without gate stacks [23], no hysteresis effect with pressure was observed, corroborating the hypothesis that the $BaTiO_3$ layer is responsible for the hysteresis.

4.2 Transistor-Hall-bars

The FET measurements probe properties of the 2DEL which are different from those probed by a Hall-bar. In order to obtain a direct link between the two measurement methods, a sample was designed which allowed for simultaneous transistor and Hall-Bar measurements (see section 3.2.6 and Fig. 4.4). The gate length of 20 µm is the same for both transistor designs, therefore the characteristics of both designs are similar. However, the source and drain input leads are longer for the transistor-Hall-bar and hence resistances are increased, resulting in lower ON/OFF-ratios of approximately 10^5 at low temperature and lower on-state conductivity than in sample 029. The $LaAlO_3$ layer of sample 053 was grown at an oxygen pressure of 8×10^{-5} mbar with a laser fluence of 0.8 J cm^{-2} at a temperature of 800 °C. The $LaAlO_3$ layer had a thickness of 6 u.c. and the $BaTiO_3$ gate dielectric a thickness of 20 u.c. This sample was grown at lower laser fluence and oxygen pressure than sample 029, therefore the native carrier density of the interface is higher and the threshold voltage more negative as is shown

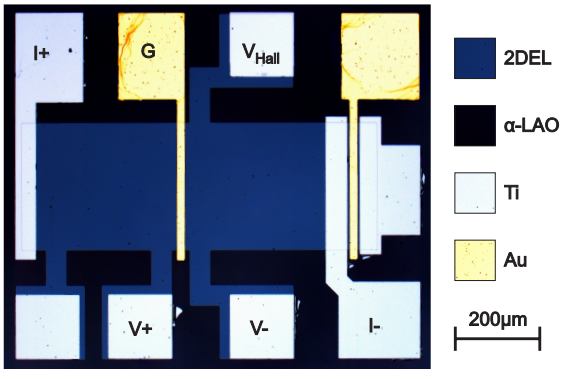

Figure 4.4: Optical micrograph of the transistor Hall-bar sample 053. The device consists of a transistor (right) and a combined transistor-Hall-bar structure with additional voltage probes for Hall and four-wire measurements (left). The $LaAlO_3$–$SrTiO_3$ 2DEL constitutes the conducting channel of the device, whereas regions defined by amorphous $LaAlO_3$ are not conductive. The functions of the contacts on the transistor-Hall-bar section of the sample are indicated.

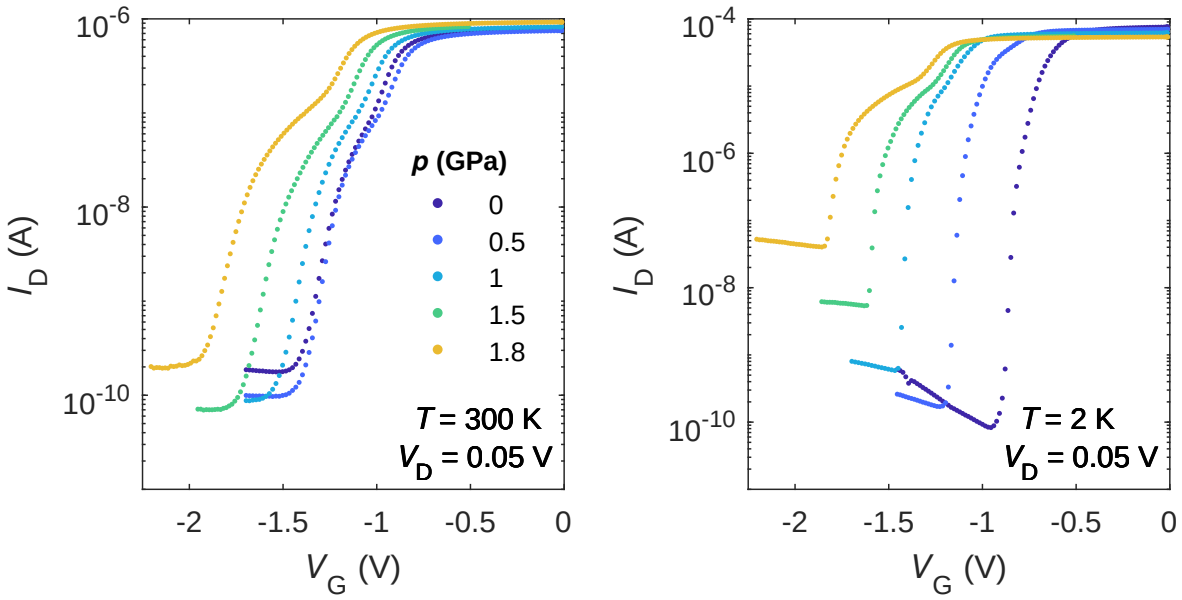

Figure 4.5: Transfer characteristics of sample 053 at different temperatures and pressures. (a) Transfer characteristics at 300 K (b) Transfer characteristics at 2 K. As compared to sample 029 (Fig. 4.1), the intrinsic carrier density of the 2DES is higher, *i.e.*, the threshold voltages are more negative. In addition, the increased channel length leads to a lower ON/OFF-ratio and higher ON-state resistance.

in Fig. 4.5. Additional voltage probes are attached to the channel in order to measure Hall and four-wire resistances. All transistor characteristics presented here, including those for transistor-Hall-bars, are pure 3-terminal measurements since the additional voltage probes were only used for Hall measurements.

In Sec. 4.1, the uncertainty in extracting carrier densities from transistor characteristics due to the uncertainty in the oxide capacitance was discussed. Additional discrepancies between

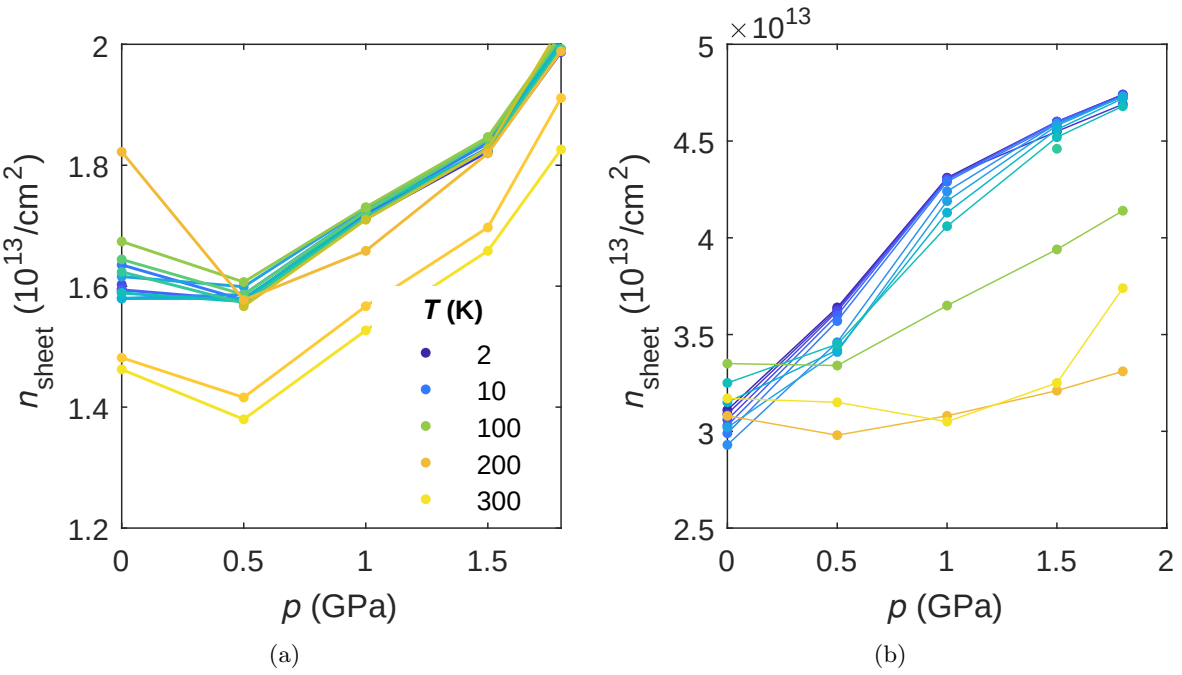

(a) (b)

Figure 4.6: Sheet carrier density of sample 053 assuming single-band transport as a function of pressure for different temperatures. (a) Sheet carrier density as calculated from the threshold voltage of the FET for a drain bias of $V_{\mathrm{D}} = 1\,\mathrm{V}$. (b) Sheet carrier density as calculated from Hall measurements.

transistor and Hall measurements can be attributed to the fact that they probe different parts of the electron system: The transistor characteristics are only sensitive to the 2DES below the gate stack, whereas the Hall bar probes the entire channel. Furthermore, changes of the transistor characteristics with pressure are possibly not only due to changes in the 2DES itself, but also due to changes of the gate insulator.

It is not surprising, therefore, that the sheet carrier densities of sample 053 as extracted from transistor and Hall measurements assuming single-band transport shown in Fig. 4.6 differ from one another not only in value, but also in response to pressure and temperature. One might then conclude that Hall measurements are always the better means of determining the carrier density as compared to transistor characteristics. This is not the case, however, because Hall measurements are also susceptible to a number of artifacts, especially when fitting multiple bands, as will be shown below.

A Lifshitz transition between single-band and multiband transport with variation of the carrier density has been reported to occur at the $LaAlO_3$–$SrTiO_3$ interface [65, 66]. In particular, recent experiments on pressurized $LaAlO_3$–$SrTiO_3$ Hall-bars have reported the presence of positively charged charge carriers [24]. In order to clarify the contribution of separate bands to conductivity in sample 053, Hall and magnetoresistance data up to 8 T were measured (Fig. 4.7). Intriguingly, the nonlinearities due to multiple bands decrease with pressure, even though the total carrier density increases. This is most likely due to the decrease of mobility with pressure, which makes it more difficult to disentangle the two bands. Models were fitted to this data, which gave information on the carrier densities and mobilities of these bands. Two different models, one fitting the measured resistances (see Sec.D.2) and one fitting the conductivities

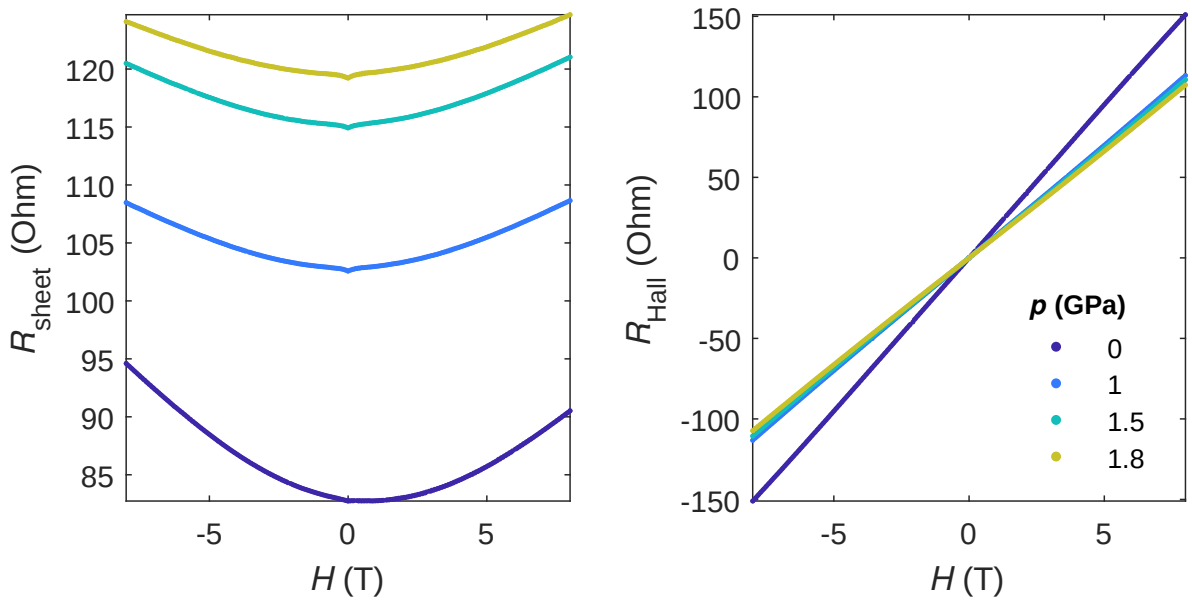

(a) (b)

Figure 4.7: Hall- and Magnetoresistance measurements as a function of hydrostatic pressure in the $LaAlO_3$–$SrTiO_3$ 2DES of sample 053 at T=4 K. (a) Magnetoresistance at different pressures. (b) Hall resistance at different pressures. The Hall curves show a weak nonlinearity which can indicate multiband conductivity. The nonlinearities decrease with increasing pressure.

calculated from these resistances (see Sec.D.1) gave consistent results and reproduced the result of negative charge carriers (Fig. 4.8). However, the nonlinearities in the Hall curve are quite weak (Fig. 4.7 (b)), which makes multiband fits to this data difficult. As is explained in Appendix D, these fits can often encounter local minima. These appear to fit the data well, but they do not describe the real system.

Analysing the measurements on the transistor can give additional insight on the multiband nature of the system. In contrast to the standard transistor characteristics observed on sample 029 and other transistor samples, on sample 053, which has a higher carrier density, peculiar kinks are observed in the transfer curves at high pressures (Fig. 4.9). As described by Eq. 4.1, plotting $\sqrt{I_D}$ versus V_G, one expects to obtain a linear dependence. However, in the present case several distinct linear regions, each with separate slopes and intercepts are observed. These correspond according to Eq. 4.1 to separate mobilities and threshold voltages, respectively. One can in this case assume that the FET consecutively depletes separate conduction channels or separate bands. Indeed, these results closely resemble measurements on individually depletable double quantum wells in GaAs heterostructures [95].

Even though quantitative comparison between Hall-bar and transistor results is difficult, the transistor data can give a clear verdict on the most surprising result of the Hall fits, *i.e.*, the positive charge of the carriers in the second band. Fig. 4.10 shows two different model calculations for transfer curves of a two-band transistor: In Fig. 4.10 (a), a simulated transfer curve for the saturation region of two bands with negatively charged carriers with different densities and mobilities is plotted, where values for carrier densities and mobilities are taken from the Hall fit result for sample 053 at 1.8 GPa, but all with positive sign. The simulation

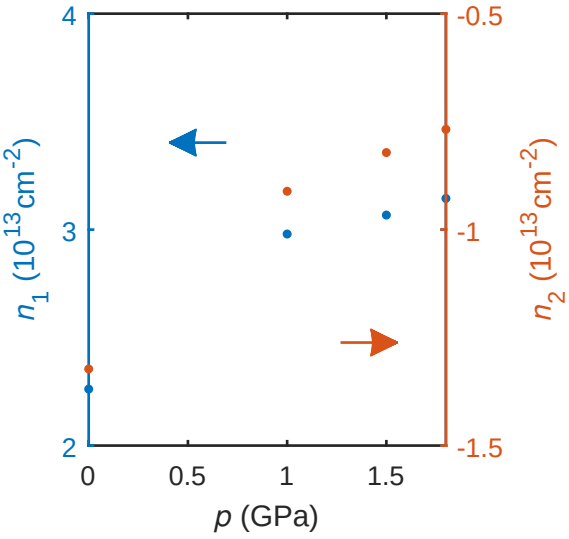

(a)

Figure 4.8: Carrier density of sample 053 at 4 K as a function of hydrostatic pressure as extracted from fits to the conductivity curve. Fits to the Hall and longitudinal resistance curves give similar results (not shown). The fit results yield a positive carrier density n_1 which increases with pressure, and a negative carrier density n_2 which decreases with pressure. The negative charge carrier density represents a band of positively charged carriers.

reproduces the kink which was observed in the data shown in Fig. 4.9. Fig. 4.10 (b) shows the same simulation, but with the polarity of the second band inverted. The behavior of the drain current differs clearly from the that in Fig. 4.10 (a): As the gate voltage becomes more negative, the band of negatively charged carriers is depleted, but charge carriers are accumulated in the band of positive carriers. Hence the drain current does not vanish, but passes through a minimum and subsequently increases again. This model is not compatible with the data shown in Fig. 4.9, ruling out the presence of positive charge carriers at the interface.

It is not clear whether the small linear region observed in Fig. 4.9 at very negative gate voltages just above the onset of conductivity represents a third band or is due to an additional anomaly of the transistor. If it is indeed an indication of a third band, the Hall and magnetoresistance data would have to be fitted with three instead of two bands, which is a computationally rather involved task. Nonetheless, the conclusion that all charge carriers have negative sign remains valid for both two- and three-band scenarios.

Inspecting Fig. 4.10 (a) more closely also aids the interpretation of the different linear regions of the transfer curve shown in Fig. 4.9 because it shows how the current of the two bands adds up to the total measured current: The onset of conductivity corresponds to the threshold voltage of the band with the highest carrier density and the initial slope represents the mobility of this band. The voltage at which the kink is observed in the total current corresponds to the threshold voltage of the second band. $\sqrt{I}$ in this region is the square root of the sum of the two currents from the two bands, therefore the slope of the curve above the kink is not simply $\mu_1 + \mu_2$, but μ_2 can be calculated from it since all other quantities are known. In this simplistic model, the influence of the current in band 1 on the current in band 2 is not taken into account. It is conceivable that the carrier density (and consequently the current) in

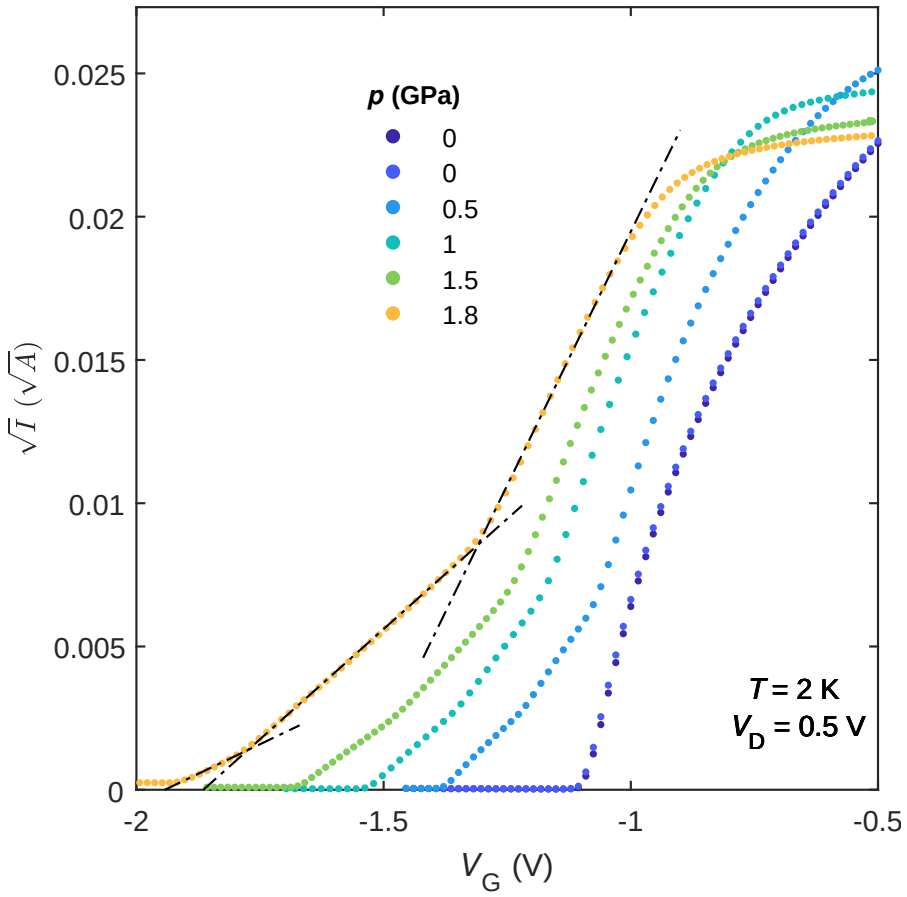

Figure 4.9: Transfer characteristics of sample 053 at 2 K with drain bias of 0.5 V as a function of pressure. Whereas at 0 GPa the results from sample 029 are reproduced, with increasing pressure kinks develop in the transfer curve. According to Eq. 4.1, a plot of $\sqrt{I_D}$ versus gate voltage should be linear in the saturation region. However, at high pressures several distinct linear regions are observed as is shown exemplarily for the 1.8 GPa curve. This behavior can be attributed to the successive depletion of multiple conduction channels, each with individual mobility and carrier density.

band 1 saturates or drops once band 2 begins to be populated. Furthermore, as this model only describes the saturation region, it does not reproduce the eventual leveling off of the drain current increase observed in a real transistor. The model can therefore only serve as a first approximation to interpret results such as shown in Fig. 4.9.

4.3 Conclusion

This chapter presented several new results about the $LaAlO_3$–$SrTiO_3$ 2DES which were obtained by transistor measurements. First, the results on the pressure dependence of conductivity in the 2DES under hydrostatic pressure from Refs [23, 90, 91] were confirmed. Then, it was proven that transistors built from $LaAlO_3$–$SrTiO_3$ can be subjected to hydrostatic pressure and still retain their functionality.

The experiments on combined transistor-Hall-bar samples made it possible to probe the interface 2DES using two different methods and revealed differences between the results from

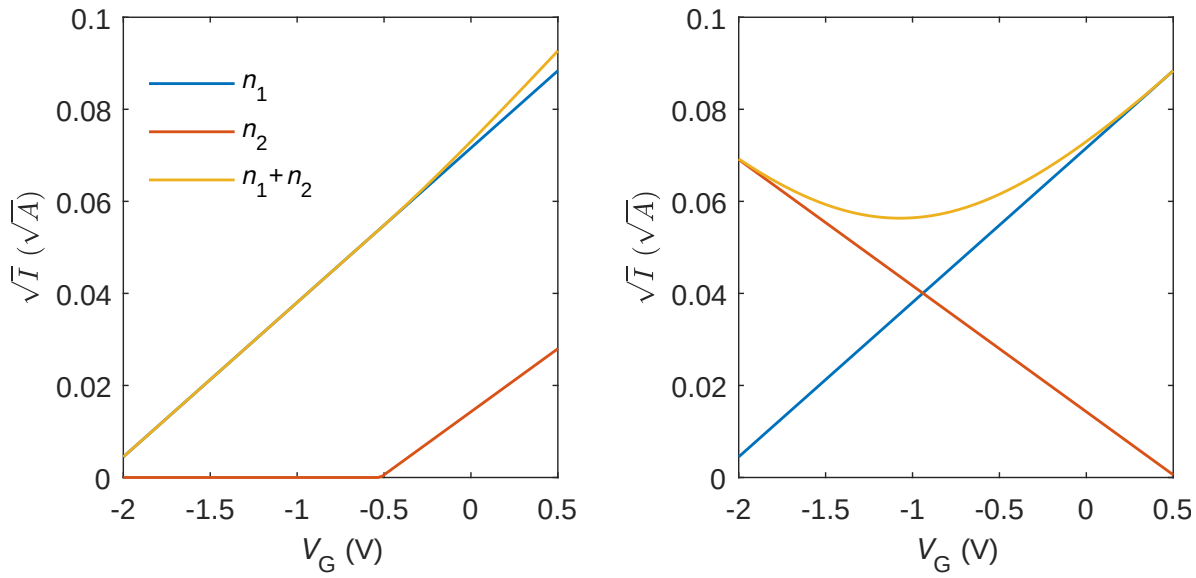

Figure 4.10: Simulations of the saturation region of a transistor with multiple bands. Blue and red curves correspond to the currents in each band, the yellow curve corresponds to the total current. (a) Two bands with negative charge carriers. (b) One band with negative and one with positive charge carriers. The absolute values of carrier densities and mobilities for both simulations correspond to the Hall fit results for sample 053 at 1.8 GPa.

the Hall-bar and the transistor-type devices. In particular, comparison of Hall and transistor data showed that the result of positively charged carriers obtained from multiband Hall fits is most likely an artifact.

THE CRITICAL MAGNETIC FIELD OF THE $LaAlO_3$ – $SrTiO_3$ 2DES

5

5.1 Introduction

The band structure of the 2DES at the $LaAlO_3$–$SrTiO_3$ interface is a combination of bands formed from the titanium d_{xy}, d_{xz} and d_{yz} orbitals residing at the $SrTiO_3$ side of the interface (see section 1.3.3). Even though it has been shown that, depending on the growth parameters and the applied gate voltages, multiple bands can participate in conductivity at the $LaAlO_3$–$SrTiO_3$ interface, the question whether superconductivity in $LaAlO_3$–$SrTiO_3$ is present in multiple bands is at the moment still unresolved.

In electron tunneling experiments on the $LaAlO_3$–$SrTiO_3$ interface, the superconducting gap usually appears without side peaks [57, 58], indicating a single gap. Rare exceptions to the standard gaps observed in $LaAlO_3$–$SrTiO_3$ tunneling experiments will be discussed in chapter 7. However, because of the planar geometry of the interface, which dictates a tunneling current perpendicular to the interface, tunneling electrons have only access to the d_{xz} and d_{yz} orbitals. The d_{xy} orbital is inaccessible to tunneling measurements and is therefore a candidate to host the second band. Indeed, in tunneling measurements on MgB_2 at first only a single gap was observed [96]. Only when samples were prepared with controlled surface orientation so that both gap momenta were accessible did the second gap become visible [97].

An alternative probe for multiband superconductivity is the temperature dependence of the upper critical field [98–104]. In single band s-wave superconductors the superfluid density is almost constant at temperatures lower than $0.5 \cdot T_c$ and therefore the upper critical field saturates in this region. In multiband superconductors, however, the superfluid density in the non-dominant bands increases with decreasing temperatures, because the gap in this band is expected to have a linear temperature dependence instead of the BCS dependence [67, 102]. Thus, in multiband superconductors $H_{c2}(T)$ does not saturate at low temperatures, it rather continuously increases with decreasing temperature. This chapter presents the temperature dependence of $H_{c2}(T)$ as probed by both transport and tunneling spectroscopy. In the measured samples, $H_{c2}(T)$ is linear down to $0.2 \cdot T_c$, consistent with the $LaAlO_3$–$SrTiO_3$ interface 2DES being a multiband superconductor. However, other mechanisms can also cause linear $H_{c2}(T)$, which will be discussed below.

The analysis presented in this chapter is based on data from two different samples: sample 011 is a circular junction design sample grown and measured by the author. The second sample, T36, was grown by Christoph Richter and measured by Evangelos Fillis-Tsirakis.

In sample 011, the doping range beyond $\pm 150\,\mathrm{V}$ was not accessible because high leakage currents led to significant heating at low temperatures. It is superconducting over the entire

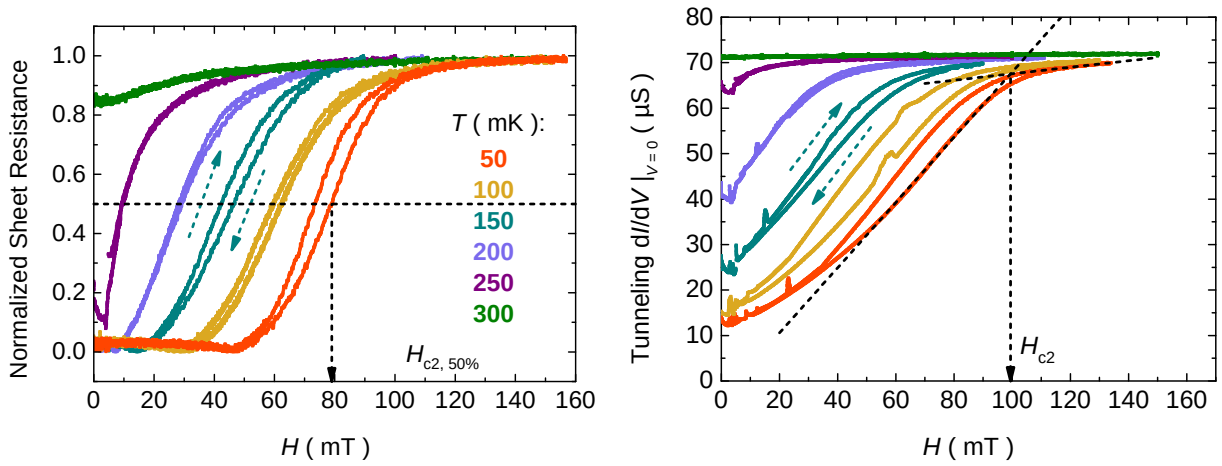

Figure 5.1: Data from sample 011 for a back-gate voltage of −100 V. The data shown here have been obtained by AC lock-in measurements: a) Sheet resistance plotted over applied perpendicular magnetic field for different temperatures. The difference between up- and down sweeps, as indicated by arrows, is due to a heating effect of the cryostat at very low fields and temperatures. b) Tunneling conductance plotted over applied perpendicular magnetic field for different temperatures. The methods employed to extract H_{c2} are illustrated for the 50 mK curves.

accessible voltage range, with the critical temperature, the critical magnetic field and the size of the gap monotonously increasing towards more negative gate voltages. At −150 V the critical temperature (defined as the temperature where the resistance is 50% of the normal state value) is 270 mK with a transition width of 50 mK. At the same gate voltage the critical field is 0.08 T. Typical curves for a gate voltage of −100 V are shown in figure 5.1. At gate voltages of 0 V and 100 V, the behavior of the sample is similar.

The phase diagram of sample T36 has been described extensively elsewhere [25, 57, 58]. Tuning the charge carrier concentration with a back gate voltage, the resistive state is reached at −200 V. The optimally doped superconducting state with a critical temperature of 300 mK and critical field of 0.5 T is at 0 V. Positive gate voltages correspond to an overdoped superconducting regime in this sample.

5.2 H_{c2} (T) measurements

On sample 011, magnetic fields were applied perpendicular to the plane of the 2DES and the dependence of sheet resistance on the field at different temperatures and gate voltages was measured. In addition, the zero-bias tunneling conductivity ($\mathrm{d}I/\mathrm{d}V_{V=0}$) from the top-gate to the 2DES was measured.

Fig. 5.1 (a) shows the AC sheet resistance of sample 011 plotted against the applied magnetic field at different temperatures. Above a certain field value, the measured resistance increases from the noise level to the normal-state value. The hysteresis-like difference between up- and down-sweeps (arrows) is due to a heating effect of the cryostat at very low fields and temperatures. For consistency, the following analysis only takes into account data from downward sweeps where the heating effect is negligible for most of the curve. As for all two-dimensional superconductors,

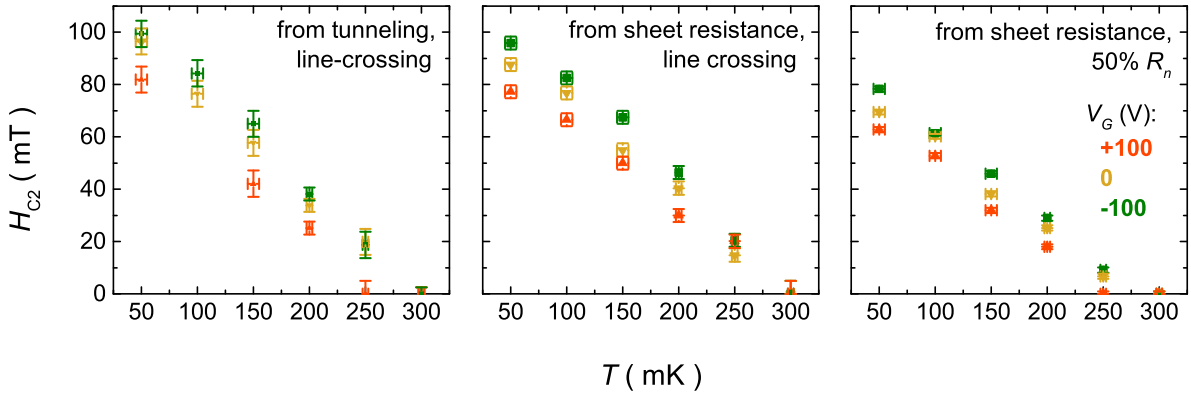

Figure 5.2: The trends for perpendicular $H_{c2}(T)$ extracted from tunneling and sheet resistance measurements for sample 011, using different criteria. The vertical error bars denote the uncertainty in extracting the $H_{c2}(T)$-values and account for the uncertainty in locating the exact onset of the plateaus. Since the transition is more abrupt for the sheet resistance measurement, its errors are smaller than for the tunneling measurements. The horizontal error bars denote the temperature instability in our system, arising from the H-field sweep-induced heating. The latter is more pronounced at lower temperatures where additional heating due to magnetization effects becomes significant.

the superconducting condensate is more susceptible to fluctuations than in a bulk superconductor and hence the width of the superconducting transition is broadened. The upper critical field H_{c2} was defined as the field where the resistance has dropped to half of the normal-state value (50%-criterion), as illustrated in Fig. 5.1 (a).

Fig. 5.1 (b) shows the AC tunneling conductance between gold top electrode and 2DES plotted against magnetic field. At low fields, the conductivity is reduced at zero bias because electrons cannot tunnel into the superconducting gap in the density of states. Following the suppression of the gap with magnetic field, tunneling conductivity recovers to the normal-state value. In accordance with previously published data [56, 57], the suppresion of the gap is more gradual than the resistive transition. For the tunneling conductivity, it is not meaningful to define the field value of half the normal-state conductivity as H_{c2}, since the transition is wider and does not terminate in perfect zero conductivity. Instead, another criterion (line criterion) is applied, illustrated in Fig. 5.1 (b): two lines are fitted to the curve, one in the region of maximum slope and one in the normal conducting region. The intersection of these two lines is taken as H_{c2}. As is explained in more detail in Ref. [58], this method is a reliable and reproducible way to define the critical magnetic field for tunneling measurements. The line criterion inherently yields higher values for H_{c2} than the 50 %-criterion and the values derived from that criterion can be regarded as an upper limit of H_{c2}. Since the width of the superconducting transition is not negligible, the line criterion is also applied to the sheet resistance data to make the different measurements more comparable.

The dependence of critical magnetic field on temperature extracted in the way described above is plotted in Fig. 5.2 for sample 011. For all gate voltages and irrespective which criterion is used to extract H_{c2}, the critical magnetic field depends linearly on the temperature across the entire temperature range, for both in-plane and tunneling measurements. This behavior is distinctly different from the linear behavior predicted by Ginzburg-Landau-theory, which is only valid in a small region close to T_c. The critical magnetic fields extracted from tunneling and sheet resistance measurements show good quantitative agreement with one another, indicating

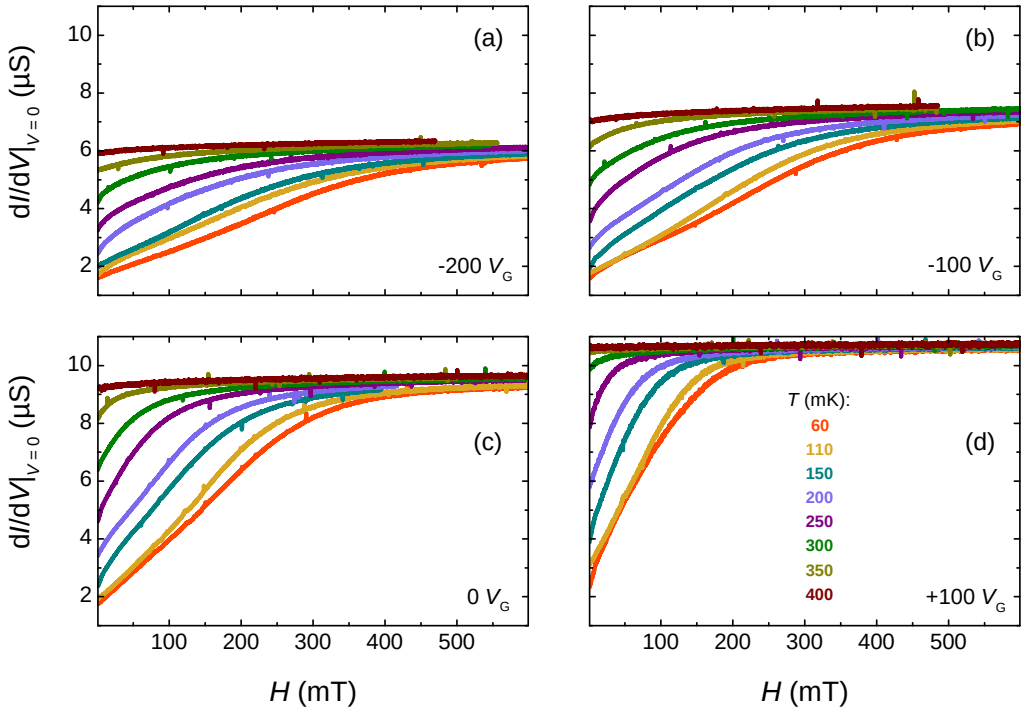

Figure 5.3: Tunneling $\mathrm{d}I/\mathrm{d}V_{V=0}$ characteristics of sample T36 as a function of magnetic field at different temperatures, for back-gate fields of -200, -100, 0 and 100 V. For every temperature and gate voltage set, H_{c2} is derived directly from the respective curve as illustrated in Fig. 5.1 (b). The gap closure corresponds to a positive slope in conductance while the magnetic field H is swept upwards. Reproduced from Ref. [105].

that the electron system of the sample is homogeneous.

The data from sample 011 is especially relevant, because sheet resistance and tunneling conductivity could be measured simultaneously. However, it was not possible to obtain information over the entire phase diagram from superconducting to normal conducting. An additional sample (T36) was measured, where tuning of the entire phase diagram was possible. For this sample, the evolution of tunneling conductivity with magnetic field H is shown in Fig. 5.3. Curves were recorded for fixed gate-voltage values of -200, -100, 0 and 100 V, in each case for eight temperature steps, from a base value of approximately 60 mK up to 400 mK. At this value, superconductivity is destroyed and the superconducting gap at the density of states disappears for all four gate voltages.

From Fig. 5.3, the values of H_{c2} were extracted as described above for different temperatures and gate voltages. Figure 5.4 depicts $H_{c2}(T)$ curves at four different gate voltage values of (a) -200, (b) -100, (c) 0 and (d) 100 V, which respectively correspond to the resistive state (where macroscopic superconductivity disappears), underdoped, optimally doped and overdoped regions in the phase diagram of the $LaAlO_3$–$SrTiO_3$ superconductor [56–58]. In all cases, the $H_{c2}(T)$ curve follows a linear trend, from T_c, throughout the entire temperature range of investigation and to the cryostat base temperature, confirming the results from sample 011.

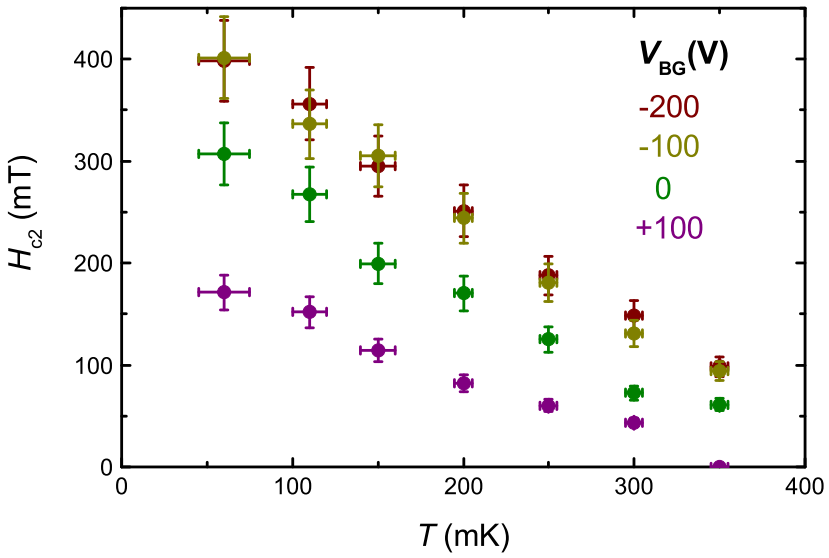

Figure 5.4: The $H_{c2}(T)$ curves across the phase diagram of sample T36. The temperature dependence is linear across the entire temperature range of investigation. Error bars are calculated by the same method as for Fig. 5.2.

5.3 Discussion

It was found that for both samples, regardless of the method used to determine $H_{c2}(T)$ and at all doping levels, the critical magnetic field scales linearly with temperature over the whole accessible temperature range. Different models exist predicting different behaviors of $H_{c2}(T)$ for different properties of the superconductor. The standard model is the Gorter-Casimir two-fluid model [106], predicting a relationship of the form:

$$H_{c2}(t) = H_{c2}(T=0) \cdot \left(1 - t^2\right), \tag{5.1}$$

where $t = T/T_c$ is the reduced temperature. A more refined equation derived by Mühlschlegel from the BCS theory yields a similar behavior [107]. This simple model predicts a strongly curved $H_{c2}(T)$ and is not consistent with our data. However, different mechanisms exist in which the $H_{c2}(T)$ curve is linear down to lower temperatures:

- A model by Tinkham [108] for the critical magnetic field of two-dimensional superconductors:

$$H_{c2}(t) = H_{c2}(T=0) \cdot \frac{1-t^2}{1+t^2}, \tag{5.2}$$

  where $t = T/T_c$ is again the reduced temperature.

- A model by Maki and de Gennes [109] for dirty 3-dimensional superconductors:

$$\ln(t) = \psi\left(\frac{1}{2}\right) - \psi\left(\frac{1}{2} + \frac{\hbar D H_{c2} T_c}{2\phi_0 k_B t}\right), \tag{5.3}$$

where $\psi(x) = \frac{d}{dx} \ln(\Gamma(x))$ is the digamma function.

- A model for two-band superconductivity by Gurevich [100]:

$$a_0 \left[\ln(t) + \psi\left(\frac{1}{2}\right) - \psi(h)\right] \left[\ln(t) + \psi\left(\frac{1}{2}\right) - \psi(\eta h)\right] + a_2 \left[\ln(t) + \psi\left(\frac{1}{2}\right) - \psi(\eta h)\right] + a_1 \left[\ln(t) + \psi\left(\frac{1}{2}\right) - \psi(h)\right] = 0, \quad (5.4)$$

  where a_i are coupling constants, η is the ratio of diffusivity of the two bands and $h = H/H_{c2}$ is the reduced magnetic field. Depending on the choice of parameters, the $H_{c2}(T)$ curve in this model can take different shapes, including linear behavior at low temperatures and upward curvature at T_c.

- Youngner and Klemm [110] showed that anisotropies in the Fermi surface or pairing parameter can also cause a linear behavior of $H_{c2}(T)$. Their equations can not be written in closed form and are not reproduced here. However, nodes in the superconducting can be considered unlikely in the present case, since all measurements and published data consistently show that the $LaAlO_3$–$SrTiO_3$ interface is a nodeless s-wave superconductor.

- The linear behavior of $H_{c2}(T)$ observed in the present experiments is different from the behavior predicted by Ginzburg-Landau-Theory, which predicts linear behavior, but only in the vicinity of T_c.

Figure 5.5 summarizes the $H_{c2}(T)$ results from samples 011 and T36, together with theoretical curves predicting $H_{c2}(T)$ according to the different models described above. When normalized to reduced magnetic field and temperature, all data points fall onto one line. It is clear that the standard BCS curve does not fit the data, but due to the large scatter of the data points, it is not possible to make a clear statement which of the other models fits the data best. In particular, the value of $H_{c2}(T = 0)$, which is used to normalize the curve, depends on the choice of extrapolation to zero temperature, *i.e.*, on the model itself and induces a large source of error. In addition, because of the large transition width, the critical temperature T_c is subject to significant uncertainty.

In conclusion, it was not possible to unequivocally identify the physical origin of the observed $H_{c2}(T)$ behavior. However, it should be emphasized that the two-dimensionality of the electron system by itself can be the cause of the linear $H_{c2}(T)$ according to Tinkham's model [108], without the need to assume any additional physical mechanisms. Spectroscopic measurements on Nb-doped $SrTiO_3$ recently showed that this system, which is closely related to the $LaAlO_3$–$SrTiO_3$ interface, has only a single superconducting gap, even though conductivity is present in multiple bands [43]. To explain this apparent discrepancy, the authors note that strong impurity scattering averages out the contribution of multiple bands. Since at the $LaAlO_3$–$SrTiO_3$ interface, the number of impurities is also significant, this scenario might very well also apply to the interface superconductor.

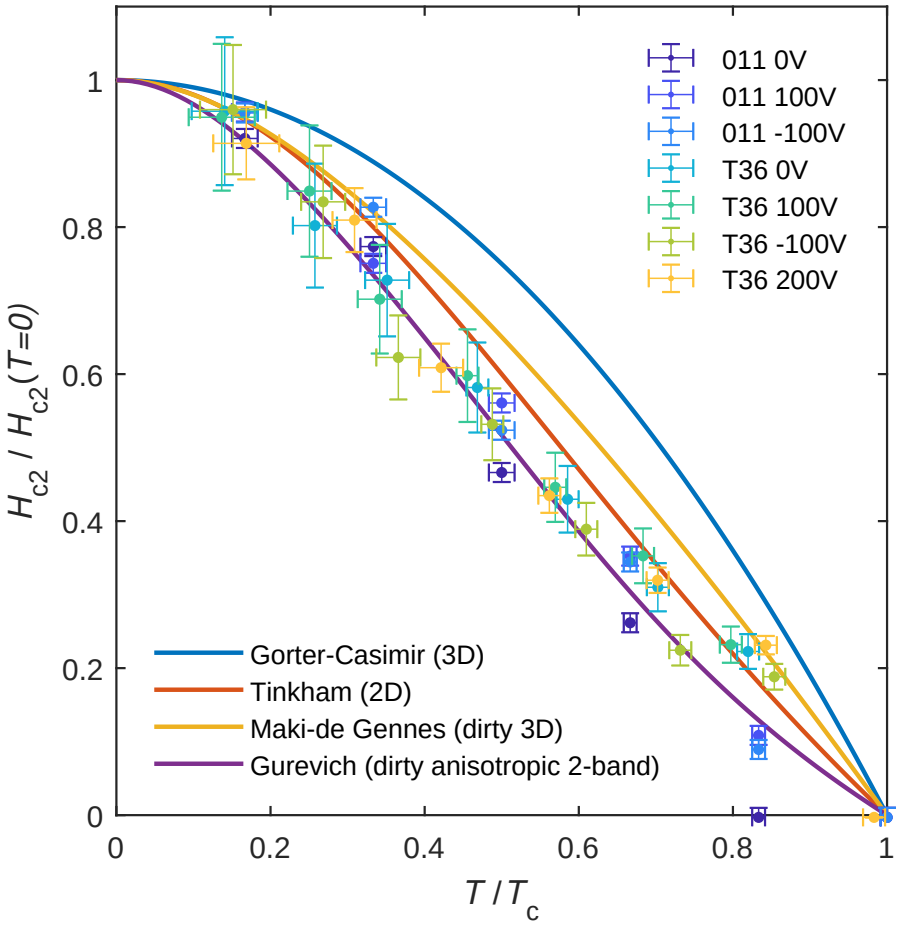

Figure 5.5: The combined normalized $H_{c2}(T)$ data from both samples which were measured. All normalized datapoints fall on a single line. The linear behavior of $H_{c2}(T)$ clearly deviates from the standard Gorter-Casimir curve. However, because of the scatter and the error margin of the data points, it is not possible to unequivocally identify the correct model. For the multiband curve, coupling parameters for $SrTiO_3$ from literature [111] were used and a diffusivity ratio of η=7 was found to give the best fit to the data. Error bars for sample 011 are smaller than for sample T36 because the 50%-criterion is a more precise method of determining H_{c2} than the line criterion.

THE SUPERCONDUCTOR-INSULATOR TRANSITION OF THE $LaAlO_3$ – $SrTiO_3$ 2DES

6

The SIT is a special phase transition occurring solely in two-dimensional superconductors. It is particularly interesting because it is a *quantum* phase transition which occurrs at zero Kelvin, which makes it distinctly different from thermodynamic phase transitions observed at finite temperatures (See section 1.1). Another special *topological* phase transition of two-dimensional superconductors is the BKT transition (See section 2.2). The $LaAlO_3$–$SrTiO_3$ interface is a promising candidate for investigations of these transitions because of the easy tunability of the 2DES by a back-gate, which means that the superconducting and insulating states can both be observed in the same sample. Even though both transitions have already been observed experimentally [55, 56], open questions remain: With respect to the SIT, it is not yet clear how far superconducting pairing persists into the insulating regime. For the BKT transition, it has not yet been shown how the transition evolves as the 2DEL is tuned across its phase diagram by a back-gate.

This chapter describes various aspects of the SIT at the $LaAlO_3$–$SrTiO_3$ interface. First, the optimization of PLD growth parameters is described. This optimization was necessary to obtain $LaAlO_3$–$SrTiO_3$ samples which could be tuned from superconductor to insulator by the application of a back-gate voltage. Measurements on samples from this optimization series are presented. Then several attempts to measure the BKT transition in these samples are described, and several reasons why these measurements were not successful are discussed. The subsequent section concerns an anomalous increase of resistance which occurs before the onset of the superconducting transition in these samples and is possibly related to the SIT. Finally, characteristics of a superconducting transistor with the $LaAlO_3$–$SrTiO_3$ interface as channel are presented.

6.1 Growth optimization

The $LaAlO_3$–$SrTiO_3$-interface has a large number of different functionalities, but the properties of each individual $LaAlO_3$–$SrTiO_3$ sample depend crucially on the growth conditions, such as ablation laser fluence, oxygen pressure and substrate temperature. Fig. 6.1 illustrates different classes of $LaAlO_3$–$SrTiO_3$ samples. In most samples, the carrier density can be tuned by the application of a back-gate gate voltage (center). A subset of these tunable samples, which is grown at relatively high laser fluences and oxygen pressures and consequently shows low carrier densities, exhibits high carrier mobilities (left). $LaAlO_3$–$SrTiO_3$ samples grown at low

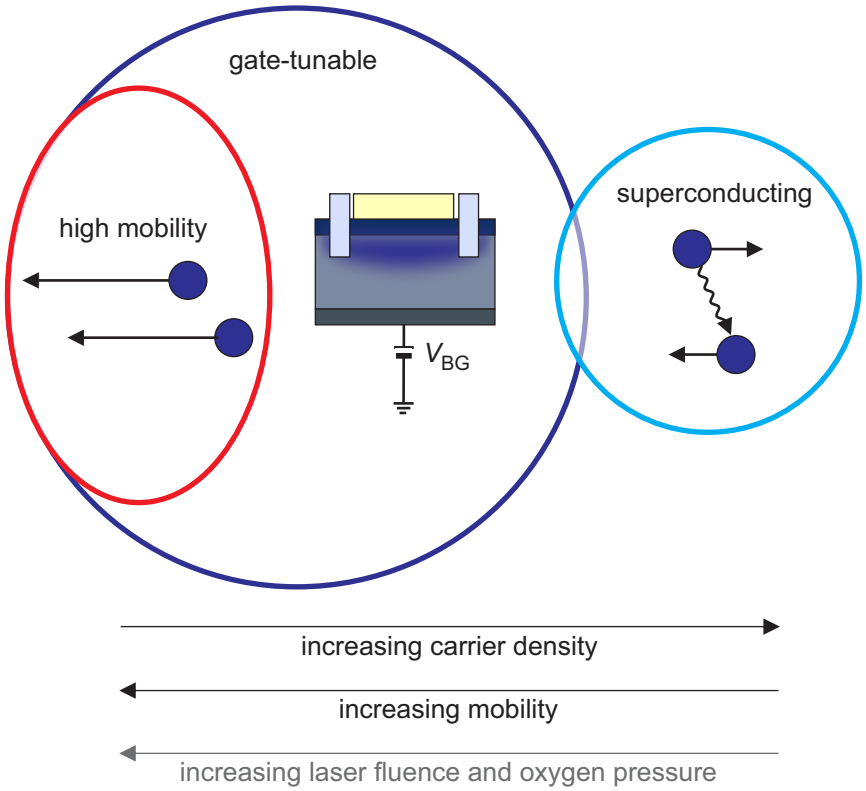

Figure 6.1: Classification of $LaAlO_3$–$SrTiO_3$ samples depending on the growth parameters. In most $LaAlO_3$–$SrTiO_3$ samples the carrier density can be tuned by the application of a back-gate voltage (center). For low carrier densities, these samples can exhibit high mobilities (left). Samples grown at low fluences and oxygen pressures exhibit a high carrier density and are superconducting (right). Only a subset of these superconducting samples is also tunable by a back-gate voltage. The growth parameters necessary to reach this subset are explored in this growth optimization.

oxygen pressure and low fluence have sufficiently high carrier densities to be superconducting (right), but the intrinsic carrier densities can be so high that they are no longer tunable with a back-gate voltage. The aim of the growth optimization presented in this section was to produce samples from the overlap between superconducting and tunable samples.

At the onset of the work presented in this thesis, two different parameter sets were in use for the growth of $LaAlO_3$–$SrTiO_3$ samples in our PLD system:

	Laser fluence:	$0.8\,\mathrm{J\,cm^{-2}}$
Set 1:	Oxygen pressure:	$8 \times 10^{-5}\,\mathrm{mbar}$
	Temperature:	$800\,^{\circ}\mathrm{C}$
	Laser fluence:	$1.2\,\mathrm{J\,cm^{-2}}$
Set 2:	Oxygen pressure:	$8 \times 10^{-4}\,\mathrm{mbar}$
	Temperature:	$800\,^{\circ}\mathrm{C}$

The first parameter set reliably produced superconducting samples, but these samples could not or could only marginally be depleted by application of a back-gate voltage. On the other hand, the second parameter set reliably produced samples which could be depleted to sheet resistances in the MΩ range for negative back-gate voltages, but these samples did not become superconducting at the base temperature of the cryostat (50 mK). It appears that the charge carrier densities generated by parameter set 1 were too high to be entirely depleted, whereas the charge carrier densities generated by parameter set 2 were to small to induce superconductivity. Since the SIT can only be measured in samples which can be both superconducting and insulating, a major part of this thesis was devoted to finding a growth parameter set which yields samples with these desired properties. A series of $LaAlO_3$–$SrTiO_3$-samples was grown while systematically varying the growth parameters to create a simultaneously superconducting and switchable sample. Due to the ring structure of the circular tunnel junction devices (see section 3.2.1) of this first series it was not possible to perform Hall measurements on these samples to quantify the charge carrier density. However, information was obtained on whether the samples were superconducting and depletable. For the samples in van der Pauw geometry with gold top electrodes (see section 3.2.2), Hall measurements were performed on all samples that were well-conducting in order to determine carrier density and mobility. The results obtained from these samples will be discussed below.

This growth optimization process is time-consuming because the time between the first step of sample preparation and the first measurement results amounts to approximately one week. The whole process of sample fabrication from substrate termination to the final deposition of electrodes takes several days, and even longer if intermediate patterning steps are performed. To check for superconductivity, the sample has to be mounted and cooled in a dilution refrigerator, which is also a lengthy process. In consequence, usually the next sample had already been grown before the results of a given sample were evaluated, leading to a delay in the feedback loop of growth parameters. In order to expedite the sample preparation process, usually two samples were grown on the same day.

In addition to the growth parameters which were varied systematically, there are also parameters beyond the control of the experimenter. The influence of these parameters on sample quality is sometimes difficult to disentangle from that of the known and controllable parameters. The most important of the external parameters is the quality of substrates. Even though each substrate was screened by AFM before use, the region of the AFM image is only a small fraction of the total substrate surface, and AFM gives no information on substrate stoichiometry.

Another example for an uncontrollable parameter is that two changes of unknown origin occurred in the PLD system during the process of this growth optimization, the first between the growth of samples 037 and 058 and the second between the growth of samples 065 and 066. Whereas the first change of the system shifted the phase diagram of the growth parameters so that the “sweet spot” for the growth of simultaneously superconducting and switchable samples disappeared, the second change of the PLD system caused most of the samples grown subsequently to become insulating.

Taken together, these external parameters explain why samples which were nominally grown with the same parameters can show disparate measurement results. These fluctuation make a systematic growth optimization difficult, and because of the long sample preparation cycle, it is difficult to accumulate enough statistics to compensate for the fluctuations.

Table 6.1 lists all $LaAlO_3$–$SrTiO_3$ samples with unpatterned electron system which were grown during this thesis. Samples with patterned electron system are not included because the

Table 6.1: Growth Parameters of $LaAlO_3$–$SrTiO_3$-samples and their superconducting and depletion properties. Resistance values are those from the best conducting device of a sample, other devices on the same sample may be completely insulating. A T_c of less than 50 mK indicates that only the onset of a superconducting transition was observed a the cryostat base temperature of 50 mK. Samples with patterned channel are not listed here, because their properties are different from those of samples with pristine electron system. Growth temperature for all samples was 800 °C, except for sample 030, for which growth temperature was 750 °C.
This table: samples 002 - 037 in circular circular junction geometry.

	Growth Parameters			Properties			
Sample	p_{O_2} (mbar)	F (J cm^{-2})	u.c.	$R_{\square,300\,K}$ (Ω)	$R_{\square,4\,K}$ (Ω)	T_c (mK)	gating
002	8.3×10^{-5}	0.8	5	9.7×10^4	7×10^6	insulating	
003	8×10^{-5}	0.8	4	2.8×10^4	240	0	leakage
004	8×10^{-5}	0.8	8	3.1×10^4	440	0	leakage
005	8×10^{-5}	0.8	4	1×10^4	110	125	No
007	8×10^{-5}	0.8	4	3.1×10^4	250	150	No
009	8×10^{-5}	0.8	4	2.5×10^4	200		
011	8.1×10^{-5}	0.8	5	6×10^3	300	150	No
019	8.1×10^{-4}	1.2	4	2×10^4	4×10^3	No	Yes
020	7.8×10^{-4}	1.2	3	1×10^5	1×10^7	insulating	
021	7.8×10^{-4}	1.2	4	5×10^4	500	No	Yes
022	8.1×10^{-4}	1.2	3				
025	7.8×10^{-4}	1.2	4	5×10^4			
026	4×10^{-4}	1	4	2×10^4	100	50	Yes
027	4×10^{-4}	1	4	2×10^4	320	0	Yes
030	4×10^{-4}	1.2	4	2×10^4	1×10^6	No	Yes
031	8×10^{-5}	0.8	4	2.4×10^4	300	No	Yes
032	7.9×10^{-5}	1	3				
033	3.7×10^{-4}	0.8	4	8×10^3	150	200	No
034	8×10^{-5}	0.8	N/A	1×10^8		insulating	
035	2×10^{-4}	1	4	1.4×10^4	90	275	Yes
036	8.2×10^{-4}	0.8	4	1×10^8		insulating	
037	7.9×10^{-4}	0.8	4	1.1×10^4	160	150	No

patterning changes the properties of the electron system and hence the two kinds of samples cannot easily be compared to one another.

The only sample in the series of circular junction-design samples which showed good superconducting properties and could be tuned from insulator to superconductor was sample 035. Consequently, this sample was thoroughly investigated by sheet resistance and tunneling spectroscopy measurements at different back-gate voltages, temperatures and magnetic fields. The relevant properties of this sample are shown in Fig. 6.2: Fig. 6.2 (a) shows the normal-state resistance at 50 mK and 400 mT as a function of back-gate voltage. The logarithmic plot shows a sharp increase of resistance for negative back-gate voltage. Fig. 6.2 (b) shows on the

Table 6.1: (cont.) Samples 058 - 067: van der Pauw structures with gold top electrode.

	Growth Parameters			Properties			
Sample	p_{O_2} (mbar)	F (J cm^{-2})	u.c.	$R_{\square,\,300\,K}$ (Ω)	$R_{\square,\,4\,K}$ (Ω)	T_c (mK)	gating
058	8.1×10^{-5}	0.8	4	3×10^4	2.2×10^3	150	No
059	2.0×10^{-4}	1	4	5.4×10^4	900	No	Yes
060	8.6×10^{-5}	0.8	4	1.4×10^4	2×10^3	0	Yes
061	2.0×10^{-4}	1	4	1.4×10^4	3×10^3	No	Yes
062	2.1×10^{-4}	0.8	4	2.3×10^4	1.1×10^3	100	No
063	8×10^{-5}	1	4	3.2×10^5	270	No	Yes
064	8.1×10^{-5}	0.9	6	7.7×10^4	2.9×10^3	No	Yes
065	2×10^{-4}	0.9	6	1.2×10^5	900	125	No
066	2×10^{-4}	0.9	5	1.3×10^7	2.7×10^6	insulating	
067	7.9×10^{-4}	0.9	5	4.5×10^7	1×10^7	insulating	

Table 6.1: (cont.) Samples 068-073: superconducting transistor geometry.

	Growth Parameters			Properties			
Sample	p_{O_2} (mbar)	F (J cm^{-2})	u.c.	$R_{\square,\,300\,K}$ (Ω)	$R_{\square,\,4\,K}$ (Ω)	T_c (mK)	gating
068	8.00×10^{-5}	0.8	6	$>100 \times 10^6$	$>100 \times 10^6$	insulating	
069	8.00×10^{-5}	0.8	6	43 000	200		
070	7.90×10^{-5}	0.8	6	28 000	50	0	Yes
071	8.20×10^{-4}	1.2	6	9×10^6	insulating	insulating	
072	8.00×10^{-5}	0.8	6	27 000	drifting	insulating	
073	8.10×10^{-5}	0.8	6	30 000	30 000, upturn	insulating	

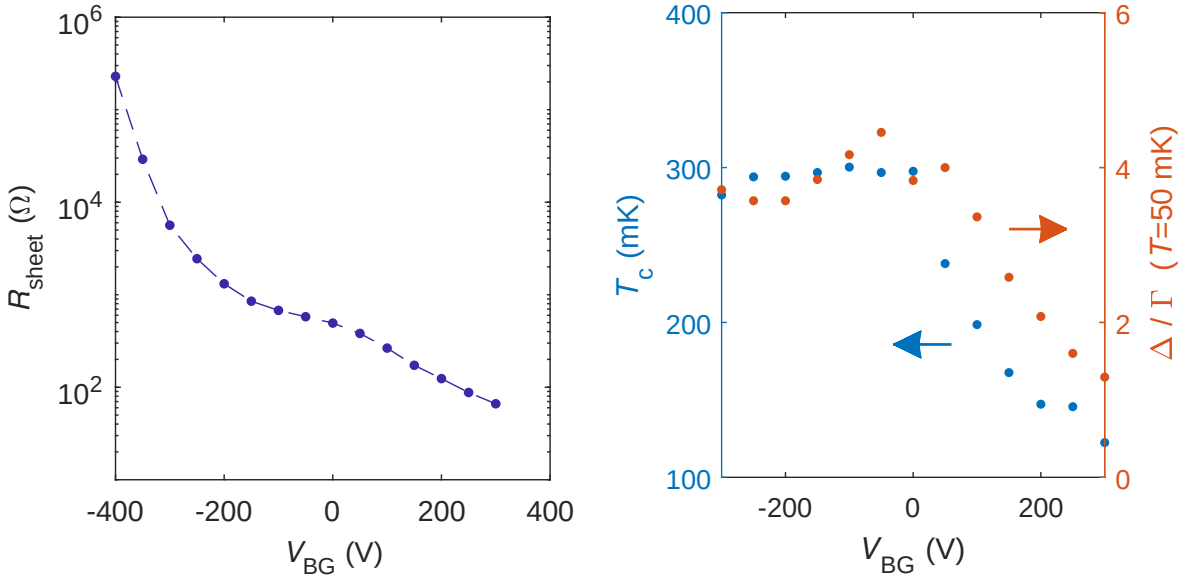

(a) (b)

Figure 6.2: Properties of sample 035 as a function of gate voltage. (a) Sheet resistance at $T = 50\,\mathrm{mK}$ and magnetic field of 400 mT. (b) Critical temperature and gap size Δ divided by lifetime-broadening parameter Γ at 50 mK. Comparison of (a) and (b) shows that superconductivity persists into the region where the normal-state sheet resistance reaches the MΩ range.

left axis the critical temperature (extracted according to the 75-%-criterion) as a measure of the superconductivity observed in transport. The right axis shows the superconducting gap size Δ divided by the lifetime-broadening parameter Γ as a measure of the superconductivity observed in tunneling. In accordance with results published previously (*e.g.* Fig. 4 of Ref. [57]), superconductivity persists well into the region where the normal-state resistance is on the order of MΩ. It was also confirmed that even though Δ/Γ decreases in the depletion range, Δ increases.

However, for reasons described in section 6.2, it was not possible to clearly measure the BKT transition in this sample geometry. Therefore, a number of samples with patterned 2DES were grown to investigate current flow in a well-defined region without constrictions (see section 3.2.4). However it became clear that patterning is so detrimental to the electron system that it destroys superconductivity.

For this reason, and in order to gain quantitative information on charge carrier density and mobility, the sample design for BKT samples was changed to the van der Pauw geometry with a gold top electrode described in section 3.2.2. For these samples, sheet carrier densities and mobilities were determined in addition to resistance measurements. Fig. 6.3 shows the sheet resistance of these samples as a function of back-gate voltage. Due to the aforementioned change in the PLD system, the dependence of the sample properties on the growth parameters had changed between the growth of the series of circular junction samples and the series of van der Pauw samples. Hence, van der Pauw samples grown with the same growth parameters as sample 035 were still tunable by a back-gate, but no longer superconducting. Only those van der Pauw samples grown at low laser fluence and oxygen pressure (058, 062) were superconducting. Consistent with the hypothesis that a high charge carrier density is necessary for supercon-

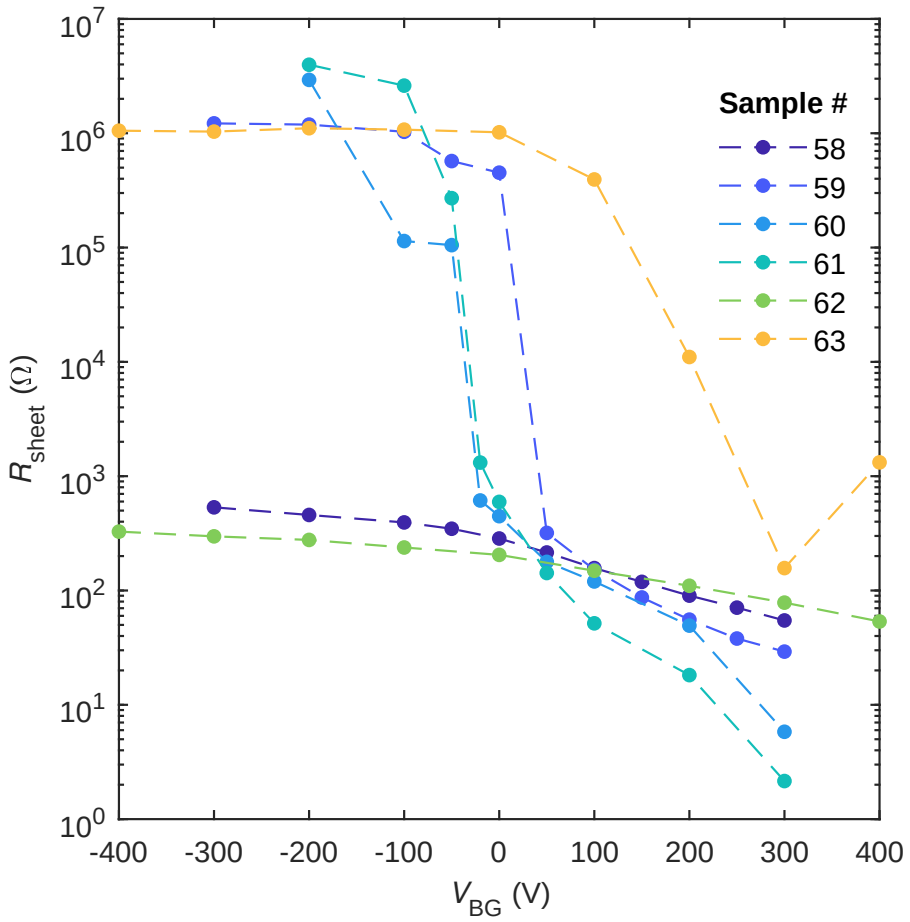

Figure 6.3: Normal-state sheet resistance of van der Pauw samples 058-063 at $T = 50\,\mathrm{mK}$ as function of back-gate voltage. In the two superconducting samples 058 and 062, the carrier density is so high that they can not be depleted and their resistance changes only slightly with back-gate voltage. Samples 059-061 can be turned insulating when applying negative back-gate voltage. Sample 063 only becomes conducting at high positive back-gate voltages.

ductivity, these are the two samples with the the highest native carrier density. Indeed, their carrier density is so high that these two samples could not be depleted by the application of a back-gate voltage. In the other four samples (059-061, 063) the electron system could be tuned from insulating to normal conducting, but no superconducting phase was observed. It appears that the range of carrier densities which allow both for superconductivity and tunability is very small for samples grown in our PLD system, in contrast to most other reports from literature, where gate-tunable superconducting $LaAlO_3$–$SrTiO_3$ samples appear to be easily obtainable.

6.1.1 The Lifshitz transition and its connection to superconductivity

Figure 6.4 shows the charge carrier density and mobility of the van der Pauw samples as extracted form magnetic field measurements up to 2 T as function of back-gate voltage. For negative gate voltages, the charge carrier density decreases until it is no longer measurable. However, the behavior at positive gate voltage is incompatible with the naive picture of charge accumulation in a plate capacitor as a model of the field effect at the interface. In this model,

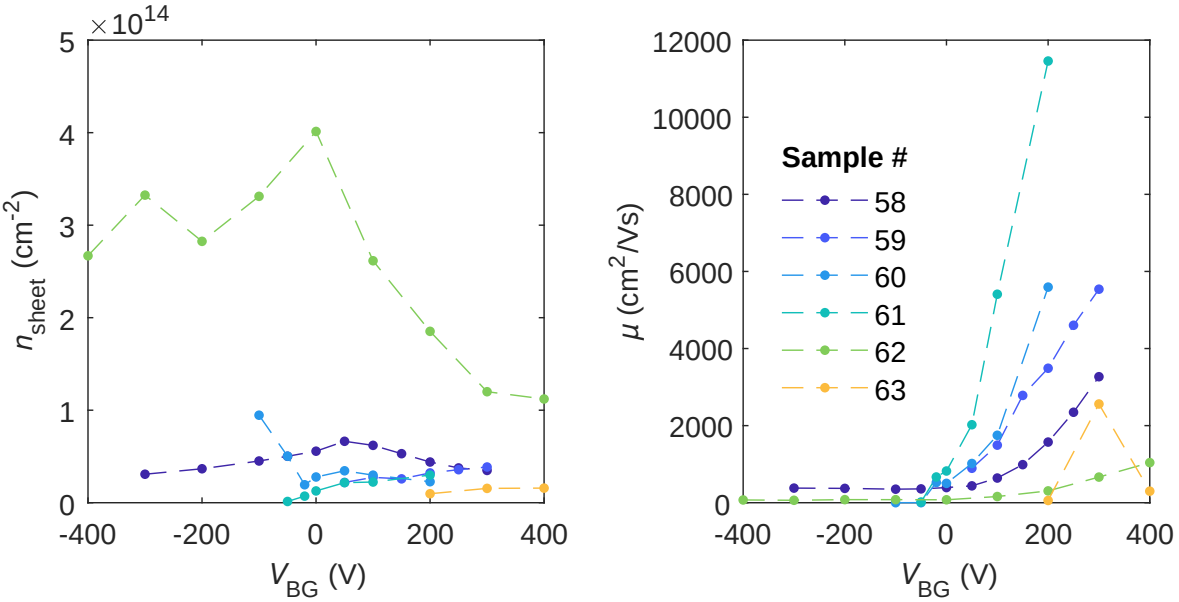

(a) (b)

Figure 6.4: (a) Carrier density of van der Pauw samples 058-063 as a function of back-gate voltage. (b) Mobility of van der Pauw samples 058-063 as a function of back-gate voltage. The data show that the maximum carrier density is not at the maximum of the gate voltage, but at $V_G \approx 0$. The decrease in resistance at high gate voltages is not due to accumulation of carriers, but due to increasing mobility of those carriers. All data shown here have been measured at $T = 50\,\mathrm{mK}$.

the charge carrier density should increase linearly with the applied voltage. However, the carrier density reaches its maximum around 0 V and slightly decreases upon further increase of the back-gate voltage. Instead of further charge accumulation, an increase of mobility causes the decrease of resistance at positive back-gate voltage (cf. *e.g.*[112]). This behavior can be understood with the following arguments: As the back-gate voltage is increased to more positive values, the mobile electrons are pulled further into the $SrTiO_3$ substrate and away from the interface. Since the density of scattering centers is significantly higher at the interface than in the bulk, this causes an increase in mobility. The apparent decrease of carrier density can be explained by the appearance of an additional band, which is not measurable in low-field Hall measurements. Such a Lifshitz transition from single-band to multiband at positive gate voltage has been reported previously in $LaAlO_3$–$SrTiO_3$ [25, 65, 66, 113].

In order to gain additional information on this additional band, high field measurements were performed on sample 058 and on the superconducting transistor sample 070. The multiband-band nature of conductivity is already visible from the increasing nonlinearities in the Hall conductivity and magnetoconductivity with increasing back-gate voltage shown in Fig. 6.5. These strong nonlinearities imply that multiband fits will be reliable on this data and unperturbed by the shortcomings discussed in Sec. 4.2. Multiband fits (see Appendix D) to the Hall and magnetoresistance data showed that at negative back-gate voltage a single conduction band is present at the interface. At V_{BG}=0 V, this band is fully populated at approximately $5.5 \times 10^{13}\,\mathrm{cm}^{-2}$ for sample 058 and $1.55 \times 10^{13}\,\mathrm{cm}^{-2}$ for sample 070. Increasing the back-gate voltage above zero changes the carrier density in the primary band only slightly in sample 070 and even leads to a decrease in sample 058, but leads to a significant increase in carriers in an

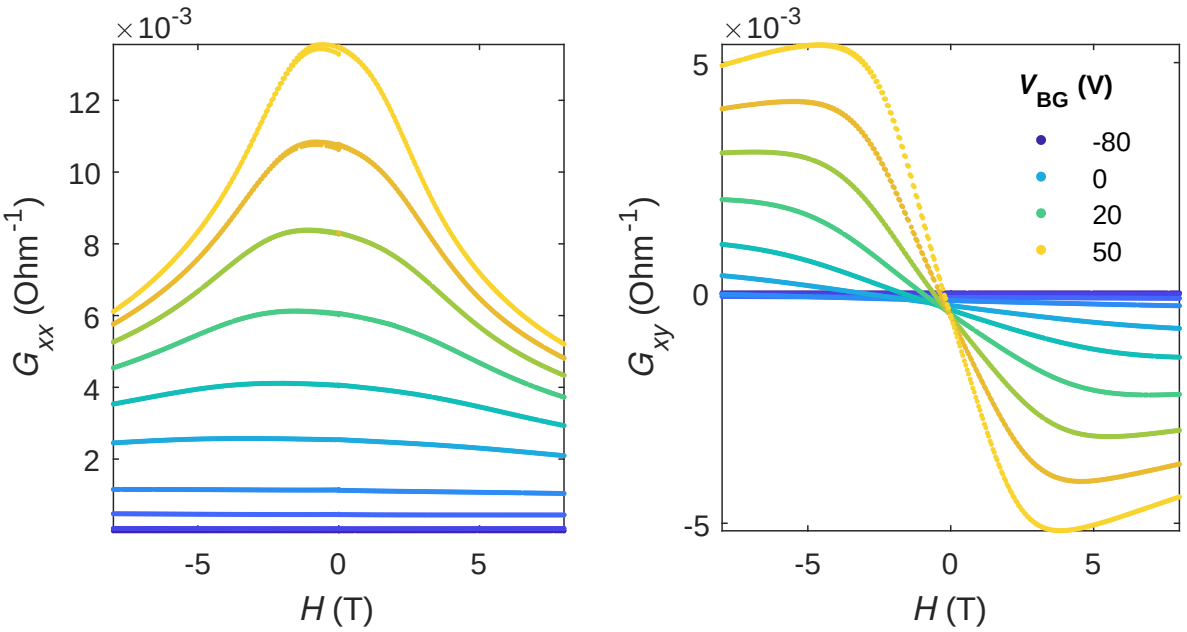

(a) (b)

Figure 6.5: Signature of the single-band to multiband Lifshitz transition in the Hall conductivity and magnetoconductivity of the $LaAlO_3$–$SrTiO_3$ 2DES in sample 070 at T= 4 K with applied backgate voltage. There is a clear transition from single-band linear behavior to multiband non-linear behavior with increasing backgate voltage (*i.e.*, carrier density). (a) Magnetoconductivity. (b) Hall conductivity. Results on sample 058 are similar (not shown).

additional band with lower density (Fig. 6.6).

The point of maximum carrier density in the primary band also corresponds to the maximum strength of superconductivity. Fig. 6.7 shows the gap width Δ divided by the quasiparticle lifetime broadening parameter Γ for samples 058 and 062 as a function of backgate voltage. The maximum of the ratio is at V_{BG}=0 V and coincides with the measured carrier maximum, thus indicating that the population of a second band is detrimental to superconductivity. This is consistent with previously published data on superconductivity at the $LaAlO_3$–$SrTiO_3$ interface [25] and doped $SrTiO_3$ [40]. However, the demise of superconductivity can also be attributed to a decrease in the electron-phonon coupling strength at higher carrier densities [25].

6.1.2 Alternative growth optimization: high electron mobility

In parallel to the efforts presented above, another optimization of $LaAlO_3$–$SrTiO_3$ growth parameters was performed by Ali Teker, with the intention to produce samples of highest electron mobility. Even though PLD growth parameters for high-mobility samples do not yield a superconducting 2DES, some results of Ali Teker's investigation, such as the deterioration of the electron system with patterning, were concurrent with the findings presented in this thesis. In order to increase the mobility of the electrons in the 2DES, the $LaAlO_3$ top layer was supplemented with an overlayer of $SrCuO_2$ and a capping layer of $SrTiO_3$. The $SrCuO_2$ is intended to act as an oxygen supplier filling up possible defects at the interface. The $SrTiO_3$ layer protects the $SrCuO_2$ from outside influences. In measurements performed by the author on

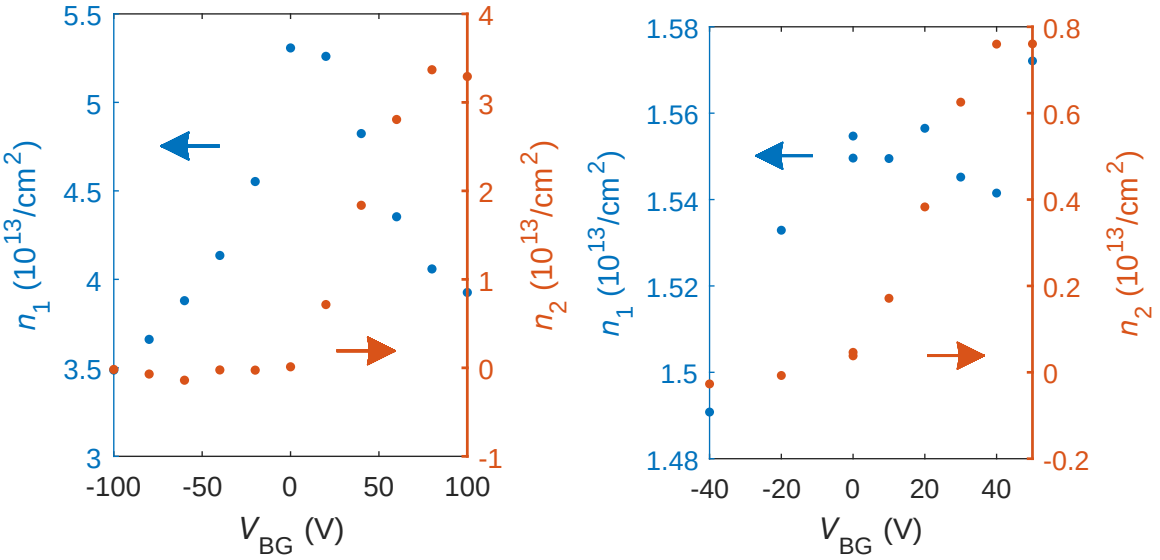

(a) (b)

Figure 6.6: Evolution of the carrier density of samples 058 and 070 at T=4 K with backgate voltage and the appearance of a second band. For voltages below −60 V, the carrier density in sample 070 is so small that Hall measurements are not possible. Increasing the backgate voltage, the carrier density n_1 of the first band increases until it saturates at $V_{BG} = 0$ V. At higher backgate voltages, n_1 increases only slightly in sample 070 and decreases in sample 058. However, a second band with smaller carrier density n_2 gets populated, thus marking the onset of the Lifshitz transition. (a) Carrier densities of sample 058. (b) Carrier densities of sample 070.

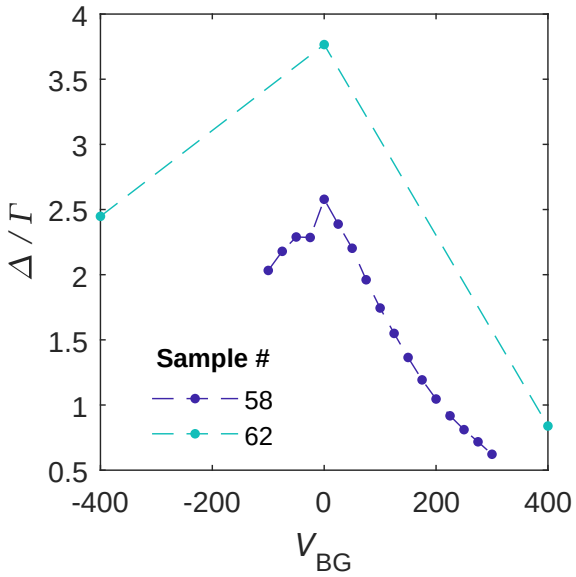

Figure 6.7: The ratio of gap width Δ over quasiparticle lifetime broadening parameter Γ at 50 mK for van der Pauw samples 058 and 062. The maximum of the ratio is at V_{BG}=0 V, concomitant with the maximum occupation of the primary band (cf. Fig. 6.6).

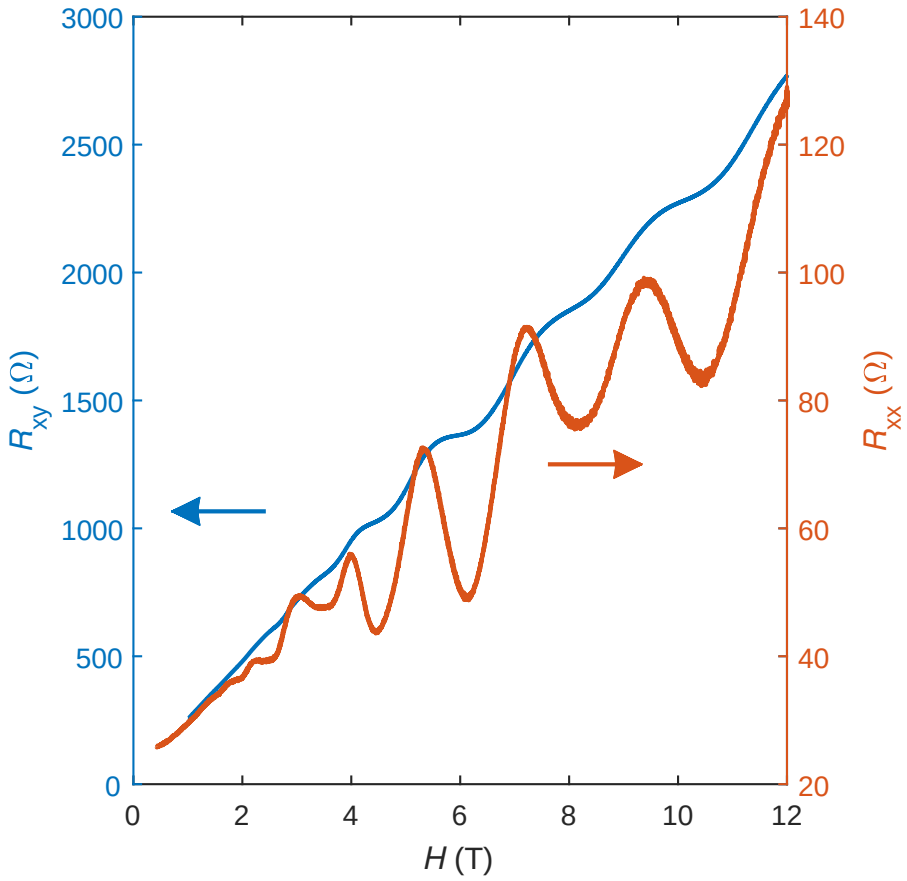

Figure 6.8: Longitudinal and transverse resistance of the high-mobilty sample P-ATK190 as function of magnetic field measured at $T = 50\,\mathrm{mK}$ and $V_{\mathrm{BG}} = -40\,\mathrm{V}$. The longitudinal resistance shows Shubnikov-de Haas oscillations at comparably low fields, indicating high mobility of the electrons. Plateaus in the transverse resistance may indicate the occurrence of the Quantum Hall Effect.

these samples using the dilution refrigerator, clear Shubnikov-de Haas oscillations were observed in the longitudinal resistance. In addition, plateaus were observed in the transverse resistance. Exemplary data from one of these samples, P-ATK190, is shown in Fig. 6.8. Hall resistance plateaus are a signature of the Quantum Hall Effect. However, the resistance plateaus of the Quantum Hall Effect are expected to occur at well defined resistance values $R_H = \frac{h}{\nu e^2} = \frac{R_K}{\nu}$, where ν is the integer filling factor and $R_K \approx 25.8\,\mathrm{k\Omega}$ is the quantum of resistance (von-Klitzing constant). The Hall resistance plateaus shown in Fig. 6.8 do not occur at resistance values corresponding to integer ν. In addition, unlike in the Quantum Hall Effect, the longitudinal resistance does not drop to zero at the magnetic fields where plateaus appear in the transverse resistance. High mobilities and anomalous Quantum-Hall-like oscillations have been reported previously in a $SrTiO_3$-amorphous $LaAlO_3$ system [114].

Plotting the longitudinal resistance over $1/H$ in Fig. 6.9 shows oscillations at multiple frequencies, indicating that multiple bands participate in conductivity, which may also be an explanation for the non-standard Hall plateaus. Shubnikov-de Haas oscillations at multiple frequencies have previously also been detected in doped $SrTiO_3$, where they are also attributed to conductivity in multiple bands [40, 44]. It is remarkable that multiple bands are populated

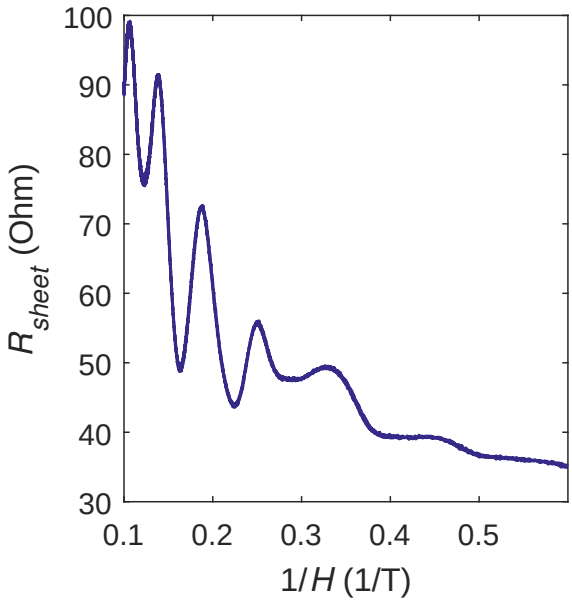

Figure 6.9: The longitudinal resistance R_{xx} of Sample P-ATK190 from Fig. 6.8 measured at $T = 50\,\mathrm{mK}$ and $V_{\mathrm{BG}} = -40\,\mathrm{V}$ plotted over $1/H$. The occurrence of multiple oscillation frequencies indicates conductivity by more than one band.

in this section of the phase diagram, which corresponds to low carrier densities.

6.2 Measurement of the Berezinski-Kosterlitz-Thouless transition

A signature of the BKT transition in a two-dimensional superconductor is the change of the exponent of the current-voltage characteristics from $V \propto I^3$ for $T < T_{\mathrm{BKT}}$ to $V \propto I$ for $T > T_{\mathrm{BKT}}$ as presented in section 2.2.2. This signature of the BKT transition has already been measured in the $LaAlO_3$–$SrTiO_3$ interface, *e.g.*, by Reyren *et al.* [55]. However, these measurements were performed only without a back-gate voltage, *i.e.*, approximately in the center of the superconducting dome. One of the questions which motivated the work in this thesis was how the BKT transition would evolve as the 2DES is tuned across its SIT, in particular, if the BKT transition would still be observable in the underdoped and insulating parts of the phase diagram. The observation of a superconducting effect such as the BKT transition in an insulator could be an indication for the existence of pre-formed pairs or a superinsulating phase. If a *superinsulating* phase exists as the dual partner of superconductivity on the opposite side of the SIT, the characteristic signature of the BKT transition should be inverted in such a phase, *i.e.*, $I \propto V^3$ [15, 16]. In addition, a motivation of the work in this thesis was to combine measurements of $I - V$ characteristics with tunneling spectroscopy in order to simultaneously observe the evolution of the BKT transition and the superconducting gap.

Once an optimized sample which was both switchable and superconducting had been obtained with sample 035, measurements of the $I - V$ characteristics at different gate voltages were undertaken. Results of these measurements are shown in Fig. 6.10. The $I - V$ curves are nonlinear, indicating superconductivity, even at negative gate voltages for which the sheet

resistance is orders of magnitude higher than at 0 V. However, the curves exhibit several jumps and "wiggles", which are attributed to intrinsic heating effects. These make it impossible to reliably determine the two linear regions of the curve in the double logarithmic plot and hence the BKT transition temperature can not be reliably determined from the data. The heating problem is twofold: On the one hand it is a known intrinsic problem when measuring BKT signatures: As soon as current transport is no longer fully lossless, resistive heating sets in and accelerates the transition process [17]. On the other hand, another problem lies with the geometry of the circular junction: Fig. 6.11 shows the the distribution of a constant current flowing from the inner to the outer ring. Because the diameter of each ring segment increases as one goes from the inside to the outside, the current density decreases. This implies that the same total current corresponds to different local current densities depending on the radial position r. If the current is swept with the intent to measure $I - V$ characteristics, the critical current density will first be reached at the edge of the inner electrode. Once this part of the 2DES is no longer superconducting, it will cause additional heating, which then destroys superconductivity in the adjacent regions, triggering a cascade of further heating. It is clear that this cascade obscures the true superconducting-to-normal transition.

In order to avoid the shortcomings of the circular junction design, a number of samples were grown in the tunnel junction designs with patterned electron system described in section 3.2.4. In these designs, current flows in a well-defined path without constrictions, therefore the effect of heating is expected to be limited. In addition, the Hall-bar structure of the electron system allows determination of the carrier density and mobility of the 2DES. However, since none of the patterned samples grown in this design were superconducting, the BKT transition could not be measured.

It was therefore necessary to measure in a sample geometry which neither contained constrictions of the current, nor a patterned electron system. For this purpose, the van der Pauw sample design described in section 3.2.2 was employed, and 10 samples were grown in this geometry. $I - V$ measurements on sample 058 in van der Pauw geometry at a back-gate voltage of 0 V showed clear superconducting nonlinearities, however it was not possible to deplete this sample to the insulating state. Therefore, it was not possible to measure the BKT transition across the phase diagram.

In conclusion, it was not possible to measure a clear BKT transition signature at different regions of the phase diagram in any of the approximately fifty samples which were analyzed. Reasons were the intrinsic difficulty to measure a BKT transition without heating artifacts, deficiencies in the sample design, detrimental effects of electron system patterning and changes in the PLD chamber which obstructed finding a set of growth parameters for the growth of simultaneously superconducting and gate-tunable samples.

6.3 Resistance anomaly in the superconducting transition

In a number of samples, measuring the dependence of resistance on temperature and magnetic field revealed a plateau of increased resistance at values of T or H just above the superconducting transition. Exemplary data from sample 035 is shown in Fig. 6.12. As the gate voltage is increased to positive values and carriers are accumulated at the interface, a plateau of higher resistance than the normal-state resistance appears between the normal-conducting region at high temperatures and the onset of the superconducting transition. This effect is observable both in measurements of $R(T)$ (Fig. 6.12 (a)) and $R(H)$ (Fig. 6.12 (b)). When sweeping the

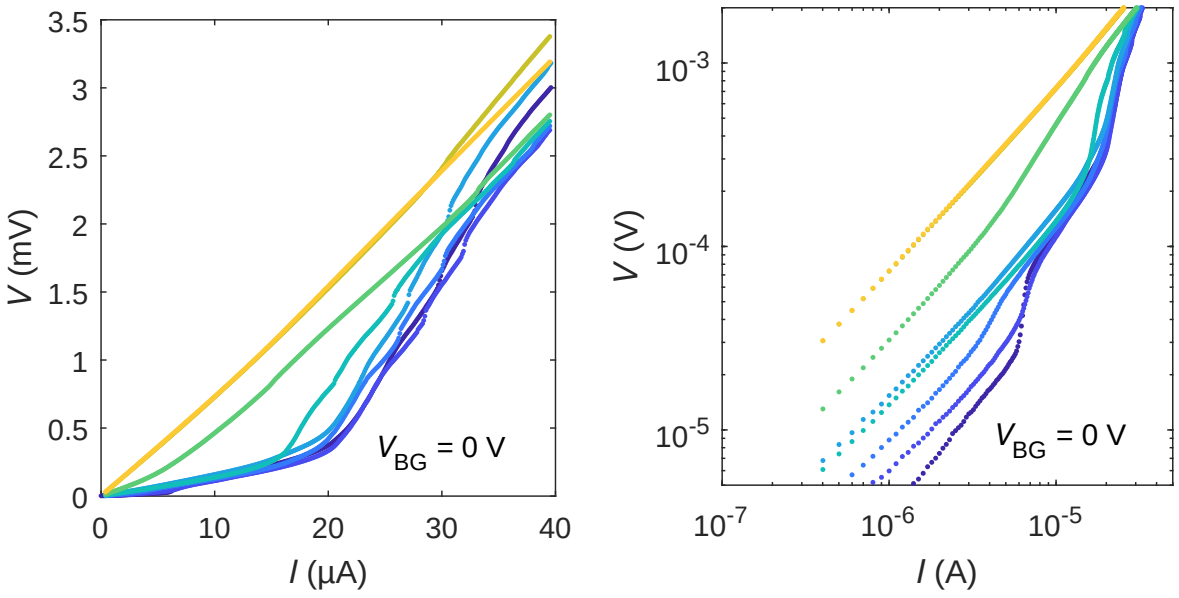

(a)

(b)

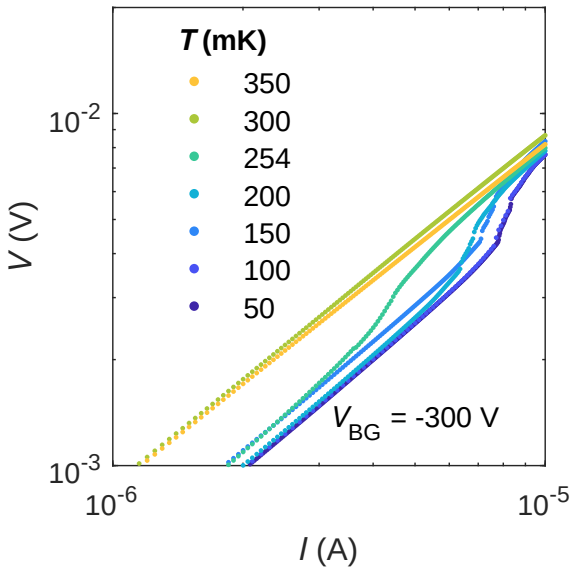

(c)

Figure 6.10: $I-V$-characteristics of sample 035 at different temperatures in linear and double logarithmic plots. (a) Plot on linear scale, with superconducting characteristics clearly visible in the low-temperature curves. (b) and (c) Plots in logarithmic scale. A change in slope, indicating a change in the exponent of the power law and consequently a BKT transition, is visible. However, the curves exhibit several jumps and "wiggles", which are attributed to intrinsic heating effects which obscure the true BKT transition. (b) Data recorded at $V_{\mathrm{BG}} = 0\,\mathrm{V}$ (c) Data recorded at $V_{\mathrm{BG}} = -300\,\mathrm{V}$. Even though the sheet resistance of the sample is approximately $10\,\mathrm{k}\Omega$ for this back-gate voltage, superconducting nonlinearities can still clearly be seen in the $I-V$ characteristics.

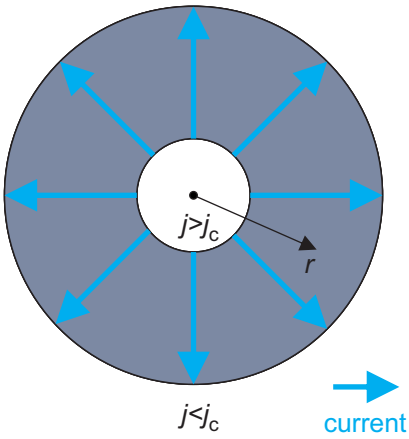

Figure 6.11: Illustration of the current distribution in a circular junction device. Since the current density j is higher at the inner ring than at the outer ring, the critical current density j_c is exceeded earlier for smaller radii r. This leads to heating of the electron system from the inside to the outside, which obscures the BKT transition.

magnetic field at a temperature which corresponds to the plateau region, a state with increased resistance is found for low magnetic fields at high positive gate voltages (Fig. 6.12 (c)). This effect is most likely not caused by geometrical issues, because it was observed in a number of devices of different sizes and shapes.

Tunneling spectroscopy reveals that in the temperature range in which the plateau is observed, a superconducting gap exists in the density of states, even though the sheet resistance measured in transport is still finite. The width of the superconducting gap Δ as a function of temperature for different gate voltages in sample 035 is plotted in Fig. 6.13 (a) and the quasiparticle-lifetime parameter Γ in Fig. 6.13 (b). The value of Δ is finite in the relevant temperature range of 100 mK to 200 mK, with a high value of Γ.

A trivial explanation for the observed effects would be an imperfection of the four-wire measurement due to incomplete separation of the electrodes. If the 2DES around the voltage electrode becomes superconducting before the 2DES around the current electrode, a small contact between current and voltage electrode is enough to reroute the current from the current electrode through the voltage electrode. In this case, there will be an increased voltage drop due to the contact resistance between electrode and 2DES and an increased voltage will be recorded. This scenario is conceivable in the circular junction geometry, where the current electrodes and voltage probes are very close together. However, the resistance anomaly was also observed in samples in van der Pauw geometry, where the separation between the voltage and current electrodes is on the order of millimeters and a short is unlikely.

In a superconductor-insulator transition it is expected that the slope of $R(T)$ changes from positive to negative as the electron system changes from superconductor to insulator [11, 79, 115]. Therefore, the increase in resistance before the transition can be regarded as the signature of an incipient SIT, which is supported by the evidence of finite Δ in this region. It can also indicate the suppressed onset of a superinsulating phase, where the Cooper pairs are localized

as described in section 2.2.3. However, it is not clear why the transition to an insulator should occur at positive back-gate voltage, corresponding to carrier accumulation and low normal-state resistance, and not at negative back-gate voltage corresponding to carrier depletion.

6.4 Superconducting transistor

The 2DEL at the $LaAlO_3$–$SrTiO_3$-interface is the only known superconductor which can be tuned from superconducting to insulating by the application of a gate voltage on short timescales. In this section, investigations are described on whether it is possible to use this functionality to construct a superconducting transistor with the superconducting 2DEL acting as the channel. A superconducting transistor would be superior to a normal-conducting transistor mainly in three aspects: First, the superconductor can support a large on-current at very low (ideally zero) voltage. Second, because superconducting current is lossless and dissipates no heat in the ON-state, an large number of superconducting transistors could be placed close together without causing overheating of the array. Third, because charge carriers in a superconductor are Cooper pairs instead of single electrons, the sub-threshold swing (Eq. 2.37) of a superconducting transistor should be reduced with respect to the normal state, resulting in a significant increase in switching speed. Certainly, a transistor operating at millikelvin temperatures is not suitable for broad applications, but it will allow an insight into the specifics of the SIT.

Experiments on topgated superconducting $LaAlO_3$–$SrTiO_3$-samples have already been performed [116, 117], but a comprehensive study of superconducting transistor transfer characteristics has not yet been published. In order to obtain superconducting transistors, initially several attempts were made to measure transistor characteristics in samples with conducting channels defined by patterning of the 2DEL (specifically the patterned junction, transistor and transistor-Hall-bar designs). However, it became apparent that patterning of the 2DEL is detrimental to superconductivity and hence no superconducting properties could be investigated on these samples.

In order to overcome these challenges, the superconducting transistor device design (section 3.2.3) was developed, which requires no patterning of the electron system. In this device design it was possible to measure the transistor characteristics of a superconducting channel. However, cutting the edges of the top gate electrode with a wiresaw makes the barrier between gate and channel permeable to electrons in this part. This significantly reduces the accessible topgate voltage ranges, making it difficult to tune a sample across the entire phase diagram. In sample 070, which was the source of the results shown below, it was not possible to access topgate voltages V_G below $-0.45\,V$ or above $1.6\,V$ due to high gate leakage. In addition, the large size of the sample channel makes it more likely that inhomogeneities of the 2DEL compromise the measurement, as evidenced by the humps in the transfer curves measured on sample 070. In this sample, a finite resistance remained even at the base temperature of the cryostat, which is beneficial for transistor measurements.

Measurements on this sample showed that the SIT induced by the topgate is not a direct transition from superconductor to insulator, but that there is an intermediate metallic state between the two phases in which the electron density is too small for effective pairing, but large enough to facilitate normal-state conductivity. This intermediate metallic state had already been known from the back-gate transition [58], but its discovery in the top-gated transition is new.

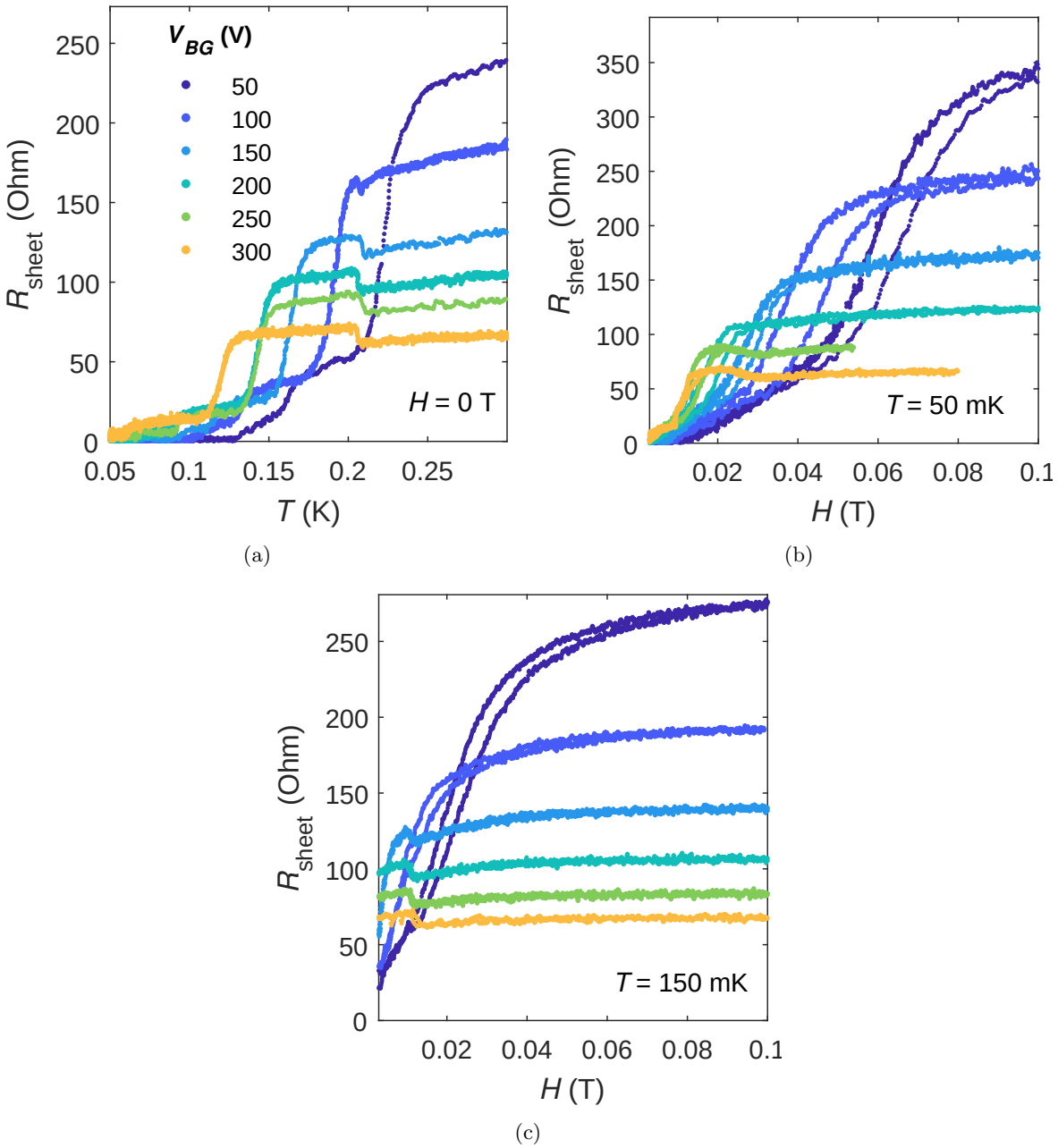

(a) (b)

(c)

Figure 6.12: Plateau with increased resistance observed at temperatures and magnetic fields directly above the superconducting transition in sample 035. (a) Superconducting transition in $R(T)$-measurements. (b) Superconducting transition in $R(H)$-measurements. (c) Sweeps of the magnetic field at T =150 mK. In both (a) and (b), a plateau of increased resistance is present between the normal state and the onset of superconductivity. In (c), sweeping the magnetic field at a temperature corresponding to the plateau region reveals an increase in resistance at low magnetic fields and positive gate voltage.

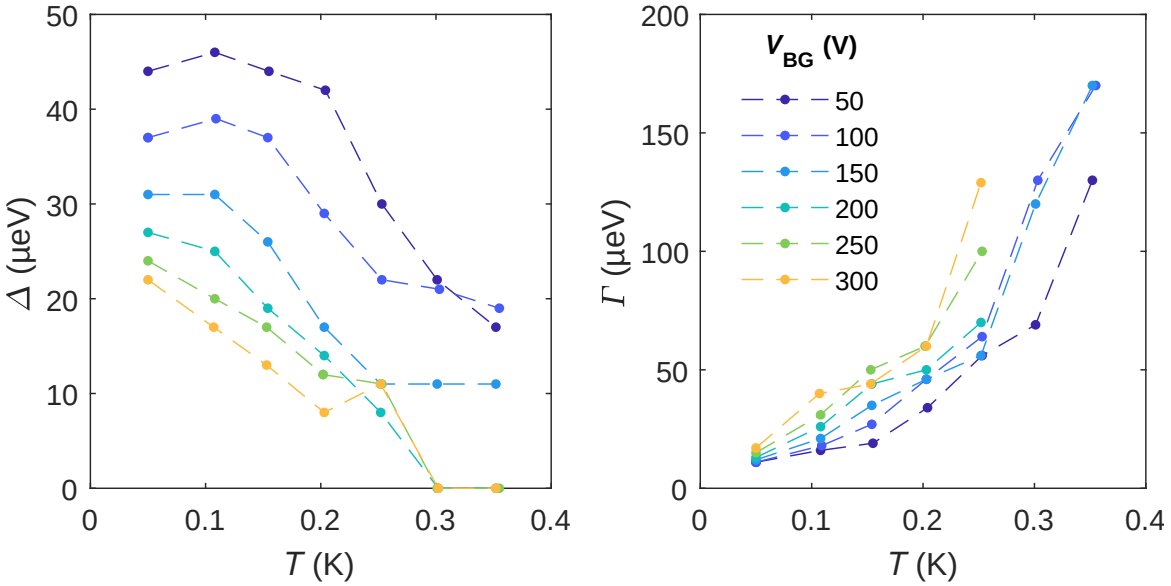

(a) (b)

Figure 6.13: Superconducting parameters as a function of temperature for different back-gate voltages. (a) Superconducting gap width Δ. (b) Quasiparticle-lifetime parameter Γ.

The intermediate metallic state is evident from the data in Fig. 6.14: Fig. 6.14 (a) shows source-drain characteristics of the transistor without back-gate or magnetic field measured in four-wire mode. The channel has finite resistance, but the presence of superconductivity is evidenced by a change in slope from low current below the critical current to high current. The superconducting kink in the current-voltage curves gets weaker when the topgate voltage is reduced and has disappeared at the lowest accessible topgate voltage of $-0.45\,\mathrm{V}$. However, the conductivity of the channel is still well measurable for this topgate voltage. Fig. 6.14 (b) shows transfer curves at a back-gate voltage of $-10\,\mathrm{V}$ with and without applied magnetic field. For positive topgate voltage, the sample is superconducting for $H = 0\,\mathrm{T}$ but not for $H = 2\,\mathrm{T}$, hence the $H = 0\,\mathrm{T}$-curve has a higher conductivity. However, as the topgate voltage is decreased, superconductivity disappears while the normal-state conductance is still appreciable and the two curves fall on top of each other.

The results shown here indicate that a transistor built from the superconducting 2DEL at the $LaAlO_3$–$SrTiO_3$-interface would not feature lower sub-threshold swings than a geometrically identical transistor made from a non-superconducting material. This is because, going from positive to negative topgate voltages, superconductivity disappears before conductivity and hence in the relevant sub-threshold region, superconducting pairing no longer plays a role.

Nonetheless, a superconducting $LaAlO_3$–$SrTiO_3$ transistor would still be advantageous in terms of high current flow at low voltages and low power dissipation, since current in transistors in the on-state is lossless when the 2DEL is fully superconducting.

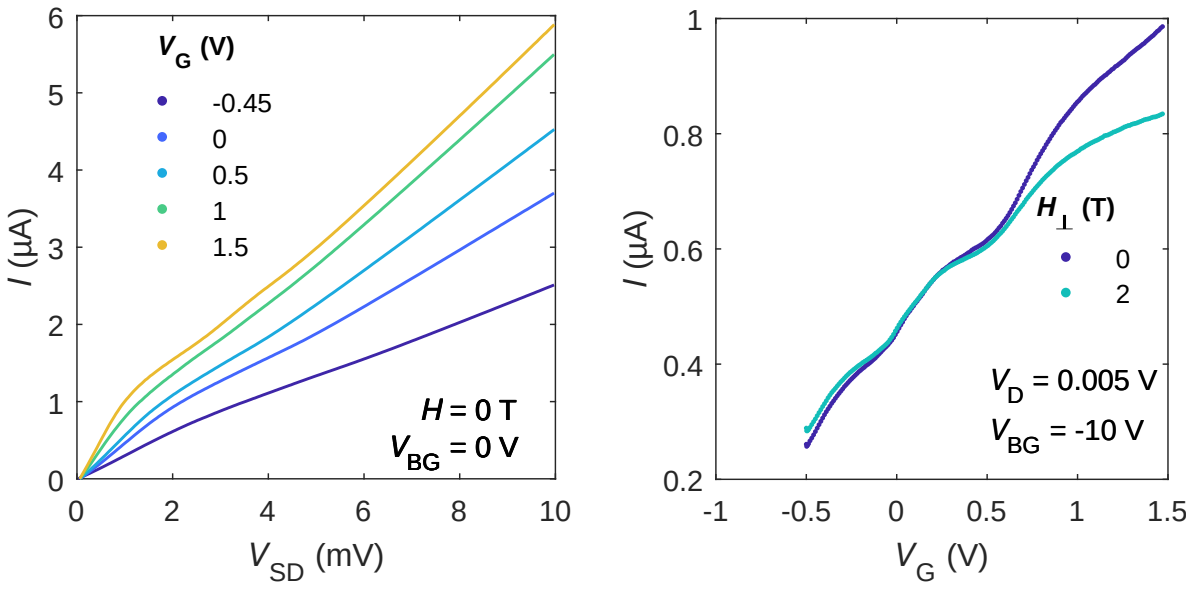

(a) (b)

Figure 6.14: Superconducting switching characteristics of transistor T2 on sample 070. (a) Source-drain characteristics for different topgate voltages V_G without magnetic field or back-gate. (b) Transfer curves at back-gate voltage $V_{BG} = -10\,\mathrm{V}$, with and without applied magnetic field.

IN-GAP STATES IN SUPERCONDUCTING $LaAlO_3$ - $SrTiO_3$ INTERFACES

7

While most of the tunnel spectra observed on the superconducting samples investigated in the present thesis showed standard lifetime-broadened superconducting gaps, on some samples (011 and T41), states inside the superconducting gap were observed. These states depend upon the thermal-cycling history of the samples and the applied backgate voltage. The states consist of a peak at zero energy and other peaks at finite energies, symmetrically placed around zero energy. These peaks disappear, together with the superconducting gap, with increasing temperature and magnetic field. Below, the likelihood of various physical mechanisms that are known to cause in-gap states in superconductors are discussed and it is found that none of these mechanisms can easily explain the results. The conceivable scenarios are the formation of Majorana bound states, Andreev bound states, or the presence of an odd-frequency spin triplet component in the superconducting order parameter.

The data and analysis presented in this chapter were published in [118]. Sample 011 was grown and measured by the author of this thesis. Sample T41 was grown and measured by Christoph Richter. The data analysis was performed by the author of this thesis. The manuscript of Ref. [118], on which this chapter is based, was written in collaboration between the author of this thesis, Christoph Richter, Narayan Mohanta, Thilo Kopp, Arno Kampf, Jochen Mannhart and Hans Boschker.

7.1 Introduction

Superconductors are characterized by the opening of a gap in the quasiparticle spectrum at the Fermi energy. The presence of states inside this gap indicates physics beyond conventional superconducting behavior and is, therefore, an exciting topic in science [119–142]. There are different mechanisms that can cause a finite spectral density inside the superconducting gap. For example, for nodal superconductors, only a part of the Fermi surface is gapped, resulting in a smooth variation of the density of quasi-particle states as a function of energy inside the gap. In some cases, however, a peak in the spectral density is present at zero energy, or multiple peaks are present at finite energies. These peaks can be caused by, for example, Andreev bound states at interfaces between unconventional superconductors and normal metals [122–128], an odd-frequency spin triplet component of the superconducting order parameter [129–132], the solid-state analog of Majorana fermions [133–137], and by bound states due to the presence of magnetic impurities [138–141]. Zero bias anomalies also frequently appear in tunneling

studies on high-temperature cuprate superconductors [142].The study of the in-gap states gives crucial information about the pairing symmetry of a superconductor. Here, the presence of quasiparticle states inside the superconducting gap of the two-dimensional $LaAlO_3$–$SrTiO_3$ interface superconductor is reported.

In previous works of our group, tunneling measurements on $LaAlO_3$–$SrTiO_3$ interfaces were performed, allowing measurements of the superconducting gap, map the corresponding phase diagram [57, 58], and to identify electron-phonon coupling as a likely origin of the superconductivity [25]. Almost all $LaAlO_3$–$SrTiO_3$ tunneling samples investigated exhibit superconducting gap spectra with the expected BCS density of states consisting of a full gap and coherence peaks. In some cases, however, spectra were observed which exhibited distinct peaks inside the superconducting gap. The in-gap features appear and disappear non-deterministically upon different thermal cycles and gate-voltage sweeps. This chapter describes the structure and occurrence of these features and discusses the most likely scenarios of their origin.

7.2 In-gap states observed in tunneling spectroscopy

An overview is given over a selection of various in-gap states that can be observed in superconducting tunnel junctions and their origins and properties are briefly explained In the case of a superconducting system with multiple gaps, all states at energies smaller than the largest superconducting gap in the system are referred to as in-gap states. These states are summarized in Table 7.1.

First, in-gap states which may appear in systems with a single superconducting gap are described. Combinations of single-gap states may also occur in systems with multiple gaps.

Kondo resonance

The Kondo effect [143] introduces a resonance at magnetic impurities, *e.g.*, in tunneling processes through quantum dots [162]. The resonance effect is observable as a peak in conductivity. The peak appears usually at zero voltage bias, but can also be generated at finite voltage bias [163]. Kondo resonances do not require superconductivity and, therefore, the in-gap states which originate from this mechanism do not in general disappear upon a superconducting transition. In the presence of an external magnetic field, the zero-bias peak splits by an amount equal to the Zeeman energy of the magnetic field. The splitting of the side peaks varies linearly with magnetic field [164]. With increasing temperature, there is a reduction and broadening of the Kondo resonance [165].

Anderson-Appelbaum states

In the early 1960s, a zero-bias anomaly was observed in tunneling experiments in *p*-*n* junctions [119, 166] and in tunnel junctions composed of normal metals separated by oxide barriers [167]. It was found that the zero-bias conductance peak varies logarithmically with temperature and, thereafter, this zero-bias anomaly was also known, in the literature, as the logarithmic anomaly. Anderson [144] and Appelbaum [145, 146] showed that magnetic impurities located inside the tunneling barrier close to the electrodes can participate in an exchange interaction with the tunneling electrons, resulting in the zero-bias anomaly. The characteristics of these states are similar to those generated by the Kondo resonance.

Table 7.1: A compilation of mechanisms that can produce in-gap states in tunnel spectra of SCs. For more detailed information and additional references, see Sec. 7.2. The left column denotes the names and origins of the phenomena and the right column describes their properties. This part of the table describes states observable in systems with a single superconducting gap, whereas the second part describes states due to the presence of multiple superconducting gaps. Combinations of single-gap states may also occur in systems with multiple gaps. Note that many of the mechanisms listed here are interdependent. Their relation to one another is further discussed in Sec 7.2.

Name **Origin**	**Properties**
Systems with a single superconducting gap	
Kondo resonance [143] Resonance at magnetic impurities located inside the conducting host.	• Resonance effects observable as peaks in conductivity. • Zero-bias peak splits in a finite magnetic field. • Side-peak separation varies linearly with external magnetic field. • Does not require superconductivity.
Anderson-Appelbaum states[144–146] Interaction between electrons and magnetic impurities inside the barrier.	• Similar to Kondo resonance (see above).
Impurity states Tunneling via intermediate impurity states in barrier or surface.	• Decrease of conductivity at zero bias (barrier states) [147]. • Increase of conductivity at zero bias (surface states) [148]. • In-gap states are particle-hole asymmetric.
Caroli-de Gennes-Matricon states [149] Andreev reflection at a vortex core.	• States below the gap energy. • Bound states which are localized at the core of vortices. • Comparable to Andreev Bound states (see below).
Yu-Shiba-Rusinov states [138–140] Bound states due to magnetic impurities in SC.	• Paired peaks symmetric around zero energy. • States are localized at the impurity sites. • Peak positions move with varying magnetic field [141].
Majorana bound states [133, 134] Emergent states at the boundary of topological superconductors.	• Zero-energy bound state for well-separated Majoranas. • Paired states at finite energies for interacting Majoranas [137, 150, 151]. • Located at defects at which the SC gap closes. • Conductance peak height quantized in units of $2e^2/h$ for specific situations.
Andreev Bound states[128] Successive Andreev reflections at NS-interfaces.	• For non-s-wave NS junction: peak at zero energy. • For SNS junction: peaks at finite energies, depending on the phase difference between the SCs.

Table 7.1: (continued) This part part of the table describes in-gap states due to systems with multiple superconducting gaps.

Name Origin	Properties
Systems with multiple superconducting gaps	
Josephson junction characteristics Tunneling from SC_1 to SC_2.	• Gap of size $\Delta_1 + \Delta_2$. • Peaks inside the larger gap at the gap difference $\pm\lvert\Delta_1 - \Delta_2\rvert$.
Multiband Superconductivity[42] SC pairing in multiple bands.	• Two gaps inside one another. • Two pairs of coherence peaks.
Order-parameter admixtures Unconventional order parameter symmetry.	• Two pairs of coherence peaks in density of states if multiple order parameters are present. • Example 1: p-wave spin-triplet pairing [135, 152–156] • Example 2: Odd-frequency spin triplet pairing [129–132, 157–161]

Barrier and surface impurities

In tunnel junctions with a thick barrier, in which the probability for direct tunneling from one electrode to the other is small, impurity states enclosed in the barrier provide an alternative pathway for tunneling. In this case, electrons can tunnel via an intermediate state localized on the impurity state. Due to the finite capacitance of the particle, a minimum charging energy is required to add an electron to it. Such junctions show, therefore, a suppression in conductance around zero voltage bias [147]. Localized states due to imperfections of the surface of a superconductor may facilitate bound states at low energy, causing peaks in the conductance around zero voltage bias [148].

Caroli-de Gennes-Matricon states

The electron system in the core of an Abrikosov vortex in a type-II superconductor can host localized fermionic bound states which are populated at energies smaller than the superconducting gap energy [149]. The origin of this effect can be regarded as a specific form of Andreev reflection (see below), since a vortex core is a normal metal confined in a superconductor.

Yu-Shiba-Rusinov states

Based on Abrikosov-Gorkov theory [168], Yu [138], Shiba [139] and Rusinov [140] showed that magnetic impurities can facilitate bound states inside the superconducting gap. Tunneling

measurements revealing such states were performed early [169], and it was possible to resolve the contribution of individual impurity atoms on a Nb surface by scanning tunneling spectroscopy [170–172]. Yu-Shiba-Rusinov (YSR) states always appear in pairs symmetrically around zero energy and move to higher energy with increasing magnetic field [141]. For a review on impurity states in superconductors, see, *e.g.*, Ref. [173].

Majorana bound states

Majorana fermions are particles which are their own antiparticles. While it is not yet clear whether elementary Majorana particles exist, there is growing evidence that collective states with Majorana-like properties can be created in solid-state systems [136, 174]. Superconductors are the primary candidate to host such Majorana states, since Bogoliubov quasiparticles, the elementary excitations of a superconductor, are particle-hole symmetric and can indeed be described using Majorana's original equations [175]. Since a pair of Majoranas constitutes a Dirac fermion, the challenge is to create unpaired or spatially separated Majoranas. The two most common proposals to achieve this goal are either to combine a superconductor with a material with strong spin-orbit coupling (*e.g.*, a topological insulator) [134, 136, 176] or to create a ferromagnetic chain at the surface of a superconductor [133, 174]. In these cases, topological superconductivity is induced and isolated Majorana zero modes emerge at the edges of one-dimensional sample structures. If the two Majorana pair partners are well-separated, Majorana bound states (MBS) are observed at zero energy, where superconducting quasiparticles are electron-hole symmetric. However, if the wavefunctions of the two pair partners overlap, a level splitting to finite energies can occur [137, 150, 151]. In the limit of zero temperature and ballistic conductance, the height of the zero-bias peak generated by MBS is quantized in units of $2e^2/h$. Reviews of the research on MBS in solid-state and other systems can be found, *e.g.*, in Refs. [137, 177, 178].

Andreev bound states

Andreev reflections can facilitate bound states at zero energy in normal metal–superconductor (NS) junctions if the pairing symmetry of the superconductor is non s-wave [122–128]. Andreev bound states (ABS) also appear in SNS junctions, irrespective of the pairing symmetry [120, 179–181]. It has been reported that ABS can also be generated at a SC-vacuum interface without any normal metal [182, 183]. The ABS in SNS-junctions is located at zero bias if there is a phase difference of π between the two superconductors. For other phase differences, it consists of two peaks at finite energies [123, 126]. The peak height of these bound states may exceed the normal-state conductance. A zero-bias peak generated by an Andreev bound state is expected to split upon the application of magnetic field [184]. Andreev processes require sufficiently good conductance between the superconductor and the normal metal, usually a NS-contact without insulating barrier.

Now in-gap states which are due to the presence of multiple superconducting gaps are described.

SIS tunneling

The tunnel spectra observed in junctions of two superconductors separated by an insulating barrier show gaps of $\Delta_1 + \Delta_2$, where Δ_1 and Δ_2 are the gaps in the spectra of the two

superconductors. At zero bias, a DC Cooper-pair current is observable, which depends on the relative phase of the two superconductors according to the first Josephson effect [185, 186]. At finite temperatures, a tunneling current flows at bias voltage equal to $\pm|\Delta_1 - \Delta_2|$.

Multiband superconductivity

If two bands of a material participate in superconductivity, tunneling spectra can reveal a double gap structure with two sets of coherence peaks corresponding to the two separate pairing strengths. The coherence peaks of the band with smaller gap width will appear inside the gap of the band with larger pairing strength [42]. In contrast to SIS-tunneling, the double gap of a multiband superconductor does not show a Josephson-current peak at zero bias.

Order-parameter admixtures

Systems in which superconducting pairing occurs with a combination of different order parameters show multiple gaps with multiple coherence peaks. Examples for such unconventional order parameter pairing are p-wave spin-triplet pairing or odd-frequency spin-triplet pairing.

p-wave spin-triplet pairing has been reported to occur, *e.g.*, in Sr_2RuO_4 [152, 153], in heavy-fermion superconductors [154], in combinations of superconductors with nanowires with strong spin-orbit coupling [135], or in two-dimensional superconductors without inversion symmetry due to the resulting Rashba spin-orbit coupling [155, 156]. In this case, the fractions of conventional s-wave pairing and p-wave pairing depend, *e.g.*, on the strength of the spin-orbit coupling [155]. If both p and s-wave-pairing are present in the superconductor, the coherence peaks due to one pairing symmetry can appear as peaks inside the gap due to the other pairing symmetry.

At superconductor–ferromagnet (SF) interfaces, a long-range proximity effect can induce odd-frequency spin-triplet superconductivity in the ferromagnet if magnetic disorder is present [157, 158]. This proximity-coupled superconductivity exhibits an odd-frequency, s-wave, spin-triplet component of the superconducting order parameter which generates in-gap peaks in tunnel spectra. The peaks appear at either finite or zero energy, depending on the relative thicknesses of the ferromagnetic and superconducting layers and on the magnetic disorder of the magnetic layer [129–132, 159–161].

Having discussed a number of effects which can cause states inside the superconducting gap in tunnel spectra, now the experimental observations will be described.

7.3 Experiments

The in-gap states were measured in two different samples, 011, which was of the circular junction design described in section 3.2.1 and T41, which was of an older junction design. The samples were grown according to the procedure described in 3.1, 011 in Stuttgart and T41 in Augsburg.

Tunneling measurements were performed in 4-point configuration using a Keithley 6430 Femtoamp Sourcemeter as current source and a Keithley 2001 or Keithley 2812 nanovolt meter. The polarity was such that a positive bias corresponds to electrons tunneling from the 2DEL into the gold electrode.

The shape of the superconducting gap observed in the tunneling spectra of $LaAlO_3$–$SrTiO_3$-interfaces follows the one of a standard s-wave BCS superconductor taking into account finite

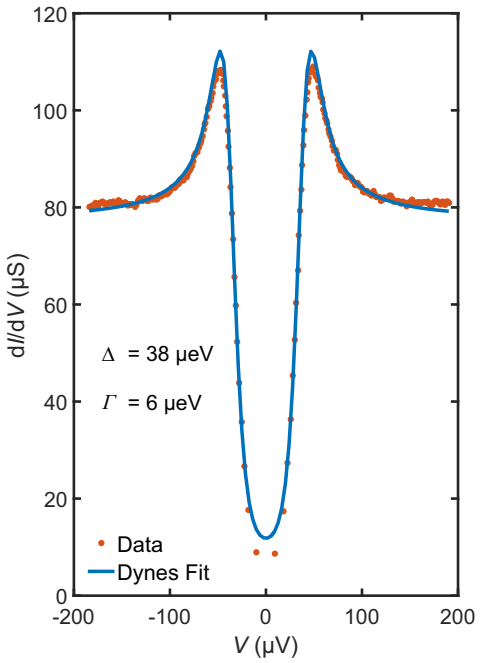

Figure 7.1: A typical tunneling spectrum of sample 011 from the first measurement run without in-gap features measured at base temperature of the cryostat (50 mK). The Dynes fit [187] used to extract the gap width Δ and quasiparticle lifetime parameter Γ is shown in addition to the data. The deviation between data and fit around zero bias is attributed to a minor Altshuler-Aronov offset [121]. ©(2017) APS.

quasiparticle lifetime [187] (Fig. 7.1). The small deviation between data and fit around zero bias is attributed to a Altshuler-Aronov correction [121]. However, in some samples and in some measurement runs, distinct in-gap features were observed inside the superconducting gap. These features are observable regardless of the sweep direction or sweep rate of the measurement. The in-gap features appear or disappear between different measurement runs, *i.e.*, after a thermal cycle to room temperature: On sample 011, in the first measurement run, standard tunneling spectra were observed on both of the tunnel junctions which had been connected (Fig. 7.1). After a thermal cycle to room temperature, both devices showed in-gap features such as shown in Fig. 7.2 (a) and (b). Normal-state conductance differs between the data in Figs. 7.1 and 7.2 (a)-(c). This data was obtained in two different tunnel junctions (on the same substrate) of different size. Tunnel spectra without in-gap features were measured in both tunnel junctions in the first measurement run, and tunnel spectra with in-gap features were measured in both tunnel junctions in the second measurement run. Here, the spectra with the highest data resolution are shown. In a number of subsequent warming and cooling cycles, in-gap features of varying strength were observed in this sample (Fig. 7.2 (c)). On sample T41, in the first measurement run the in-gap features shown in Fig. 7.2 (d) were observed after saturating the sample with charge carriers at high positive backgate voltage and then returning to zero backgate. The in-gap features were not observed in subsequent measurement runs on sample T41. It is not clear why only specific samples show these anomalies and others do not.

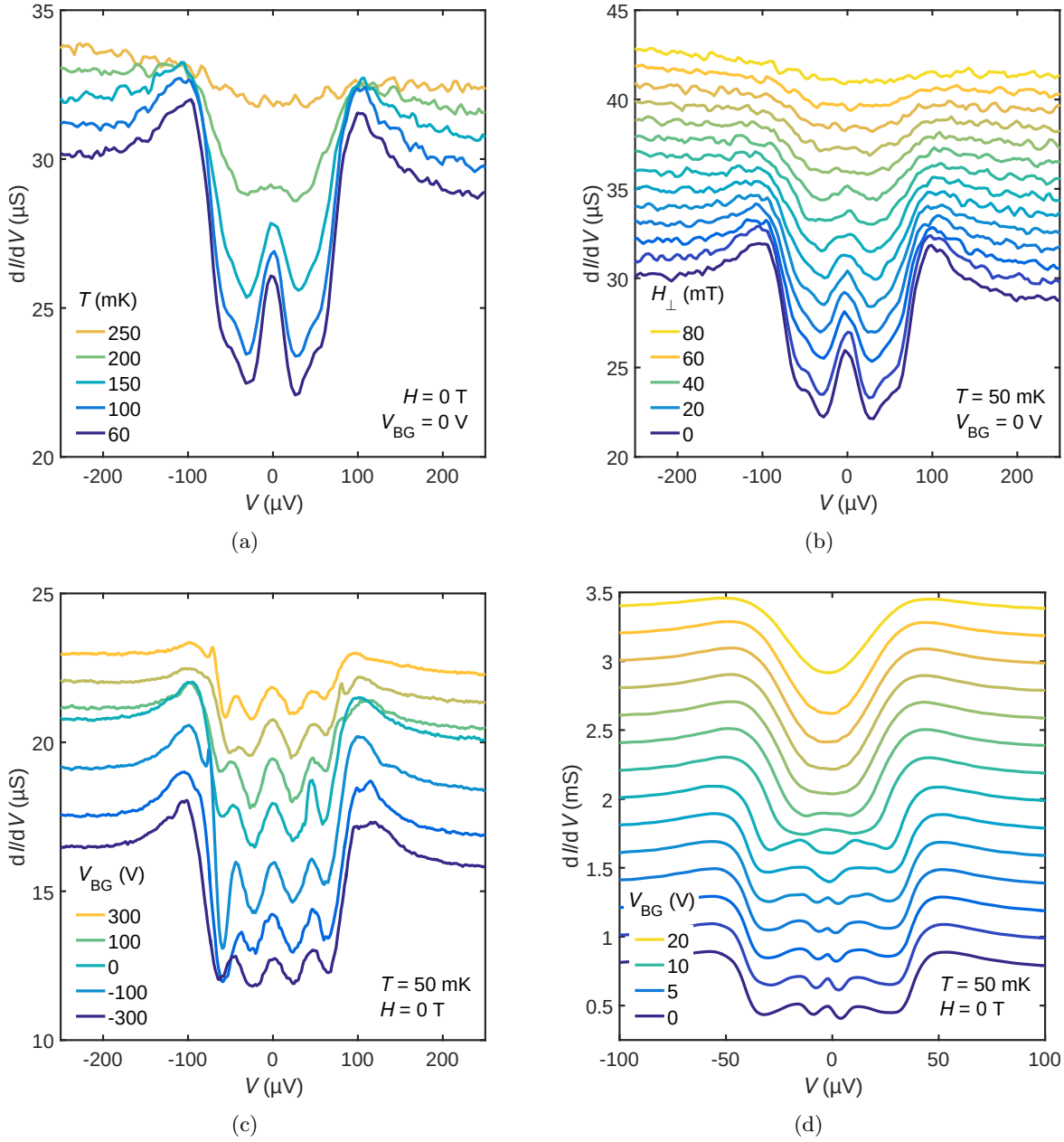

Figure 7.2: Tunneling spectra of samples 011 and T41 illustrating the emergence of in-gap features: (a) Evolution of in-gap features in sample 011 with temperature (b) Evolution of in-gap features in sample 011 with magnetic field (c) Evolution of in-gap features in sample 011 with back-gate voltage, data measured in a different measurement run than (a) and (b). (d) Evolution of in-gap features in sample T41 with backgate voltage. In-gap features in (a) and (b) consist of a strong peak at zero bias and smaller peaks on either side inside the superconducting gap. In-gap features in (c) and (d) appear less systematic, but can be seen to be qualitatively similar to those of the other measurements when a different distribution of spectral weight between central and side peaks is assumed. Curves are vertically shifted for visibility by 1 µS for (a)-(c) and by 200 µS for (d), respectively. The conductivity is calculated by numerical differentiation with adaptive smoothing which does not change the in-gap feature characteristics. Negative backgate voltage corresponds to depletion of the interface, whereas positive backgate voltage corresponds to carrier accumulation. ©(2017) APS.

7.4 Results

The in-gap features are shown in Fig. 7.2 for two different samples grown in two different PLD systems. Fig. 7.2 (a) shows tunnel spectra of sample 011 as a function of temperature, Fig. 7.2 (b) shows spectra of sample 011 as a function of magnetic field, Fig. 7.2 (c) shows spectra of sample 011 from a different measurement run as a function of back-gate voltage and Fig. 7.2 (d) shows spectra from sample T41 as a function of back-gate voltage. The in-gap-features observed in Fig. 7.2 (a) and (b) consist of a strong peak at zero bias and two smaller peaks, one at either side of the gap. Additionally, the width of the gap is increased compared to the standard spectra with the smaller peaks appearing at voltage values comparable to those of the coherence peaks in the standard spectra. The in-gap features disappear at the same temperature and field scales as the superconducting gap itself, *i.e.*, it is neither possible to observe the features without the gap, nor the gap without the features. Both the application of field and temperature suppress the gap and the features, but do not destroy them. Temperature was increased to 1 K and field to 5 T, after which the features reappeared when returning to base temperature and zero field. The evolution of the gap and the features is the same for both polarities of magnetic field, without magnetic hysteresis. The intrinsic charge carrier density of sample 011 was so high that the 2DEL could not be depleted completely with the gate voltages accessible in the experiment. Only minor changes of the in-gap states were observed for -300 $< V_G <$ 300 V (Fig. 7.2(c)).

In contrast to sample 011, the spectra of sample T41 depend strongly on the applied gate voltage. For $V_G > 10$ V, no in-gap states were observed. For $V_G < 10$ V, first a single zero bias peak is present, then for decreasing V_G gradually more peaks appear. The normal-state conductivity of sample T41 differs from that of sample 011 due to differences in tunnel electrode size and barrier thickness. At first sight, the tunneling spectra observed in Fig. 7.2 (c) and (d) appear to be quantitatively different from those observed in Fig. 7.2 (a) and (b). However, their similarity becomes obvious when a different distribution of spectral weight between the central and the side peaks is taken into account.

To gain quantitative information on the properties of the observed in-gap-peaks, the fitting routine illustrated in Fig. 7.3 was performed: For each curve, a lifetime-broadened BCS fit (Dynes fit) was adjusted to the part of the superconducting gap without peaks to create a reference curve corresponding to a standard $LaAlO_3$–$SrTiO_3$ gap. Since spectral weight is shifted from the coherence peaks into the in-gap peaks, the coherence peaks are not described well by this fit. The Dynes curve was subtracted from the data points to obtain the deviation from standard superconducting behavior. Three Gaussians were fitted to this subtracted peak to obtain the position, size and full width at half maximum (FWHM) of the central zero-bias peak and the separation of the side peaks.

Results of this analysis are shown in Fig. 7.4: The relative peak height (*i.e.*, the difference between measured the conductivity and the Dynes fit) decreases monotonically with increasing temperature or magnetic field and disappears at the same values of temperature and field at which the gap closes. On the other hand, the absolute height (*i.e.*, the measured conductivity value) of the peak remains almost constant over the entire measurement range close to the value corresponding to $\mathrm{d}I/\mathrm{d}V$ outside the gap. Also both the FWHM of the central peak and the separation of the outer peaks is independent of temperature and magnetic field. Since only few data points are available for the Dynes fits, the error bars given in Fig. 7.4 are based on the fit uncertainty: For the optimal fit, the sum of residuals, *i.e.*, of the weighted difference squares

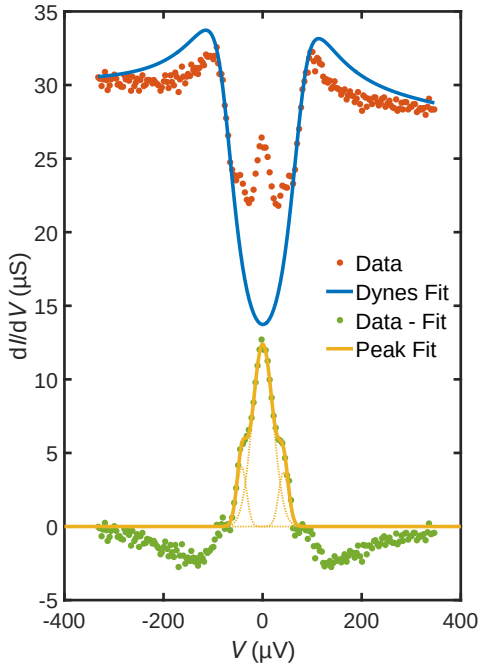

Figure 7.3: Illustration of the quantitative analysis used to characterize the in-gap peaks: A Dynes fit to the gap part without peaks is used to calculate the difference between expected and measured conductivity values. Three Gaussians are fitted to the subtracted peak to determine position, height and FWHM of the central peak and the separation of the side peaks. The dotted yellow lines indicate the three single Gaussians and the continuous yellow line indicates the sum of all three Gaussians. Note that because spectral weight is shifted from the coherence peaks into the in-gap peaks, the coherence peaks are not described well by the lifetime-broadened BCS fit. The red data points correspond to the 60 mK curve in Fig. 7.2 (a). ©(2017) APS.

between data and fit curve, is minimal. Error bars denote results from fits at the border of the confidence interval, for which the sum of residuals is twice as large as for the optimal fit.

7.5 Discussion

Origin of the in-gap features

Now the applicability of the phenomena described in section 7.2 to the experimental data is discussed. Since always either three peaks or no peaks at all are observed, it is conjectured that all peaks are caused by the same mechanism. Therefore, the discussion concentrates on those mechanisms which can account for all observed peaks.

Kondo resonance

A strong peak at zero bias can be caused by a Kondo resonance. However, the observed side peaks cannot be easily explained in a Kondo framework. Also, a zero-bias anomaly caused by Kondo scattering is expected to split with increasing magnetic field, which is not observed. Finally, the zero-bias peak in the measurements disappears at the same temperature and field as the superconducting gap, hinting at an intimate connection between the peak and

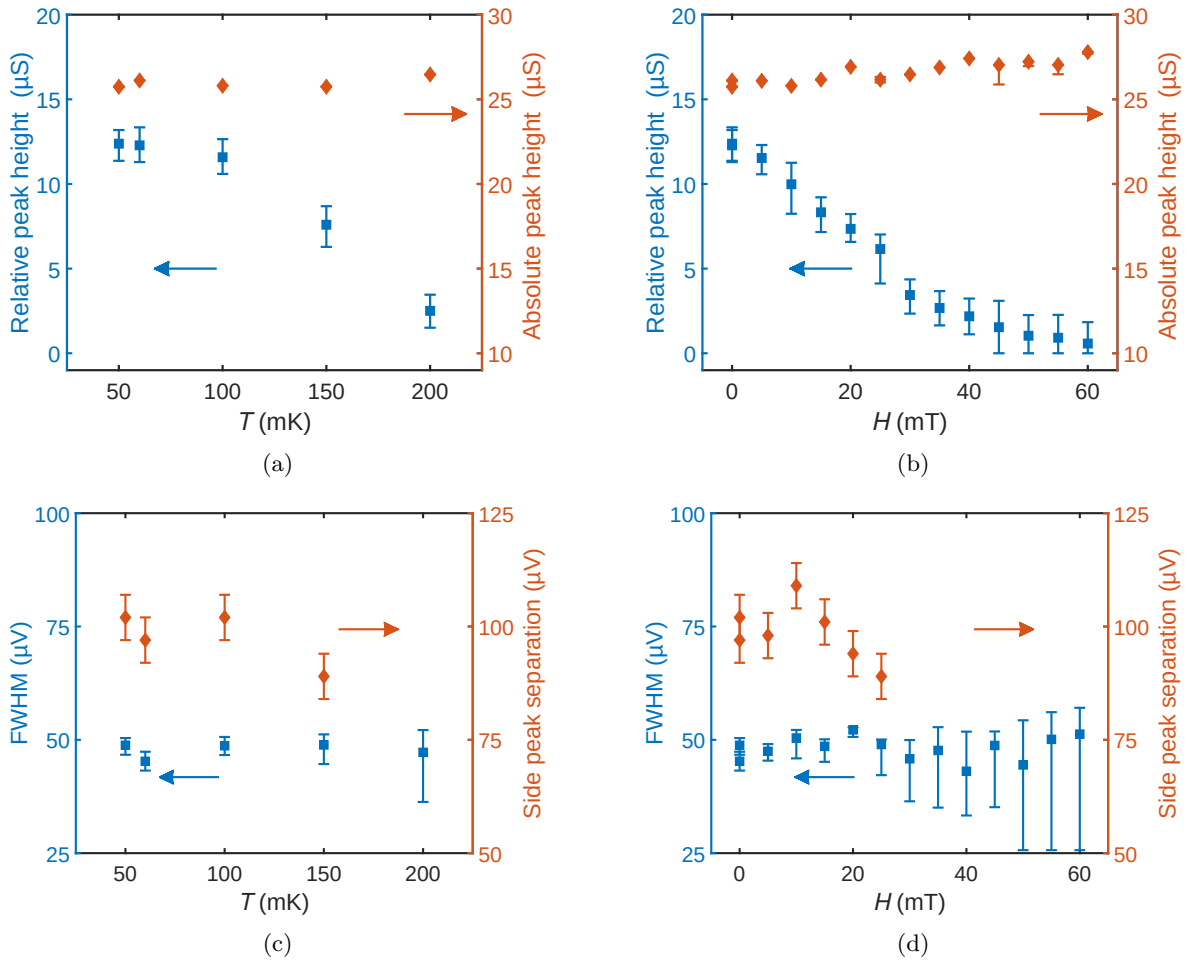

Figure 7.4: Evolution of height and FWHM of the zero bias peak and of the separation of the side peaks observed in sample 011. In (a) and (b) both the relative height of the peak, *i.e.*, the difference between data and BCS fit (blue squares), and the absolute size of the peak *i.e.*, the conductivity value at zero bias in the measured data (red diamonds) are plotted. Error bars indicate values obtained for BCS fits where the sum of weighted residuals is double that of the optimal fit. Since the absolute height of the peak depends only marginally on the fit, error bars for the absolute peak are smaller than the data points (a) Evolution with temperature. (b) Evolution with magnetic field. Whereas the relative peak height decreases with increasing magnetic field or temperature, the absolute peak height remains almost constant. In (c) and (d) the evolution of the FHWM of the central peak (blue squares) and the separation of the side peaks (red diamonds) is plotted. Again, error bars are obtained from data calculated for BCS fits with twice the minimum residual. (c) Evolution with temperature. (d) Evolution with magnetic field. Both the FWHM of the central peak and the spacing of the side peaks remain approximately constant over the field and temperature range in which the superconducting gap can be observed. Values of the side peak separation are only shown for those curves in which side peaks can be clearly discerned. The data shown here was obtained from that of Fig. 7.2 (a) and (b) using the procedure illustrated in Fig. 7.3. ©(2017) APS.

superconductivity. Therefore, Kondo scattering is unlikely to be the origin of the observed in-gap features.

Anderson-Appelbaum states

Similarly to Kondo resonances, Anderson-Appelbaum states are not connected to superconductivity. Also, the side-peak separation does not vary linearly with external magnetic field, as expected for these states. They are therefore not likely candidates for the origin of the observed in-gap features.

Barrier and surface impurities

Both the barrier and surface impurity models account only for features at zero bias but cannot explain the side peaks at finite voltage. Therefore they are unlikely to be the origin of the observed in-gap features.

Caroli-de Gennes-Matricon states

In the experiment, the peak at zero bias becomes weaker with increasing magnetic field, *i.e.*, with an increasing number of vortices. Thus it shows the opposite behavior of that expected for CdGM-states. Therefore it appears that the CdGM-mechanism is not the origin of the observed in-gap features.

Yu-Shiba-Rusinov states

YSR states can cause multiple peaks inside the gap of superconductors with magnetic impurities. However, YSR states always appear in pairs around zero, therefore the single peak at zero bias shown in Fig. 7.2 would be explicable only as a smeared pair of two YSR states. Such a smeared peak should broaden as the two constituent peaks move apart with increasing magnetic field, which is not observed. Also the two peaks on either side remain at the same position independent of magnetic field, in contrast to the outward movement expected for YSR states. The range of magnetic fields accessible in our experiment is limited because the critical magnetic field of the $LaAlO_3$–$SrTiO_3$ samples is small. Therefore, simulations were performed to assure that the movement of the peak positions should indeed be observable on the magnetic field scales investigated, if the peaks were due to YSR states. Since neither a broadening of the central peak nor a movement of the side peaks is observed, YSR states are most likely not the origin of the observed in-gap features.

Majorana bound states

The zero bias peak observed on sample 011 is of almost constant height as expected for a MBS. The fixed position of the peak at zero bias is consistent with the hypothesis of MBS, with the peaks at finite voltage bias possibly indicating Majoranas with overlapping wavefunctions [137, 150, 151]. The $LaAlO_3$–$SrTiO_3$-interface has been suggested as a candidate host for MBS [188], since it comprises the basic ingredients required for topological superconductivity *viz.* *s*-wave superconductivity, Rashba spin-orbit coupling and magnetism. Depending on the scattering parameters of the electron system, topological superconductivity and hence MBS may exist even without magnetism due to unequal signs of the superconducting order parameter in the

Rashba-split subbands [189, 190]. The appearance of Majorana modes usually requires specific configurations of the 2DES, *e.g.*, magnetic oxygen vacancies arranged in a linear chain which is quite unlikely to be readily available at the inhomogenous interface. However, scanning superconducting quantum interference device (SQUID) measurements provide evidence for the existence of one-dimensional conducting channels at the domain boundaries of substrate $SrTiO_3$ [191]. The possibility of MBS as the origin of the in-gap features cannot be ruled out.

Andreev bound states

ABS can generate conductance peaks at zero bias as well as at finite energy, consistent with the present observations. However, a zero-bias conductance peak caused by an ABS is expected to split upon increasing the magnetic field, which is not observed. Andreev bound states usually occur at junctions of superconductors with metals which have sufficiently high conductivity, whereas in the present samples, gold electrode and superconductor are separated by an insulating layer. However, the NS contact can be situated within the 2DES, either as an in-plane combination of normal and superconducting islands or as separate normal and superconducting layers. The application of gate voltage changes the carrier density and hence the superconducting volume fraction, changing the number of the ABS.

SIS tunneling

Both the zero bias current and the broadening of the gap to approximately twice the value of standard $LaAlO_3$–$SrTiO_3$ (cf. Fig. 7.1) can clearly be seen in the data from sample 011. Thus the tunnel characteristics observed here strongly resemble that of a hypothetical SIS junction, with the side peaks representing the coherence peaks of the inner gap. However, there is only one superconducting electrode in the tunnel junction. It is implausible that the superconducting $LaAlO_3$–$SrTiO_3$ interface induces superconductivity in the gold top electrode through the insulating $LaAlO_3$ tunneling barrier. Therefore SIS tunneling is an unlikely explanation of the observed in-gap features.

Multiband superconductivity

The side peaks observed in the tunneling spectra are explicable as the coherence peaks of a second superconducting band. However, the strong peak at zero bias cannot be explained in this framework. Also, the coherence peaks of a second gap should move closer together as the gap closes with increasing magnetic field or temperature, which is not observed. Therefore, multiband superconductivity is not a likely explanation of our observations.

Order-parameter admixtures

In the $LaAlO_3$–$SrTiO_3$-interface, two forms of unconventional order parameters are concievable: p-wave spin-triplet pairing due to Rashba spin-orbit coupling and odd-frequency spin-triplet pairing due to an inhomogeneous ferromagnetic state.

The side peaks observed in the tunneling data are compatible with a double gap, one due to s-wave pairing and one due to p-wave pairing. The evolution with backgate voltage is also explicable by the gate-dependence of the Rashba spin-orbit coupling. However, the strong central peak can not be explained in this framework. Even though several works predict p-wave superconductivity at the $LaAlO_3$–$SrTiO_3$-interface due to Rashba spin-orbit coupling (*e.g.*,

[192]), it is unlikely that the p-wave component is strong enough to cause the observed peaks. Therefore it is unlikely that the observed in-gap features are caused by p-wave spin-triplet pairing.

Odd-frequency spin-triplet pairing can account for both the zero bias peak and the side peaks [132]. It requires an inhomogeneous magnetization at the interface, which in some regions of the sample generates zero-bias peaks and peaks at finite bias in other regions. Since the area of the tunnel junctions is larger than the domain size, the peaks from different regions are observed together in the spectra. However, the gap size for singlet pairing and triplet pairing is likely to differ and therefore an averaging over triplet and singlet regions should show a double gap with two pairs of coherence peaks, unless the condensate is always either completely singlet or completely triplet. Magnetism has been observed to coexist with superconductivity in $LaAlO_3$–$SrTiO_3$ [59, 60] and it has been shown to be rather superparamagnetic than truly ferromagnetic in nature [59]. Therefore, the difference between the superparamagnetic domains could generate an inhomogeneous magnetization if the variation of magnetization between domains is strong enough.

Another mechanism to generate a mixture of singlet and and triplet pairing is the combination of a two-dimensional superconductor with broken inversion symmetry (which is the case for the $LaAlO_3$–$SrTiO_3$-interface) with strong Rashba spin-orbit coupling [155]. Since gate-tunable Rashba spin-orbit coupling has been reported at the $LaAlO_3$–$SrTiO_3$-interface [52–54], this is a likely scenario for our observations.

Origin of the dependence on thermal cycling

Finally, some scenarios are discussed which could explain the fact that the in-gap features are only observed in a small fraction of samples and that they depend on thermal cycling. A tentative explanation for the appearance and disappearance of sub-gap states may lie in the domain structure of the $SrTiO_3$ substrate: as the crystal structure changes from cubic to tetragonal when the crystal is cooled below 105 K, a domain structure forms, which is randomly different in each measurement run. When the in-gap features are assumed to depend on a specific domain configuration, then this scenario can also explain why the in-gap features sometimes disappear irreversibly when sweeping the gate voltage, because the gate voltage influences the $SrTiO_3$ domain structure [193]. Another possible explanation is that the in-gap features depend on a specific configuration of defects in the samples, for example oxygen vacancies. Oxygen vacancies form magnetic centers[194, 195] and could thereby influence the superconductivity. A number of scenarios are conceivable in which single or multiple magnetic oxygen vacancies can generate peaks inside the superconducting gap: An isolated magnetic impurity can generate a Kondo peak. A region of the 2DEL in which superconductivity is suppressed because of an accumulation of magnetic moments can form Andreev bound states at its boundary to the surrounding superconductor. Magnetic centers arranged in a line, *e.g.*at a $SrTiO_3$ domain boundary, can host Majorana-like modes. Inhomogeneous magnetism can induce odd-frequency spin-triplet pairing. It is conceivable that the configuration of these magnetic defects is pinned to the domain structure of the $SrTiO_3$, thus being susceptible to thermal and gate voltage cycling. Finally, the back-gate voltage also affects the thickness d of the superconducting sheet, with d increased up to a factor of three in the overdoped region [29].

7.6 Conclusions

Using tunneling spectroscopy on the two-dimensional superconductor, in-gap features in spectra of several superconducting $LaAlO_3$–$SrTiO_3$ tunnel devices were observed. The features appear and disappear non-deterministically between different warming and cooling cycles. The in-gap features were found not to move with either temperature or magnetic field, yet to change under the application of back-gate voltage. The real challenge is to disentangle the true origin of these in-gap features with the limited information available at the buried interfaces. It was possible to exclude some of the proposed scenarios with relative certainty. However, none of the known mechanisms that can cause in-gap states easily explains the results. Conceivable scenarios involve Majorana bound states, Andreev bound states, or the presence of an odd-frequency spin-triplet component in the superconducting order parameter caused by an inhomogeneous ferromagnetic state in the electron system.

On ne découvre pas de terre nouvelle sans consentir à perdre de vue, d'abord et longtemps, tout rivage.

André Gide

8 CONCLUSIONS AND OUTLOOK

8.1 Conclusions

This thesis presents a number of new insights on the versatile 2DES at the $LaAlO_3$–$SrTiO_3$ interface, which will extend the understanding of this two-dimensional electron system and its superconducting ground state. A specific emphasis of these investigations is on the phase transitions observable only in two-dimensional superconductors, the SIT and BKT transition. The appearance of states inside the superconducting gap observed in tunneling spectroscopy indicates that much is still to be learned about the 2DES at the $LaAlO_3$–$SrTiO_3$ interface.

An important application of a 2DES is a FET. In chapter 4, a new design of FETs using the $LaAlO_3$–$SrTiO_3$ 2DES has been presented. These transistors combine the previous works on $LaAlO_3$–$SrTiO_3$ transistors [20–22] with the investigations of $LaAlO_3$–$SrTiO_3$ under hydrostatic pressure [23, 24]. This is the first investigation of oxide transistors under pressure, making a new axis of the phase diagram accessible. Not only are the results relevant as a confirmation of the earlier results [23], but they also show that delicate $LaAlO_3$–$SrTiO_3$ devices can be subjected to such harsh physical conditions as pressures of 1.8 GPa and still retain their functionality.

The second part of chapter 4, describing results on combined transistor-Hall-bars, provides new insights on the multiband nature of the $LaAlO_3$–$SrTiO_3$ 2DES. In particular, by the analysis of the transistor data, the existence of a band of positive charge carriers which is often observed inthe Hall data analysis is ruled out. In addition, it demonstrates the respective merits of transistors on the one hand and Hall-bars on the other hand for the determination of charge carrier densities and mobilities, a result relevant for any conductive material system.

In chapter 5, the change of the perpendicular critical magnetic field H_{c2} of the superconducting 2DES with temperature is investigated. In contrast to the parabolic curve expected for a standard BCS superconductor, the temperature dependence of H_{c2} is linear down to the lowest accessible temperature of 50 mK. Several mechanisms exist which can explain this linear behavior of $H_{c2}(T)$, among them multiband superconductivity. However, also the two-dimensional nature of the 2DES itself is a possible cause for the linear $H_{c2}(T)$ curve. Since in $LaAlO_3$–$SrTiO_3$, as in all other two-dimensional superconductors, the superconducting transition is broadened, the error margins on $H_{c2}(T)$ are large and prohibit a clear distinction between the different theoretical models.

The extended process of growth optimization described at the beginning of chapter 6 highlights the central challenge when investigating the $LaAlO_3$–$SrTiO_3$ system: Because of a large number of uncontrollable (and sometimes even unknown) external influences, the properties of samples which are grown at nominally the same parameters can vary significantly. It is clear that further advances in the growth process are desirable, particularly for a minimization of

the influence of the substrate.

The combined analysis of high-magnetic field and tunneling data presented in chapter 6 points to the connection between the onset of multiband conductivity and the demise of superconductivity in the overdoped region of the $LaAlO_3$–$SrTiO_3$ phase diagram. Here, results from tunneling and Hall data on the same sample were combined for the first time. It offers an explanation for the non-BCS behavior observed in the overdoped region, even though the exact mechanism by which carriers in the second band destroy superconductivity is not yet clear.

The attempts to measure the BKT transition across the range of the $LaAlO_3$–$SrTiO_3$ phase diagram from superconductor to insulator presented in chapter 6 were not successful due to a variety of difficulties. The main and most fundamental of these is certainly the heating of the electron system. It is particularly pronounced at millikelvin temperatures at which systems such as $LaAlO_3$–$SrTiO_3$ are investigated. At these low temperatures the electron system decouples from the phonons, which makes effective cooling difficult. Measurements of the BKT transition in two-dimensional superconducting systems with transition temperatures at liquid helium temperature or above will provide more reliable results. The crucial question is whether a system can be found in which superconductivity is so strong that it can exist at sufficiently high temperatures, yet is weak enough to be tuned by the application of a voltage, ideally without the need for a liquid electrolyte.

At the end of chapter 6, the design of a superconducting transistor using the $LaAlO_3$–$SrTiO_3$ interface electron system as channel has been presented. The performance of this transistor is reduced by design limitations, but switching of the channel with a topgate voltage is demonstrated and the difference between transistor behavior in the normal and superconducting state is shown. Furthermore, the data show that switching from the superconducting to the insulating state traverses an intermediate metallic state.

The in-gap states observed in tunneling spectra of the superconducting $LaAlO_3$–$SrTiO_3$ condensate discussed in chapter 7 are exemplary of the many fascinating, yet unexplained phenomena at the $LaAlO_3$–$SrTiO_3$ interface. While it has not been possible to reach a definitive conclusion on the nature of these states due to their non-deterministic appearance and disappearance, by careful analysis of the available data it is possible to exclude some of the proposed mechanisms with relative certainty. Of the remaining scenarios, many point to the existence of states with interesting properties at the interface, such as Majorana bound states.

A reccuring theme of this thesis is to disentangle the contribution of multiple bands to conductivity and superconductivity at the $LaAlO_3$–$SrTiO_3$ interface. The emerging picture is consistent with that presented in [25]: Even at low carrier density, two sub-bands are occupied, specifically the low-lying d_{xy} orbital and one of the Rashba-split $d_{xz/yz}$ orbitals. Multiple bands must be occupied even at low doping because tunneling perpendicular to the interface is only possible into the energetically higher $d_{xz/yz}$ sub-bands because of momentum conservation, and a measurable tunneling current is indeed observed for all gate voltages at which the interface is conducting. This implies that the energetically lower d_{xy} sub-band is also populated. The multiple frequencies in Shubnikov-de Haas-oscillations presented in Sec. 6.1.2 also give an indication for conductivity in multiple bands even at low carrier densities.

For higher carrier densities, an additional band is populated as is indicated by the Hall data presented in Sec. 6.1.1. The carriers in this additional band, the one of the Rashba-split $d_{xz/yz}$ orbitals that has a higher energy, do not contribute to superconductivity, but instead lead to a decrease in T_c, possibly due to increased electron-electron scattering. Thus it is clear from the tunneling data that the lower-lying Rashba-split $d_{xz/yz}$ sub-band is superconducting and from the Hall data it appears that its higher-lying partner is not. It remains an open

question whether the d_{xy} sub-band is also superconducting, which could not be resolved by the investigations of the critical magnetic field discussed in Chapter 5. However, if the d_{xy} sub-band would also participate in superconductivity, this can be a possible cause of the in-gap states discussed in chapter 7.

In a different scenario, it is also possible that the d_{xy} sub-band is not conductive at all: The charge carriers are present, but because the electrons of the d_{xy} sub-band are so close to the interface, where the defect density is high, they are almost localized [26]. This hypothesis might explain why the Hall measurements presented in this thesis show single-band behavior at negative back-gate voltage, why the measured carrier density at the interface is always smaller than predicted by the polar catastrophe scenario and why photoemission measurements give higher values for the carrier density than transport measurements [27].

The results presented in this thesis show that the 2DES at the $LaAlO_3$–$SrTiO_3$ interface is both interesting in terms of applications, because resilient and even superconducting transistors and tunnel junctions with areas of several square millimeters can be fabricated from it, and also in terms of basic research, because many new and unconventional phenomena can be observed in it. However, the difficulties of precise and clean sample growth and measurements at millikelvin temperatures remain a challenge for the experimenter.

8.2 Outlook

The great advantage of oxide materials which lies in their versatility is also the greatest challenge for their study and use. The multivalency and complex stoichiometry of oxide materials make them susceptible to impurities and defects. It can be a daunting task when investigating oxides to separate the effects due to defects and impurities from the intrinsic properties of the materials.

The largest source of defects when growing oxide materials is often the substrate, with $SrTiO_3$ being notorious in this respect. Instead of relying on sub-optimal commercially available substrates grown by the Verneuil method, Czochralsky-grown substrates of highest purity may significantly enhance oxide reliability. Furthermore, growth of $SrTiO_3$ buffer layers on the substrate before $LaAlO_3$ deposition can protect the 2DES from the influence of substrate impurities. The fine-tuning of the layers close to the 2DES to reduce scattering was successfully implemented before, *e.g.*, at GaAs /AlGaAs interfaces [196, 197] or in MgZnO/ZnO heterostructures [198] and has made exceptionally high charge carrier mobilities possible in these systems.

Many open questions concerning the superconductivity of the $LaAlO_3$–$SrTiO_3$ 2DES still remain. The most interesting of them may be which of the different conducting bands contribute to superconductivity. One way to elucidate this question would be measurements of horizontal tunneling current into the 2DES to resolve the d_{xy} orbitals. Fabrication of horizontal tunneling junctions is a very challenging task, because the edges have to be controlled very precisely in order to create a thin, yet defect-free insulating barrier.

Extending the results from chapter 5, careful measurement of the curvature of $H_{c2}(T)$ around T_c can also give an indication on the multiband character of superconductivity at the interface. However, this requires an improvement in measurement precision in order to be able to unequivocally attribute the data to one of the different predicted behaviors.

In order to improve the resolution of the tunneling spectra observed in co-planar devices, top electrodes made from superconducting materials instead of gold could be grown. In the case

of elemental superconductors such as niobium or lead, this task should be fairly straightforward. Indeed, indium electrodes have been grown on doped $SrTiO_3$ substrates in our laboratory to form Schottky barriers [105].

Since the experiments on transistors presented in chapter 4 showed that entire $LaAlO_3$–$SrTiO_3$ devices can be subjected to hydrostatic pressure without breakthrough, a further step would be to pressurize $LaAlO_3$–$SrTiO_3$ tunnel junctions. The tunneling data obtained from such junctions will make it possible to measure the phonons of the $SrTiO_3$ substrate as a function of pressure and possibly shed light on the quantum criticality of the $SrTiO_3$ lattice.

Beyond the $LaAlO_3$–$SrTiO_3$ superconductor, interface superconductivity and two-dimensional superconductivity in general promise to be interesting topics in the field of superconductivity in the future. One of the most surprising developments in this field is the observation of superconductivity of monolayers of FeSe grown on $SrTiO_3$ substrates with critical temperatures in the range of 60 K, which is significantly higher than the critical temperature of bulk FeSe [199]. It appears that interface superconductivity and the investigation of superconducting 2DESs is indeed a promising pathway for the search for superconductors with high critical temperatures, one of the long-standing ideas being, *e.g.*, to separate the superconducting charge carriers and their "glue" into separate layers [200]. Since this is only one of the few possibilities which can be used to custom-tailor interface superconductors, they are equally fascinating because of their versatility as well as the many unique phenomena which can be observed in them.

Appendices

BCS THEORY

A

A superconductor is characterized by two observable properties: The eponymous disappearance of resistance below a certain critical temperature T_c and the complete expulsion of a magnetic field up to some critical field H_c. Quantum mechanically, a more fundamental property of the superconducting condensate is the existence of a macroscopic wavefunction $\Psi(\mathbf{r}, t) = \sqrt{n_S}e^{i\phi}$ where n_S is the superconducting carrier density and ϕ the macroscopically definite phase.

The following introduction to key concepts of BCS theory is closely based on [67]. Superconductivity was experimentally discovered in 1911, but it took until 1957 to find a microscopic explanation of the phenomenon when Bardeen, Cooper and Schrieffer (BCS) published their microscopic theory of superconductivity [201]. Its essential ingredient is the formation of pairs of electrons, which had been proposed shortly before by Leon Cooper, and which have since become known as *Cooper Pairs* [202]. Cooper showed that if one considers a filled Fermi sea, any attractive interaction $V_{\mathbf{k}\mathbf{k}'}$, however small, between two electrons with momenta $\mathbf{k}$ and $\mathbf{k}'$ will facilitate a condensation into a bound ground state. These pairs of electrons have integer spin, therefore they qualify as Bosons and can condense to energy levels below the filled Fermi sea into a condensate to which pairs can be added or subtracted without energy cost. This pairing will be predominantly between electrons of equal and opposite momentum, so that their total momentum is zero. At the same time the spins of the pairing electrons will be opposite, since an antisymmetric spin wavefunction implies a symmetric spatial wavefunction with a higher probabilty of the electrons being near each other. Since we expect this particular electron-electron interaction to be attractive, a smaller distance between the electrons means a lowering in energy. In the following calculations, the attractive interaction is modeled by the very crude approximation that it is a constant V below and zero above a certain cutoff frequency ω_c. Even though this approximation is very simple, it has been very successful for reasons that will become evident below.

In most standard superconductors, the attrative interaction $V_{\mathbf{k}\mathbf{k}'}$ is due to the interaction of the electrons with the atomic lattice, or more precisely, with the vibrational excitations of this lattice, i.e. the phonons. In a very naive picture, one could imagine a first electron polarizing the (positively charged) atomic lattice, which in turn would attract a second electron. However, one should not take this simple picture too literally. The two electrons in a Cooper pair have opposite momenta, so they do not follow one another. Also, Cooper pairs have a large spatial extent and are highly overlapping. Thus, it is quite misleading to consider individual Cooper pairs where instead the entirety of the superconducting condensate comprising all pairs has to be taken into account.

We proceed by constructing the BCS ground state in second quantization. We write $c_{\mathbf{k}\uparrow}$ and $c^\dagger_{\mathbf{k}\uparrow}$ for the single-electron annihilation and creation operators, respectively. The most general

way to write an N-electron wavefuntion with these operators in pairs is to let them act on the vacuum state $|\phi_0\rangle$ with weighting coeffcients $g(\mathbf{k_i}, ...\mathbf{k_t})$:

$$|\Psi_N\rangle = \sum g(\mathbf{k_i}, ...\mathbf{k_t}) c^\dagger_{\mathbf{k_i}\uparrow} c^\dagger_{-\mathbf{k_i}\downarrow} ... c^\dagger_{\mathbf{k_t}\uparrow} c^\dagger_{-\mathbf{k_t}\downarrow} |\phi_0\rangle \,. \tag{A.1}$$

For any macroscopic sample this construction has so many combinatorial possibilities that it is impossible to calculate. Therefore, BCS made the simplifying assumption that the occupancy of each pair state only depends on the mean field generated by the average of all other states. Under this condition, the wavefunction factorizes and the ground state can be written in the form of:

$$|\Psi_G\rangle = \prod_{\mathbf{k}=\mathbf{k}_1 ... \mathbf{k}_\mathbf{M}} \left(u_\mathbf{k} + v_\mathbf{k} c^\dagger_{\mathbf{k}\uparrow} c^\dagger_{-\mathbf{k}\downarrow} \right) |\phi_0\rangle \,, \tag{A.2}$$

for a state in which M pair states are occupied. $|u_\mathbf{k}|^2$ and $|v_\mathbf{k}|^2 = 1 - |u_\mathbf{k}|^2$ are the probabilities that a particular pair state with momentum $\mathbf{k}$ is unoccupied or occupied, respectively. We assume $u_\mathbf{k}$ and $v_\mathbf{k}$ to be real.

In order to find the ground state for a particular system, the $u_\mathbf{k}$ and $v_\mathbf{k}$ have to be calculated. BCS solved this problem by a variational method, but we will present here Bogoliubuv's and Valatins's more elegant method using canonical transformations [203, 204]. Ignoring all energy contributions except the chemical potential and the pairing potential, the Hamiltonian containing those energies relevant for superconductivity is:

$$H = \sum_{\mathbf{k}\sigma} \epsilon_\mathbf{k} n_{\mathbf{k}\sigma} + \sum_{\mathbf{kl}} V_\mathbf{kl} c^\dagger_{\mathbf{k}\uparrow} c^\dagger_{-\mathbf{k}\downarrow} c_{-\mathbf{l},\downarrow} c_{\mathbf{l}\uparrow} \tag{A.3}$$

where $\epsilon_\mathbf{k}$ denotes the energy of an electron plane wave with momentum $\mathbf{k}$. The first term counts this energy for the individual electrons, whereas the second term describes the energy contribution of scattering a pair ($\mathbf{l}$, $-\mathbf{l}$) into a pair($\mathbf{k}$, $-\mathbf{k}$).

In a normal conductor, the probabilty to find two electrons with precisely opposite spin and momentum is very small and when integrating the expectation value of such a pair state, it vanishes because of phase fluctuations. In a superconductor, on the other hand, these pair states are very likely to be occupied together and their expectation value is nonzero because they have a fixed phase relation. Therefore, the pairing operators $c_{-\mathbf{l}\downarrow} c_{\mathbf{l}\uparrow}$ and $c^\dagger_{\mathbf{k}\uparrow} c^\dagger_{-\mathbf{k}\downarrow}$ in the Hamiltonian can be approximated by their expectation values $b_\mathbf{l}$ and $b^\dagger_\mathbf{k}$. Writing the operators as expectation value plus the deviation from that expectation value:

$$c_{-\mathbf{l}\downarrow} c_{\mathbf{l}\uparrow} = b_\mathbf{l} + (c_{-\mathbf{l}\downarrow} c_{\mathbf{l}\uparrow} - b_\mathbf{l}) \,. \tag{A.4}$$

We insert this expansion into the Hamiltonian (Eq. A.3) and neglect any terms that are of higher order than linear in the deviation (the term in parentheses):

$$H = \sum_{\mathbf{k}\sigma} \xi_\mathbf{k} c^\dagger_{\mathbf{k}\sigma} c_{\mathbf{k}\sigma} + \sum_{\mathbf{kl}} V_\mathbf{kl} \left(c^\dagger_{\mathbf{k}\uparrow} c^\dagger_{-\mathbf{k}\downarrow} b_\mathbf{l} + b^\dagger_\mathbf{k} c_{-\mathbf{l}\downarrow} c_{\mathbf{l}\uparrow} - b^\dagger_\mathbf{k} b_\mathbf{l} \right) . \tag{A.5}$$

We have now reduced the Hamiltonian from a quartic to a bilinear form in the single-electron operators corresponding to the constituents of a Cooper pair. Also we have written the energies with respect to the Fermi surface: $\xi_\mathbf{k} = \epsilon_\mathbf{k} - E_F$. This form is called the *Model Hamiltonian*. To simplify the Hamiltonian further, we define:

$$\Delta_{\mathbf{k}} = -\sum_{\mathbf{l}} V_{\mathbf{kl}} b_{\mathbf{l}}, \tag{A.6}$$

where the corresponding $\Delta_{\mathbf{l}}^{\dagger}$ is calculated accordingly. This allows us to write the Hamiltonian slightly differently:

$$H = \sum_{\mathbf{k}\sigma} \xi_{\mathbf{k}} c_{\mathbf{k}\sigma}^{\dagger} c_{\mathbf{k}\sigma} + \sum_{\mathbf{k}} \Delta_{\mathbf{k}} c_{\mathbf{k}\uparrow}^{\dagger} c_{-\mathbf{k}\downarrow}^{\dagger} + \Delta_{\mathbf{k}}^{\dagger} c_{-\mathbf{k}\downarrow} c_{\mathbf{k}\uparrow} - \Delta_{\mathbf{k}} b_{\mathbf{k}}^{\dagger}. \tag{A.7}$$

To find the simplest form of the Hamiltonian, we wish to find some base of operators in which it is diagonal, i.e. where there are only terms that are either constant or proportional to particle occupation numbers. The operators that give diagonal form to the Hamiltonian were shown to be [203, 204]:

$$\gamma_{\mathbf{k}0}^{\dagger} = u_{\mathbf{k}} c_{\mathbf{k}\uparrow}^{\dagger} - v_{\mathbf{k}} c_{-\mathbf{k}\downarrow} \tag{A.8}$$

$$\gamma_{\mathbf{k}1}^{\dagger} = u_{\mathbf{k}} c_{-\mathbf{k}\downarrow}^{\dagger} + v_{\mathbf{k}} c_{\mathbf{k}\uparrow}. \tag{A.9}$$

The coefficients $u_{\mathbf{k}}$ and $v_{\mathbf{k}}$, satisfying $|u_{\mathbf{k}}|^2 + |v_{\mathbf{k}}|^2 = 1$ are identical to the probabilities $u_{\mathbf{k}}$ and $v_{\mathbf{k}}$ which first appeared in Eq . A.2. We now have to find values for these coefficients such that cross terms between the two operators A.8 and A.9 disappear from the Hamiltonian. This is the case for

$$|v_{\mathbf{k}}|^2 = 1 - |u_{\mathbf{k}}|^2 = \frac{1}{2}\left(1 - \frac{\xi_{\mathbf{k}}}{E_{\mathbf{k}}}\right), \tag{A.10}$$

where

$$E_{\mathbf{k}} = \left(\Delta_{\mathbf{k}}^2 + \xi_{\mathbf{k}}^2\right)^{\frac{1}{2}}. \tag{A.11}$$

Upon inspection of $|v_{\mathbf{k}}|^2$, it becomes evident that it converges quickly towards 1 for $\xi < 0$ and 0 for $\xi > 0$. It varies only in the immediate vicinity of the Fermi surface $\xi \approx 0$. Therefore, the precise behavior of the pairing potential far away from the Fermi surface does not matter, justifying the very crude approximation given to the pairing potential by Cooper. Having found the optimal $u_{\mathbf{k}}$ and $v_{\mathbf{k}}$ finally allows us to write the Hamiltonian in diagonal form:

$$H = \sum_{\mathbf{k}} \left(\xi_{\mathbf{k}} - E_{\mathbf{k}} + \Delta_{\mathbf{k}} b_{\mathbf{k}}^{\dagger}\right) + \sum_{\mathbf{k}} E_{\mathbf{k}} \left(\gamma_{\mathbf{k}0}^{\dagger} \gamma_{\mathbf{k}0} + \gamma_{\mathbf{k}1}^{\dagger} \gamma_{\mathbf{k}1}\right). \tag{A.12}$$

The first sum contains the ground state energy of a superconductor, whereas the second sum contains the energies of excitations above the superconducting ground state given by the operators A.8 and A.9. These *Quasiparticle Operators* and the corresponding *Quasiparticle States* which they describe are not intuitively clear. However, they will be very important for the following discussion of tunneling, therefore we will describe them in some more detail:

Most importantly, a Bogoliubov quasiparticle is neither simply an electron nor a hole, but a superposition of both. This is possible because the quasiparticle only exists in connection with a condensate of Cooper pairs. Since these are Bosons, they can be added or subtracted without energy cost and therefore supply the charge difference of 2e between electron and hole. Indeed, the number of pairs is not fixed. The operator $\gamma_{\mathbf{k}0}^{\dagger}$ creates an electron with amplitude $u_{\mathbf{k}}$ that

the pair state $\mathbf{k}$ is unoccupied, thus not changing the number of pairs. But with amplitude $u_{\mathbf{k}}$ the pair state is occupied and the operator destroys one of its constituent electrons, thus destroying the pair.

If we apply the creation operator $\gamma^\dagger_{\mathbf{k}0}$ to a BCS state, we either create an electron with spin up and momentum $\mathbf{k}$ with probability $u_{\mathbf{k}}$ or we destroy an electron with spin down and momentum $-\mathbf{k}$ with the probability $v_{\mathbf{k}}$. In either case, the total momentum increases by $\mathbf{k}$ and the spin increases by 1/2. The operator $\gamma^\dagger_{\mathbf{k}1}$ has the opposite effect: It either creates or destroys an electron, but in either case the total momentum decreases by $\mathbf{k}$ and the spin decreases by 1/2.

To illustrate this concept further, consider the quasiparticle creation operator acting on the BCS ground state. Expanding in single-electron operators, it can be shown by combining Eqs. A.2 and A.8 that:

$$\gamma^\dagger_{\mathbf{k}0} |\Psi_G\rangle = c^\dagger_{\mathbf{k}\uparrow} \prod_{\mathbf{l}\neq\mathbf{k}} \left(u_{\mathbf{l}} + v_{\mathbf{l}} c^\dagger_{\mathbf{l}\uparrow} c^\dagger_{\mathbf{l}\downarrow} \right) |\psi_0\rangle \,. \tag{A.13}$$

Before the action of the operator, the pair state with momentum ($\mathbf{k}$, $-\mathbf{k}$)was empty with probability $|u_{\mathbf{k}}|^2$ and occupied by a pair with probability $|v_{\mathbf{k}}|^2$. After the action of the operator, the state with momentum $\mathbf{k}$ is occupied by an electron whereas the state with momentum $-\mathbf{k}$ is empty. Whether this corresponds to the creation of an electron or the destruction of one (one of the pair partners) depends on the initial probabilities of pair occupation.

The $|0\rangle$ state for the quasiparticle operators is the BCS ground state $|\Psi_G\rangle$ defined in Eq. A.2 and not the vacuum state of the single-electron operators $|\phi_0\rangle$. By again expanding the quasiparticle operators and the ground state in terms of the single-electron operators, it can be shown that

$$\gamma_{\mathbf{k}0} |\Psi_G\rangle = \gamma_{\mathbf{k}1} |\Psi_G\rangle = 0. \tag{A.14}$$

As can be seen from the definition of the quasiparticle energy Eq. A.11, the minimum energy a quasiparticle can have is $|\Delta_{\mathbf{k}}| > 0$, i.e. there is an energy gap for excitations from the Fermi surface.

Since there is a one-to-one correspondence between the quasiparticle operators and the single-electron operators, the densities of state for the superconducting and the normal state are related by:

$$N_S(E_{\mathbf{k}}) dE_{\mathbf{k}} = N_n(\xi_{\mathbf{k}}) d\xi_{\mathbf{k}}. \tag{A.15}$$

In the small energy range around the Fermi surface in which superconducting pairing occurs, we can consider the density of states of the normal metal to be constant $N(\xi) = N(0)$. Thus:

$$N_S(E_{\mathbf{k}}) = \frac{dn}{dE_{\mathbf{k}}} = \frac{dn}{d\xi_{\mathbf{k}}} \frac{d\xi_{\mathbf{k}}}{dE_{\mathbf{k}}} = N(0) \begin{cases} \frac{E_{\mathbf{k}}}{(E^2_{\mathbf{k}} - \Delta^2)^{(1/2)}} & (E_{\mathbf{k}} > \Delta) \\ 0 & (E_{\mathbf{k}} < \Delta) \end{cases} . \tag{A.16}$$

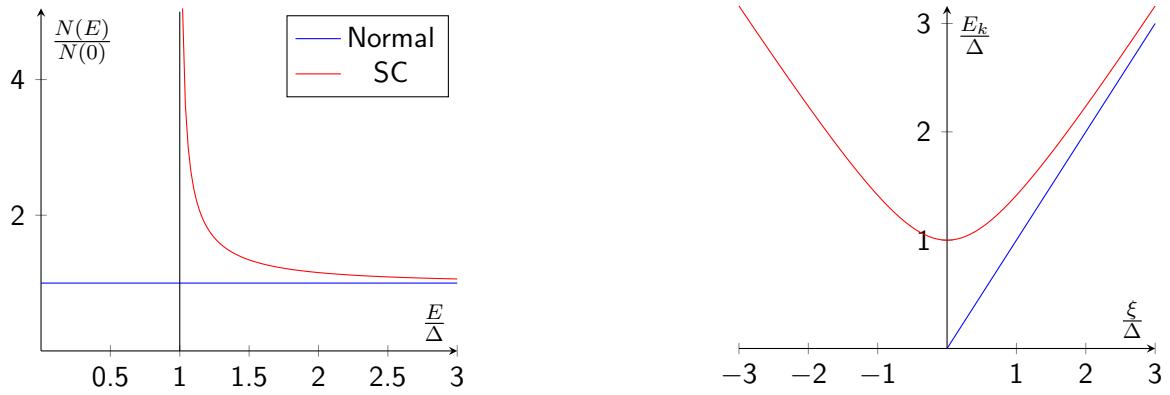

(a) (b)

Figure A.1: (a) Normalized density of states as a function of energy for a normal metal (blue) and a BCS superconductor according to Eq. A.16 (red). There is a gap of size Δ in the superconducting density. The states from the gap are raised into the coherence peak, so that the total spectral weight is conserved. (b) Energy of normal state excitations (blue) and superconducting quasiparticle excitations according to Eq. A.11 (red). The quasiparticles change smoothly from hole-like ($\xi_{\mathbf{k}} < 0$) to electron-like($\xi_{\mathbf{k}} > 0$).

RENORMALIZATION GROUP THEORY B

Renormalization group theory in statistical physics is predominantly used to calculate the critical exponents of physical systems close to second-order phase transitions. However, it is also possible to find the entire partition function of a system using this approach. The underlying idea of the renormalizatuion group is to reduce the complexity of a system (and consequently to simplify the calculations) by replacing the system under consideration by a self-similar, but smaller copy of itself, *i.e.*, reducing the number of atoms, spins etc. to be calculated. This approach is made possible by the fact that for many physical systems, the laws governing the system at one scale are similar to the laws governing the system at another scale. The challenge is to find out how one transforms the system from one scale to another, the "Renormalization Flow". This appendix is based on a concise, undergraduate level introduction to the renormalization group in solid state physics, written by pioneers of the field [205].

Following the approach of [205], let us consider the Ising model for illustration. In one dimension, it is a chain of spins σ_i with magnitude 1 which can point either up or down. There is a coupling energy between nearest neighbors of $-J$ when the spins are parallel and $+J$ when they are antiparallel. To obtain the partition function, one has to sum over all possible configurations of spins:

$$Z = \sum \exp\left[\frac{J}{k_B T}\left(\sigma_1\sigma_2 + \sigma_2\sigma_3 + \sigma_3\sigma_4 + ...\right)\right]. \tag{B.1}$$

It is possible to modify the calculation in such a way that it is only necessary to sum over the odd-numbered spins, effectively reducing the system size by half, by the following rearrangements. Introducing the coupling strength $K = \frac{J}{k_B T}$ for convenience, we single out those terms containing σ_2 :

$$Z = \sum ... \times e^{K(\sigma_1\sigma_2 + \sigma_2\sigma_3)} \times ... . \tag{B.2}$$

The summation of the two possible configurations $+1$ and -1 of σ_2 gives:

$$Z = \sum ... \times \left[e^{K(\sigma_1+\sigma_3)} + e^{-K(\sigma_1+\sigma_3)}\right] \times e^{K(\sigma_3\sigma_4+\sigma_4\sigma_5)} \times ... . \tag{B.3}$$

A similar summation is performed over all other spins with even indices, so that only the sum over the odd indices remains. Now we have obtained a sum over terms of the form

$$... \times \left[e^{K(\sigma_1+\sigma_3)} + e^{-K(\sigma_1+\sigma_3)}\right] \times ... . \tag{B.4}$$

We want to find a function $f(K)$ and a new coupling strength K' relating this form to the original form:

$$e^{K(\sigma_1+\sigma_3)} + e^{-K(\sigma_1+\sigma_3)} = f(K)e^{K'(\sigma_1\sigma_3)}. \tag{B.5}$$

The solutions are

$$K' = \frac{1}{2}\ln\cosh(2K) \tag{B.6}$$

$$f(K) = 2\cosh^{\frac{1}{2}}(2K). \tag{B.7}$$

Therefore, we can write the partition function as:

$$Z = \sum ... \times f(K)e^{K'(\sigma_1\sigma_3)} \times ... . \tag{B.8}$$

It is now clear that equations B.6 and B.7 relate a system with N spins and coupling constant K to a system with $N/2$ spins and coupling constant K'. Given the partition function for one particular system, the partition function for another system can be recursively calculated with these equations. We define a reduced partition function ξ which does not depend on N by $\ln Z = \xi N$. The recursion relation for ξ is:

$$\xi(K') = 2\xi(K) - ln\left[\cosh^{\frac{1}{2}}(2K)\right]. \tag{B.9}$$

Since with each iteration more individual spins are combined into one, the assumption is that each iteration brings us closer to the "true" macroscopic behavior of the system. Using Eq. B.6, the value of K decreases with each iteration. In terms of renormalization group terminology, the *renormalization flow* is one-directional and the only *fixed point* is at 0.

Having demonstrated the mechanism of rescaling a system, we now want to apply the renormalization group to phase transitions. Since the 1D Ising model does not exhibit a phase transition, we turn to the 2D model.

In the 2D Ising model, each spin has 4 nearest neighbors with which it interacts. Following a similar course as in the 1D calculations, summation over half of the spins is performed:

$$Z = \sum ... \times \left[e^{K(\sigma_1\sigma_2\sigma_3\sigma_4)} + e^{-K(\sigma_1\sigma_2\sigma_3\sigma_4)}\right] \times ... . \tag{B.10}$$

We would like to relate this new summation to the old form like we did in the 1D model (Eq. B.6, B.6 and B.8). However, the form of the partition function is more complicated:

$$Z = f(K)^{\frac{1}{2}} \sum \exp\left(K_1 \sum_{nn} \sigma_p\sigma_q + K_2 \sum_{nnn} \sigma_p\sigma_q + K_3 \sum_{square} \sigma_p\sigma_q\sigma_r\sigma_s\right), \tag{B.11}$$

with *nn* denoting summation over nearest neighbors, *nnn* over next nearest neighbors, and *square* around the respective square. $f(K)$, K_1 , K_2 and K_3 are all functions of K. The decisive difference between Eq. B.8 and Eq. B.11 is that in the 2D case, contributions from next-nearest neighbors (K_2) and even farther away (K_3) are taken into account. In order to obtain the same recursive relations as in the 1D case, it is necessary to make an approximation. This can be done by setting $K_3 = 0$ and $K_2 = 0$ and replacing K_1 by $K' = K_1 + K_2$. With this method, we obtain the recursion relations:

$$K' = \frac{3}{8}\ln\cosh(4K) \tag{B.12}$$

$$\xi(K') = 2\xi(K) - \ln\left[\cosh^{\frac{1}{2}}(2K)\cosh^{\frac{1}{8}}(4K)\right]. \tag{B.13}$$

In the 1D case the renormalization flow was one-directional, *i.e.*, independent of the start value of K, the iterations would always yield a decrease. In the 2D case the direction of the flow depends on the starting point. Above a critical point K_C, the value of K will continually increase to infinity. Below K_C, K will continually decrease towards 0. This means the renormalization flow can have two directions, and there are three fixed points: 0, K_C and infinity. Remembering that $K = \frac{J}{k_B T}$, we can identify $K \to \infty$ as $J \to \infty$, i.e. the coupling strength becomes large and the system is in an ordered phase. Conversely, $K \to 0$ ($J \to 0$) can be identified as a disordered phase. K_C gives the critical ratio of coupling strength versus temperature of the transition between the two phases. Furthermore, because the energy of the system can be calculated from Z as $E = k_B T \ln Z$ and the specific heat is $c_V = dE/dT$, it is possible to calculate the singularity in c_V which is typical for second-order phase transitions. One obtains by expansion around the transition:

$$c_V \propto |1 - \frac{T}{T_C}|^{-\alpha}, \tag{B.14}$$

with the critical exponent

$$\alpha = 2 - \frac{\ln 2}{\ln\left[\left(\frac{dK'}{dK}\right)_{K=K_C}\right]}. \tag{B.15}$$

The renormalization group is often used in particle physics, where it is investigated how a system changes with a change in the energy (or length) scale. In a general form, the renormalization allows to compute the strength of a coupling parameter g at a scale μ from the value of g at some other scale M using a function G and a constant d:

$$g(\mu) = G^{-1}\left[\left(\frac{\mu}{M}\right)^d G\left(g(M)\right)\right]. \tag{B.16}$$

One important quantity is the beta function, which gives the differential change of the coupling strength with scale:

$$\beta = \frac{\partial g}{\partial \ln \mu}. \tag{B.17}$$

The renormalization group is usually not a true group in the mathematical sense, because in many cases information is lost when going from a system of many constitutents to a system of fewer constitutents and therefore the transformation is not reversible.

Any sufficiently advanced technology
is indistinguishable from magic.
Arthur C. Clarke

C DILUTION REFRIGERATOR

Since the superconducting transition of the 2DEL at the $LaAlO_3$–$SrTiO_3$ interface occurs at approximately 300 mK, it is necessary to use a dilution refrigerator to cool the sample to millikelvin temperatures.

The dilution refrigerator utilizes an anomaly in the phase diagram of liquid Helium isotopes: Below 870 mK, a mixture of the two stable isotopes ^{4}He and ^{3}He will spontaneously separate into two phases by an endothermic process, one of which is predominantly composed of ^{4}He and one consisting mostly of ^{3}He.

The principle of operation of a dilution refrigerator is sketched in Fig. C.1. Beginning from the top left, a mixture of ^{3}He and ^{4}He is pre-cooled by heat exchange with a 1K-Pot. This is a reservoir of ^{4}He, which is pumped to reduce the pressure and correspondingly also to depress the boiling point. Using this method, temperatures as low as approximately 1 K can be reached.

The mixture which has been cooled and liquefied in this manner is cooled further by heat exchange with the cold mixture flowing upwards from the mixing chamber. In this way a temperature below the phase separation threshold at 870 mK can be reached. Therefore, in the mixing chamber the mixture separates into a ^{3}He-rich phase and a ^{4}He-rich phase. ^{3}He transfers spontaneously into the ^{4}He-rich phase, absorbing energy from the surroundings and thereby supplying cooling power. To sustain the flow, the ^{4}He-rich phase is pumped to the still where the ^{3}He is boiled off, ensuring that the ^{4}He-rich phase remains dilute in ^{3}He. The ^{3}He is then re-liquefied and supplied back to the circulation.

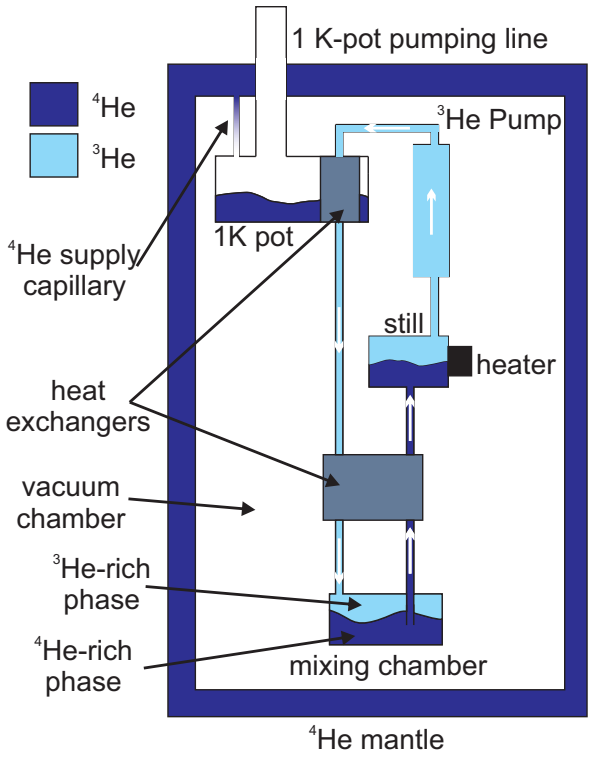

Figure C.1: Technical sketch of a dilution refrigerator. For explanation of the components and operation, see text.

Il me semble que la perfection soit atteinte non quand il n'y a plus rien à ajouter, mais quand il n'y a plus rien à retrancher.

Antoine de Saint-Exupéry

D MULTIBAND FITTING

In order to gain quantitative information on the charge carriers and mobilities in the separate bands of a multiband conductor, different model curves can be fitted to Hall and magnetoresistance data from the conductor. These models will be described below. Before any fitting was performed, the Hall data was anti-symmetrized and the conductivity data was symmetrized to remove spurious contributions of the longitudinal conductivity to the Hall conductivity and vice-versa. The measured resistance is converted to sheet resistance by a geometrical factor which depends on the position of the voltage probes. Both in the transistor-Hall-bar and in the superconducting transistor sample designs, the width of the voltage probes is comparable to their longitudinal separation, which causes an uncertainty in the conversion factor.

Fitting of the models to the curve was performed using MATLAB. The complicated structure of the fit may generate local minima leading to undesired fit results when using standard gradient-search methods. Therefore, the genetic algorithm fitting function `ga` was used to obtain the global optimum of the fit independent of initial guess values. At magnetic fields around zero, additional effects influence the magnetoresistance and Hall signal: Since the $LaAlO_3$–$SrTiO_3$ interface hosts ferromagnetic moments, a Hall offset around zero field due to the anomalous Hall effect has to be considered. Because of the spin-orbit coupling of the interface electrons, the magnetoresistance around zero field is reduced due to weak antilocalization. Finally, in superconducting samples the resistance vanishes at low magnetic fields. To exclude interference of these effects with the fit results, only datapoints with $|B| > 1$ T were considered for the fit.

D.1 Fitting of the conductivities

For this fitting procedure, described in Ref. [206], the 2x2 resistance tensor has to be inverted to obtain the longitudinal and Hall conductivities G_{xx} and G_{xy} from the measured resistivities R_{xx} and R_{xy}:

$$G_{xx} = \frac{R_{xx}}{R_{xx}^2 + R_{xy}^2} \tag{D.1}$$

and

$$G_{xy} = -\frac{R_{xy}}{R_{xx}^2 + R_{xy}^2}. \tag{D.2}$$

Since the total conductivity is the sum of the individual conductivities, they can be expressed in terms of the mobilities μ_i and carrier densities n_i and as a function of magnetic field B as:

$$G_{xx} = e\left(\frac{n_1\mu_1}{1+\mu_1^2B^2} + \frac{n_2\mu_2}{1+\mu_2^2B^2}\right), \tag{D.3}$$

$$G_{xy} = eB\left(\frac{n_1\mu_1^2}{1+\mu_1^2B^2} + \frac{n_2\mu_2^2}{1+\mu_2^2B^2}\right). \tag{D.4}$$

In order to reduce the number of free parameters for the fit, two constants are introduced:

$$C_1 = G_{xx}(B=0) = e\left(n_1\mu_1 + n_2\mu_2\right), \tag{D.5}$$

$$C_2 = \lim_{B\to 0}\frac{G_{xy}(B)}{B} = e\left(n_1\mu_1^2 + n_2\mu_2^2\right). \tag{D.6}$$

Which allow to eliminate the carrier densities n_i from the equations for the conductivities, effectively reducing the four-parameter fit to a two-parameter fit. The conductivities in terms of C_1 and C_2 are:

$$G_{xx}(B) = \frac{1}{\mu_2-\mu_1}\left(\frac{C_1\mu_2 - C_2}{1+\mu_1^2B^2} - \frac{C_1\mu_1 - C_2}{1+\mu_2^2B^2}\right), \tag{D.7}$$

$$G_{xy}(B) = B\left(\frac{C_1\mu_1 - C_2}{(\mu_1/\mu_2 - 1)\left(1+\mu_2^2B^2\right)} + \frac{C_1\mu_2 - C2}{(\mu_2/\mu_1 - 1)\left(1+\mu_1^2B^2\right)}\right). \tag{D.8}$$

Before the fitting, the constants C_1 and C_2 are calculated from the data. Then, the models for the longitudinal and transverse conductivities are fitted to the respective data simultaneously.

Due to the reduced number of fitting parameters, this method converges better than a full fit of the resistivity with four parameters. For curves with many datapoints, the necessary matrix inversion from measured resistances to conductivities can be computationally costly, but this is usually more than compensated by the reduction of fit parameters.

D.2 Fitting of the resistances

The equations for fitting resistances in a multiband scenario are obtained by summing the conductivities of the individual bands and then inverting the resulting conductivity tensor [207]. In terms of mobilities and sheet carrier densities they are given as:

$$R_{xx} = \frac{n_1\mu_1 + n_2\mu_2 + \left(n_2\mu_2\mu_1^2 + n_1\mu_1\mu_2^2\right)B^2}{\left(n_1\mu_1 + n_2\mu_2\right)^2 + \left(n_1+n_2\right)^2\mu_1^2\mu_2^2B^2} \tag{D.9}$$

$$R_{xy} = B\cdot\frac{n_1\mu_1^2 + n_2\mu_2^2 + \left(n_1+n_2\right)\mu_1^2\mu_2^2H^2}{\left(n_1\mu_1 + n_2\mu_2\right)^2 + \left(n_1+n_2\right)^2\mu_1\mu_2^2H^2}, \tag{D.10}$$

for the longitudinal resistance R_{xx} and the transverse resistance R_{xy}, respectively. These models are then fitted to the measured longitudinal and transverse resistance data. For better performance, the Hall coefficient $R_H = R_{xy}/B$ is fitted instead of the Hall resistance. An exemplary plot of this fitting procedure is shown in Fig. D.2.

The main disadvantage of this fitting procedure is that there are four parameters to be fitted, which makes it computationally very costly and leads to poor convergence.

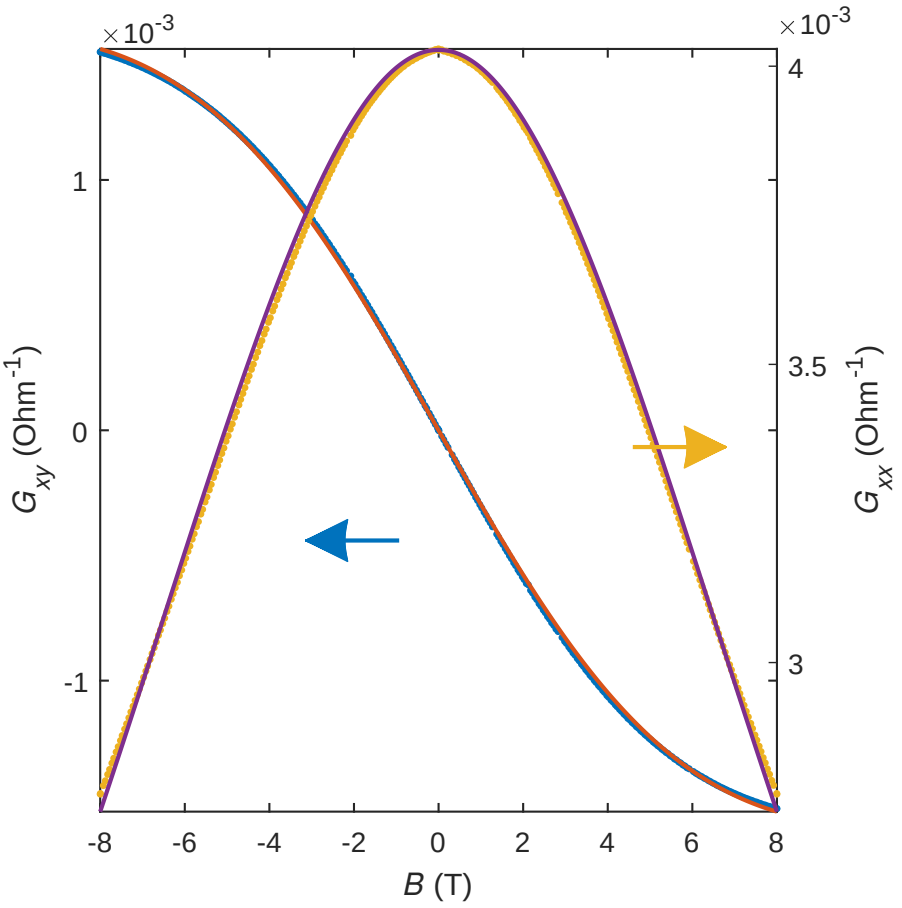

Figure D.1: Illustration of the procedure employed to extract multiple carrier densities from simultaneous fits to the Hall and magnetoconductance data described in section D.1. The fit to the curves yields good agreement with the data. Data from sample 053 for 0 GPa.

D.3 Fitting of the Hall curve

The simplest approach to extract the carrier densities from Hall measurements is to fit the Hall curve directly, as described, *e.g.*, in [208]. In the case of two bands, the two separate conductivities can be extracted as follows: One line is fitted to the Hall curve at low magnetic fields, and the carrier density of band 1 is calculated from the slope as $n_1 = -(e\Delta R_{xx}/\Delta B)^{-1}$. The slope at high fields (ideally $B \to \infty$) then gives the sum of the two carrier densities $n_1 + n_2 = -(e\Delta R_{xx}/\Delta B)^{-1}$, so that n_2 can be obtained by subtraction. This procedure is illustrated in Fig. D.3. In addition, the offset due to the anomalous Hall effect [209] can be obtained from the difference between the two lines at positive and negative low field.

The crucial advantages of this fitting procedure are that both fits are simple linear regressions and that the two fit parameters are independent instead of interdependent as in the other methods. This means that the fit converges reliably and that its goodness can be easily judged with the naked eye. In addition, the fit can be performed directly on the (antisymmetrized) Hall data without pre-processing. Finally, since the longitudinal resistance is not considered, the geometrical factor for sheet conversion cannot induce errors. A disadvantage of this method are that it does not give the mobilities of the carriers and an additional error is introduced because

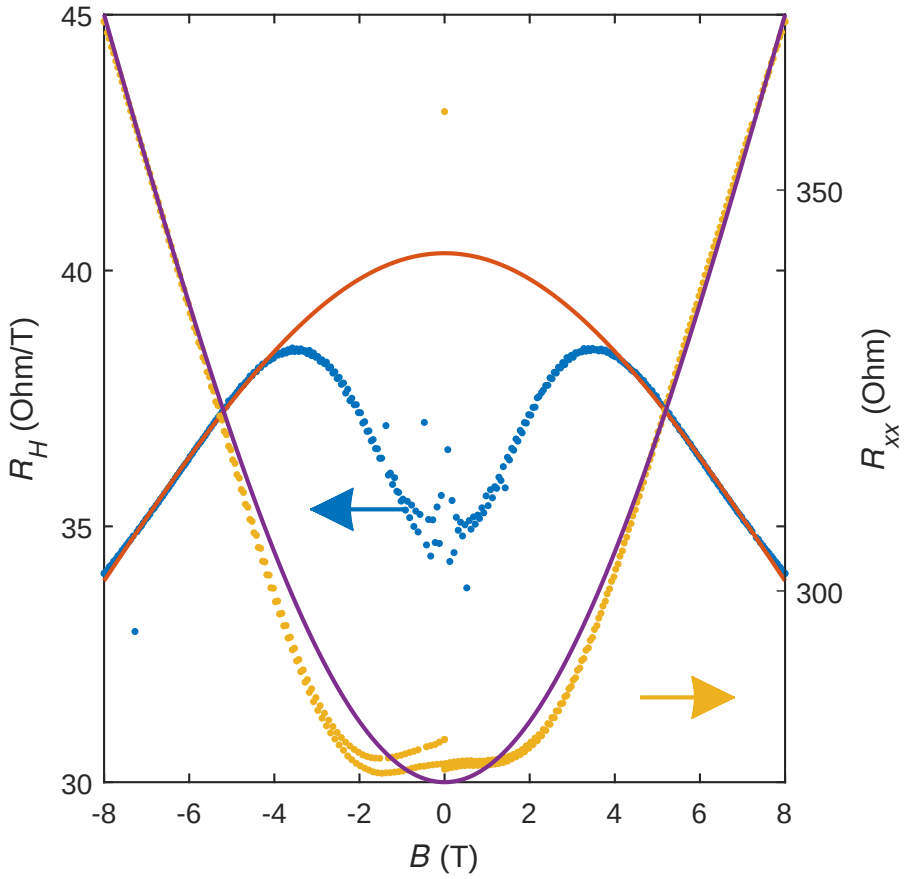

Figure D.2: Illustration of the procedure employed to extract multiple carrier densities from simultaneous fits to the Hall and magnetoresistance data described in section D.2. The fit to the curves for ($|B|$ >6 T) yields good agreement with the data, whereas at low field a clear divergence is visible. Data from sample 070 for $V_{\mathrm{BG}} = 40\,\mathrm{V}$.

the fit of the second band is not performed at $B = \pm\infty$, but at high but finite B. Furthermore, if one of the bands has very low mobility, its signature in the Hall data may not be detectable.

D.4 Discussion

The fitting methods presented in this chapter can only be applied reliably if the underlying data shows a clear multiband signature, with clearly differing slopes in the Hall curves. Otherwise it is possible that other physical mechanisms which can also lead to changes in the slope of the Hall curve, for example the anomalous Hall effect, are interpreted as multiband signatures. In any case, a consistency check of the results is always necessary because the fitting of the resistivities and conductivities can yield unwanted local minima of the fit curve. As an example, in Fig. D.4, two different fits to the magnetoresistance and Hall data from sample 053 measured at 4 K and 0 GPa are shown. The first fit (Fig. D.4 (a)) yields two bands of approximately the same carrier density, but different signs of the charge carriers. The second fit (Fig. D.4 (a)) yields one band with very high carrier density and very low mobility and another band with normal $LaAlO_3$–$SrTiO_3$ carrier density and mobility, but both with charge carriers of

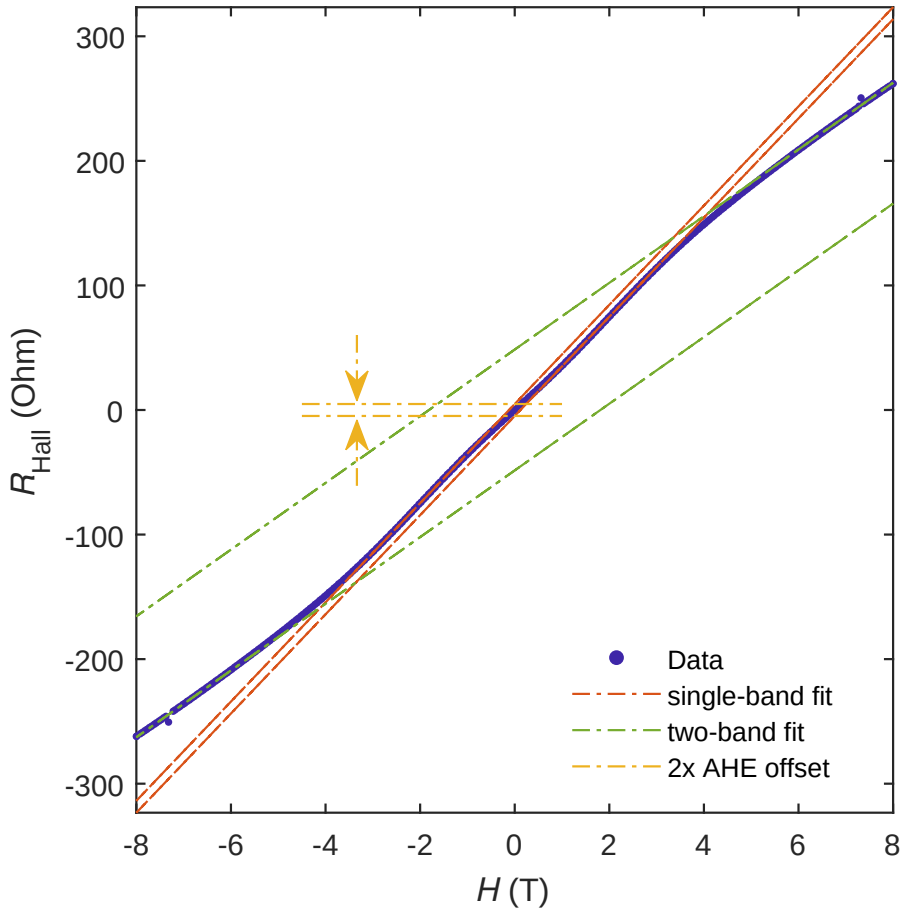

Figure D.3: Illustration of the procedure employed to extract multiple carrier densities in the presence of the anomalous Hall effect described in section D.3. After antisymmetrization, lines are fitted to the linear regions of the Hall curve. The slope of the linear region at intermediate magnetic fields ($1\,\mathrm{T} < |B| < 2.5\,\mathrm{T}$) yields the carrier density of the majority band. The slope of the linear region at high fields ($|B| > 6\,\mathrm{T}$) yields the total carrier density, and, by subtraction, the carrier density of the minority band. The offset between the two inner fits corresponds to the strength of the anomalous Hall effect. Data from sample 070 for $V_{\mathrm{BG}} = 50\,\mathrm{V}$.

the same sign. Even though the results from the two fits are very different from one another, they both yield curves which model the data reasonably well in the relevant high-field region. This comparison clearly shows that fit results from such multiband fitting routines have to be treated with care in order not to mistake local minima of the fit for the true result. This can be particularly complicated when the multiband signature is weak (in the case shown here the Hall constant varies only by about 1 %) and obscured by additional effects.

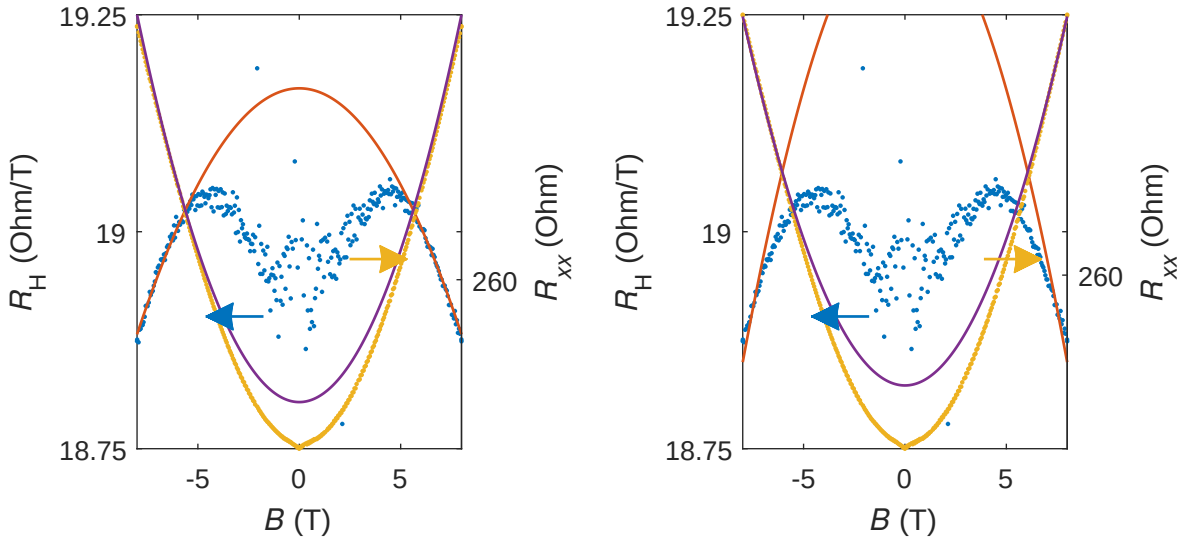

Figure D.4: Comparison of two fits to the magnetoresistance and Hall data from sample 053 measured at 4 K and 0 GPa. (a) Fit with result n_1=2.100 $\times$ 10^{13} cm^{-1}, n_2=−5.015 $\times$ 10^{13} cm^{-1}, $mu_1 = 960\,\mathrm{cm}^2\,\mathrm{V}^{-1}\,\mathrm{s}$, $mu_2 = -93\,\mathrm{cm}^2\,\mathrm{V}^{-1}\,\mathrm{s}$. (b) Fit with result n_1=1.700 $\times$ 10^{20} cm^{-1}, n_2=1.995 $\times$ 10^{13} cm^{-1}, $mu_1 = 3.1 \times 10^{-9}\,\mathrm{cm}^2\,\mathrm{V}^{-1}\,\mathrm{s}$, $mu_2 = 975\,\mathrm{cm}^2\,\mathrm{V}^{-1}\,\mathrm{s}$.

LIST OF SAMPLES

E

Table E.1: A list of all samples grown during the work described in this thesis. Sample design and growth parameters are specified. For the electrical properties of non-patterned samples, refer to table 6.1. $LaAlO_3$ Deposition temperature for all samples was 800 °C, except for sample 030 for which $LaAlO_3$ deposition temperature was 750 °C. The sample designs are described in section 3.2.

Sample	Design	u.c. $LaAlO_3$	u.c. $BaTiO_3$	p_{O_2} (mbar)	F (J cm^{-2})
001	circular junction	4	0	8×10^{-5}	0.8
002	circular junction	5	0	8.3×10^{-5}	0.8
003	circular junction	4	0	8×10^{-5}	0.8
004	circular junction	8	0	8×10^{-5}	0.8
005	circular junction	4	0	8×10^{-5}	0.8
006	no patterning	4	0	8×10^{-5}	0.8
007	circular junction	5	0	8×10^{-5}	0.8
008	circular junction	4	0	8×10^{-5}	0.8
009	circular junction	4	0	8×10^{-5}	0.8
010	circular junction	4	0	7.8×10^{-5}	0.8
011	circular junction	4	0	8.1×10^{-5}	0.8
012	circular junction	4	0	8.5×10^{-5}	0.8
013	transistor	2	0	8.1×10^{-5}	0.8
014	transistor	2	0	8.1×10^{-5}	0.8
015	test for deposition rate	19	0	8.0×10^{-5}	0.8
016	test for deposition rate	27	0	8.0×10^{-5}	0.8
017	circular junction	5	0	7.9×10^{-5}	0.8
018	circular junction	4	0	8.1×10^{-5}	0.8
019	circular junction	4	0	8.1×10^{-4}	1.2
020	circular junction	3	0	7.8×10^{-4}	1.2
021	circular junction	4	0	8×10^{-4}	1.2
022	circular junction	3	0	8.1×10^{-4}	1.2
023	transistor	5	50	7.8×10^{-4}	1.2
024	transistor	5	10	7.9×10^{-4}	1.2
025	circular junction	4	0	7.8×10^{-4}	1.2
026	circular junction	4	0	4×10^{-4}	1
027	circular junction	4	0	4×10^{-4}	1

Table E.1: (continued)

Sample	Design	u.c. $LaAlO_3$	u.c. $BaTiO_3$	p_{O_2} (mbar)	F ($J\,cm^{-2}$)
028	transistor	5	10	8.2×10^{-4}	1.2
029	transistor	5	10	8.2×10^{-4}	1.2
030	circular junction	4	0	4×10^{-4}	1.2
031	circular junction	4	0	8×10^{-5}	0.8
032	circular junction	4	0	7.9×10^{-5}	1
033	circular junction	4	0	3.7×10^{-4}	0.8
034	circular junction	N/A	0	8×10^{-5}	0.8
035	circular junction	4	0	2.0×10^{-4}	1
036	circular junction	4	0	8.2×10^{-4}	0.8
037	circular junction	4	0	7.9×10^{-4}	0.8
038	no growth because of plasma cleaner contamination				
039	no growth because of plasma cleaner contamination				
040	patterned junction	4	0	1.9×10^{-4}	1
041	patterned junction	5	10	2×10^{-4}	1
042	patterned junction	4	0	2×10^{-4}	1
043	patterned junction	6	20	1.91×10^{-4}	1
044	patterned junction	4	0	2.1×10^{-4}	1
045	patterned junction	4	0	2×10^{-4}	1
046	new patterned junction	4	0	2×10^{-4}	1
047	transistor-Hall	6	20	1.9×10^{-4}	1
048	new patterned junction	4	0	8.2×10^{-5}	0.8
049	transistor-Hall	6	20	8×10^{-5}	0.8
050	new patterned junction	4	0	2.1×10^{-4}	1
051	transistor-Hall	6	20	7.8×10^{-5}	0.8
052	new patterned junction	4	0	8.0×10^{-5}	0.8
053	transistor-Hall	6	20	7.7×10^{-5}	0.8
054	new patterned junction	4	0	8.1×10^{-5}	0.8
055	new patterned junction	4	0	8.2×10^{-5}	0.8
056	transistor-Hall	5	20	4.1×10^{-5}	0.8
057	transistor-Hall	5	20	2.1×10^{-5}	0.8
058	Vdp+Gold	4	0	8.1×10^{-5}	0.8
059	Vdp+Gold	4	0	2.0×10^{-4}	1
060	Vdp+Gold	4	0	8.6×10^{-5}	0.8
061	Vdp+Gold	4	0	2×10^{-4}	1
062	Vdp+Gold	4	0	2.1×10^{-4}	0.8
063	Vdp+Gold	4	0	8×10^{-5}	1
064	Vdp+Gold	6	0	8.1×10^{-5}	0.9
065	Vdp+Gold	6	0	2×10^{-4}	0.9
066	Vdp+Gold	5	0	2×10^{-4}	0.9
067	Vdp+Gold	5	0	7.9×10^{-4}	0.9
068	SC Transistor	6	20	8×10^{-5}	0.8

Table E.1: (continued)

Sample	Design	u.c. $LaAlO_3$	u.c. $BaTiO_3$	p_{O_2} (mbar)	F ($J\,cm^{-2}$)
069	SC Transistor	6	20	8×10^{-5}	0.8
070	SC Transistor	6	30	7.9×10^{-5}	0.8
071	SC Transistor	6	30	8.2×10^{-4}	1.2
072	SC Transistor	6	30	8×10^{-5}	0.8
073	SC Transistor	6	30	8.1×10^{-5}	0.8

Some books are to be tasted,
others to be swallowed,
and some to be chewed and digested.
Sir Francis Bacon

BIBLIOGRAPHY

[1] J. F. Schooley and W. R. Hosler. "Superconductivity in Semiconducting $SrTiO_3$". *Phys. Rev. Lett.* **12** 17 (1964). DOI: 10.1103/PhysRevLett.12.474.

[2] J. G. Bednorz and K. A. Müller. "Possible High T_c Superconductivity in the Ba — La — Cu — O System". **193** (1986), pp. 267–271. DOI: 10.1007/978-94-011-1622-0_32.

[3] J. R. Schrieffer and J. S. Brooks. *Handbook of High-Temperature Superconductivity*. Berlin, Heidelberg: Springer, 2007.

[4] J. Van Santen and G. Jonker. "Electrical conductivity of ferromagnetic compounds of manganese with perovskite structure". *Physica* **16** 3 (1950), pp. 337–349. DOI: 10.1016/0031-8914(50)90033-4.

[5] E. Dagotto. *Nanoscale Phase Separation and Colossal Magnetoresistance*. Berlin, Heidelberg: Springer, 2003.

[6] K. Rabe, C. H. Ahn, and J.-M. Triscone. *Physics of Ferroelectrics*. Berlin, Heidelberg: Springer, 2007.

[7] I. Zutic, J. Fabian, and S. D. Sarma. "Spintronics: Fundamentals and applications". *Rev. Mod. Phys.* **76** 2 (2004), pp. 323–410. DOI: 10.1103/RevModPhys.76.323.

[8] V. K. Joshi. "Spintronics: A contemporary review of emerging electronics devices". *Eng. Sci. Technol. an Int. J.* **19** 3 (2016), pp. 1503–1513. DOI: 10.1016/j.jestch.2016.05.002.

[9] H. U. Habermeier. "Thin films of perovskite-type complex oxides". *Mater. Today* **10** 10 (2007), pp. 34–43. DOI: 10.1016/S1369-7021(07)70243-2.

[10] H. Kroemer. "Nobel lecture: Quasielectric fields and band offsets: Teaching electrons new tricks". *Rev. Mod. Phys.* **73** 3 (2001), pp. 783–793. DOI: 10.1103/RevModPhys.73.783.

[11] D. B. Haviland, Y. Liu, and A. M. Goldman. "Onset of superconductivity in the two-dimensional limit". *Phys. Rev. Lett.* **62** 18 (1989), pp. 2180–2183. DOI: 10.1103/PhysRevLett.62.2180.

[12] A. M. Goldman. "Superconductor-Insulator Transitions". *Int. J. Mod. Phys. B* **24** 20 (2010), pp. 4081–4101. DOI: 10.1142/S0217979210056451.

[13] Y. Saito, T. Nojima, and Y. Iwasa. "Highly crystalline 2D superconductors". *Nat. Rev. Mater.* **2** (2016), p. 16094. DOI: 10.1038/natrevmats.2016.94.

[14] A. Krämer and S. Doniach. "Superinsulator Phase of two-dimensional Superconductors". *Phys. Rev. Lett.* **81** 16 (1998), pp. 3523–3526.

[15] V. M. Vinokur, T. I. Baturina, M. V. Fistul, A. Y. Mironov, M. R. Baklanov, and C. Strunk. "Superinsulator and quantum synchronization." *Nature* **452** 7187 (2008), pp. 613–5. DOI: 10.1038/nature06837.

[16] T. I. Baturina and V. M. Vinokur. "Superinsulator–superconductor duality in two dimensions". *Ann. Phys.* **331** (2013), pp. 236–257. DOI: 10.1016/j.aop.2012.12.007.

[17] L. Benfatto, C. Castellani, and T. Giamarchi. "Broadening of the Berezinskii-Kosterlitz-Thouless superconducting transition by inhomogeneity and finite-size effects". *Phys. Rev. B* **80** 21 (2009), p. 214506. DOI: 10.1103/PhysRevB.80.214506.

[18] C. Richter. *Experimental Investigation of Electronic and Magnetic Properties of $LaAlO_3$ -$SrTiO_3$ Interfaces*. PhD thesis. 2012.

[19] I. Giaever. "Energy Gap in Superconductors Measured by Electron Tunneling". *Phys. Rev. Lett.* **5** 4 (1960), pp. 147–148. DOI: doi.org/10.1103/PhysRevLett.5.464.

[20] B. Förg, C. Richter, and J. Mannhart. "Field-effect devices utilizing $LaAlO_3$-$SrTiO_3$ interfaces". *Appl. Phys. Lett.* **100** 5 (2012), p. 053506. DOI: 10.1063/1.3682102.

[21] R. Jany, C. Richter, C. Woltmann, G. Pfanzelt, B. Förg, M. Rommel, T. Reindl, U. Waizmann, J. Weis, J. A. Mundy, D. A. Muller, H. Boschker, and J. Mannhart. "Monolithically integrated circuits from functional oxides". *Adv. Mater. Interfaces* (2014), p. 1300031. DOI: 10.1002/admi.201300031.

[22] C. Woltmann. *Oxidische FETs mit sub-100 nm Gatelänge*. PhD thesis. 2016.

[23] J. Zabaleta, V. S. Borisov, R. Wanke, H. O. Jeschke, S. C. Parks, B. Baum, A. Teker, T. Harada, K. Syassen, T. Kopp, N. Pavlenko, R. Valentí, and J. Mannhart. "Hydrostatic pressure response of an oxide-based two-dimensional electron system". *Phys. Rev. B* **93** 235117 (2016), p. 235117. DOI: 10.1103/PhysRevB.93.235117.

[24] P. Seiler, J. Zabaleta, R. Wanke, J. Mannhart, T. Kopp, and D. Braak. "The mechanism of spin-orbit coupling in a 2D oxide interface". *arXiv* (2016). DOI: arXiv:1609.0742.

[25] H. Boschker, C. Richter, E. Fillis-Tsirakis, C. W. Schneider, and J. Mannhart. "Electron-phonon Coupling and the Superconducting Phase Diagram of the $LaAlO_3$-$SrTiO_3$ Interface". *Sci. Rep.* **5** (2015), p. 12309. DOI: 10.1038/srep12309.

[26] A. Brinkman, M. Huijben, M. van Zalk, J. Huijben, U. Zeitler, J. C. Maan, W. G. van der Wiel, G. Rijnders, D. H. A. Blank, and H. Hilgenkamp. "Magnetic effects at the interface between non-magnetic oxides." *Nat. Mater.* **6** 7 (2007), p. 493. DOI: 10.1038/nmat1931.

[27] G. Berner, M. Sing, H. Fujiwara, A. Yasui, Y. Saitoh, A. Yamasaki, Y. Nishitani, A. Sekiyama, N. Pavlenko, T. Kopp, C. Richter, J. Mannhart, S. Suga, and R. Claessen. "Direct k -Space Mapping of the Electronic Structure in an Oxide-Oxide Interface". *Phys. Rev. Lett.* **110** 24 (2013), p. 247601. DOI: 10.1103/PhysRevLett.110.247601.

[28] H. Y. Hwang, Y. Iwasa, M. Kawasaki, B. Keimer, N. Nagaosa, and Y. Tokura. "Emergent phenomena at oxide interfaces." *Nat. Mater.* **11** 2 (2012), pp. 103–13. DOI: 10.1038/nmat3223.

[29] S. Gariglio, M. Gabay, and J.-M. M. Triscone. "Research Update: Conductivity and beyond at the $LaAlO_3/SrTiO_3$ interface". *APL Mater.* **4** 6 (2016), p. 060701. DOI: 10.1063/1.4953822.

[30] H. Boschker and J. Mannhart. "Quantum-Matter Heterostructures". *Annu. Rev. Condens. Matter Phys.* **8** (2017), pp. 145–64. DOI: 10.1146/annurev-conmatphys-031016-025404.

[31] O. N. Tufte and P. W. Chapman. "Electron Mobility in Semiconducting Strontium Titanate". *Phys. Rev.* **155** 1964 (1967), p. 796. DOI: 10.1103/PhysRev.155.796.

[32] T. Sakudo and H. Unoki. "Dielectric Properties of $SrTiO_3$ at Low Temperatures". *Phys. Rev. Lett.* **26** 14 (1971), pp. 851–853. DOI: 10.1103/PhysRevLett.26.851.

[33] A. Bhattacharya, M. Eblen-Zayas, N. E. Staley, W. H. Huber, and A. M. Goldman. "Micromachined $SrTiO_3$ single crystals as dielectrics for electrostatic doping of thin films". *Appl. Phys. Lett.* **85** 6 (2004), pp. 997–999. DOI: 10.1063/1.1777415.

[34] K. A. Müller and H. Burkard. "$SrTiO_3$: An intrinsic quantum paraelectric below 4 K". *Phys. Rev. B* **19** 7 (1979), pp. 3593–3602. DOI: 10.1103/PhysRevB.19.3593.

[35] J. Haeni, P. Irvin, W. Chang, R. Uecker, and P. Reiche. "Room-temperature ferroelectricity in strained $SrTiO_3$". *Nature* **430** (2004), pp. 583–586. DOI: 10.1038/nature02773.

[36] H. Uwe, T. Sakudo, and H. Yamaguchi. "Interband electronic Raman scattering in $SrTiO_3$". *Jpn. J. Appl. Phys.* **519** (1985). DOI: doi.org/10.7567/JJAPS.24S2.519.

[37] Y. Tokura and N. Nagaosa. "Orbital physics in transition-metal oxides". *Science* **288** (2000), p. 462. DOI: 10.1126/science.288.5465.462.

[38] L. F. Mattheiss. "Effect of the 110K Phase Transition on the $SrTiO_3$ Conduction Bands". *Phys. Rev. B* **6** 12 (1972), p. 4740. DOI: 10.1103/PhysRevB.6.4740.

[39] D. van der Marel, J. L. M. van Mechelen, and I. I. Mazin. "Common Fermi-liquid origin of T^2 resistivity and superconductivity in n -type $SrTiO_3$". *Phys. Rev. B* **84** 20 (2011), p. 205111. DOI: 10.1103/PhysRevB.84.205111.

[40] X. Lin, G. Bridoux, A. Gourgout, G. Seyfarth, S. Krämer, M. Nardone, B. Fauqué, and K. Behnia. "Critical Doping for the Onset of a Two-Band Superconducting Ground State in $SrTiO_{3-\delta}$". *Phys. Rev. Lett.* **112** 20 (2014), p. 207002. DOI: 10.1103/PhysRevLett.112.207002.

[41] J. G. Bednorz and K. A. Müller. "Perovskite-type oxides – the new approach to high-T_c superconductivity". *Rev. Mod. Phys.* **60** 3 (1988). DOI: 10.1002/anie.198807351.

[42] G. Binnig, A. Baratoff, H. E. Hoenig, and J. G. Bednorz. "Two-band superconductivity in Nb-Doped $SrTiO_3$". *Phys. Rev. Lett.* **45** 16 (1980), pp. 1352–1355. DOI: 10.1103/PhysRevLett.45.1352.

[43] M. Thiemann, M. H. Beutel, M. Dressel, N. R. Lee-Hone, D. M. Broun, E. Fillis-Tsirakis, H. Boschker, J. Mannhart, and M. Scheffler. "Single-gap superconductivity in $SrTiO_3$". *arXiv* (2017). DOI: arXiv:1703.04716.

[44] Y. Kozuka. *High Mobility Electrons and Two-Dimensional Superconductivity in $SrTiO_3$ Heterostructures*. PhD thesis. 2009.

[45] S.-G. G. Lim, S. Kriventsov, T. N. Jackson, J. H. Haeni, D. G. Schlom, A. M. Balbashov, R. Uecker, P. Reiche, J. L. Freeouf, and G. Lucovsky. "Dielectric functions and optical bandgaps of high- K dielectrics for metal-oxide-semiconductor field-effect transistors by far ultraviolet spectroscopic ellipsometry". *J. Appl. Phys.* **91** 7 (2002), pp. 4500–4505. DOI: 10.1063/1.1456246.

[46] R. Berktold. *Kapazitätsmessungen an Feldeffekttransistoren auf $LaAlO_3$-$SrTiO_3$-Basis*. PhD thesis. University of Stuttgart, 2017.

[47] J. Krupka, R. G. Geyer, M. Kuhn, and J. H. Hinken. "Dielectric properties of single crystals of Al_2O_3, $LaAlO_3$, $NdGaO_3$, $SrTiO_3$, and MgO at cryogenic temperatures". *IEEE Trans. Microw. Theory Tech.* **42** 10 (1994), pp. 1886–1890. DOI: 10.1109/22.320769.

[48] A. Ohtomo and H. Hwang. "A high-mobility electron gas at the $LaAlO_3$/$SrTiO_3$ heterointerface". *Nature* **427** January (2004), pp. 423–427. DOI: 10.1038/nature02308.

[49] S. Thiel, G. Hammerl, A. Schmehl, C. W. Schneider, and J. Mannhart. "Tunable Quasi-Two-Dimensional Electron Gases in Oxide Heterostructures". *Science* **313** 5795 (2006), pp. 1942–1945. DOI: 10.1126/science.1131091.

[50] M. Breitschaft, V. Tinkl, N. Pavlenko, S. Paetel, C. Richter, J. R. Kirtley, Y. C. Liao, G. Hammerl, V. Eyert, T. Kopp, and J. Mannhart. "Two-dimensional electron liquid state at $LaAlO_3$ -$SrTiO_3$ interfaces". *Phys. Rev. B* **81** 15 (2010), p. 153414. DOI: 10.1103/PhysRevB.81.153414.

[51] E. Maniv, M. B. Shalom, A. Ron, M. Mograbi, A. Palevski, M. Goldstein, and Y. Dagan. "Strong correlations elucidate the electronic structure and phase diagram of $LaAlO_3$/$SrTiO_3$ interface". *Nat. Commun.* **6** (2015), p. 8239. DOI: 10.1038/ncomms9239.

[52] Z. Zhong, A. Tóth, and K. Held. "Theory of spin-orbit coupling at $LaAlO_3$ /$SrTiO_3$ interfaces and $SrTiO_3$ surfaces". *Phys. Rev. B* **87** 16 (2013), p. 161102. DOI: 10.1103/PhysRevB.87.161102.

[53] M. Ben Shalom, M. Sachs, D. Rakhmilevitch, A. Palevski, and Y. Dagan. "Tuning Spin-Orbit Coupling and Superconductivity at the $SrTiO_3$ / $LaAlO_3$ Interface: A Magnetotransport Study". *Phys. Rev. Lett.* **104** (2010), p. 126802. DOI: 10.1103/PhysRevLett.104.126802.

[54] A. D. Caviglia, M. Gabay, S. Gariglio, N. Reyren, C. Cancellieri, and J.-M. Triscone. "Tunable Rashba spin-orbit interaction at oxide interfaces." *Phys. Rev. Lett.* **104** 12 (2010), p. 126803. DOI: 10.1103/PhysRevLett.104.126803.

[55] N. Reyren, S. Thiel, A. D. Caviglia, L. F. Kourkoutis, G. Hammerl, C. Richter, C. W. Schneider, T. Kopp, A.-S. Ruetschi, D. Jaccard, M. Gabay, D. A. Muller, J.-M. Triscone, and J. Mannhart. "Superconducting Interfaces Between Insulating Oxides". *Science* **317** 5842 (2007), pp. 1196–1199. DOI: 10.1126/science.1146006.

[56] A. D. Caviglia, S. Gariglio, N. Reyren, D. Jaccard, T. Schneider, M. Gabay, S. Thiel, G. Hammerl, J. Mannhart, and J.-M. Triscone. "Electric field control of the $LaAlO_3$ / $SrTiO_3$ interface ground state". *Nature* **456** (2008), p. 624. DOI: 10.1038/nature07576.

[57] C. Richter, H. Boschker, W. Dietsche, E. Fillis-Tsirakis, R. Jany, F. Loder, L. F. Kourkoutis, D. A. Muller, J. R. Kirtley, C. W. Schneider, and J. Mannhart. "Interface superconductor with gap behaviour like a high-temperature superconductor". *Nature* **502** 7472 (2013), pp. 528–531. DOI: 10.1038/nature12494.

[58] E. Fillis-Tsirakis, C. Richter, J. Mannhart, and H. Boschker. "Evidence for superconducting phase coherence in the metallic/insulating regime of the $LaAlO_3$ –$SrTiO_3$ interface electron system". *New J. Phys.* **18** 1 (2016), p. 013046. DOI: 10.1088/1367-2630/18/1/013046.

[59] L. Li, C. Richter, J. Mannhart, and R. C. Ashoori. "Coexistence of magnetic order and two-dimensional superconductivity at $LaAlO_3/SrTiO_3$ interfaces". *Nat. Phys.* **7** 10 (2011), pp. 762–766. DOI: 10.1038/nphys2080.

[60] J. A. Bert, B. Kalisky, C. Bell, M. Kim, Y. Hikita, H. Y. Hwang, and K. A. Moler. "Direct imaging of the coexistence of ferromagnetism and superconductivity at the $LaAlO_3/SrTiO_3$ interface". *Nat. Phys.* **7** 10 (2011), pp. 767–771. DOI: 10.1038/nphys2079.

[61] Z. S. Popović, S. Satpathy, and R. M. Martin. "Origin of the Two-Dimensional Electron Gas Carrier Density at the $LaAlO_3$ on $SrTiO_3$ Interface". *Phys. Rev. Lett.* **101** 25 (2008), p. 256801. DOI: 10.1103/PhysRevLett.101.256801.

[62] Ariando, X. Wang, G. Baskaran, Z. Q. Liu, J. Huijben, J. B. Yi, A. Annadi, A. R. Barman, A. Rusydi, S. Dhar, Y. P. Feng, J. Ding, H. Hilgenkamp, and T. Venkatesan. "Electronic phase separation at the $LaAlO_3/SrTiO_3$ interface." *Nat. Commun.* **2** (2011), p. 188. DOI: 10.1038/ncomms1192.

[63] M. Salluzzo, J. C. Cezar, N. B. Brookes, V. Bisogni, G. M. De Luca, C. Richter, S. Thiel, J. Mannhart, M. Huijben, A. Brinkman, G. Rijnders, and G. Ghiringhelli. "Orbital reconstruction and the two-dimensional electron gas at the $LaAlO_3/SrTiO_3$ interface". *Phys. Rev. Lett.* **102** 16 (2009), p. 166804. DOI: 10.1103/PhysRevLett.102.166804.

[64] A. Rubano, M. Fiebig, D. Paparo, A. Marino, D. Maccariello, U. Scotti di Uccio, F. Miletto Granozio, L. Marrucci, C. Richter, S. Paetel, and J. Mannhart. "Spectral and spatial distribution of polarization at the $LaAlO_3$/ $SrTiO_3$ interface". *Phys. Rev. B* **83** 15 (2011), p. 155405. DOI: 10.1103/PhysRevB.83.155405.

[65] A. Joshua, S. Pecker, J. Ruhman, E. Altman, and S. Ilani. "A universal critical density underlying the physics of electrons at the $LaAlO_3$ / $SrTiO_3$ interface". *Nat. Commun.* **3** (2012), p. 1129. DOI: 10.1038/ncomms2116.

[66] A. E. M. Smink, J. C. de Boer, M. P. Stehno, A. Brinkman, W. G. van der Wiel, and H. Hilgenkamp. "Gate-Tunable Band Structure of the $LaAlO_3$ /$SrTi_3$ interface". *Phys. Rev. Lett.* **118** 10 (2017), p. 106401. DOI: 10.1103/PhysRevLett.118.106401.

[67] M. Tinkham. *Introduction to Superconductivity*. Dover Publications, 2004.

[68] E. L. Wolf. *Principles of Electron Tunneling Spectroscopy*. 2nd ed. Oxford: Oxford University Press, 2011.

[69] A. Altland and B. Simons. *Condensed Matter Field Theory*. Cambridge, 2006.

[70] D. Packard. *Introduction to the Berezinskii-Kosterlitz-Thouless Transition*. Tech. rep. 2013, pp. 1–11.

[71] J. M. Kosterlitz and D. J. Thouless. "Long range order and metastability in two dimensional solids and superfluids". *J. Phys. C* **124** 5 (1972). DOI: 10.1088/0022-3719/5/11/002.

[72] J. M. Kosterlitz and D. J. Thouless. "Ordering, metastability and phase transitions in two-dimensional systems". *J. Phys. C* **6** (1973), pp. 1181–1203. DOI: 10.1088/0022-3719/6/7/010.

[73] V. L. Berezinskii. "Destruction of long-range order in one-dimensional and two- dimensional systems with a continuous symmetry group." *Sov. Phys. - JETP* **61** 3 (1971), pp. 1144–56.

[74] N. D. Mermin and H. Wagner. "Absence of ferromagnetism or antiferromagnetism in one- two- dimensional isotropic Heisenberg models". *Phys. Rev. Lett.* **17** 22 (1966), pp. 1133–1136.

[75] A. Goldman. "The Berezinskii-Kosterlitz-Thouless Transition in Superconductors". In: *40 Years Berezinskii-Kosterlitz-Thouless Theory*. Ed. by J. V. Jose. Singapore: World Scientific Publishing, 2013, p. 135.

[76] A. Widom and S. Badjou. "Quantum displacement-charge transitions in two-dimensional granular superconductors". *Phys. Rev. B* **37** 13 (1988), pp. 37–38.

[77] J. Mooij, B. V. Wees, L. Geerligs, and M. Peters. "Unbinding of charge-anticharge pairs in two-dimensional arrays of small tunnel junctions". *Phys. Rev. ...* **65** 5 (1990), pp. 645–648.

[78] R. Fazio and G. Schön. "Charges and Vortices in Josephson Junction Arrays". In: *40 Years Berezinskii-Kosterlitz-Thouless Theory*. Ed. by J. V. Jose. Singapore: World Scientific Publishing, 2013, p. 237.

[79] T. Baturina, A. Mironov, V. Vinokur, M. Baklanov, and C. Strunk. "Localized Superconductivity in the Quantum-Critical Region of the Disorder-Driven Superconductor-Insulator Transition in TiN Thin Films". *Phys. Rev. Lett.* **99** 25 (2007), p. 257003. DOI: 10.1103/PhysRevLett.99.257003.

[80] N. Poccia, T. I. Baturina, F. Coneri, C. G. Molenaar, R. X. Wang, G. Bianconi, A. Brinkman, H. Hilgenkamp, A. A. Golubov, and V. M. Vinokur. "Critical behavior at a dynamic vortex insulator-to-metal transition". *Science* **349** 6253 (2015), pp. 1202–1206. DOI: 10.1126/science.1260507.

[81] J. Bardeen and W. H. Brattain. "The Transistor, A Semi-Conductor Triode". *Phys. Rev.* (1948), pp. 230–231.

[82] S. M. Sze and K. K. Ng. *Physics of Semiconductor Devices*. Hoboken, NJ: Wiley, 2007.

[83] M. Kawasaki, A. Ohtomo, T. Arakane, K. Takahashi, M. Yoshimoto, and H. Koinuma. "Atomic control of $SrTiO_3$ surface for perfect epitaxy of perovskite oxides". *Appl. Surf. Sci.* **107** (1996), pp. 102–106. DOI: 10.1016/S0169-4332(96)00512-0.

[84] G. Koster, B. L. Kropman, G. J. H. M. Rijnders, D. H. A. Blank, and H. Rogalla. "Quasi-ideal strontium titanate crystal surfaces through formation of strontium hydroxide". *Appl. Phys. Lett.* **73** 20 (1998), pp. 2920–2922. DOI: 10.1063/1.122630.

[85] H. M. Smith and A. F. Turner. "Vacuum Deposited Thin Films Using a Ruby Laser". *Appl. Opt.* **4** 1 (1965), pp. 147, 148. DOI: 10.1364/AO.4.000147.

[86] D. Dijkkamp, T. Venkatesan, X. D. Wu, S. A. Shaheen, N. Jisrawi, Y. H. Min-Lee, W. L. McLean, and M. Croft. "Preparation of Y-Ba-Cu oxide superconductor thin films using pulsed laser evaporation from high Tc bulk material". *Appl. Phys. Lett.* **51** 8 (1987), pp. 619–621. DOI: 10.1063/1.98366.

[87] C. W. Schneider and T. Lippert. "Laser ablation and thin film deposition". In: *Laser Processing of Materials: Fundamentals, Applications and Developments*. Berlin, Heidelberg: Springer, 2010, pp. 89–112.

[88] W. Braun. *Apllied RHEED*. Berlin, Heidelberg, New York: Springer, 1999.

[89] C. Woltmann, T. Harada, H. Boschker, V. Srot, P. a. van Aken, H. Klauk, and J. Mannhart. "Field-Effect Transistors with Submicrometer Gate Lengths Fabricated from $LaAlO_3$ - $SrTiO_3$ -Based Heterostructures". *Phys. Rev. Appl.* **4** 6 (2015), p. 064003. DOI: 10.1103/PhysRevApplied.4.064003.

[90] J. Zabaleta, S. C. Parks, B. Baum, A. Teker, K. Syassen, and J. Mannhart. "Electrical transport measurements of thin film samples under high hydrostatic pressure". *Rev. Sci. Instrum.* **88** (2017), p. 033901. DOI: 10.1063/1.4977221.

[91] D. Fuchs, A. Sleem, R. Schäfer, and A. Zaitsev. "Incipient localization of charge carriers in the two-dimensional electron system in $LaAlO_3/SrTiO_3$ under hydrostatic pressure". *Phys. Rev. B* **155313** (2015), pp. 1–7. DOI: 10.1103/PhysRevB.92.155313.

[92] Z. Rang, M. I. Nathan, P. P. Ruden, R. Chesterfield, and C. D. Frisbie. "Hydrostatic-pressure dependence of organic thin-film transistor current versus voltage characteristics". *Appl. Phys. Lett.* **85** 23 (2004), pp. 5760–5762. DOI: 10.1063/1.1829388.

[93] Y. Liu, P. P. Ruden, J. Xie, H. Morkoc, and K. A. Son. "Effect of hydrostatic pressure on the dc characteristics of AlGaN/GaN heterojunction field effect transistors". *Appl. Phys. Lett.* **88** 1 (2006), p. 013505. DOI: 10.1063/1.2161812.

[94] Y. Chen, F. Ke, P. Ci, C. Ko, T. Park, S. Saremi, H. Liu, Y. Lee, J. Suh, L. W. Martin, J. W. Ager, B. Chen, and J. Wu. "Pressurizing field-effect transistors of few-layer MoS2 in a diamond anvil cell". *Nano Lett.* **17** (2016), pp. 194–199. DOI: 10.1021/acs.nanolett.6b03785.

[95] J. P. Eisenstein, L. N. Pfeiffer, and K. W. West. "Independently contacted two-dimensional electron systems in double quantum wells". *Appl. Phys. Lett.* **57** 22 (1990), pp. 2324–2326. DOI: 10.1063/1.103882.

[96] G. Karapetrov, M. Iavarone, W. K. Kwok, G. W. Crabtree, and D. G. Hinks. "Scanning Tunneling Spectroscopy in MgB_2". *Phys. Rev. Lett.* **86** 19 (2001), pp. 4374–4377. DOI: 10.1103/PhysRevLett.86.4374.

[97] M. Iavarone, G. Karapetrov, A. E. Koshelev, W. K. Kwok, G. W. Crabtree, D. G. Hinks, W. N. Kang, E.-M. Choi, H. J. Kim, H.-J. Kim, and S. I. Lee. "Two-Band Superconductivity in MgB_2". *Phys. Rev. Lett.* **89** 18 (2002), p. 187002. DOI: 10.1103/PhysRevLett.89.187002.

[98] J. M. Edge and A. V. Balatsky. "Upper critical field as a probe for multiband superconductivity in bulk and interfacial STO". *J. Supercond. Nov. Magn.* **28** 8 (2015), pp. 2373–2384. DOI: 10.1007/s10948-015-3052-3.

[99] G. Zhang, M. Zeleznik, J. Vanacken, P. W. May, and V. V. Moshchalkov. "Metal–Bosonic Insulator–Superconductor Transition in Boron-Doped Granular Diamond". *Phys. Rev. Lett.* **110** 7 (2013), p. 077001. DOI: 10.1103/PhysRevLett.110.077001.

[100] A. Gurevich. "Enhancement of the upper critical field by nonmagnetic impurities in dirty two-gap superconductors". *Phys. Rev. B* **67** 18 (2003), p. 184515. DOI: 10.1103/PhysRevB.67.184515.

[101] D. R. Tilley. "The Ginzburg-Landau equations for pure two band superconductors". *Proc. Phys. Soc.* **84** (1964), p. 573. DOI: 10.1088/0370-1328/84/4/313.

[102] V. A. Moskalenko, M. E. Palistrant, and V. M. Vakalyuk. "High-Temperature Superconductivity Based on Account of the Electron Band Spectrum Peculiarities". *Usp. Fiz. Nauk.* **161** 155 (1991).

[103] E. Helfand and N. R. Werthamer. "Temperature and Purity Dependence of the Superconducting Critical Field, H_{c2}". *Phys. Rev.* **147** 1 (1966), pp. 288–294. DOI: 10.1103/PhysRev.147.288.

[104] Y. B. Kim, C. F. Hempstead, and A. R. Strnad. "Flux-Flow Resistance in Type-II Superconductors". *Phys. Rev.* **139** 1962 (1965). DOI: 10.1103/PhysRev.139.A1163.

[105] E. Fillis-Tsirakis. *Investigating Superconductivity by Tunneling Spectroscopy Using Oxide Heterostructures.* PhD thesis. Stuttgart, 2017.

[106] C. J. Gorter and H. Casimir. "On Supraconductivity I". *Physica* **1** (1934), pp. 306–320. DOI: 10.1103/PhysRev.52.1256.3.

[107] B. Mühlschlegel. "Die thermodynamischen Funktionen des Supraleiters". *Zeitschrift für Phys.* **155** 3 (1959), pp. 313–327. DOI: 10.1007/BF01332932.

[108] M. Tinkham. "Consequences of Fluxoid Quantization Transitions of Superconducting Films". *Phys. Rev.* **15** (1964), pp. 268–276. DOI: 10.1103/PhysRev.129.2413.

[109] P. G. de Gennes. *Superconductivity of Metals and Alloys.* Boulder, CO: Westview Press, 1999.

[110] D. W. Youngner and R. A. Klemm. "Theory of the upper critical field in layered superconductors". *Phys. Rev. B* **12** 9 (1980), p. 3890.

[111] R. M. Fernandes, J. T. Haraldsen, P. Wölfle, and A. V. Balatsky. "Two-band superconductivity in doped $SrTiO_3$ films and interfaces". *Phys. Rev. B* **87** 1 (2013), p. 014510. DOI: 10.1103/PhysRevB.87.014510.

[112] C. Bell, S. Harashima, Y. Kozuka, M. Kim, B. G. Kim, Y. Hikita, and H. Y. Hwang. "Dominant mobility modulation by the electric field effect at the $LaAlO_3/SrTiO3_3$ interface". *Phys. Rev. Lett.* **103** (2009), p. 226802. DOI: 10.1103/PhysRevLett.103.226802.

[113] D. Rakhmilevitch, I. Neder, M. B. Shalom, A. Tsukernik, M. Karpovski, Y. Dagan, and A. Palevski. "Anomalous response to gate voltage application in mesoscopic LaAlO 3/SrTiO3 devices". *Phys. Rev. B - Condens. Matter Mater. Phys.* **87** 12 (2013), pp. 1–5. DOI: 10.1103/PhysRevB.87.125409.

[114] F. Trier, G. E. D. K. Prawiroatmodjo, Z. Zhong, and N. Pryds. "Quantum Hall effect at the metallic interface between an oxide insulator and $SrTiO_3$". *arXiv* (2016), p. 59.

[115] A. Yazdani and A. Kapitulnik. "Superconducting-insulating transition in two-dimensional a-MoGe thin films". *Phys. Rev. Lett.* **74** 15 (1995), pp. 3037–3040.

[116] P. D. Eerkes, W. G. Van Der Wiel, and H. Hilgenkamp. "Modulation of conductance and superconductivity by top-gating in $LaAlO_3/SrTiO_3$ 2-dimensional electron systems". *Appl. Phys. Lett.* **103** 20 (2013), p. 201603. DOI: 10.1063/1.4829555.

[117] P. Eerkes. *Top-Gating of the two-dimensional electron gas at complex oxide interfaces.* PhD thesis. Twente, 2014.

[118] L. Kuerten, C. Richter, N. Mohanta, T. Kopp, A. Kampf, J. Mannhart, and H. Boschker. "In-gap features in superconducting $LaAlO_3$ -$SrTiO_3$ interfaces observed by tunneling spectroscopy". *Phys. Rev. B* **96** (2017), p. 014513. DOI: 10.1103/PhysRevB.96.014513.

[119] R. N. Hall, J. H. Racette, and H. Ehrenreich. "Direct observation of polarons and phonons during tunneling in group 3-5 semiconductor junctions". *Phys. Rev. Lett.* **4** 9 (1960), pp. 456–458. DOI: 10.1103/PhysRevLett.4.456.

[120] J. M. Rowell and W. L. McMillan. "Electron interference in a normal metal induced by superconducting contracts". *Phys. Rev. Lett.* **16** 11 (1966), pp. 453–456.

[121] B. L. Altshuler and A. G. Aronov. "Zero bias anomaly in tunnel resistance and electron-electron interaction". *Solid State Commun.* **30** (1979), pp. 115–117. DOI: 10.1016/0038-1098(79)90967-0.

[122] L. J. Buchholtz and G. Zwicknagl. "Identification of p-wave superconductors". *Phys. Rev. B* **23** 11 (1981), p. 5788. DOI: 10.1103/PhysRevB.23.5788.

[123] G. E. Blonder, M. Tinkham, and T. M. Klapwijk. "Transition from metallic to tunneling regimes in superconducting microconstrictions: Excess current, charge imbalance, and supercurrent conversion". *Phys. Rev. B* **25** 7 (1982), pp. 4515–4532. DOI: 10.1103/PhysRevB.25.4515.

[124] L. Alff, S. Kleefisch, U. Schoop, M. Zittarz, T. Kemen, T. Bauch, A. Marx, and R. Gross. "Andreev bound states in high temperature superconductors". *Eur. Phys. J. B* **438** (1998), pp. 423–438. DOI: 10.1007/s100510050463.

[125] S. Kashiwaya, Y. Tanaka, M. Koyanagi, and K. Kajimura. "Bound states in superconductors". *Jpn. J. Appl. Phys.* **34** (1995), pp. 4555–4558. DOI: 10.1143/JJAP.34.4555.

[126] S. Kashiwaya and Y. Tanaka. "Tunnelling effects on surface bound states in unconventional superconductors". *Reports Prog. Phys.* **63** 10 (2000), pp. 1641–1724. DOI: 10.1088/0034-4885/63/10/202.

[127] T. Löfwander. "Andreev bound states in high-T_c superconducting junctions". *Supercond. Sci. Technol.* **14** (2001), R53–R77. DOI: 10.1088/0953-2048/14/5/201.

[128] G. Deutscher. "Andreev–Saint-James reflections: A probe of cuprate superconductors". *Rev. Mod. Phys.* **77** (2005), pp. 109–135. DOI: 10.1103/RevModPhys.77.109.

[129] P. SanGiorgio, S. Reymond, M. R. Beasley, J. H. Kwon, and K. Char. "Anomalous double peak structure in superconductor/ferromagnet tunneling density of states." *Phys. Rev. Lett.* **100** 23 (2008), p. 237002. DOI: 10.1103/PhysRevLett.100.237002.

[130] J. Linder, A. Sudbø, T. Yokoyama, R. Grein, and M. Eschrig. "Signature of odd-frequency pairing correlations induced by a magnetic interface". *Phys. Rev. B* **81** 21 (2010), p. 214504. DOI: 10.1103/PhysRevB.81.214504.

[131] K. M. Boden, W. P. Pratt, and N. O. Birge. "Proximity-induced density-of-states oscillations in a superconductor/strong-ferromagnet system". *Phys. Rev. B* **84** 2 (2011), p. 020510. DOI: 10.1103/PhysRevB.84.020510.

[132] A. Di Bernardo, S. Diesch, Y. Gu, J. Linder, G. Divitini, C. Ducati, E. Scheer, M. G. Blamire, and J. W. A. Robinson. "Signature of magnetic-dependent gapless odd frequency states at superconductor/ferromagnet interfaces." *Nat. Commun.* **6** (2015), p. 8053. DOI: 10.1038/ncomms9053.

[133] A. Y. Kitaev. "Unpaired Majorana fermions in quantum wires". *Physics-Uspekhi* **171** 10 (2001), pp. 131–136. DOI: 10.1070/1063-7869/44/10S/S29.

[134] L. Fu and C. L. Kane. "Superconducting Proximity Effect and Majorana Fermions at the Surface of a Topological Insulator". *Phys. Rev. Lett.* **100** 9 (2008), p. 096407. DOI: 10.1103/PhysRevLett.100.096407.

[135] J. Alicea. "New directions in the pursuit of Majorana fermions in solid state systems." *Reports Prog. Phys.* **75** 7 (2012), p. 076501. DOI: 10.1088/0034-4885/75/7/076501.

[136] V. Mourik, K. Zuo, S. M. Frolov, S. R. Plissard, E. P. A. M. Bakkers, and L. P. Kouwenhoven. "Signatures of Majorana Fermions in Hybrid Superconductor-Semiconductor Nanowire Devices". *Science* **336** 6084 (2012), pp. 1003–1007. DOI: 10.1126/science.1222360.

[137] C. Beenakker. "Search for Majorana Fermions in Superconductors". *Annu. Rev. Condens. Matter Phys.* **4** 1 (2013), pp. 113–136. DOI: 10.1146/annurev-conmatphys-030212-184337.

[138] L. Yu. "Bound state in superconductors with paramagnetic impurities". *Acta Phys. Sin.* **21** 1 (1965), pp. 75–91. DOI: 10.7498/aps.21.75.

[139] H. Shiba. "Classical Spins in Superconductors". *Prog. Theor. Phys.* **40** 3 (1968), pp. 435–451. DOI: 10.1143/PTP.40.435.

[140] A. I. Rusinov. "On the theory of gapless superconductivity in alloys containing paramagnetic impurities". *Sov. Phys. JETP* **29** 6 (1969).

[141] J. Zittartz and E. Müller-Hartmann. "Theory of magnetic impurities in superconductors. I Exact Solution of the Nagaoka Equations". *Zeitschrift für Phys.* **232** (1970), pp. 11–31. DOI: 10.1007/BF01391983.

[142] J. R. Kirtley and F. Tafuri. "Tunneling Measurements of the Cuprate Superconductors". In: *Handbook of High-Temperature Superconductivity*. Ed. by J. R. Schrieffer and J. S. Brooks. Springer, 2007.

[143] J. Kondo. "Resistance Minimum in Dilute Magnetic Alloys". *Prog. Theor. Phys.* **32** 1 (1964), pp. 37–49. DOI: 10.1143/PTP.32.37.

[144] P. W. Anderson. "Localized magnetic states and Fermi-surface anomalies in tunneling". *Phys. Rev. Lett.* **17** 2 (1966), p. 95. DOI: 10.1103/PhysRevLett.17.95.

[145] J. A. Appelbaum. ""s-d" exchange model of zero-bias tunneling anomalies". *Phys. Rev. Lett.* **7** 2 (1966), pp. 91–95. DOI: 10.1103/PhysRevLett.17.91.

[146] J. A. Appelbaum. "Exchange model of zero-bias tunneling anomalies". *Phys. Rev.* **154** 1963 (1967), pp. 633–643. DOI: 10.1103/PhysRev.154.633.

[147] I. Giaever and H. R. Zeller. "Superconductivity of small tin particles measured by tunneling". *Phys. Rev. Lett.* **20** 26 (1968), p. 1504. DOI: 10.1103/PhysRevLett.20.1504.

[148] K. V. Samokhin and M. B. Walker. "Localized surface states in high-temperature superconductors: Alternative mechanism of zero-bias conductance peaks". *Phys. Rev. B* **64** 17 (2001), p. 172506. DOI: 10.1103/PhysRevB.64.172506.

[149] C. Caroli, P. G. De Gennes, and J. Matricon. "Bound fermion states on a vortex line in a type II superconductor". *Phys. Lett.* **9** 4 (1964), pp. 307–309. DOI: 10.1016/0031-9163(64)90375-0.

[150] J. Nilsson, A. R. Akhmerov, and C. W. J. Beenakker. "Splitting of a Cooper pair by a pair of Majorana bound states." *Phys. Rev. Lett.* **101** 12 (2008), p. 120403. DOI: 10.1103/PhysRevLett.101.120403.

[151] K. Flensberg. "Tunneling characteristics of a chain of Majorana bound states". *Phys. Rev. B* **82** 18 (2010), p. 180516. DOI: 10.1103/PhysRevB.82.180516.

[152] A. P. Mackenzie and Y. Maeno. "The superconductivity of Sr_2RuO_4 and the physics of spin-triplet pairing". *Rev. Mod. Phys.* **75** 2 (2003), pp. 657–712. DOI: 10.1103/RevModPhys.75.657.

[153] S. Raghu, A. Kapitulnik, and S. A. Kivelson. "Hidden quasi-one-dimensional superconductivity in Sr_2RuO_4". *Phys. Rev. Lett.* **105** 13 (2010), pp. 1–4. DOI: 10.1103/PhysRevLett.105.136401.

[154] G. R. Stewart. "Heavy-fermion systems". *Rev. Mod. Phys.* **56** 4 (1984), pp. 755–787. DOI: 10.1103/RevModPhys.56.755.

[155] L. P. Gor'kov and E. I. Rashba. "Superconducting 2D System with Lifted Spin Degeneracy: Mixed Singlet-Triplet State". *Phys. Rev. Lett.* **87** 3 (2001), p. 037004. DOI: 10.1103/PhysRevLett.87.037004.

[156] Y. Tanaka, T. Yokoyama, A. V. Balatsky, and N. Nagaosa. "Theory of topological spin current in noncentrosymmetric superconductors". *Phys. Rev. B* **79** 6 (2009), pp. 1–4. DOI: 10.1103/PhysRevB.79.060505.

[157] F. S. Bergeret, A. F. Volkov, and K. B. Efetov. "Long-range proximity effects in superconductor-ferromagnet structures". *Phys. Rev. Lett.* **86** 18 (2001), pp. 4096–4099. DOI: 10.1103/PhysRevLett.86.4096.

[158] M. Eschrig and T. Löfwander. "Triplet supercurrents in clean and disordered half-metallic ferromagnets". *Nat. Phys.* **4** 2 (2008), pp. 138–143. DOI: 10.1038/nphys831.

[159] M. Alidoust, K. Halterman, and O. T. Valls. "Zero-energy peak and triplet correlations in nanoscale superconductor/ferromagnet/ferromagnet spin valves". *Phys. Rev. B* **92** 1 (2015), p. 014508. DOI: 10.1103/PhysRevB.92.014508.

[160] K. Halterman and M. Alidoust. "Half-metallic superconducting triplet spin valve". *Phys. Rev. B* **94** 6 (2016), p. 064503. DOI: 10.1103/PhysRevB.94.064503.

[161] M. Alidoust, A. Zyuzin, and K. Halterman. "Pure Odd Frequency Superconductivity at the Cores of Proximity Vortices". *Phys. Rev. B* **95** (2017), p. 045115. DOI: 10.1103/PhysRevB.95.045115.

[162] D. Goldhaber-Gordon, H. Shtrikman, D. Mahalu, D. Abusch-Magder, U. Meirav, and M. A. Kastner. "Kondo effect in a single-electron transistor". *Nature* **391** (1998), pp. 1996–1999. DOI: 10.1038/34373.

[163] G. Sellier, T. Kopp, J. Kroha, and Y. S. Barash. "π junction behavior and Andreev bound states in Kondo quantum dots with superconducting leads". *Phys. Rev. B* **72** 17 (2005), p. 174502. DOI: 10.1103/PhysRevB.72.174502.

[164] T. Costi. "Kondo effect in a magnetic field and the magnetoresistivity of Kondo alloys". *Phys. Rev. Lett.* **85** 7 (2000), p. 1504. DOI: 10.1103/PhysRevLett.85.1504.

[165] T. Hänke, M. Bode, S. Krause, L. Berbil-Bautista, and R. Wiesendanger. "Temperature-dependent scanning tunneling spectroscopy of Cr(001): Orbital Kondo resonance versus surface state". *Phys. Rev. B* **72** 8 (2005), p. 085453. DOI: 10.1103/PhysRevB.72.085453.

[166] R. A. R. Logan and J. M. J. Rowell. "Conductance anomalies in semiconductor tunnel diodes". *Phys. Rev. Lett.* **13** 13 (1964), pp. 404–406. DOI: 10.1103/PhysRevLett.13.404.

[167] A. F. G. Wyatt. "Anomalous densities of states in normal tantalum and niobium". *Phys. Rev. Lett.* **13** 13 (1964), pp. 401–404. DOI: 10.1103/PhysRevLett.13.401.

[168] A. A. Abrikosov and L. P. Gorkov. "Contribution to the Theory of Superconducting Alloys with Paramagnetic Impurities". *Sov. Phys. - JETP* **12** 6 (1961), pp. 1243–1253.

[169] M. A. Woolf and F. Reif. "Effect of Magnetic Impurities on the Density of States of Superconductors". *Phys. Rev.* **137** 2 (1965). DOI: 10.1103/PhysRev.137.A557.

[170] A. Yazdani, B. A. Jones, C. P. Lutz, M. F. Crommie, and D. M. Eigler. "Probing the local effects of magnetic impurities on superconductivity". *Science* **275** (1997).

[171] M. I. Salkola, A. V. Balatsky, and J. R. Schrieffer. "Spectral properties of quasiparticle excitations induced by magnetic moments in superconductors". *Phys. Rev. B* **55** 18 (1997), p. 12648. DOI: 10.1103/PhysRevB.55.12648.

[172] M. E. Flatté and J. M. Byers. "Local electronic structure of defects in superconductors". *Phys. Rev. B* **56** 17 (1997), p. 11231. DOI: 10.1103/PhysRevB.56.11213.

[173] A. V. Balatsky, I. Vekhter, and J.-X. Zhu. "Impurity-induced states in conventional and unconventional superconductors". *Rev. Mod. Phys.* **78** 2 (2006), pp. 373–433. DOI: 10.1103/RevModPhys.78.373.

[174] S. Nadj-Perge, I. K. Drozdov, J. Li, H. Chen, S. Jeon, J. Seo, A. H. MacDonald, B. A. Bernevig, and A. Yazdani. "Observation of Majorana fermions in ferromagnetic atomic chains on a superconductor". *Science* **346** 6209 (2014), pp. 602–607. DOI: 10.1126/science.1259327.

[175] C. Chamon, R. Jackiw, Y. Nishida, S.-Y. Pi, and L. Santos. "Quantizing Majorana fermions in a superconductor". *Phys. Rev. B* **81** 22 (2010), p. 224515. DOI: 10.1103/PhysRevB.81.224515.

[176] A. Das, Y. Ronen, Y. Most, Y. Oreg, M. Heiblum, and H. Shtrikman. "Zero-bias peaks and splitting in an Al–InAs nanowire topological superconductor as a signature of Majorana fermions". *Nat. Phys.* **8** 12 (2012), pp. 887–895. DOI: 10.1038/nphys2479.

[177] M. Leijnse and K. Flensberg. "Introduction to topological superconductivity and Majorana fermions". *Semicond. Sci. Technol.* **27** 12 (2012), p. 124003. DOI: 10.1088/0268-1242/27/12/124003.

[178] S. R. Elliott and M. Franz. "Colloquium : Majorana fermions in nuclear, particle, and solid-state physics". *Rev. Mod. Phys.* **87** 1 (2015), pp. 137–163. DOI: 10.1103/RevModPhys.87.137.

[179] P. G. de Gennes and D. Saint-James. "Elementary excitations in the vicinity of a normal metal-superconducting metal contact". *Phys. Lett.* **4** 2 (1963), pp. 4–5. DOI: 10.1016/0031-9163(63)90148-3.

[180] W. Tomasch. "Geometrical resonance in the tunneling characteristics of superconducting Pb". *Phys. Rev. Lett.* **1** 16 (1965), pp. 672–675. DOI: 10.1103/PhysRevLett.15.672.

[181] W. L. W. McMillan and P. W. P. Anderson. "Theory of geometrical resonances in the tunneling characteristics of thick films of superconductors". *Phys. Rev. Lett.* **16** 6 (1966), pp. 16–18. DOI: 10.1103/PhysRevLett.16.85.

[182] C.-R. Hu. "Midgap Surface States as a Novel Signature for d -Wave Superconductivity". *Phys. Rev. Lett.* **72** 10 (1994), pp. 1526–1529. DOI: 10.1103/PhysRevLett.72.1526.

[183] A. Carrington, F. Manzano, R. Prozorov, R. W. Giannetta, N. Kameda, and T. Tamegai. "Evidence for surface Andreev bound states in cuprate superconductors from penetration depth measurements." *Phys. Rev. Lett.* **86** 6 (2001), pp. 1074–7. DOI: 10.1103/PhysRevLett.86.1074.

[184] M. Fogelström, D. Rainer, and J. A. Sauls. "Tunneling into current-carrying surface states of high-T c superconductors". *Phys. Rev. Lett.* **79** 2 (1997), pp. 281–284. DOI: 10.1103/PhysRevLett.79.281.

[185] B. D. Josephson. "Possible new effects in superconductive tunnelling". *Phys. Lett.* **1** 7 (1962), pp. 251–253. DOI: 10.1016/0031-9163(62)91369-0.

[186] P. W. Anderson and J. M. Rowell. "Probable observation of the Josephson superconducting tunneling effect". *Phys. Rev. Lett.* **10** (1963), pp. 230–232. DOI: 10.1103/PhysRevLett.10.230.

[187] R. C. Dynes, V. Narayanamurti, and J. P. Garno. "Direct measurement of quasiparticle-lifetime broadening in a strong-coupled superconductor". *Phys. Rev. Lett.* **41** 21 (1978), pp. 1509–1512. DOI: 10.1103/PhysRevLett.41.1509.

[188] N. Mohanta and A. Taraphder. "Topological superconductivity and Majorana bound states at the $LaAlO_3/SrTiO_3$ interface". *Europhys. Lett.* **108** 6 (2014), p. 60001. DOI: 10.1209/0295-5075/108/60001.

[189] M. S. Scheurer and J. Schmalian. "Topological superconductivity and unconventional pairing in oxide interfaces." *Nat. Commun.* **6** May 2014 (2015), p. 6005. DOI: 10.1038/ncomms7005.

[190] M. S. Scheurer. "Mechanism, time-reversal symmetry, and topology of superconductivity in noncentrosymmetric systems". *Phys. Rev. B* **93** 17 (2016), p. 174509. DOI: 10.1103/PhysRevB.93.174509.

[191] B. Kalisky, E. M. Spanton, H. Noad, J. R. Kirtley, K. C. Nowack, C. Bell, H. K. Sato, M. Hosoda, Y. Xie, Y. Hikita, C. Woltmann, G. Pfanzelt, R. Jany, C. Richter, H. Y. Hwang, J. Mannhart, and K. A. Moler. "Locally enhanced conductivity due to the tetragonal domain structure in $LaAlO_3/SrTiO_3$ heterointerfaces." *Nat. Mater.* **12** (2013), p. 1091. DOI: 10.1038/nmat3753.

[192] K. Yada, S. Onari, Y. Tanaka, and J. I. Inoue. "Electrically controlled superconducting states at the heterointerface $SrTiO_3/LaAlO_3$". *Phys. Rev. B* **80** 14 (2009). DOI: 10.1103/PhysRevB.80.140509.

[193] M. Honig, J. A. Sulpizio, J. Drori, A. Joshua, E. Zeldov, and S. Ilani. "Local electrostatic imaging of striped domain order in $LaAlO_3/SrTiO_3$." *Nat. Mater.* **12** 12 (2013), pp. 1112–8. DOI: 10.1038/nmat3810.

[194] N. Pavlenko, T. Kopp, E. Y. Tsymbal, G. A. Sawatzky, and J. Mannhart. "Magnetic and superconducting phases at the $LaAlO_3/SrTiO_3$ interface: The role of interfacial Ti 3d electrons". *Phys. Rev. B* **85** 2 (2012), p. 020407. DOI: 10.1103/PhysRevB.85.020407.

[195] M. Salluzzo, S. Gariglio, D. Stornaiuolo, V. Sessi, S. Rusponi, C. Piamonteze, G. M. De Luca, M. Minola, D. Marré, A. Gadaleta, H. Brune, F. Nolting, N. B. Brookes, and G. Ghiringhelli. "Origin of interface magnetism in $BiMnO_3/SrTiO_3$ and $LaAlO_3/SrTiO_3$ heterostructures". *Phys. Rev. Lett.* **111** (2013), p. 087204. DOI: 10.1103/PhysRevLett.111.087204.

[196] V. Umansky and M. Heiblum. "MBE growth of high-mobility 2DEG". In: *Mol. Beam Ep. From Res. to Mass Prod.* Ed. by M. Henini. Amsterdam: Elsevier, 2013.

[197] M. J. Manfra. "Molecular Beam Epitaxy of Ultra-High Quality AlGaAs/GaAs Heterostructures: Enabling Physics in Low-Dimensional Electronic Systems". *Annu. Rev. Condens. Matter Phys.* **5** (2014), pp. 347–373. DOI: 10.1146/annurev-conmatphys-031113-133905.

[198] J. Falson, Y. Kozuka, M. Uchida, J. H. Smet, T.-H. Arima, A. Tsukazaki, and M. Kawasaki. "MgZnO/ZnO heterostructures with electron mobility exceeding 1 × 106 cm2/Vs". *Sci. Rep.* **6** (2016), p. 26598. DOI: 10.1038/srep26598.

[199] Q.-Y. Wang, Z. Li, W.-H. Zhang, Z.-C. Zhang, J.-S. Zhang, W. Li, H. Ding, Y.-B. Ou, P. Deng, K. Chang, J. Wen, C.-L. Song, K. He, J.-F. Jia, S.-H. Ji, Y.-Y. Wang, L.-L. Wang, X. Chen, X.-C. Ma, and Q.-K. Xue. "Interface-Induced High-Temperature Superconductivity in Single Unit-Cell FeSe Films on SrTiO 3". *Chinese Phys. Lett.* **29** 3 (2012), p. 037402. DOI: 10.1088/0256-307X/29/3/037402.

[200] W. A. Little. "Vitaly Ginzburg and high-temperature superconductivity". *J. Supercond. Nov. Magn.* **19** 3-5 (2006), pp. 443–447. DOI: 10.1007/s10948-006-0170-y.

[201] J. Bardeen, L. N. Cooper, and J. R. Schrieffer. "Theory of superconductivity". *Phys. Rev.* **108** 5 (1957). DOI: 10.1103/PhysRev.108.1175.

[202] L. N. Cooper. "Bound electron pairs in a degenerate Fermi gas". *Phys. Rev.* **104** 4 (1956), p. 1189. DOI: 10.1103/PhysRev.104.1189.

[203] N. N. Bogoliubov. "A new method in the theory of superconductivity". *JETP* **7** 1 (1958), pp. 41–46.

[204] J. Valatin. "Comments on the theory of superconductivity". *Nuovo Cim.* **7** 6 (1958), pp. 843–857. DOI: 10.1007/BF02745589.

[205] H. J. Maris and L. P. Kadanoff. "Teaching the renormalization group". *Am. J. Phys.* **46** 6 (1978), p. 652. DOI: 10.1119/1.11224.

[206] N. Bansal, Y. S. Kim, M. Brahlek, E. Edrey, and S. Oh. "Thickness-independent transport channels in topological insulator Bi 2Se 3 thin films". *Phys. Rev. Lett.* **109** 11 (2012), pp. 1–5. DOI: 10.1103/PhysRevLett.109.116804.

[207] R. Pentcheva, M. Huijben, K. Otte, W. E. Pickett, J. E. Kleibeuker, J. Huijben, H. Boschker, D. Kockmann, W. Siemons, G. Koster, H. J. W. Zandvliet, G. Rijnders, D. H. a. Blank, H. Hilgenkamp, and a. Brinkman. "Parallel Electron-Hole Bilayer Conductivity from Electronic Interface Reconstruction". *Phys. Rev. Lett.* **104** 16 (2010), p. 166804. DOI: 10.1103/PhysRevLett.104.166804.

[208] D. Stornaiuolo, C. Cantoni, G. M. De Luca, R. Di Capua, E. Di. Gennaro, G. Ghiringhelli, B. Jouault, D. Marrè, D. Massarotti, F. Miletto Granozio, I. Pallecchi, C. Piamonteze, S. Rusponi, F. Tafuri, and M. Salluzzo. "Tunable spin polarization and superconductivity in engineered oxide interfaces". *Nat. Mater.* **15** (2016), pp. 278–283. DOI: 10.1038/nmat4491.

[209] N. Nagaosa, J. Sinova, S. Onoda, A. H. MacDonald, and N. P. Ong. "Anomalous Hall effect". *Rev. Mod. Phys.* **82** 2 (2010), pp. 1539–1592. DOI: 10.1103/RevModPhys.82.1539.

LIST OF PUBLICATIONS

1. **Journal Publications**

2017 Lukas Kuerten, Cristoph Richter, Narayan Mohanta, Thilo Kopp, Arno Kampf, Jochen Mannhart, and Hans Boschker. "In-gap features in superconducting $LaAlO_3$–$SrTiO_3$ interfaces observed by tunneling spectroscopy" *Phys. Rev. B.* **96** 014513

2. **Conference talks**

2015 Lukas Kuerten Evangelos Fillis-Tsirakis, Christoph Richter, Jochen Mannhart, and Hans Boschker. "Critical magnetic fields of superconducting $LaAlO_3$–$SrTiO_3$ interfaces". *Workshop on Oxide Electronics 22*, Paris, France

2016 Lukas Kuerten Evangelos Fillis-Tsirakis, Jochen Mannhart, and Hans Boschker. "In-gap features in tunnel spectra of the superconducting $LaAlO_3$–$SrTiO_3$ 2DEL". *International Conference on Superconductivity and Magnetism 2016*, Fethiye, Turkey

3. **Conference posters**

2015 Lukas Kuerten, Evangelos Fillis-Tsirakis, Hans Boschker, Christoph Richter, and Jochen Mannhart. "Critical Magnetic Fields in Superconducting $LaAlO_3$–$SrTiO_3$ interfaces". *International School on Oxide Electronics 2015*, Cargèse, France

2016 Lukas Kuerten, Evangelos Fillis-Tsirakis, Hans Boschker and Jochen Mannhart. "States inside the superconducting gap of the $LaAlO_3$–$SrTiO_3$ interface electron system". *Spectroscopies in Novel Superconductors 2016*, Ludwigsburg, Germany

2017 Lukas Kuerten, Christoph Richter, Narayan Mohanta, Thilo Kopp, Arno Kampf, Jochen Mannhart, and Hans Boschker. "In-gap states in superconducting $LaAlO_3$–$SrTiO_3$ interfaces observed by tunneling spectroscopy". *28th International Conference on Low Temperature Physics*, Göteborg, Sweden

If I have seen further it is by standing on the shoulders of Giants.
Sir Isaac Newton

ACKNOWLEDGEMENTS

Mein aufrichtiger Dank gilt zuallererst Herrn Professor Mannhart für die Betreuung meiner Arbeit und seine permanente Unterstützung meiner Bemühungen. Ich möchte Ihm danken für seinen Optimismus und seine Begeisterung für die Wissenschaft und auch ganz besonders für sein Verständnis dafür, dass die Familie zeitweilig Vorrang vor der Arbeit nehmen musste.

Danken möchte ich auch Herrn Professor Dressel dafür, dass er die Aufgabe des Zweitgutachters übernommen hat und für sein Interesse an meiner Arbeit.

A huge thanks goes to Hans Boschker, who gave me all the freedom I wanted but was always available for advice when I needed it. Even if he did not know the answer right away, he had the Socratean gift of asking the right questions. But we also share many memories from outside the institute such as, going on bike tours, visiting the opera or half a ballet, or simply enjoying good food, good drink and good company.

Many thanks are due to Jone Zabaleta for her tireless efforts fighting with feedthroughs and epoxy for the pressure cell. Thank you also for many days together in the life-draining PPMS lab and for your (hectic) energy.

Vielen Dank an René Berktold, der mir geduldig alle Details der Probenherstellung beibrachte und nicht müde wurde zu betonen, dass man eine Sache besser gleich von Anfang an sauber und richtig macht. Natürlich auch vielen Dank für Beratung in allen Lebenslagen - und für all den Unfug!

Carsten Woltmann gebührt mein Dank dafür, dass er mir alles über Transistoren beibrachte und mich immer zum Biertrinken motivierte.

I learned many PLD tricks from Takayuki Harada - many thanks, and also for the unfailingly positive attitude!

Thanks Aggelos for all our joint efforts to keep the cryostat running far beyond its retirement age and for good times in the office.

I would like to thank all my office-mates, Yeliz, Aggelos and Ali for their good spirits, for their teasing and the help in adjusting to the group. Let's hope for a office-reunion wine!

Meinen Nachbarn Pascal, Robin und Flo danke ich für zahllose Expeditionen auf der Suche nach Eis oder Bier und für so manchen Plausch zwischendurch.

Renate Zimmermann danke ich dafür, dass alle bürokratischen Hindernisse so reibungslos aus dem Weg geräumt wurden und zudem für die zuverlässige Versorgung mit Schokolade.

Meine Arbeit hat immens profitiert von all den Menschen, die unsere Maschinen und Labore zuverlässig am Laufen halten: Zuvorderst möchte ich den Technikern der Mannhart-Gruppe danken, insbesondere Manfred Schmid, der unseren Kryostaten von den Toten auferweckte und Wolfgang Winter, der unermüdlich alles vom Handschuh bis zur Vakuumkammer besorgen konnte. Außerdem auch Wolfgang Braun für viele Lektionen über RHEED und Vakuum und für Perfektionismus in allen Lebenslagen. Aber auch alle Beschäftigten von Tieftemperaturservice,

Forscherbedarfslager, Elektronik und Verwaltung haben dafür gesorgt, dass ich mich ungehindert auf meine Arbeit konzentrieren konnte.

Many thanks are also due to all other members of the Mannhart group, who have made the past three and a half years a memorable experience.

I would also like to thank Professor Matt Dawber for kindling my interest in solid state physics - without him I would not be where I am today.

Der letzte Abschnitt der Danksagung gilt den Menschen, die nicht meine Arbeit im Besonderen, sondern vielmehr mich als Ganzes geprägt haben. Hier möchte ich zunächst meinen Eltern danken, die mich stets ermuntert haben zu lesen, zu fragen und zu verstehen, die mich immer unterstützt haben, die es aber auch verstanden loszulassen.

Zuletzt, aber ganz sicher nicht am Wenigsten, möchte ich Julia danken für moralische und auch tatkräftige Unterstützung zu jeder Zeit, für Ansporn und Ablenkung und dafür, dass sie mich immer motiviert über meinen Tellerrand hinaus zu blicken.